Two Parameter Engineering Fracture Mechanics.

By

Iain James MacLennan

Submission for Degree of Doctor of Philosophy.
(Ph.D)

January 1996

Department of Mechanical Engineering
University of Glasgow
Glasgow
G12 8QQ

Abstract.

The object of this work was to investigate and expand on previously carried out research into elastic-plastic crack tip fields using the first two terms of the Williams expansion to characterise the degree of crack tip constraint. As a precursor to this research a history of fracture mechanics is also presented.

In the present work crack tip fields in small scale yielding have been determined using modified boundary layer formulations in an attempt to model the influence of the second order term of the Williams expansion, the T-stress. The prime object of this thesis was to investigate and expand on previously carried out research into a two parameter characterisation of elastic-plastic crack tip fields using the second parameter of the Williams expansion(T), which attempts to characterise the degree of crack tip constraint. Modified Boundary Layer formulations in conditions of plane strain were implemented to derive a suitable reference solutions, against which the effects of out of plane strains can be compared and the validity of presently established reference fields can be gauged. The effect of out of plane non-singular stress, S, on the crack tip stress field were also considered, where constraint was largely determined by T.

A wide range of analyses have been carried out, from the microstructural scale to complete engineering components in an attempt to characterise crack tip stress fields. The ability to apply two parameter fracture concepts to real engineering structures requires methods for calculating T for complex components with realistic semi-elliptical defects. A simple engineering method for achieving this was developed making use of linespring elements in the finite element package ABAQUS. This approach was validated by the calculation of T for semi-elliptical cracks at the chord-brace intersection of a tubular welded joint, modelled using the mesh generation program PATRAN.

The micromechanics of cleavage, using the Ritchie-Knott-Rice model have also been constructed. This work relates the ratio of J for unconstrained and constrained geometries to critical microstructural distance, critical cleavage stress and the toughness ratio on the strain

hardening effect. The elastic-plastic behaviour of short and deeply cracked bend bars has previously been described by Betegón and Hancock based on the first two terms of the Williams expansion. A local cleavage criterion has been applied to these fields to indicate the effect of loss of constraint on lower shelf toughness of shallow cracked bend bars. The work models the maximum temperature at which cleavage can occur in these geometries to show the effect of constraint and a/W ratio of cracked bend bars on the ductile-brittle transition temperature. This has also been backed by a significant experimental research program.

Finally constraint dependent toughness has been considered in relation to failure assessment methodologies. A simple engineering method for modifying these Failure Assesssment Diagrams has been presented, this consists of considering the constraint matched toughness of the strucutre. This procedure recovers the original Failure Assessment Line and unifies the constraint dependent fracture toughness within defect assessment schemes which utilise Failure Assessment Diagrams.

Acknowledgements.

I wish to express my sincere gratitude to my supervisor Professor John. W. Hancock, for his invaluable guidance, patience, constant advice and encouragement throughout the course of this research, and afterwards. Thanks are also due to Dr. John Sumpter of the Defence Research Agency under whose auspices this research under a Ministry of Defence research grant was carried out.

Gratitude is also extended to Hibbit, Karlsson and Sorensen, INC. for access to ABAQUS under academic licence.

I would also like to express my thanks to Mr Alex Torry for his great assistance in the experimental research carried out within this thesis. There are numerous other people who in some way have contributed to this thesis and the work contained within, to you all, thank you.

Finally I would like to thank my family, especially my mother for all her support throughout.

Table of Contents.

Abstract.

Acknowledgements.

Contents.

List of Figure Captions.

Introduction. 1

Chapter 1: Linear Elastic Fracture Mechanics.

1.1: Griffith's Criterion. 3

1.2: Stress Field at a Crack Tip. 5

1.3: Determination of Stress Intensity Factors. 8

1.4: Small Scale Yielding. 10

1.5: Validity of Linear Elastic Fracture Mechanics. 11

Chapter Two: Benchmarking Linear Elastic Fracture Mechanics

2.1: Introduction. 13

2.2: Numerical Methods. 13

2.3: Determination of the Stress Intensity Factor. 15

2.3.1: Displacement Method. 15

2.3.2: Stress Method. 15

2.3.3: Virtual Crack Extension Method. 16

2.3.4: Line Spring and Shell Element Method. 16

2.3.5: Published Solutions. 16

2.4: Conclusion. 18

Chapter Three: Elastic Plastic Fracture Mechanics.

3.1: Introduction. 19

3.2: Crack Tip Opening Displacement, (δ). 20

3.3:The J-Integral. 21

3.4: The Engineering Approach. 29

3.5: Limits of Single Parameter Characterisation. 31

3.6: Two Parameter Characterisation. 33

3.7: Elastic T-Stress. 34

3.8: Higher Order Asymptotic Solutions. 37

3.9: Small Strain Difference Term, Q. 39

3.10: Local Failure Criterion. 41

3.11: Conclusion. 47

Chapter Four: Boundary Layer Formulations.

4.1: Introduction. 48

4.2: Numerical Methods. 49

4.3: Results. 51

4.4: Discussion. 52

4.5: Conclusion. 53

Chapter Five: Generalised Plane Strain Analysis.

5.1: Introduction. 55

5.2: Numerical Methods. 57

5.3: Results. 58

5.3.1: Positive T-Stress Analysis. 58

5.3.2: Negative T-Stress Analysis. 58

5.4: Neutral Axis. 59

5.5: Conclusion. 60

Chapter Six: Line Spring Analysis of Semi-Elliptical Cracks in a Tubular T-Joint.

6.1: Introduction. 61

6.2: Determination of Non-Dimensional Stress Intensity Factor. 63

6.3: Determination of T-Stress. 64

6.4: Numerical Method. 66

6.4.1: Benchmarking. 66

6.4.2: Tubular T-Joint Analysis. 66

6.5: Results. 67

6.5.1: Benchmarking. 67

6.5.2: Tubular T-Joint Analysis. 67

6.6: Discussion. 68

6.7: Conclusion. 68

Chapter Seven: The Effect of Constraint on the Micro-Mechanics of the Ductile-Brittle Transition.

7.1: Introduction. 69

7.2: Cleavage Fracture. 70

7.3: Ductile Fracture. 71

7.4: Temperature Effects on Material Properties 72

7.5: Numerical Methods. 73

7.6: Discussion. 76

7.7: Conclusions. 77

Chapter Eight: Constraint Based Failure Assessment Diagrams.

8.1: Introduction. 78

8.2: R6 Failure Assessment Diagrams. 79

8.3: Classical Failure Assessment Diagrams. 82

8.4: Constraint Based Failure Assessment Diagrams. 84

8.5: Analytical Results. 88

8.6: Experimental Validification. 89

8.7: Discussion. 90

8.8: Conclusion. 92

Chapter Nine: Experimental Fracture Mechanics.

9.1: Introduction. 93

9.2: Notch Tensile Experiments. 93

9.2.1: Experimental Notch Theory. 93

9.2.2: Experimental Results. 95

9.3: Torsion Experiments. 96

9.3.1: Torsion Theory. 96

9.3.2: Torsion and Tension Experimental Results. 97

9.4: Finite Element Analysis of Notch Tensile Specimens. 98

9.4.1: Notch Tensile Finite Element Results. 98

9.5: Three Point Bend Experiments. 99

9.5.1: Three Point Bend Theory. 100

9.5.2: Three Point Bend Experimental Results. 102

9.6: Conclusion. 103

Final Conclusions. 105

References. 107

Figure Captions.

Figure 1.1: Infinite Centre Cracked Panel with Fixed Ends.

Figure 1.2: Load-Displacement Graph for crack of Length a.

Figure 1.3: Elastic Energy Release Graph for Propogation of Crack from a to a+da.

Figure 1.4: Schematic of Fracture Modes.

Figure 1.5: Crack in an Infinite Plate Stress Distribution.

Figure 1.6: Geometric Parameter for Centre Cracked Test Specimen.

Figure 1.7: Contour Placement as Crack Tip Advances for Virtual Crack Extension.

Figure 1.8: Definition of Small Scale Yielding.

Figure 1.9: Graphical Representations of Plastic Zones.

Figure 2.1: Schematic of Model Analysis.

Figure 2.2: Model of an Eight Noded Biquadratic Displacement, Linear Pressure Element with Reduced Integration.

Figure 2.3: Schematic of Displacement Loading.

Figure 2.4: Deformed Displaced Analysis Mesh.

Figure 2.5: Midside Node Illustration on a Collapsed Eight Noded Plane Strain Element at a Crack Tip.

Figure 2.6: Line-Spring Element (LS3S).

Figure 2.7: Normal Midside Node Position.

Figure 2.8: Quarter Point Node Arrangement.

Figure 2.9: Results from LEFM Benchmarking.

Figure 3.1: Dugdale 'Strip-Yield' Model for Crack Tip Plasticity.

Figure 3.2: Idealised Schematic of the Results of Rosenfield et al. Investigation.

Figure 3.3: Definition of Crack Tip Displacement (δ).

Figure 3.4: Determination of J by Potential Energy Difference.

Figure 3.5: Definition of the J-Integral.

Figure 3.6: Crack Contour Integral and Crack Tip Coordinate System.

Figure 3.7: Path Independence of the J-Integral.

Figure 3.8: Varaition of d_n for Plane Strain (Shih et al. 1981).

Figure 3.9: I_n for Various Work Hardening Exponents.

Figure 3.10: Deeply Cracked Bend Bar in Pure Bending.

Figure 3.11: Moment-Rotation Diagram for a Non-Hardening Material.

Figure 3.12: Change in Work Done for a Non-Hardening Material.

Figure 3.13: Load-CMOD Experimental Trace.

Figure 3.14: Slip Line Fields for CCP and DECB in Tension and SECB.

Figure 3.15: Biaxiality Parameters for Single Edge Cracked Specimens, Sham (1991).

Figure 3.16: Full Prandtl Field.

Figure 3.17: Plasticity around Crack Tip for $\frac{T}{\sigma_0}$ = 0 Field.

Figure 3.18:Plasticity around Crack Tip for $\frac{T}{\sigma_0}$ = -0.443 and -0.7 Fields.

Figure 3.19: Graphed Value of the Power of the Second term in the Asymptotic Expansion of Sharma and Aravas(1991).

Figure 3.20: Site of Most Probable Crack Initiation.

Figure 4.1: Small Strain Crack Tip Node Arrangement.

Figure 4.2: Large Strain Crack Tip Node Arrangement.

Figure 4.3: Boundary Layer Formulation Mesh.

Figure 4.4: Ramberg-Osgood Stress-Strain Curves (n=3, 6, 13 and ∞).

Figure 4.5: Hoop Stress Directly Ahead of the Crack Tip (n=∞, T=0).

Figure 4.6: Normalised Mean Stress Directly Ahead of the Crack Tip (n=∞, T=0).

Figure 4.7: Hoop Stress Directly Ahead of the Crack Tip (n=3, T=0).

Figure 4.8: Normalised Mean Stress Directly Ahead of the Crack Tip (n=3, T=0).

Figure 4.9: Small Strain Normalised Hoop Stresses (n=6).

Figure 4.10: Large Strain Normalised Hoop Stresses (n=6).

Figure 4.11: Small Strain Normalised Mean Stresses (n=6).

Figure 4.12: Large Strain Normalised Mean Stresses Directly Ahead of the Crack Tip (n=6).

Figure 4.13: Plastic Equivalent Strain Directly Ahead of the Crack Tip (n=6).

Figure 4.14: Small Strain Normalised Hoop Stress Directly Ahead of the Crack Tip (n=13).

Figure 4.15: Large Strain Normalised Hoop Stress Directly Ahead of the Crack Tip (n=13).

Figure 4.16: Small Strain Normalised Mean Stress Directly Ahead of the Crack Tip (n=13).

Figure 4.17: Large Strain Normalised Mean Stress Directly Ahead of the Crack Tip (n=13).

Figure 4.18: Plastic Equivalent Strain Directly Ahead of the Crack Tip (n=13).

Figure 4.19: Curve fit for Boundary Layer Formulation of $n=\infty$, T=0.

Figure 4.20: Curve fit for Boundary Layer Formulation of n=3, T=0.

Figure 4.21: Curve fit for Boundary Layer Formulation of n=6, T=0.

Figure 4.22: Curve fit for Boundary Layer Formulation of n=13, T=0.

Figure 5.1: Bounded Planes Diagram.

Figure 5.2: Finite Element Mesh.

Figure 5.3: Displaced Mesh for Deep Crack Analysis.

Figure 5.4: Displaced Mesh for Shallow Crack Analysis.

Figure 5.5: Generalised Plane Strain Analysis of a body exhibiting +T and -S stresses.

Figure 5.6: Generalised Plane Strain Analysis of a body exhibiting +T and +S stresses.

Figure 5.7: Plane Strain Analysis of a body exhibiting +T stress.

Figure 5.8: Generalised Plane Strain Analysis of a body exhibiting -T and -S stresses.

Figure 5.9: Generalised Plane Strain Analysis of a body exhibiting -T and+S stresses.

Figure 5.10: Plane Strain Analysis of a body exhibiting -T stress.

Figure 5.11: Neutral Axis for Tension Loading.

Figure 5.12: Neutral Axis for Pure Bending.

Figure 5.13: Comparison of Tension and Bending Fields.

Figure 6.1: Part Through Surface Crack.

Figure 6.2: Line-Spring Modelling.

Figure 6.3: Idealised Model of Line-Spring Concept.

Figure 6.4: Idealisation of Semi-Elliptical Crack.

Figure 6.5: Geometry and Load Dependent Parameters after Sham (1991).

Figure 6.6 Schematic of Tubular Welded Joint

Figure 6.7: Geometry of Tubular Welded Joint (Huang and Hancock (1986)).

Figure 6.8: Benchmarking Results.

Figure 6.9: Comparison of Benchmark Analyses Biaxiality with Sham (1991).

Figure 6.10: Comparison of Stress Intensity Ratios for T-Joint Analyses.

Figure 6.11: T-Joint Analysis Results.

Figure 7.1: Transgranular Cleavage.

Figure 7.2: Ductile Failure.

Figure 7.3: Ductile-Brittle Transition.

Figure 7.4: Cleavage Steps.

Figure 7.5: Cleavage Tongues.

Figure 7.6: Ritchie, Knott and Rice Stress Contolled Cleavage Model.

Figure 7.7: Temperature Dependent Yield Stress after Benett and Sinclair (1966).

Figure 7.8: Idealsied Failure Loci.

Figure 7.9: Family of Small and Large Strain Solutions for n=13.

Figure 7.10: Non-dimensionalised J-T loci for Cleavage at a Range of fracture Stresses for n=13.

Figure 7.11: Normalised Experimental J-T loci, after Betegón (1990).

Figure 7.12: Effect of Temperature on Toughness with varying Degreees of Constraint.

Figure 7.13: Effect of Temperature on Toughness with varying Degrees of Constraint.

Table 1: Chemical Composition of BS4360 grade 50D Steel.

Figure 7.14: Temperature Dependence of J-T Loci for a Critical Cleavage Stress of 1400 MPa.

Figure 7.15: Temeprature Dependence of J-T Loci for a Critical Cleavage Stress of 1800 MPa.

Figure 7.16: The Influence of Geometry on Toughness.

Figure 7.17: The Effect of $\frac{a}{W}$ on the Transition Temperature for a Range of Specimen Widths.

Figure 7.18: The Effect of Size on the Transition Temperature for a Range of Geometries.

Figure 7.19: Variation of Initiation J as a Function of Temperature, after Al-Ani (1991).

Figure 7.20: Experimental Results for Deep and Shallow Cracks, after Sumpter (1982).

Figure 7.21: Variation of Initiation J as a Function of Temperature for BS4360 Grade 50D.

Figure 8.1: Original and Simplest Form of a Failure Assessment Diagram.

Figure 8.2: The General Failure Line as given by R6 Revision 3.

Figure 8.3: Single Edge Cracked Bar under Three Point Bending (SEC3PB).

Figure 8.4: Centre Cracked Plate under Remote Tension.

Figure 8.5: Refence and Limit Loads as Derived by Shih and Millar.

Figure 8.6: h_1 factors for CCP and SEC3PB.

Figure 8.7: Idealised Failure Loci.

Figure 8.8: J-T History showing the Intersection Point for Loci, described by m=0.1.2, n=13.

Figure 8.9: Geometry Specific Failure Assessment Diagram, SEC3PB, n=13.

Figure 8.10: Geometry Specific Failure Assessment Diagram, SEC3PB, n=6.

Figure 8.11: Geometry Specific Failure Assessment Diagram, CCP, n=13.

Figure 8.12: Geometry Specific Failure Assessment Diagram, CCP, n=6.

Figure 8.13: Failure Assessment Diagram, SEC3PB, n=13, m=0.

Figure 8.14: Failure Assessment Diagram, SEC3PB, n=6, m=0.

Figure 8.15: Effect of Strain Hardening Rate (m=0).

Figure 8.16: Failure Assessment Diagram, SEC3PB, n=13,m=1.

Figure 8.17: Modified Failure Assessment Diagram, SEC3PB, n=13, m=1.

Figure 8.18: Failure Assessment Diagram, SEC3PB, n=6, m=1.

Figure 8.19: Modified Failure Assessment Diagram, SEC3PB, n=6, m=1.

Figure 8.20: Failure Assessment Diagram, SEC3PB, n=13, m=2.

Figure 8.21: Modified Failure Assessment Diagram, SEC3PB, n=13, m=2.

Figure 8.22: Failure Assessment Diagram, SEC3PB, n=6, m=2.

Figure 8.23: Modified Failure Assessment Diagram, SEC3PB, n=6, m=2.

Figure 8.24: Failure Assessment Diagram, SEC3PB, n=13, m=3.

Figure 8.25: Modified Failure Assessment Diagram, SEC3PB, n=13, m=3.

Figure 8.26: Failure Assessment Diagram, SEC3PB, n=6, m=3.

Figure 8.27: Modified Failure Assessment Diagram, SEC3PB, n=6, m=3.

Figure 8.28: Mild Steel Plate Three Point Bend Tests (Sumpter and Forbes (1992)).

Figure 8.29: Mild Steel Plate Centre Crack Tension Tests (Sumpter and Forbes (1992)).

Figure 8.30: Weld Data Three Point Bened Tests, Sumpter (1993).

Figure 8.31: Plate Steel Three Point Bend Tests (Betegón (1991)).

Figure 8.32: BS 4360 Grade 50D Steel Three Point Bend Tests (MacLennan).

Figure 8.33: A710 Three Point Bend Tests (Hancock, Reuter and Parks (1991).

Figure 8.34: Chemical Composition of low grade Mild Steel.

Figure 8.35: Chemical Composition of Betegón Test Plate.

Figure 8.36: Chemical Composition of A710 Steel.

Figure 8.37: Experimental Material Loci.

Figure 8.38: Experimental Material Loci.

Figure 8.39: Failure Assessment Diagram, Sumpter and Forbes (1992), SEC3PB, n=5.

Figure 8.40: Modified Failure Assessment Diagram, Sumpter and Forbes (1992) ,SEC3PB , n=5.

Figure 8.41: Failure Assessment Diagram, Sumpter and Forbes (1992), CCP, n=5.

Figure 8.42: Modified Failure Assessment Diagram, Sumpter and Forbes (1992) ,CCP , n=5.

Figure 8.43: Failure Assessment Diagram, Sumpter Weld Data, SEC3PB, n=10.

Figure 8.44: Modified Failure Assessment Diagram, Sumpter Weld Data ,SEC3PB , n=10.

Figure 8.45: Failure Assessment Diagram, Betegón (1991), SEC3PB, n=14.

Figure 8.46: Modified Failure Assessment Diagram, Betegón (1991), SEC3PB, n=14.

Figure 8.47: Failure Assessment Diagram, MacLennan, SEC3PB, n=6.

Figure 8.48: Modified Failure Assessment Diagram, MacLennan, SEC3PB, n=6.

Figure 8.49: Failure Assessment Diagram, Hancock, Reuter and Parks (1991), n=10.

Figure 8.50: Modified Failure Assessment Diagram, Hancock, Reuter and Parks (1991), n=10.

Figure 8.51: Combined Failure Assessment Diagram.

Figure 8.52: Combined Modified Failure Assessment Diagram.

Figure 8.53: Lower Bound Failure Assessment Diagram.

Figure 8.54: Modified Lower Bound Failure Assessment Diagram.

Figure 9.1: Schematic Ductile Brittle Transition.

Figure 9.2: Notch Tension Specimens.

Figure 9.3: Stress Distribution(after Bridgman (1952)).

Figure 9.4: Crack in Centre of Notch Tensile Specimen.

Figure 9.5: Liquid Nitrogen Test Setup for Notch Tensile Experiments.

Figure 9.6: Low Temperature Test Setup for Notch Tensile Experiments.

Figure 9.7: High Temperature Test Setup for Notch Tensile Experiments.

Figure 9.8: Applied Load versus Specimen Diameter Reduction.

Figure 9.9: Average Axial Stress versus Plastic Strain.

Figure 9.10: Torson Experimental Specimen.

Figure 9.11: Angle of Twist of Torsion Specimen.

Figure 9.12: Stress Triaxiality for Temperature Tests.

Table 1: Torsional Experimental Results.

Figure 9.13:Cleavage Instability for Liquid Nitrogen Experiments.

Figure 9.14a:Micromechanical Examination of Plane Tensile Specimen Experiment (-80C).

Figure 9.14b:Micromechanical Examination of A Notch Specimen Experiment (- 80C).

Figure 9.15: D Notch Finite Element Mesh.

Figure 9.16: A Notch Finite Element Mesh.

Figure 9.17: Plane Finite Element Mesh.

Figure 9.18: Triaxiality of Finite Element Analyses.

Figure 9.19: Maximum Principal Stress for Finite Element Analyses.

Figure 9.20: Equivalent Plastic Strain for Finite Element Analyses.

Figure 9.21: Diagram of Three Point Bend Specimen.

Figure 9.22: Liquid Nitrogen Temperature Experiment Set-up.

Figure 9.23: Three Point Bend Specimen with Clip Gauge Attached Knife Edges.

Figure 9.24: Tank and Specimen Arrangement.

Figure 9.25: Results of Three Point Bend Experiments.

Figure 9.26: J versus Crack Extension at Room Temperature (SEC3PB).

Figure 9.27: Crack Tip Opening versus Crack Extension at Room Temperature (SEC3PB).

Figure 9.28: J versus Crack Extension at -50C (SEC3PB).

Figure 9.29: Crack Tip Opening versus Crack Extension at -50C (SEC3PB).

Figure 9.30: Detailed Crack Tip Photograph.

Figure 9.31: Transition Curve for BS4360 Grade 50D.

Introduction.

The development of fracture mechanics was originally motivated by a series of catastrophic fractures of high strength steels associated with welded joints. With the increased usage of high strength steels in the latter half of the nineteenth century the frequency of these accidents rose to an alarming level. A number of these accidents were due to inadequate design and inept fabrication, but a high proportion were due to flaws and defects within the materials.

The advent of welding, and the introduction of covered electrodes in 1912 allowed mass production of high quality structural weldments. This allowed the complete fabrication of structures, leading to the launch in 1921 of the first all welded merchant ship. This new method of construction was to experience problems, in a catalogue of disasters. In the 1930's three truss welded bridges in Belgium failed. In 1943 the first all welded tanker constructed by the Kaiser company of the United States broke in half in the fitting out dock. By 1953 of the 4694 all welded ships constructed, 233 had been subject to hull failures of some form, and 1056 had been subject to potentially dangerous structural failures. As a result of analysis of these failures it was found that the primary causes of fracture were stress concentrations and material defects. These fractures were found to have been particularly brittle, promoted by the low temperatures and the state of the stress triaxiality at the flaw. Under these conditions steels can fracture by cleavage, with minimal energy absorption. It was also found that above a transition temperature the form of fracture changed from a brittle to ductile mode. This temperature was found to be a function of the welding procedure.

Although these findings highlighted a number of serious problems with all welded ships. It was however impossible to return to riveting because of the economic advantages of welding, and its potential to revolutionise design, as long as these problems could be overcome.

A key feature of the all welded design is that the structure is a single monolithic unit, of which even the most trivial weld is an integral part. This means that a crack propagating from a single weld is capable of passing through the whole structure with nothing to impede its progress. A prime example was the T2 tanker Ponagansett which broke up in calm conditions as a result of a crack originating at a tack weld holding a cable clip to the deck.

Stress concentrations at hatch corners in cases like this are particularly important. In real engineering structures, such as oil rig jackets it is inevitable that there will be flaws present, so there is a need for a rational method of assessing the significance of flaws, and developing materials that are capable of tolerating them.

Concurrent with the growth in welding, new high strength alloys were being developed, notably in the aerospace industries. Some of these high strength alloys were banned from use due to their small critical crack size, thereby negating any advantage of their high strength. In the aerospace industry where the weight of a component has a considerable influence on performance characteristics, lower safety factors are applied to induce a corresponding weight saving. Service stresses in these applications could be high enough to induce cracks especially when environmental effects and stress concentrations were considered. These low stress fractures induced by small critical cracks were very similar to brittle fractures of welded low strength steel structures, in that there is very little plastic deformation, although their failure micro-mechanism are frequently described as ductile.

From this background fracture mechanics was developed to meet the need to assess the effects of flaws and to measure the fracture toughness of structural materials. A central purpose of fracture mechanics is to predict the critical crack size at which fracture will occur and how long it will take the crack to grow from an initial size to the critical fracture condition.

Fracture mechanics is split into two distinct branches: linear elastic and elastic plastic fracture mechanics (henceforth lefm and epfm). The applicability of these branches is governed by the size of the plastic zone and the amount of crack tip deformation. As long as the plastic zone is small compared to the critical dimensions of the body then lefm is valid, under conditions described as small scale yielding. Outwith these conditions epfm becomes relevant since the plastic zone is no longer a minor perturbation of the elastic stress field.

Classical fracture mechanics has endeavoured to establish the relationship between the crack size and the applied load, on the basis of a one parameter characterisation, of the stress and strain fields at the crack tip. In a series of recent developments the severe restrictions of classical epfm have been relaxed by a two parameter characterisation of the elastic-plastic fields. The purpose of the present work is to extend the previous work on two parameter characterisation and determine the range of validity for such an approach, and show the applicability of the higher order terms in the description of crack tip stress fields.

1: Introduction to Linear Elastic Fracture Mechanics.

1.1: Griffith's Criterion.

A fundamental relationship of fracture mechanics was developed by A.A Griffith (1921) who considered the energetics of unstable crack growth in an elastic material. Griffith considered the problem of crack growth in an infinite plate containing a centre crack, with a constant tensile displacement applied to the remote boundaries as shown schematically in Figure 1.1. A schematic load-displacement graph for the applied remote stress is shown in Figure 1.2. The elastic energy contained in the plate is the area under the graph. As the crack increases in length by da, the stiffness decreases. As the crack length increases from a to a+da the potential energy of the body drops corresponding to the area OAC in Figure 1.3.

Griffith postulated that crack propagation could only occur if there was sufficient elastic energy released to provide the necessary energy to create fresh surfaces. Crack advance is energetically favourable when:

$$\frac{\partial U}{\partial a} \geq \frac{\partial W}{\partial a} \qquad (1.1)$$

Where U is the elastic energy and W is the energy required to break a unit area of material. Griffith then made use of the stress field calculations for a sharp crack after Inglis (1913) and calculated U and $\frac{\partial U}{\partial a}$ per unit thickness as:

$$U = \frac{\sigma^2 \pi a^2}{2E'} \qquad (1.2)$$

$$\frac{\partial U}{\partial a} = \frac{\sigma^2 \pi a}{E'} \qquad (1.3)$$

Where in plane strain E' is defined as $E' = \frac{E}{(1-\nu^2)}$ while in plane stress E' = E, E being Young's modulus. The energy release rate per unit thickness, $\frac{\partial U}{\partial a}$ is normally denoted G which is defined as the *'elastic or potential energy release rate'*. The elastic energy release rate is therefore defined as:

$$G = \frac{\pi\sigma^2 a}{E'} \qquad (1.4)$$

The energy required for crack propagation by decohesion of the atomic bonds is assumed for a first approximation to be constant for each increment of crack advance. This means that R the crack resistance is constant, and can be defined:

$$W = 2a\gamma \qquad (1.5)$$

$$R = \frac{\partial W}{\partial a} = 2\gamma \qquad (1.6)$$

γ is the surface energy per unit area. In the Griffiths criterion G is the surface energy per unit area of the material. The Griffith criterion for crack propagation requires that G must at least be equal to R before crack propagation can occur. If R is constant there must be a critical value of G denoted G_c. In plane strain conditions the critical value of the elastic energy release rate, G_{IC} is defined in terms of the fracture stress σ_f:

$$G_{IC} = \frac{\pi\sigma_f^2 a}{E'} \qquad (1.7)$$

Griffith applied the energetics of crack propagation to glass which is an extremely brittle material on the assumption that the crack resistance would only contain surface energy terms. However in almost all materials plastic flow occurs at the crack tip, and is the major energy absorption process as recognised in the important step made by McClintock and Irwin

(1965). Plastic deformation at the crack tip absorbs a large amount of energy during crack propagation, and has thus emerged as the major component energy required for the formation of the fresh surface. This therefore means that even for brittle materials R consists mainly of plastic energy and the surface energy influence is small enough to be neglected.

Irwin (1957) modified Griffiths criterion to include a plastic energy term and expressed the potential energy release rate:

$$G = 2\gamma_p \qquad (1.8)$$

Where γ_p is the plastic component of the surface energy per unit area.

1.2: The Stress Field at a Crack Tip.

The deformation of a cracked body can be described in terms of three basic loading modes. In Mode One tensile stresses are applied perpendicular to the crack, and the associated displacements are symmetric about the crack plane. Mode Two loading is described as 'in plane' shear and the associated displacements are anti-symmetric about the crack plane. Mode Three is an 'out of plane' shear sometimes referred to as 'anti-plane shear', in which the only displacements generated are parallel to the crack plane. Schematic representations of these three modes of loading are shown in Figure 1.4.

Interest is now restricted to mode one loading since in the engineering sense it is the most important form of loading for components. For linear elastic bodies the stresses, σ_{ij}, ahead of a crack can be written as a series expansion given by Williams (1957):

$$\sigma_{ij} = A_{ij}(\theta)r^{\frac{-1}{2}} + B_{ij}(\theta) + C_{ij}(\theta)r^{\frac{1}{2}} + \ldots \qquad (1.9)$$

This series expansion uses polar co-ordinates (r,θ) centred at the crack tip, with r being

the distance from the crack tip, and incorporates functions which depend on the angular coordinate θ as illustrated in Figure 1.5. As the crack tip is approached, (i.e as r tends to zero), the third and higher order terms tend to zero. At the crack tip the first term is infinite and the second term finite. In classical lefm this allows the second and higher order terms to be ignored in comparison to the first term. The first term represents the dominant singularity whereas the second term of this expansion has been denoted as the T-stress by Rice (1974). The T-stress is as a uniaxial stress parallel to the crack flank whose magnitude has been define by Levers and Radon (1983) in terms of a biaxiality parameter (β).

Irwin (1957) considered the analysis of Westergaard (1939), who had studied the stress field of an infinite plate with a crack of length 2a, located on the x-axis from -a to +a and subject to a remote tensile loading. Close to the crack tip (r<<a) classical lefm restricts interest to the first term of the Williams expansion (1.9):

$$\sigma_{xx} = \frac{\sigma\sqrt{\pi a}}{\sqrt{2\pi r}} \cos(\frac{\theta}{2}) \left[1 - \sin(\frac{\theta}{2}) \sin(\frac{3\theta}{2}) \right]$$

$$\sigma_{yy} = \frac{\sigma\sqrt{\pi a}}{\sqrt{2\pi r}} \cos(\frac{\theta}{2}) \left[1 + \sin(\frac{\theta}{2}) \sin(\frac{3\theta}{2}) \right] \qquad (1.10)$$

$$\tau_{xy} = \frac{\sigma\sqrt{\pi a}}{\sqrt{2\pi r}} \cos(\frac{\theta}{2}) \sin(\frac{\theta}{2}) \cos(\frac{3\theta}{2})$$

Irwin (1957) noted that these solutions could be written in the generalised form:

$$\sigma_{ij}(r,\theta) = \frac{K}{\sqrt{2\pi r}} f_{ij}(\theta) \qquad (1.11)$$

Where $K_I = \sigma\sqrt{(\pi a)}$ is defined as the elastic stress intensity factor, and describes the way the stresses approach the singularity at the crack tip, $f_{ij}(\theta)$ are universal functions and are independent of geometry. The stress intensity factor is dependent on geometry, unlike the stress concentration factor which is infinite for all bodies containing sharp cracks. A crack will extend when stresses and strains reach a critical value over a micro-structurally

significant distance, which is both material and loading dependent. In a linear elastic material there is a direct relationship between the potential energy release rate (G) and the stress intensity factor (K). Fracture will only occur when both the stress intensity factor and the energy release rate reach their critical values, thus the energy and the stress field approach are equivalent. The relationship between these two factors can be generalised and for mode I loading is defined as:

$$G_I = \frac{K_I^2}{E'} \qquad (1.12)$$

Given that the stress intensity factor determines the stress field, crack extension will occur at a critical value of K, denoted K_{IC}. The stress intensity factor can always be expressed in the form:

$$K = \sigma f(\frac{a}{W}) \sqrt{\pi a} \qquad (1.13)$$

Here σ is a reference stress and $f(\frac{a}{W})$ is a function of geometry, which is tabulated for a large number of geometries by Rooke and Cartwright (1976) and Tada, Paris and Irwin (1974) as well as Murakami (1987). Figure 1.6 illustrates this function of geometry, $f(\frac{a}{W})$ for a centre cracked test specimen. For the case of a single edge crack in a semi-infinite plate with $f(\frac{a}{W})$ equal to 1.12, Tada, Paris and Irwin (1974), (1.13) reduces to a simple analytic expression:

$$K = 1.12\sigma\sqrt{\pi a} \qquad (1.14)$$

The in plane stresses are independent of the thickness of the plate but the out of plane stress depends on whether plane strain or plane stress conditions apply:

$\sigma_{zz} = 0$ for conditions of plane stress.

and

$\sigma_{zz} = \nu(\sigma_{xx}+\sigma_{yy})$ for conditions of plane strain.

The displacements(u,v,w) associated with these fields have been given in a general form by Rice (1969):

$$u = \frac{K}{2G}\left(\frac{r}{2\pi}\right)^{\frac{1}{2}} \cos\left(\frac{\theta}{2}\right)\left\{\kappa-1+2\sin^2\left(\frac{\theta}{2}\right)\right\}$$

and (1.15)

$$v = \frac{K}{2G}\left(\frac{r}{2\pi}\right)^{\frac{1}{2}} \sin\left(\frac{\theta}{2}\right)\left\{\kappa+1-2\cos^2\left(\frac{\theta}{2}\right)\right\}$$

where

$\kappa = (3 - 4\nu)$ for plane strain

$\kappa = \left(\frac{3-\nu}{1+\nu}\right)$ for plane stress

The out of plane displacement w is necessarily zero in plane strain. In the case of plane stress however the out of plane strain must be integrated with respect to z to determine the out of plane displacement:

$$W = \frac{-2\nu}{E}\frac{K}{\sqrt{2\pi r}}\cos\frac{\theta}{2}Z \qquad (1.16)$$

1.3: Determination of Stress Intensity Factors.

The stress intensity factor characterises the way that the stress field approaches the singularity at the crack tip. Two simple direct methods for determining K from the stress and displacement fields are now discussed. A third method called virtual crack extension which is an indirect method is also briefly reviewed.

The stress method makes use of the Westergaard equations (1.10). Considering only the stress σ_{yy} directly ahead of the crack tip (θ=0), equation (1.11) simplifies to:

$$K = \underset{r\to 0}{\text{Limit}} \left[\sigma_{yy} \sqrt{2\pi r}\right] \qquad (1.17)$$

An alternative technique makes use of equation (1.15) to write K as:

$$K = \underset{r\to 0}{\text{Limit}} \left[u\, G \left(\frac{2\pi}{r}\right)^{\frac{1}{2}} \{\kappa\text{-}1\}\right] \qquad (1.18)$$

The third method for the calculation of the stress intensity factor is termed virtual crack extension, and is an indirect method of solution. This method relies on the relationship between the crack tip stress intensity factor (K) and the potential energy release rate (G). The crack tip is surrounded by two contours (Γ_1, Γ_2) as illustrated in Figure 1.7, virtual crack extension is achieved by moving the internal contour (Γ_1) a small distance (∂a) simulating a degree of crack advance. External to the outer contour (Γ_2) the stiffness matrix of the body remains the same. The only subsequent difference is in the region between the internal and external contours. Therefore for the unit of crack advance only the change in overall stiffness between the contours has to be resolved. The stiffness matrix of the body can be considered as the sum of the individual element stiffness matrices, Zienkiewicz (1971)

Virtual crack extension has the advantage of only requiring the calculation of the stiffness change between the contours surrounding the crack tip as opposed to a full stiffness calculation for the entire body.

1.4: Small Scale Yielding.

Linear elastic fracture mechanics is based on the requirement that the body is largely elastic, and that the zone of plastic deformation is small compared with the critical dimensions of the body. The fundamental assumption is that the size of the plastic zone is small compared with the specimen dimensions and the outer field is adequately characterised by the first term in the Williams expansion, Figure 1.8. This is the critical assumption which is the lynch pin of single parameter linear elastic fracture mechanics.

The plastic zone size can be estimated by using either the Von Mises or Tresca yield criteria in conjunction with the elastic stress field. In this context it is convenient to express the stress field in terms of principal stresses (σ_1,σ_2,σ_3):

$$\sigma_1 = \frac{K}{\sqrt{2\pi r}} \cos\frac{\theta}{2}\left(1+\sin\frac{\theta}{2}\right)$$

$$\sigma_2 = \frac{K}{\sqrt{2\pi r}} \cos\frac{\theta}{2}\left(1-\sin\frac{\theta}{2}\right) \qquad (1.19)$$

Here the third principal stress is dependent upon whether plane stress or plane strain conditions apply. For plane stress the Tresca yield criterion becomes:

$$\sigma_1 - \sigma_3 = \frac{K}{\sqrt{2\pi r}} \cos\frac{\theta}{2}\left(1+\sin\frac{\theta}{2}\right) = \sigma_0 \qquad (1.20)$$

Where σ_0 is the yield stress in uniaxial tension. This gives an approximation for the radius of the plastic zone (r_y):

$$r_y = \frac{1}{2\pi}\left(\frac{K}{\sigma_0}\right)^2 \cos^2\frac{\theta}{2}\left(1+\sin\frac{\theta}{2}\right)^2 \quad \text{Plane Stress.} \qquad (1.21)$$

$$r_y = \frac{1}{2\pi}\left(\frac{K}{\sigma_0}\right)^2 \sin^2\theta \quad \text{Plane Strain.} \qquad (1.22)$$

These equations show that the radius of the plastic zone is proportional to $\left(\frac{K}{\sigma_0}\right)^2$, as illustrated in Figure 1.9. The plane stress plastic zone is the larger of the two, especially directly ahead of the crack. The approximation for r_y for plane strain conditions tends to zero (ν=0.5) at this angle, even though at this angle the largest principal elastic stresses are encountered. This is possible because yielding is controlled by shear stresses and the difference in principal stresses is almost zero.

In plane stress the largest shear stresses cut through the body, as opposed to plane strain where they act in the plane of the crack. Irwin and Kies (1958) showed that since thickness affects the plastic zone of the body it must affect the fracture toughness (K_C) as well. Low values of fracture toughness in thick plates result directly from the small plastic zone size associated with plane strain conditions. This implies that cracks in thick sections are very dangerous. As a consequence, methods for determining fracture toughness, especially in conditions of plane strain are particularly important. K_C in general is not a material property since it is dependent upon the material thickness. However it is possible to define a material property in thick sections when K_C reduces asymptotically to the K_{IC} value for plane strain conditions.

1.5: Validity of Linear Elastic Fracture Mechanics.

The validity of classical linear elastic fracture mechanics is codified in both American and European standards:

$$B,\ a,\ W\text{-}a \geq 2.5\left(\frac{K_I}{\sigma_o}\right)^2 \quad \text{(A.S.T.M.-E399-83)}$$

$$B,\ a \geq 2.5\left(\frac{K_I}{\sigma_o}\right)^2 \quad \text{(B.S. 7448 Part 1)} \qquad (1.23)$$

Where B, a, and (W-a) are the body thickness, crack length and the remaining ligament

respectively. The aim of plane strain fracture toughness is to determine the lower limiting toughness of a thick sectioned material, Knott (1973). Conditions and test procedures for valid lefm tests are given in ASTM (1988). In plane strain and mode one conditions this is denoted as K_{IC}, the difference between K and K_{IC} can be considered as paralleling the difference between strength and stress. K_{IC} is determined by loading a test specimen with a defect present until the crack extends, the value at which the crack initiation occurs is termed K_{IC}. This form of testing however assumes a high degree of crack tip constraint, corresponding to a state of plane strain. Plane strain toughness tests are only really suitable for the testing of thick section testpieces, since plane strain conditions will prevail in the middle section of the testpiece while plane stress conditions occur at the testpiece surfaces.

The dimensions quoted in (1.23) ensure that the plastic zone radius is approximately sixteen times the maximum radius of the plastic zone for plane strain conditions. This ensures that the size of the plastic zone is small compared to the critical dimensions of the body. Outwith these dimensions it is appropriate to use elastic plastic fracture mechanics.

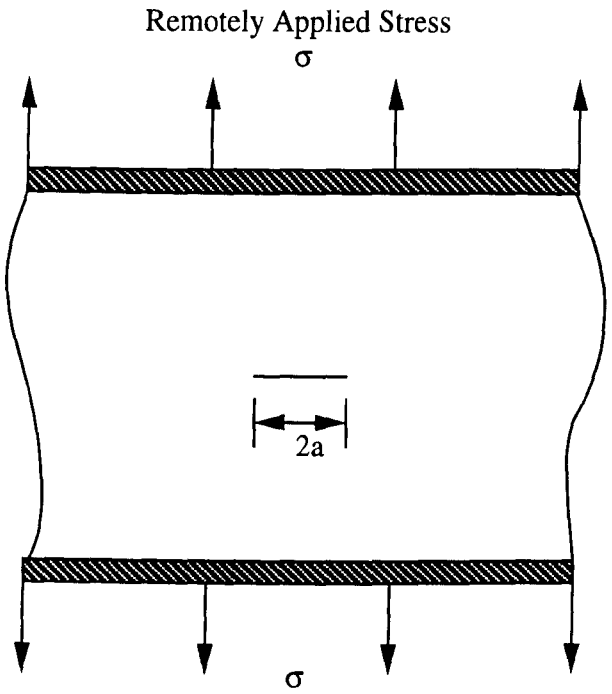

Figure 1.1: Infinite Centre Cracked Panel with Fixed Ends.

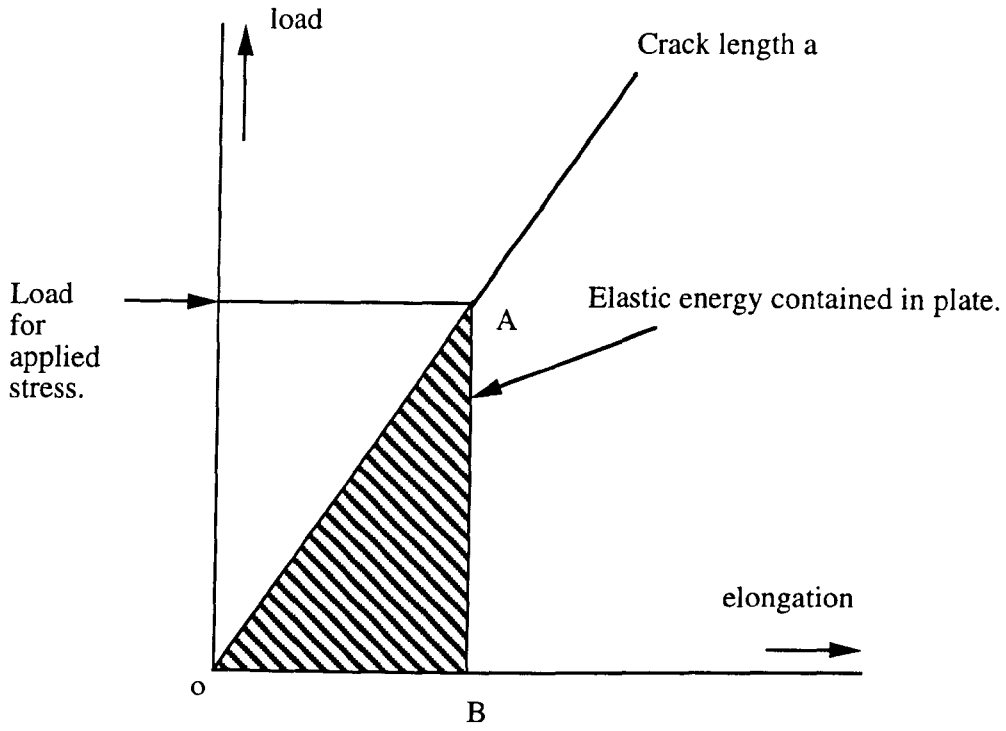

Figure 1.2: Load-Displacement Graph for crack of Length a.

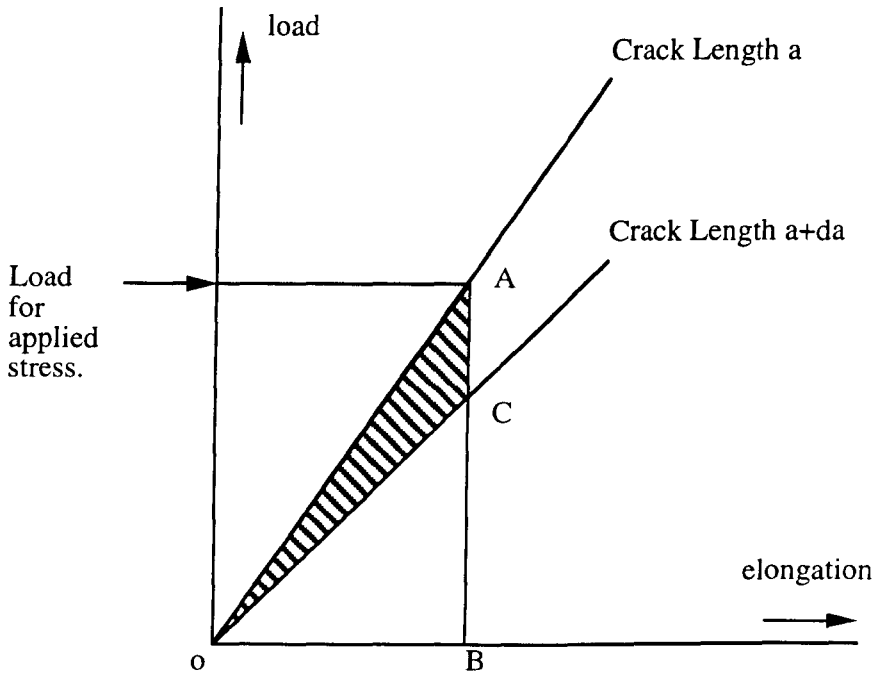

Figure 1.3: Elastic Energy Release Graph for Propagation of Crack from a to a+da.

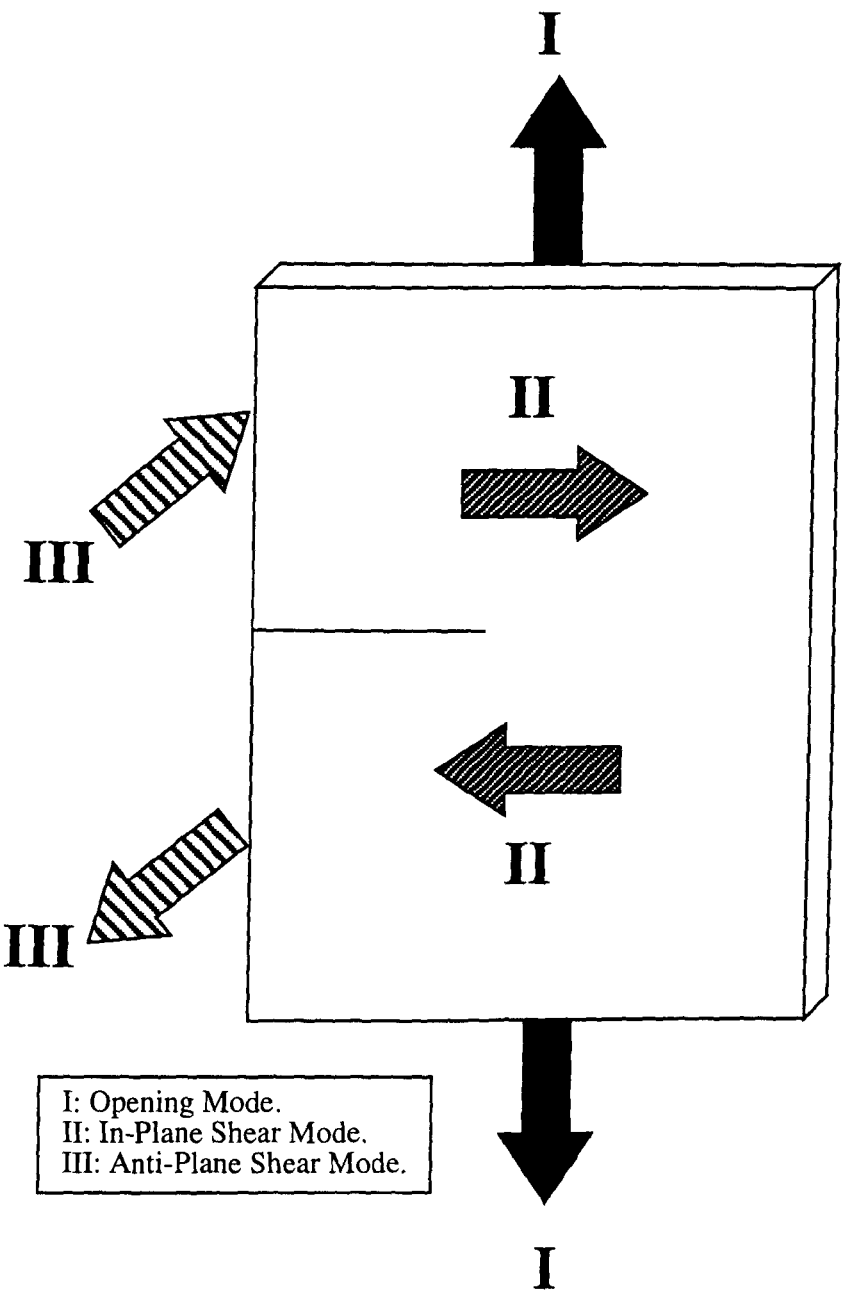

Figure 1.4: Schematic of Fracture Modes.

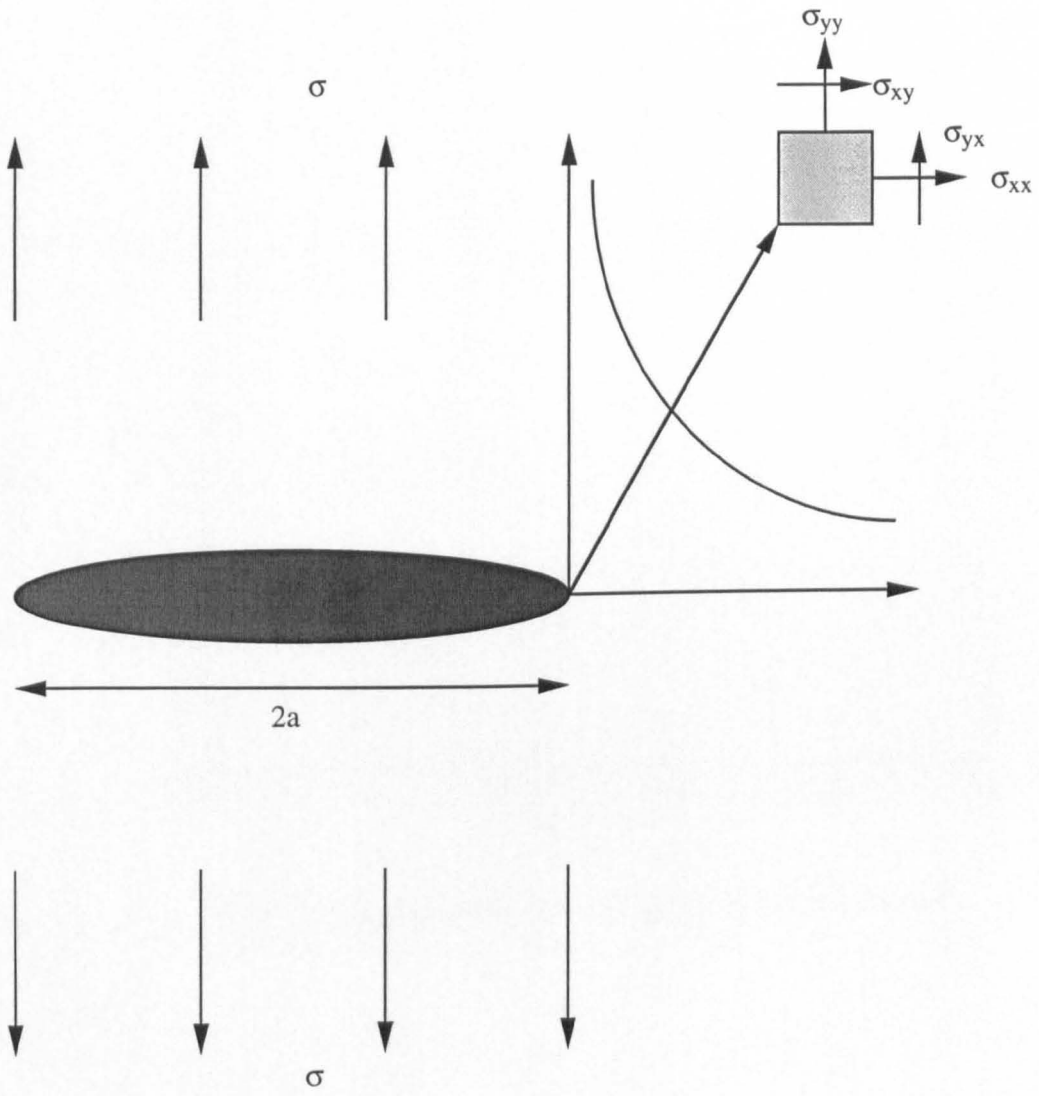

Figure 1.5: Crack in an Infinite Plate Stress Distribution.

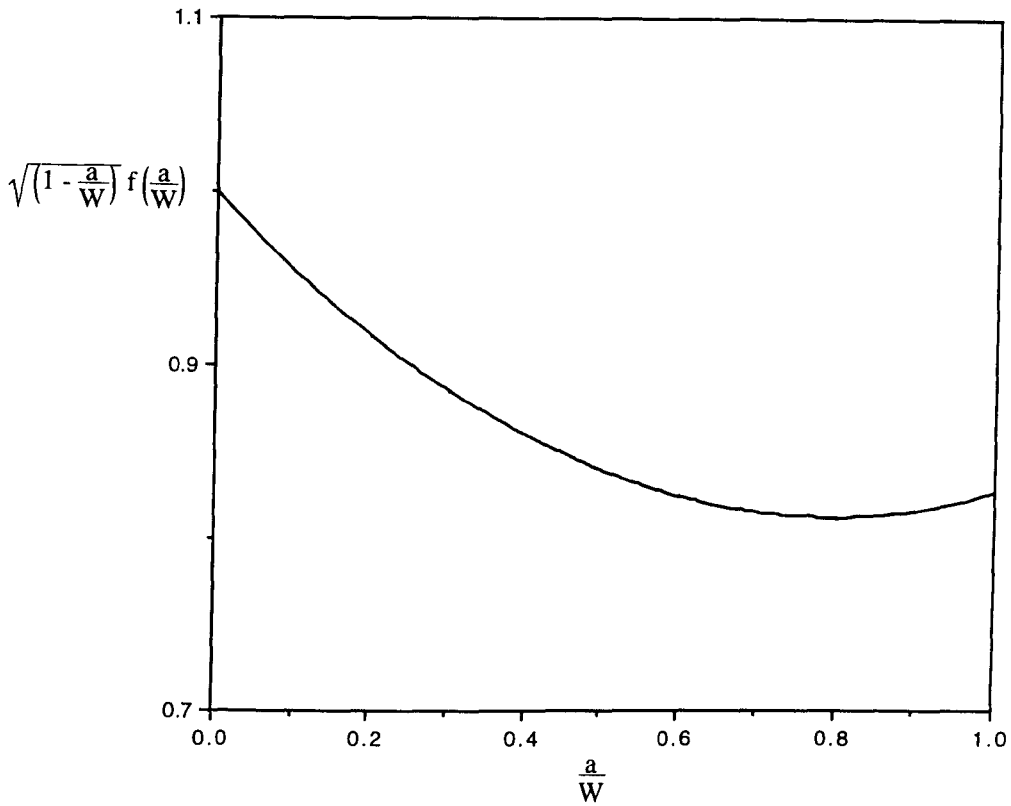

Figure 1.6: Geometric parameter for Centre Cracked Test Specimen.

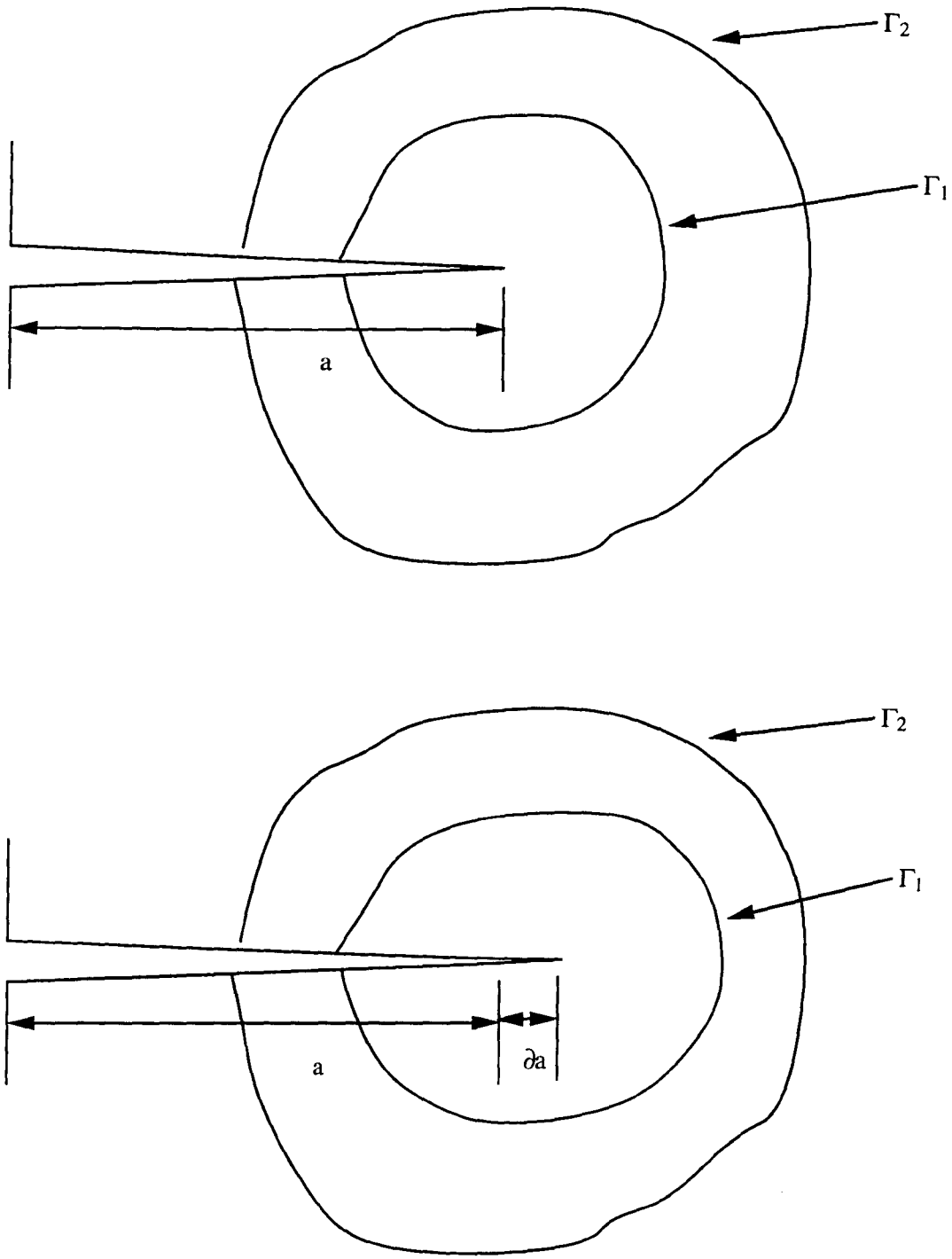

Figure 1.7: Contour Placement as Crack Tip Advances for Virtual Crack Extension.

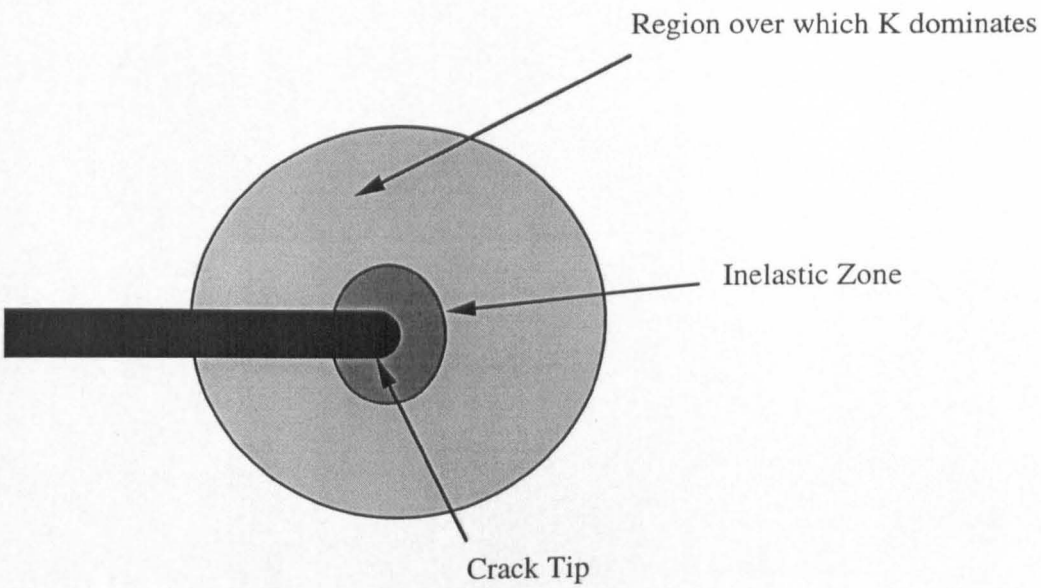

Figure 1.8: Definition of Small Scale Yielding.

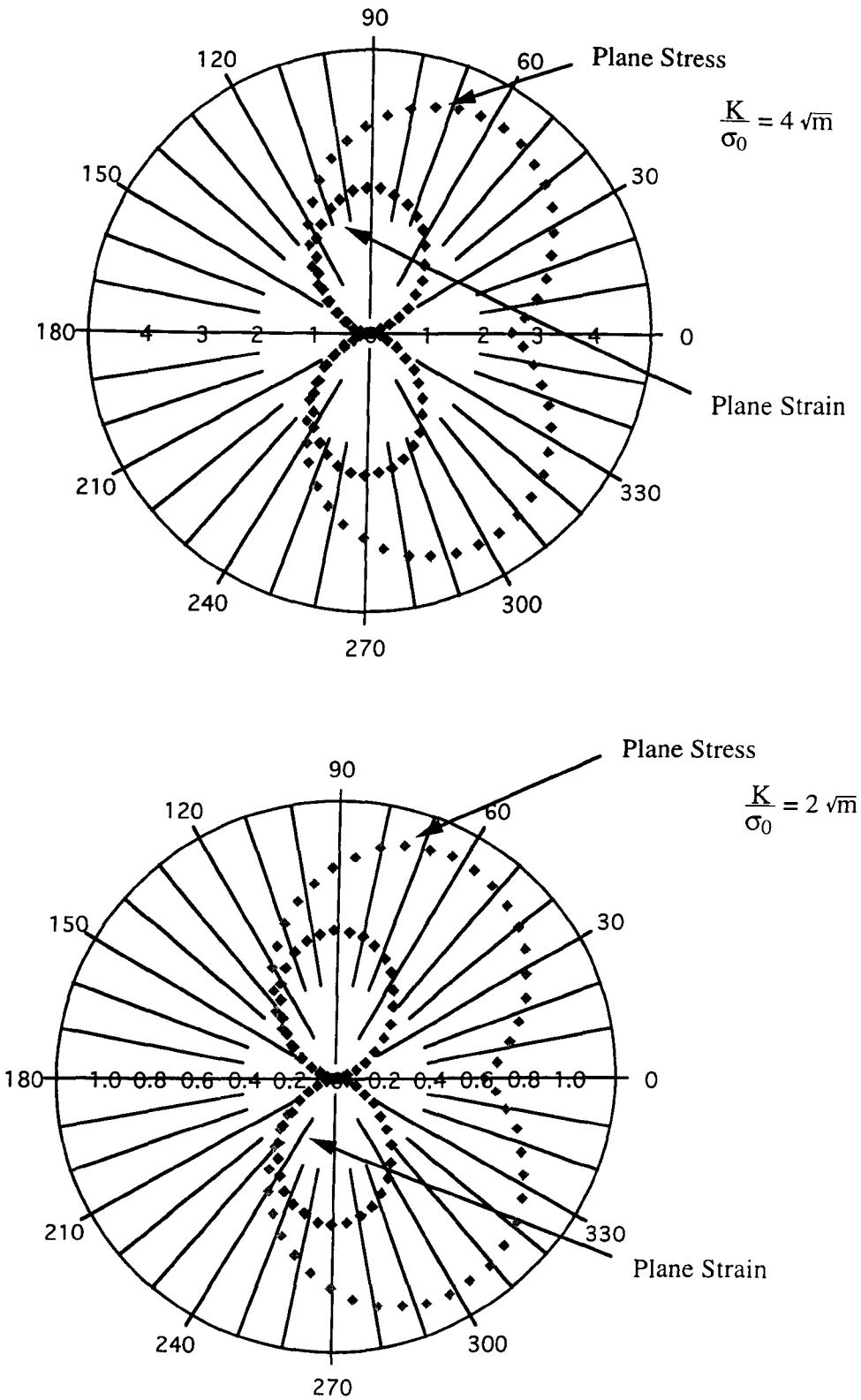

Figure 1.9: Graphical Representations of Plastic Zones

2: Benchmarking Linear Elastic Fracture Mechanics.

2.1: Introduction.

Lefm is based on the premise that it is possible to characterise the stress field near the crack tip by the stress intensity factor within the conditions of small scale yielding. In this chapter the stress intensity factor (K) is derived by a number of different analytical techniques. These analyses were conducted using a model mesh generated using the commercially available package PATRAN (1988) while the actual analyses were carried out on an IBM 3090 making use of the finite element package ABAQUS (1988a, b). These analyses were then compared with the results gained from standard solutions (Rooke and Cartwright (1976), Tada, Paris and Irwin (1973) and Murakami (1987)). The purpose was to confirm the computational techniques to be used in the thesis on well defined elastic problems before proceeding to the more complicated elastic-plastic problems.

2.2: Numerical Methods.

Two different approaches to the computational benchmarking of K were undertaken. The first utilised a full field continuum analysis using two dimensional plane strain isoparametric elements. The second approach used line-spring and shell elements.

The benchmarking analyses were carried out on a single edge cracked bar (SEC), with a crack length to body width $\left(\frac{a}{W}\right)$ ratio of 0.5, and a height to width ratio of 3 as illustrated in Figure 2.1. The continuum model comprised one hundred and eighty four eight noded second order isoparametric plane strain elements (CPE8RH) as shown in Figure 2.2. In all the analyses Poisson's ratio was set at 0.3 while Young's modulus was 200 GPa. A displacement loading was applied to the upper node set of the model shown in Figure 2.3,

this deformed the mesh as illustrated in Figure 2.4. The imposed boundary conditions were such that the ligament was fixed in the y (2) direction while the end of the ligament was fixed in the x (1) direction to prevent rigid body motion. Due to the conditions of symmetry and loading conditions of the analysis it was necessary to only model half of the body.

A second analysis was carried out using the same mesh but altering the position of a portion of the mid-side nodes at the crack tip. These mid-side nodes were moved to a quarter of the radial distance (r) of the element length, Figure 2.5. This is termed *quarter point node refinement.* This alteration forces the displacements near the crack tip to adopt the correct form of displacement function, in which the displacements approach the crack tip as a singularity of the form, $\sqrt{r}$, as discussed in detail by Barsoum (1976) and Henshell and Shaw (1975).

An alternative approach modelled the body with shell elements and the crack with line-spring elements. The line-spring elements introduce a local solution into the analysis by allowing the mesh an additional degree of freedom along the line of the crack. This is achieved by introducing a compliance with respect to the additional degree of freedom associated with the crack. Within ABAQUS, K is recalculated from the relative rotations and displacements conjugate to the compliance. The advantage of this approach is that less elements are required to model the body than in the continuum analysis and it is therefore computationally less complex, and an easier problem to solve. In this analysis fifty second order shell and ten line-spring elements, as shown in Figure 2.6 were utilised where plane strain conditions are maintained by preventing any displacement parallel to the crack face, and the analysis was no more expensive than that of an uncracked shell geometry. The results of these three analyses were then compared with published results.

2.3: Determination of the Stress Intensity Factor.

In the continuum analyses, K was determined by the stress, displacement and virtual crack extension methods using both normal and quarter point node configurations.

2.3.1: Displacement Method.

The displacement method is a direct method of evaluation of the elastic singularity, from the displacements described by (1.16), recalling that (u,v) are displacements relative to the crack tip. K was then non-dimensionalised by K_0, which is defined in terms of a nominal applied stress, σ:

$$K_0 = \sigma\sqrt{\pi a} \qquad (2.1)$$

The function $\left(\frac{\sigma_{yy}\sqrt{2\pi r}}{K_0}\right)$ was then plotted against the nodal distance from the crack tip(r) non-dimensionalised by the crack length(a). These graphs were then extrapolated to the tip to find the appropriate stress intensity factor. Figures 2.7 and 2.8 show the results for both methods of node positioning.

2.3.2: Stress Method.

The stress method is a direct method for evaluating K, making use of equation (1.16) to express the stresses directly ahead of the crack tip (θ=0), which simplifies the universal function $f_{ij}(\theta)$ to 1.

The non-dimensionalised stress intensity factor is then plotted against the non-dimensionalised distance from the crack tip. These graphs are then extrapolated to the tip to find the stress intensity factor for the geometry. Figures 2.7 and 2.8 show the results of the stress method for both mid-side node configurations.

2.3.3: Virtual Crack Extension Method.

Virtual crack extension is an indirect method of determining K through the energy release rate (G). Since G = J for plane strain conditions the stress intensity factor is related to the elastic energy release rate by (1.13). The J-Integral is determined by the virtual crack extension method established by Parks (1974). In these analyses six contours were used in the solution of the J-Integral with the second contour chosen for convenience since these contours are path independent the choice is unimportant. This method was used with both mid-side node configurations and the results are shown in Table 2.9.

2.3.4: Line Spring and Shell Element Method.

As explained in the introduction to this chapter in the line-spring analysis K is calculated from the relative rotations and displacements of the cracked geometry, with reference to the additional degree of freedom introduced by the line-spring element. K_I is therefore an output variable in this form of analysis, while K_0 was determined from the reaction forces on the body.

2.3.5: Published Solutions.

Solutions for many geometries have been tabulated by Rooke and Cartwright (1976), Tada, Paris and Irwin (1974) and Murakami (1987). A uniform displacement produces both a tensile force and a closing moment. In a linear elastic problem it is possible to consider both the force and moment components separately and then superimpose them to get the complete solution. Tada, Paris and Irwin (1974) give the stress intensity calibration functions for tension and bending$\left(\frac{a}{W} = 0.5\right)$:

$$K_I = \sigma\sqrt{\pi a}\, f\left(\frac{a}{W}\right) \qquad (2.2)$$

Tension:

$$1 = \sqrt{\left(1 - \frac{a}{W}\right)^3}\, f\left(\frac{a}{W}\right)_{Tension} \qquad (2.3)$$

Bending:

$$0.53 = \sqrt{\left(1 - \frac{a}{W}\right)^3}\, f\left(\frac{a}{W}\right)_{Bending} \qquad (2.4)$$

From (2.1) specific values can be determined for both the bending and tension components of K_I for a single edge cracked bar subject to a displacement loading and then non-dimensionalised to obtain $\frac{K_I}{K_0}$. In tension and bending the nominal stresses are defined to be:

$$\sigma_{Tension} = \frac{\Sigma \text{ Reaction Forces}}{\text{Area}} \qquad \sigma_{Bending} = \frac{6M}{B^2} \qquad (2.5)$$

Therefore the tension and bending components resolve for this specific geometry become:

$$\frac{K_{I_{Tension}}}{K_{0_{Tension}}} = 2.828 \qquad \frac{K_{I_{Bending}}}{K_{0_{Bending}}} = -1.499 \qquad (2.6)$$

Superimposing these solutions gives the final stress intensity factor:

$$K_{I_{Total}} = K_{I_{Tension}} + K_{I_{Bending}} \qquad (2.7)$$

$$\frac{K_{I_{Total}}}{K_{0_{Tension}}} = 1.9425$$

2.4: Conclusion.

The results of all the forms of analysis are compared with the published results of Tada, Paris and Irwin (1974), Table 2.9. From this table it can be seen that all of these answers are within 0.5% of each other. Of particular interest is the accuracy of the line-spring and shell analysis, which although computationally simple gives excellent accuracy and economic benefits in comparison to the continuum solution.

Comparing Figures 2.7 and 2.8 it can be seen that by altering the position of the mid-side nodes the accuracy of the solution is increased, by ensuring the displacements follow the correct displacement function, ensures the correct form of singularity.

Of the two direct methods of evaluation of K the stress method appears to be the more accurate of the two on the basis of this investigation. Although the virtual crack extension method is clearly the most accurate method of evaluating K.

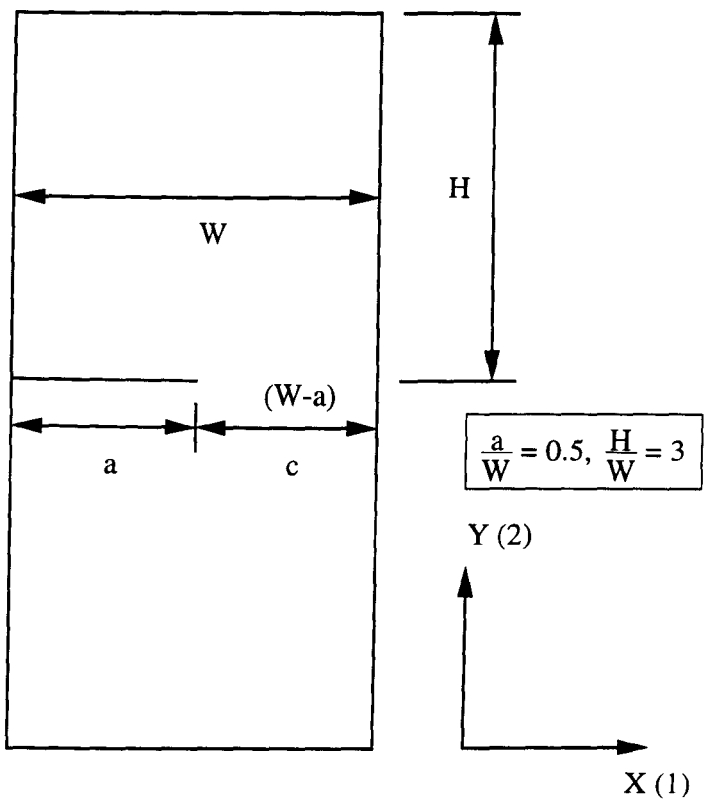

Figure 2.1: Schematic of Model Analysis

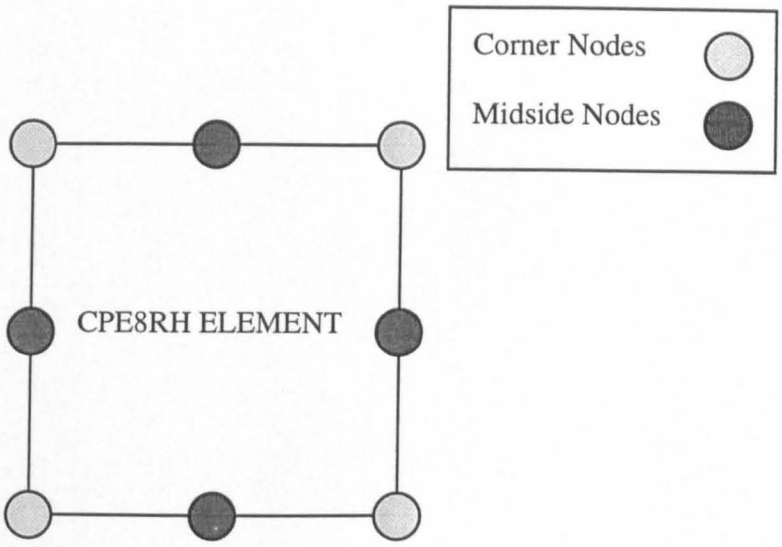

Figure 2.2: Model of an Eight Noded Biquadratic Displacement, Linear Pressure Element with Reduced Integration.

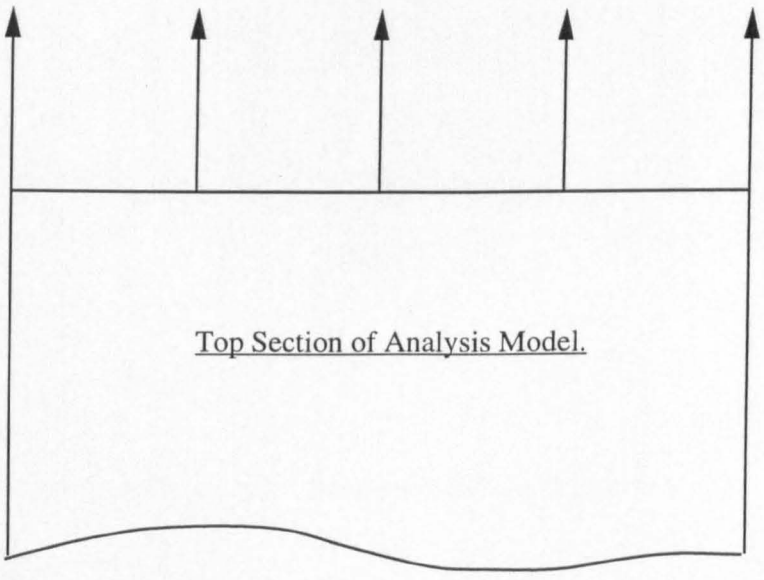

Figure 2.3: Schematic of Displacement Loading

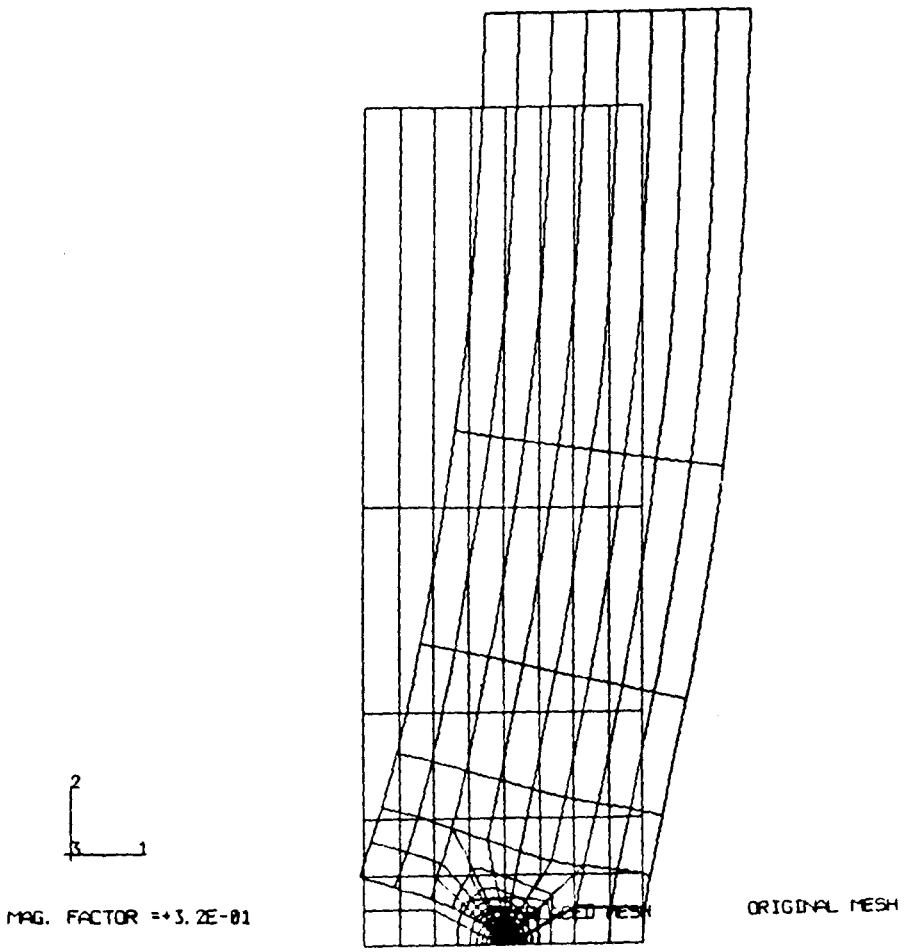

Figure 2.4: Deformed Displaced Analysis Mesh.

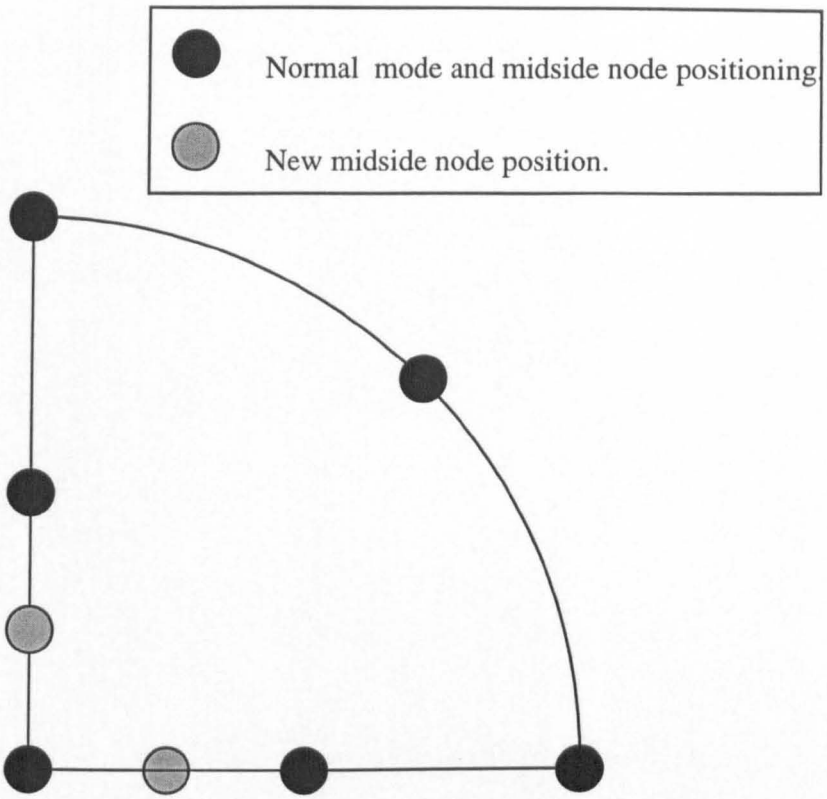

Figure 2.5: Midside Node Illustration on a Collapsed Eight Noded Plane Strain Element at a Crack Tip.

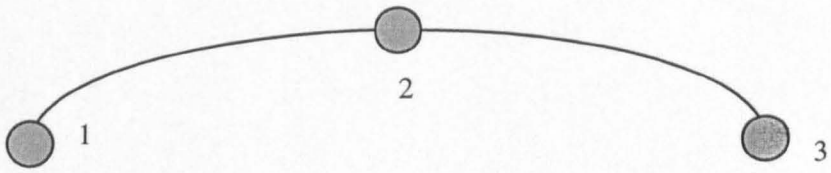

Figure 2.6: Line-Spring Element (LS3S).

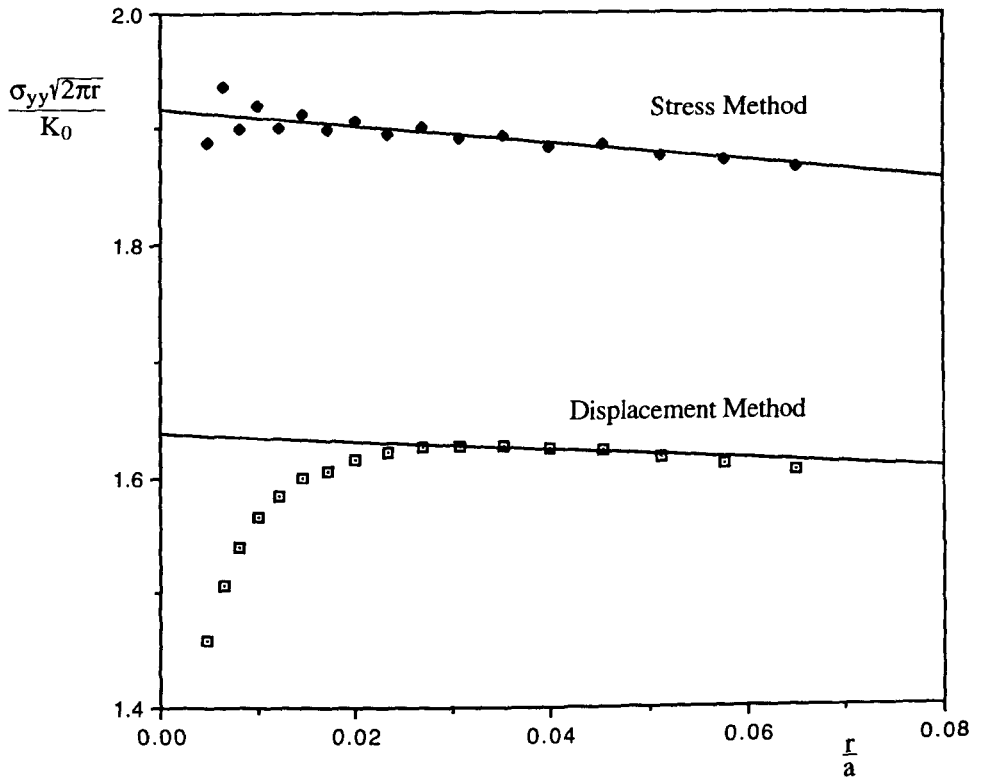

Figure 2.7: Normal Midside Node Position.

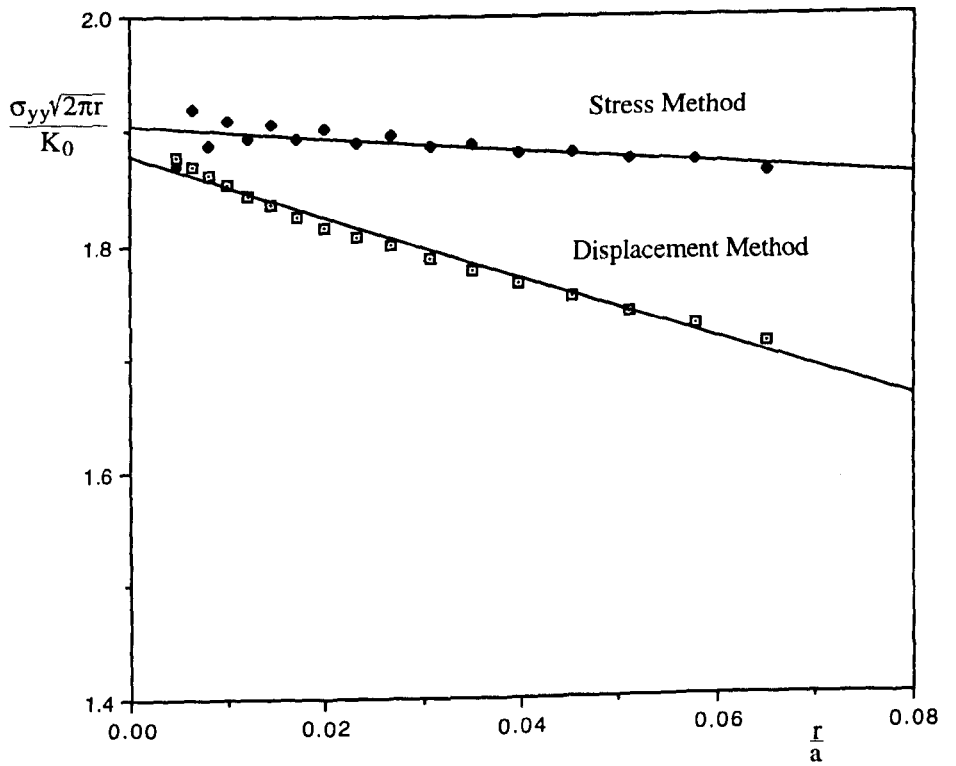

Figure 2.8: Quarter Point Node Arrangement.

Type of Analysis and Mesh.	$\frac{K_I}{K_0}$
Normal Mesh, Virtual Crack Extension.	1.94
Quarter Point Mesh, Virtual Crack Extension.	1.94
Shell and Line Spring Method.	1.95
Published Solutions, Tada, Paris and Irwin (1973)	1.94

Node Position.	Stress Method.	Displacement Method.
Normal	1.915	1.67
Quarter Point	1.92	1.87

Figure 2.9: Results from LEFM Benchmarking.

3: Elastic Plastic Fracture Mechanics.

3.1: Introduction.

Fracture mechanics is based on the ability to describe the stress fields surrounding a crack tip by a suitable characterising parameter. Within the lefm regime stress fields can be characterised by the stress intensity factor (K), or equivalently the elastic strain energy release rate (G). Within these limits, fracture occurs at stress levels appreciably below the yield stress and is colloquially termed brittle in an engineering sense, even though there is associated local plastic deformation at the crack tip. Engineering components are designed to accommodate localised plastic flow to alleviate the stress levels at stress concentrations. It is therefore necessary to find parameters that can adequately describe the crack tip stress fields when the plastic zone has developed to a size that invalidates the conditions of lefm.

In the development of classical epfm two parameters have been developed to characterise the crack tip field, the crack tip opening displacement (δ), Wells (1961), and a strain energy release rate termed the J-Integral, Rice (1968).

Wells (1961) interpreted the 'strip yield model' for plane stress which had been developed independently by Dugdale (1960) and Barenblatt (1962) in terms of fracture. In this case yielding is assumed to be confined to a narrow zone directly ahead of the crack tip. In effect, yield was accounted for by the addition of a plastic strip to the crack length as illustrated in Figure 3.1. Cohesive stresses were applied to prevent the crack opening and simulate non-hardening plasticity. Rosenfield et al (1966) have shown this model to be broadly appropriate for fully developed plane stress yielding by etching the plastic zones of thin fracture specimens, Figure 3.2 shows an idealisation of their results. Plastic flow consists of two intersecting shear bands at 45° through the thickness of the body. Yield is therefore localised to a narrow region of height equalling that of the body thickness. Wells(1961) noted that plasticity caused the crack to open with a ' near square ended

contour' which resulted in a finite crack tip opening (δ). Wells's proposition was that there would be a critical crack tip opening (δ_t) at which a crack in a laboratory specimen and in an engineering structure would both fail.

The J-Integral is an energy release rate introduced independently by Cherepanov (1967), Eshelby (1968) and Rice (1968), with the major credit towards its adoption in fracture mechanics being attributed to Rice (1968).

3.2: Crack Tip Opening Displacement (δ).

The crack tip opening displacement can be regarded as a measure of the plastic strain close to the crack tip. Wells's proposition was that the crack tip would advance when the material directly ahead of the crack tip had achieved a critical level of strain and this in turn would reflect itself in a critical level of crack tip opening as shown in Figure 3.3. This idea was extended by Dugdale (1960) into the general yielding regime by presenting δ in the form:

$$\delta = \frac{8a\sigma_0}{\pi E} \ln \sec \frac{\pi\sigma}{2\sigma_0} \qquad (3.1)$$

Expanding as a series gives:

$$\delta = \frac{\pi\sigma^2 a}{E\sigma_0}\left[1 + \frac{\pi^2}{24}\left(\frac{\sigma}{\sigma_0}\right)^2 + - -\right] \qquad (3.2)$$

For lefm conditions, ($\sigma << \sigma_0$) the strain energy release rate can be written:

$$G = \frac{\pi\sigma^2 a}{E} \qquad (3.3)$$

This allows the first term in the series to be expressed:

$$\delta = \frac{G}{\lambda \sigma_0} \qquad (3.4)$$

Where λ is dependent upon the strain hardening rate, n and the yield strain, ε_0. This is often expressed in terms of parameter d_n, Kumar, German and Shih (1981), where λ is identical to $\frac{1}{d_n}$. It is therefore possible to write a general formulation for small scale yielding in mode I deformation in the form:

$$\delta = \frac{K_I^2}{\lambda \sigma_0 E} \qquad (3.5)$$

Specific values of λ have been reported by Rice (1968), Rice and Johnson (1970), Levy et al. (1971), Rooke and Bradshaw (1969) and Robinson and Tetelman (1973) who have either determined λ computationally or experimentally. λ is approximated from these results to be 1 for conditions of plane stress and 2 for plane strain. Values of λ have been directly related to d_n as given by Hutchinson (1968) and Shih (1978).

3.3: The J-Integral

Crack tip characterisation by a path independent integral was proposed independently by Cherepanov (1967), Eshelby (1968) and Rice (1968). Most simply understood as a measure of the difference between the potential energy of two non-linear elastic bodies with slightly differing crack lengths as illustrated in Figure 3.4. Here the difference between the areas under the graph can be expressed as JB∂a and where ∂U is the potential energy change of the body:

$$J = -\frac{1}{B}\frac{\partial U}{\partial a} \qquad (3.6)$$

Eshelby (1968) has described a number of path independent contours based on a theorem of energy conservation. The nature of the argument may be developed in a qualitative manner, consider a counter-clockwise contour from the lower to the upper crack faces. This contour consists of a series of elements ds, Figure 3.5. Applied to each element is a traction force F, which is a vector and moves the contour a small distance, Δu, Figure 3.6. The work done on each element ds is $F.\Delta u$, where the dot product accounts for the different directions of the two vectors. The total work done on the material surrounding the crack tip is given by integrating around the contour:

$$\int_{\Gamma} (F.\Delta u)ds \qquad (3.7)$$

This can now be expressed in terms of crack advance, Δa:

$$\Delta a \int_{\Gamma} (F.\frac{du}{dx})ds \qquad (3.8)$$

As the contour moves the energy balance of the crack tip is changed due to the loss and gain of energy from both internal and external conditions, i.e. the work done by external forces. If the strain energy density is W then the change in strain energy in the area $\Delta a dy$ is $W\Delta a dy$. The net loss in the strain energy of the material contained within the contour can be obtained by integrating around the path:

$$\Delta a \int_{\Gamma} W\, dy \qquad (3.9)$$

The net change in energy of the system contained within the contour can be defined as:

$$\Delta U = \Delta a \int_{\Gamma} W\, dy - \Delta a \int \left(F.\frac{du}{dx}\right)ds \qquad (3.10)$$

Rice (1969) has expressed the J-Integral in the following two dimensional form for a non-linear material:

$$J = \int_{\Gamma} \left(W dy - F \frac{\partial u}{\partial a} ds \right) \qquad (3.11)$$

The J-Integral is defined as a counter-clockwise contour integral where W is the strain energy density ($W = \int_0^{\varepsilon} \sigma_{ij} d\varepsilon_{ij}$) , F is the traction vector normal to the contour integration path, u is the displacement vector and s is the arc length. This description is based upon deformation theory plasticity or equivalently non-linear elasticity.

The path independence of these integrals can be proved by considering two separate integration contours Γ_1 and Γ_2 surrounding a crack tip as shown in Figure 3.7. Since the integrand disappears on the crack faces J_2-J_1 is the integral of the boundaries surrounding the area between J_1 and J_2, thereby transforming the line integrals into an area integral by a Green-Gaussian transformation this gives J_2-J_1=0.

If an arbitrary circular contour of radius r fully encloses the crack tip, the general definition of the two dimensional J-Integral can be expressed:

$$\frac{J}{r} = \int_{-\pi}^{\pi} \left(W \sin\theta - F \frac{\partial u}{\partial a} \right) d\theta \qquad (3.12)$$

The strain, the strain density and the traction depends upon the radius and polar angle of the contour (r, θ). In conditions of small scale yielding the contour can be selected to fall completely within the area dominated by K. This establishes the relationship between the integral and K:

$$J = G = \frac{K^2}{E'} \qquad (3.13)$$

A similar direct relationship in a linear-elastic sense is possible between the crack tip opening displacement and the J-integral . The crack tip opening displacement can be related to the potential energy release rate, G and since for lefm G=J:

$$\delta = d_n \frac{G}{\sigma_0} = d_n \frac{J}{\sigma_0} \qquad (3.14)$$

Here d_n is a parameter (Hutchinson(1978) and Shih(1981)) as shown in Figure 3.8, which depends on both the strain hardening rate, n and the yield strain, ε_o.

Interest will now be focused on a non-linear elastic material that follows a constitutive relationship governed by an equation of the form described by a Ramberg-Osgood stress strain curve:

$$\frac{\varepsilon}{\varepsilon_0} = \frac{\sigma}{\sigma_0} + \alpha \left(\frac{\sigma}{\sigma_0}\right)^n \qquad (3.15)$$

Here n is the strain hardening exponent and σ_0 is a flow stress while α is a material constant and ε_0 is a reference strain defined to be $\varepsilon_0 = \frac{\sigma_0}{E}$. Close to the crack tip the plastic strains dominate and it is possible to neglect the initial linear portion of the strain relationship:

$$\frac{\varepsilon}{\varepsilon_0} = \alpha \left(\frac{\sigma}{\sigma_0}\right)^n \qquad (3.16)$$

This uniaxial stress-strain relationship is usually generalised by J_2 (Von Mises) deformation plasticity to a multiaxial stress state:

$$\frac{\varepsilon_{ij}}{\varepsilon_0} = 3J_2 = \frac{3}{2} \alpha \left(\frac{\sigma_e}{\sigma_0}\right)^{n-1} \frac{S_{ij}}{\sigma_0} \qquad (3.17)$$

Where S_{ij} is the deviatoric stress and σ_e is the effective stress defined as:

$$\sigma_e^2 = \frac{3}{2} S_{ij}S_{ij}$$

$$S_{ij} = \sigma_{ij} - \left(\frac{\sigma_{kk}}{3}\right)\delta_{ij} \qquad (3.18)$$

From (3.12) it is clear that there must be an energy singularity exhibited at the crack tip, that depends inversely on the distance from the crack tip. Since the parameters are of the order of $\sigma_{ij}\varepsilon_{ij}$ Hutchinson (1968) and Rice and Rosengren (1968) concluded that the singularity must have a strength of the order of $\frac{1}{r}$. For power law hardening materials this singularity corresponds to stress and strain singularities of the form:

$$\varepsilon_{ij} \rightarrow r^{\frac{-n}{n+1}} f_1(\theta) \quad \sigma_{ij} \rightarrow r^{\frac{-1}{1+n}} f_2(\theta) \quad u_i \rightarrow r^{\frac{1}{n+1}} f_3(\theta) \qquad (3.19)$$

Having established the strength of the stress and strain singularities and by relating the general form of the J-Integral to the dependence of r to a power it is possible to characterise the field parameters for a non-linear material in terms of J as determined independently by Hutchinson (1968) and Rice and Rosengren (1968):

$$\frac{\sigma_{ij}}{\sigma_0} = \left(\frac{J}{\alpha\sigma_0\varepsilon_0 I_n r}\right)^{\left(\frac{1}{n+1}\right)} \tilde{\sigma}_{ij}(\theta, n)$$

$$\frac{\varepsilon_{ij}}{\varepsilon_0} = \alpha\sigma_0\left(\frac{J}{\alpha\sigma_0\varepsilon_0 I_n r}\right)^{\left(\frac{n}{n+1}\right)} \tilde{\varepsilon}_{ij}(\theta, n) \qquad (3.20)$$

$$u_i = \alpha\varepsilon_0\left(\frac{J}{\alpha\sigma_0\varepsilon_0 I_n}\right)^{\left(\frac{n}{n+1}\right)} r^{\left(\frac{1}{n+1}\right)} \tilde{u}_i(\theta, n)$$

Here α is a dimensionless constant, I_n is a dimensionless function of the strain hardening exponent, n which is tabulated in Figure 3.9, while $\tilde{\sigma}_{ij}$, $\tilde{\varepsilon}_{ij}$ and $\tilde{u}_i$ are angular functions of the strain hardening rate after Shih (1983). J can now be considered both as an

energy and as a field parameter.

It is possible to express J in terms of elastic and plastic components:

$$J_{total} = J_{elastic} + J_{plastic} \qquad (3.21)$$

There are a number of methods to determine J in fracture mechanic specimens. Consider a deeply edge cracked bar subjected to a pure bending moment as shown in Figure 3.10. The moment-rotation relationship for a non-hardening material, illustrated in Figure 3.11, is only a function of the body thickness, B and the remaining ligament, (W-a). A dimensional argument shows that the moment on the body can be expressed in the following form:

$$M_{(a)} = \alpha\, \sigma_0\, B\, (W-a)^2 \qquad (3.22)$$

Where α is a dimensionless constant, not the α in the Ramberg-Osgood relationship. Now for a crack of slightly different length (a+da) the moment can be expressed as:

$$M_{(a+da)} = \alpha\, \sigma_0\, B\, (W-(a+da))^2 \qquad (3.23)$$

The change in moment is then given by dM:

$$dM = M_{(a+da)} - M_{(a)} = -2\alpha\sigma_0 B[\, (W-a)da + da^2] \qquad (3.24)$$

Neglecting second order terms the change in the moment dM can be expressed in the form:

$$dM = -2\alpha\sigma_0 B(W-a)da \qquad (3.25)$$

The work done on the body is defined as the area under the moment-rotation curve (M-θ), Figure 3.12, and the incremental change in work done is:

$$dU = \theta \, dM \qquad (3.26)$$

Now from (3.6) J can be expressed as:

$$J = \frac{2U}{B(W-a)} \qquad (3.27)$$

On this basis Rice, Paris and Merkle (1973) derived the plastic component for deeply cracked geometries from the total area under the load-displacement response. The same form of dimensional argument can be applied to a deeply cracked bar subjected to pure tension where the limit load is expressed in the form:

$$P = \alpha \, \sigma_0 \, B \, (W-a) \qquad (3.28)$$

Following the argument leading to (3.27) the plastic component can be expressed as:

$$J_{plastic} = \frac{U_{plastic}}{B \, (W-a)} \qquad (3.29)$$

This has led Sumpter and Turner (1973, 1976), to express the plastic component of J in a general relation of the form:

$$J_{plastic} = \eta_{plastic} \frac{U_{plastic}}{B \, (W-a)} \qquad (3.30)$$

Where $\eta_{plastic}$ is a geometry dependent dimensionless constant defined as:

$$\eta_{plastic} = 0.32 + 12\left(\frac{a}{W}\right) - 49.5\left(\frac{a}{W}\right)^2 + 99.8\left(\frac{a}{W}\right)^3 \qquad \frac{a}{W} \leq 0.282$$

$$\eta_{plastic} = 2 \qquad \frac{a}{W} > 0.282 \qquad (3.31)$$

Sumpter and Turner (1976) express the fracture toughness of the body in the form:

$$J = \eta_{elastic}\frac{U_{elastic}}{B(W-a)} + \eta_{plastic}\frac{U_{plastic}}{B(W-a)} \qquad (3.32)$$

Where $\eta_{elastic}$ is also a non-dimensional geometric constant. Sumpter and Turner (1976) expressed this equation in a CTOD compatible form, through a load (P_L)that would give an approximation to the plastic work term, through a conjugate displacement $V_{plastic}$.

$$J = \frac{K^2(1-\nu^2)}{E} + \frac{\eta_{plastic}P_L V_{plastic}}{B\,(W-a)} \cdot \frac{W}{a + r(W-a)} \qquad (3.33)$$

This complication was removed when they expressed their formulation in a more readily useable form which relates J to crack mouth opening displacement (CMOD):

$$J_{total} = \frac{K^2(1-\nu^2)}{E} + \frac{\eta_{plastic}U_{V_{plastic}}}{B(W-a)} \cdot \frac{W}{a + r(W-a)} \qquad (3.34)$$

In equations (3.33 and 3.34) r is a rotational constant and $U_{V_{plastic}}$ is the plastic area under the load-CMOD trace as illustrated in Figure 3.13. The rotational constant r can be expressed in the form:

$$r = 0.3 + 0.5\left(\frac{a}{W}\right) \qquad \frac{a}{W} < 0.3$$

$$r = 0.45 \qquad \frac{a}{W} \geq 0.3 \qquad (3.35)$$

3.4: The Engineering Approach.

The evaluation of J can be carried out in a manner developed by EPRI (1981), based on the work of Illyushin (1946). Illyushin (1946) first noted that the field parameters, stress, strain and displacement for a power law hardening material of the form $\varepsilon = \alpha\, \sigma^n$ must be related to the load in the following manner:

$$\sigma \alpha P \qquad \varepsilon \alpha P^n \qquad u \alpha P^n \qquad (3.36)$$

The loads are proportional to the stresses, and the strains to the load levels raised to the power of the hardening rate. Since the plastic component of J can be interpreted in relation to the work done:

$$J_{plastic} \alpha U_{plastic} \qquad (3.37)$$

This can therefore be expressed in terms of the load since the work done is a product of the load and displacement:

$$\begin{aligned} J_{plastic} &\alpha P \,.\, u \\ J_{plastic} &\alpha P \,.\, P^n \\ J_{plastic} &\alpha P^{n+1} \end{aligned} \qquad (3.38)$$

This was the basis for the EPRI (1981) approach which is an estimation procedure for elastic-plastic materials that have a power law material response. Following this dimensional argument Kumar et al (1981) expressed the plastic component of J in the form:

$$J_{plastic} = \alpha\sigma_0\varepsilon_0 c h_1\left(\frac{a}{W}, n\right)\left(\frac{P}{P_r}\right)^{n+1} \qquad (3.39)$$

Here P_r is a reference load, $h_1\left(\frac{a}{W}, n\right)$ is a non-dimensional function of the strain hardening rate and geometry dependent constant. The dimensional scale is introduced

through the ligament (c) in the case of a single edge cracked bend bar or half the crack length (a) in the case of a centre cracked panel. It is also possible to express the elastic component of J in a similar form. The full field solution for cracked configurations is then given as the sum of the elastic and plastic components:

$$J_{total} = J\,(a_e)_{elastic} + J\,(a)_{plastic} \qquad (3.40)$$

The elastic portion of the analysis is based on Irwin's effective crack length (a_e) concept. Irwin's concept is based on the influence of the plastic zone on the crack length within the elastic regime where the crack length can be considered to be effectively given by:

$$a_e = a + \varnothing r_y$$

where (3.41)

$$r_y = \frac{1}{\beta\pi}\frac{[n-1]}{[n+1]}\left(\frac{K_I}{\sigma_0}\right)^2 \quad \text{and} \quad \varnothing = \frac{1}{\left(1+\frac{P}{P_r}\right)^2}$$

Here β=2 in plane stress and β=6 for plane strain, r_y is the radius of the plastic zone. For a single edge cracked bar the full field solution can be expressed in the following manner:

$$J_{total} = \alpha\sigma_0\varepsilon_0 ch_1\left(\frac{a}{W}, n=1\right)\left(\frac{P}{P_r}\right)^2 + \alpha\sigma_0\varepsilon_0 ch_1\left(\frac{a}{W}, n\right)\left(\frac{P}{P_r}\right)^{n+1} \qquad (3.42)$$

3.5: Limits of Single Parameter Characterisation.

There are a number of limitations to the application of J in fracture mechanics. If a crack propagates there is unloading on the new surfaces formed. For materials undergoing incremental plasticity this unloading is in the form of a linear elastic unloading and since most solutions for elastic-plastic fracture mechanics are determined using deformation plasticity, J cannot be applied rigorously to an extending crack. Stump and Zywicz (1993) have shown the path dependence of incremental plasticity in small strain theory, showing its sensitivity to constraint effects.

The basis for a single parameter characterisation of the crack tip stress and strain fields is that the region described by the HRR singularity must fully encompass the fracture process zone. This condition is termed J-Dominance, McMeeking and Parks (1979) and Shih and German (1981) have given limiting conditions for J-Dominance for deeply cracked bars.

McClintock (1968) showed that the plastic slip-line solutions depend on geometry and loading. McClintock (1968) showed that the slip line fields for single edge cracked bars in bending (SECB) and double edge cracked bars (DECB) as well as centre cracked bars (CCP) in bending develop non-unique slip line fields, as shown in Figure 3.14. McClintock (1968) has also shown that within the crack tip region there can be no unique stress and strain field for weakly hardening materials in the limit of full plasticity. A dimensional argument (Rice (1976)) shows that J-Dominance applies under geometric conditions of the form:

$$c \geq M(\varepsilon_0, n)\,\frac{J}{\sigma_0}$$

$$c \geq M(\varepsilon_0, n)\,\frac{\delta}{d_n} \qquad (3.43)$$

M is a dimensionless constant which depends on the strain hardening exponent and the yield strain. Paris (1972) suggested a value for M of between 25 and 50 to maintain plane strain conditions in the fracture process zone. Rice (1976) and Amazigo (1978) have shown

that in full plasticity the distances over which J-dominance is achieved decreases directly as a function of the strain hardening rate (n). McMeeking and Parks (1979) considered deeply cracked geometries, of the form of single edge cracked bend bars (SECB) and centre cracked panels (CCP) using large strain plastic deformation theory comparing their results with the small scale yielding solution (T=0). In this case J-dominance criteria only involves the remaining ligament. For a single edge cracked bar in bending the remaining ligament has to exceed $\frac{25\ J}{\sigma_0}$ while for the centre cracked panel this value rises to $\frac{200\ J}{\sigma_0}$.

Shih and German (1981) carried out a series of detailed finite element analyses of cracked bend bars (CBB) using small strain theory. Results of these analyses were then compared with the HRR field to determine the deviation from J-dominance. Agreement was found between full field solutions and the HRR field as long as the plastic zone was substantially smaller than the remaining ligament for the CCP analyses although as soon as large scale deformation was approached the fields deviate from J-dominance due to a loss of constraint. Shih and German (1981) confirmed the size requirements given by McMeeking and Parks (1979).

These studies considered the effect of deformation on deeply cracked geometries where plasticity is confined to the uncracked ligament, whereas most defects begin not on a macrostructural but on a microstructural size scale. Al-Ani (1988) and Al-Ani and Hancock (1991) have considered shallow cracked bars in bending and tension,where shallow cracks are defined such that plasticity is not confined to the ligament. The transition from deep to shallow cracked geometries also corresponds to the transition in sign of the second term of the Williams (1957) expansion from a tensile to compressive component. Al-Ani and Hancock (1991) have shown plasticity to be confined to the ligament for single edge cracked bend bars (SEC3PB) $\frac{a}{W} \geq 0.3$. Following the same restrictions plasticity is confined to the ligament in single edge cracked tension bars (SECT) for $\frac{a}{W} \geq 0.55$ and for double edge cracked bars (DEC) $\frac{a}{W} \geq 0.95$. The results of these analyses show that for these geometries there is a loss of J-dominance before $\frac{200\ J}{\sigma_0}$, where the crack length is the controlling dimension for shallow cracks. Agreement was found with the analyses of McMeeking and

Parks (1979) and Shih and German (1981) for deeply cracked geometries.

3.6: Two Parameter Characterisation.

Larsson and Carlsson (1973) examined elastic plastic crack tip fields for a wide range of geometries including double edge cracked (DEC), single edge cracked bend bars (SECB), compact tension specimens (CTS) and centre cracked panels (CCP). Full field solutions were then compared to crack tip fields determined from boundary layer formulations.

A boundary layer formulation is a technique that allows the elastic stress and displacement distribution obtained from a K field to be applied as the boundary conditions of an area that surrounds the crack tip. Larsson and Carlsson (1973) compared the plastic zones determined from the previous analyses with reference plastic zones determined by the boundary layer technique obtained from the first term of the Williams (1957) expansion (K). This comparison showed discrepancies between the plastic zone in specific geometries and the boundary layer of up to 30%. Following discussions with Rice, Larsson and Carlsson attributed this difference to the first finite term in the Williams (1957) expansion. By modifying the boundary tractions by the addition of a non-singular term it was possible to model the stress fields of full field solutions through a two parameter characterisation based on T.

3.7: Elastic T Stress.

Following the work of Larsson and Carlsson (1973) and using the notation of Rice (1974) the first terms of the Williams (1957) infinite expansion can be expressed:

$$\sigma_{ij} = \frac{K_I}{\sqrt{2\pi r}} f_{ij}(\theta) + T_{ij}(0) + S_{ij}(\theta)\sqrt{r} \ldots \qquad (3.44)$$

The third term and higher order terms are significant only at the outer boundaries. Close to the crack tip the stress field can be approximated by the first two terms of this expansion:

$$\begin{bmatrix} \sigma_{11} & \sigma_{12} \\ \sigma_{21} & \sigma_{22} \end{bmatrix} = \frac{K_I}{\sqrt{2\pi r}} \begin{bmatrix} f_{11}(\theta) & f_{12}(\theta) \\ f_{21}(\theta) & f_{22}(\theta) \end{bmatrix} + \begin{bmatrix} T & 0 \\ 0 & 0 \end{bmatrix} \qquad (r \rightarrow 0) \qquad (3.45)$$

The elastic T-stress has been calculated for a number of geometries by Leevers and Radon (1983), Kfouri (1986), Sham (1991) and Al-Ani (1988) who gave the magnitude of the T-stress in terms of a biaxiality parameter, β:

$$\beta = \frac{T\sqrt{\pi a}}{K_I} \qquad (3.46)$$

Leevers and Radon (1983) and Sham (1991) have tabulated values of the biaxiality for a number of important geometries and these are shown in Figure 3.15.

Bilby et al. (1986) first considered the applicability and validity of J-T characterisation for a wide range of geometries, where good agreement was found between a two parameter characterisation and the finite specimen fields. Betegón and Hancock (1991) considered the loss of J-dominance with respect to the T-stress and showed that compressive T-stresses cause the stress field to diverge from the small scale yielding solution (T=0) as the load is increased. The small scale yielding solution develops self similar fields, which differ significantly from the HRR field. Tensile T-stresses were shown to cause the stress levels to

rise slightly from the small scale yielding solution as the load is increased, and approach the HRR field. Betegón and Hancock (1991) showed that the decrease in the associated stress levels from the small scale yielding solution is dependent solely on the T-stress and is independent of the distance ahead of the crack tip, $\frac{r\sigma_0}{J}$.

T-stresses were also found to affect the plastic zone following the work of Larsson and Carlsson (1973). Tensile T-stresses decrease the size of the plastic zone and cause the plastic lobes to rotate backwards, while compressive T-stresses enlarge the maximum radius of the plastic zone and cause the plastic lobes to swing forward. The angular orientation of the maximum radius of the plastic zone is located at $\frac{3\pi}{4}$ for $\frac{T}{\sigma_0} = 1$ while for a compressive T-stress of the order $\frac{T}{\sigma_0} = -1$ this same orientation was found at $\frac{\pi}{4}$, Wang (1991). Associated also with compressive T-stresses are high levels of toughness, corresponding to a reduction in constraint as load increases. Betegón and Hancock's (1989) small strain results match those of Bilby et al. (1986) who considered large geometry change solutions for a non-hardening material to gauge the effect of compressive T-stresses acting on stress fields within the blunting zone. The deviation from small scale yielding field for compressive T-stresses is independent of distance ahead of the crack tip and has been expressed by Betegón and Hancock (1991) in the form:

$$\left(\frac{\sigma_{ij}}{\sigma_0}\right)_T = \left(\frac{\sigma_{ij}^{SSY}}{\sigma_0}\right)_{T=0} + 0.6\left(\frac{T}{\sigma_0}\right) - 0.75\left(\frac{T}{\sigma_0}\right)^2, \quad n=\infty \qquad \frac{T}{\sigma_0} \le 0$$

$$\left(\frac{\sigma_{ij}}{\sigma_0}\right)_T = \left(\frac{\sigma_{ij}^{SSY}}{\sigma_0}\right)_{T=0} + 0.64\left(\frac{T}{\sigma_0}\right) - 0.4\left(\frac{T}{\sigma_0}\right)^2, \quad n=13 \qquad \frac{T}{\sigma_0} \le 0 \qquad (3.47)$$

Wang (1991) checked this calculation and gave the stress fields for a modified boundary layer formulation at a strain hardening rate of n=10 as:

$$\left(\frac{\sigma_{ij}}{\sigma_0}\right)_T = \left(\frac{\sigma_{ij}^{SSY}}{\sigma_0}\right)_{T=0} + 0.617\left(\frac{T}{\sigma_0}\right) - 0.565\left(\frac{T}{\sigma_0}\right)^2 + 0.123\left(\frac{T}{\sigma_0}\right)^3 \qquad (3.48)$$

These results showing the relationship between the local stress field and T reinforced the work of Bilby et al (1986) who considered a similar effect for non-hardening materials. Du and Hancock (1991) attributed the difference in the stress fields to the hydrostatic stress (σ_m). For sufficiently positive values of T $\left(T \geq 0.446\sigma_0\right)$ the full Prandtl field is developed and plasticity fully envelops the crack tip as shown in Figure 3.16. In this figure Region I is an area where the stress fields due to the yield criteria are homogenous in the form of either compressive or tensile component parallel to the crack flanks. This arises form the Hencky equations and the straight lines in the wedge on the crack flanks. These stresses may be expressed in polar coordinates (r, θ):

$$\begin{aligned} \sigma_{rr} &= k\,(1-\cos 2\theta) \\ \sigma_{\theta\theta} &= k\,(1-\cos 2\theta) \\ \sigma_{r\theta} &= k \sin 2\theta \\ \sigma_m &= k \end{aligned} \qquad (3.49)$$

Here k is the yield stress in shear and σ_m is the mean stress. The remaining stress fields can be deduced from the Hencky equations, Hill (1952), which express equilibrium in the form of the rotation of the slip line fields. The stress state in Region II can be expressed in the form:

$$\sigma_{\theta\theta} = \sigma_{rr} = \sigma_{zz} = \sigma_m = k\left(1 + \frac{3\pi}{2} - 2\theta\right) \qquad (3.50)$$

$$\sigma_{r\theta} = k$$

Whereas in the diamond section, Region III the stress fields are expressed in the following simple stress state:

$$\begin{aligned} \sigma_{\theta\theta} &= k\,(\pi + 1 + \cos 2\theta) \\ \sigma_{rr} &= k\,(\pi + 1 - \cos 2\theta) \\ \sigma_{zz} &= \sigma_m = k\,(\pi + 1) \\ \sigma_{r\theta} &= k \sin 2\theta \end{aligned} \qquad (3.51)$$

Du and Hancock (1991) used modified boundary layer formulations to determine the stress fields for non-hardening plane strain deformation, through the angular distributions of the stress fields at the crack tip to determine the degree of crack tip plasticity. For compressive T-stresses an elastic region is developed from the crack flanks to an angular span close to $\frac{\pi}{4}$, being at a maximum for the most compressive stresses. The extent of crack tip plasticity is as shown in Figure 3.17 where for a T=0 field the crack tip plasticity does not extend back to the crack flanks and the angular span of the field is approximately 130°. The angular spans approaching the remaining ligament are shown in Figure 3.18 as the stress fields become less constrained.

3.8: Higher Order Asymptotic Solutions.

Li and Wang (1986), Sharma and Aravas (1991) Xia, Wang and Shih (1993) and Yang, Chao and Sutton (1993a, b) have considered to varying degrees defining higher order asymptotic solutions of crack tip fields based on small strain theory, retaining the HRR field as the leading term, expressing the stress fields in the form:

$$\frac{\sigma_{ij}(r, \theta, n)}{\sigma_0} = K_s r^s \widetilde{\sigma_{ij}^{(0)}}(\theta, n) + K_t r^t \widetilde{\sigma_{ij}^{(1)}}(\theta, n) + \ldots\ldots \qquad (3.52)$$

$$s = \frac{-1}{n+1}$$

Here K_s and K_t are the amplitudes of the first and second terms respectively, while the strength of the radial dependance of each term is expressed in the form r^s and r^t. The HRR field is identified with the first term of the series, t is the radial dependence of the second term and is the order of $0.05 <= t(n) => 0.07$ for $5<n<20$ as illustrated in Figure 3.19 Sharma and Aravas (1991). It is possible to express the two components of this expansion in the same functional form:

$$\frac{\sigma_{ij}(r,\theta)}{\sigma_0} = \left(\frac{J}{\alpha\sigma_0\varepsilon_0 I_n r}\right)^{\frac{1}{1+n}} \tilde{\sigma}_{ij}(\theta, n) + K^{(1)} r^t \tilde{\sigma}_{ij}^{(1)}(\theta, n) + \ldots \qquad (3.53)$$

Li and Wang (1986) developed a similar two term approach by matching the two term expansion to the centre cracked panel results of Shih and German (1981). Yang et al. (1993a, b) and Xia et al (1993) have expressed the stress field at the crack tip including higher order terms in a form:

$$\frac{\sigma_{ij}}{\sigma_0} = \sum_{\beta=1}^{\infty} \overline{A_\beta} \overline{r_\beta^s} \sigma^{(\beta)}{}_{ij}(\theta)$$

$$\frac{\sigma_{ij}}{\sigma_0} = \overline{A_1}\,\overline{r^{s_1}}\sigma_{ij}^{(1)}(\theta) + \overline{A_2}\,\overline{r^{s_2}}\sigma_{ij}^{(2)}(\theta) + \overline{A_3}\,\overline{r^{s_3}}\sigma_{ij}^{(3)}(\theta) + \ldots\ldots \qquad (3.54)$$

Where $\bar{r} = \frac{r}{L}$, where L is the characteristic crack length, s_β is the stress exponent, $\overline{A_\beta}$ is the amplitude and $\sigma_{ij}^{\beta}(\theta)$ is the angular function for the β term in the series expansion. Yang et al. (1993a, b) identified the first term in this asymptotic expansion with the HRR field, which leads to the notation:

$$\overline{A_1} = \left(\frac{J}{\alpha\sigma_0\varepsilon_0 I_n L}\right)^{\frac{1}{n+1}} \qquad (3.55)$$

The first three terms of this infinite asymptotic series expansion (3.54) were found to be defined by two parameters(J, A_2) for all strain hardening rates. In plane strain conditions the stress (σ_{ij}) ahead of the crack tip the series can be truncated due to the similarity of the angular distributions of further higher order terms and can be expressed by the first three terms of the series:

$$\frac{\sigma_{\theta\theta}}{\sigma_0} = \left(\frac{J}{\alpha\varepsilon_0\sigma_0 I_n L}\right)^{\frac{1}{n+1}} \left[\left(\frac{r}{L}\right)^{s_1} \tilde{\sigma}_{\theta\theta}^{(1)}(\theta) + A_2\left(\frac{r}{L}\right)^{s_2} \tilde{\sigma}_{\theta\theta}^{(2)}(\theta) + (A_2)^2\left(\frac{r}{L}\right)^{s_3} \tilde{\sigma}_{\theta\theta}^{(3)}(\theta)\right] \qquad (3.56)$$

where

$$A_2 = \frac{\overline{A_2}}{\overline{A_1}} = \frac{\overline{A_2}}{\left(\frac{\alpha\varepsilon_0\sigma_0 I_n L}{J}\right)^{s_1}} \qquad (3.57)$$

The stress fields are thus expressed in terms of controlling parameters J and A_2.

3.9: Small Strain Difference Term, Q.

There is no unique choice of second global parameter to describe the stress fields that surround the crack tip. T-stress is simply an elastic parameter that has no rigorous physical basis in fully plastic conditions, although excellent qualitative and quantitative results past the region of limit load have been made by a number of researchers, Wang (1991), Parks (1991), Betegón and Hancock (1991), Du and Hancock (1991) and Al-Ani and Hancock (1991). Other research by O'Dowd and Shih (1991, 1992) has questioned the validity of the T-stress approach as you move towards full plasticity.

O'Dowd and Shih (1991, 1992) have carried out detailed finite element analyses on a large range of geometries in an attempt to determine a suitable *elastic-plastic* constraint characterising parameter. O'Dowd and Shih (1991) considered a two term expansion where the second term of the expansion is termed Q, where Q has been defined to be the amplitude of the second order field.

O'Dowd and Shih (1991, 1992) considered boundary layer formulations where the remote tractions are given by the first two terms of the linear elastic Williams (1957) expansion. From this two parameter description the only length scale introduced in the boundary layer formulation is in the form $\left(\frac{K_I}{\sigma_0} \text{ or } \frac{J}{\sigma_0}\right)$ therefore displacements and quantities with the dimension of length must scale with it. For fully plastic geometries O'Dowd and Shih (1991, 1992) have expressed the field parameters in terms of the global parameters (J, Q) where the field parameters can only depend on distance through $\frac{r\sigma_0}{J}$, therefore in a

plasticity analysis:

$$\frac{\sigma_{ij}}{\sigma_0} = f_{ij}\left(\frac{r\sigma_0}{J}, \theta; Q\right), \quad \frac{\varepsilon_{ij}}{\varepsilon_0} = g_{ij}\left(\frac{r\sigma_0}{J}, \theta; Q\right), \quad u_i = \frac{J}{\sigma_0} h_i\left(\frac{r\sigma_0}{J}, \theta; Q\right) \qquad (3.58)$$

Where f_{ij}, g_{ij} and h_i are dimensionless material dependent parameters. This description constitutes a Q-family of solutions. For a mode I small strain problem the solution is expressed in a two term expansion:

$$\frac{\sigma_{ij}}{\sigma_0} = \left(\frac{J}{\alpha\varepsilon_0\sigma_0 I_n r}\right)^{\frac{1}{n+1}} \tilde{\sigma}_{ij}(\theta; n) + Q\left(\frac{r\sigma_0}{J}\right)^q \tilde{\sigma}_{ij}(\theta; n) \qquad (3.59)$$

The second order term has also been obtained by Li and Wang (1986) and Sharma and Aravas (1991) through a perturbation analysis where the HRR field was the dominant singularity. O'Dowd and Shih (1991) followed a different course attempting to derive *difference fields*; small scale yielding solutions to modified boundary layer problems were determined and considered to be exact solutions, then compared to the HRR solution in an annular region, $1 < \frac{r\sigma_0}{J} < 5$ deriving a difference field:

$$\Delta\sigma_{ij} = \sigma_{ij\,(SSY)} - \sigma_{ij\,(HRR)} \qquad (3.60)$$

This approach differs from that of Li and Wang (1986) and Sharma and Aravas (1991) since (3.59) offers an approximation of the exact solution whereas the summation of the HRR field and the difference field must provide an exact match to the solution since it incorporates all higher order terms. O'Dowd and Shih (1991) state a distance independence in the difference field between the SSY and the HRR fields and describe the stress fields in the form:

$$\sigma_{ij} = \sigma_{ij\,(HRR)} + Q\,\tilde{\sigma}_{ij}(\theta, n) \qquad (3.61)$$

Therefore by this description the difference field is described by Q ahead of the crack.

O'Dowd and Shih (1991) state that the difference field ahead of the crack tip possesses a simple structure which corresponds to a uniform hydrostatic stress, therefore Q is defined as:

$$Q \equiv \frac{\sigma_{\theta\theta} - \sigma_{\theta\theta\,(HRR)}}{\sigma_0} \quad \theta = 0, \frac{r\sigma_0}{J} = 2 \qquad (3.62)$$

O'Dowd and Shih (1991) have proposed two forms of stress field descriptions derived from two significantly different reference fields:

$$\sigma_{ij} = \sigma_{ij\,(HRR)} + Q\sigma_0\delta_{ij}$$
$$\sigma_{ij} = \sigma_{ij\,(SSY)} + Q\sigma_0\delta_{ij} \qquad (3.63)$$

Shih, O'Dowd and Kirk (1991) offer the SSY reference field as the most accurate description of the Q-family of fields. The initial distance dependence offered by O'Dowd and Shih (1991) appears to significantly differ from that of Betegón and Hancock (1991) and Wang and Parks (1991) where the difference field between the SSY and HRR fields was shown to be distance dependent. Q can then be described at some distance ahead of the crack tip as:

$$Q = \frac{\sigma_{ij} - \sigma_{ij\,(SSY)}}{\sigma_0} \qquad (3.64)$$

3.10: Local Failure Criterion.

Fracture resistance can be expressed in global terms with parameters such as K_{IC} and J_{IC} in lefm and epfm respectively, where this is a *global approach* to fracture. Another approach is possible by modelling the macroscopic fracture behaviour in terms of a *local failure criteria*. This criteria is based on the elastic-plastic stress-strain history at the fracture point along with a micromechanical model for the physical process of fracture.

Ludwik and Scheu (1923) first postulated failure on the attainment of a critical stress

level. Slip induced cleavage cracks will propagate in an unstable manner when the local tensile stress (σ_{yy}) reaches a critical value (σ_f), which is independent, or very weakly dependent of temperature and strain, Orowan (1948), Knott (1966, 1967), Oates (1968, 1969) and Wilshaw, Tetelman and Rau (1968).

Ritchie, Knott and Rice (1973) related the critical stress approach to the macroscopic fracture toughness of a cracked body by examining the temperature dependence of K_{IC}. It is possible for the critical cleavage stress to be exceeded at the crack tip for sufficiently low load levels before fracture occurs so therefore not only must the critical stress be considered but also the size scale over which it applies, Rice and Johnson (1970). The application of the critical stress criterion in the stress strain gradients ahead of a crack requires the introduction of a microstructural size scale over which the stress levels are applicable. Ritchie, Knott and Rice (1973) postulate that brittle failure will occur when a critical cleavage stress, σ_f, is attained over a microstructurally significant distance from the crack tip, r^*. Cleavage fracture is associated with the cracking of grain boundary carbides therefore on first approximation the characteristic distance could be considered to be of the order of one grain diameter. However within the plastic zone ahead of the crack tip the stress field is non-uniform and it is possible that the stress level would be insufficient to propagate across the second grain. Therefore Ritchie, Knott and Rice (1973) have found that the necessary stress intensification ahead of the crack tip has to be achieved over a sizescale which is a small multiple of the grain diameter dependent on the form of *stress raiser*. In the case of a sharp crack the required stress level can occur very close to the crack tip therefore the crack can be initiated at the first grain boundary carbide, for unstable failure to occur the stress criterion must be met over the next grain diameter. Therefore for a sharp crack to propagate in an unstable manner in mild steel, the local tensile stress must exceed σ_f at a characteristic distance of approximately two grain diameters from the crack tip, Ritchie, Knott and Rice (1973). More sophisticated models have been developed by Beremin (1983) and Lin, Evans and Ritchie (1986) who have addressed the statistical problem associated with the application of weakest link criteria to the finite volumes of material ahead of the crack tip field. In contrast

Anderson and Dodds (1991) have developed a *contoured volume* approach.

Beremin (1983) expressed the critical cleavage stress in relation to the length of microcracks (l_0) in respect of the metallurgical features:

$$\sigma_f = \sqrt{\frac{2E\gamma_p}{\pi\,(1-\nu^2)\,l_0}} \qquad (3.65)$$

Where γ_p is the plastic surface energy, unstable fracture will occur if the principal stress normal to the boundary carbide planes is of a high enough level. From this description there is an obvious size effect in fracture, with the probability of finding a microcrack of suitable length for fracture to occur being a function of the volume involved. Beremin (1983) performed a statistical analysis considering small portions of the stressed volume (V_0) based on the probability of finding a crack of suitable length (l_0^c) to enable unstable fracture. They therefore expressed the probability of failure in terms of these portions of the total volume as simply:

$$P(\sigma_f) = \int_{l_0^c}^{\infty} P(l_0)\, dl_0 \qquad (3.66)$$

The cumulative probability of failure on the entire specimen is expressed in relation to material constants as:

$$P_f = 1 - \exp\left[-\left(\frac{\sigma_w}{\sigma_u}\right)^m\right] \qquad (3.67)$$

Where σ_u and m are material constants while σ_w is the weibull stress.

Lin, Evans and Ritchie (1986) also considered cleavage failure based on weakest link statistics applied to the microstructural failure mechanisms. Their approach is based upon the prediction of the macroscopic fracture toughness of the body based on a known distribution of particles and defines the critical distance at which the initial cracking event will occur.

Beremin (1983) based their analyses on microcrack lengths whereas Lin, Evans and Ritchie (1986) proposed a method based upon carbide size where the strength of each carbide is inversely proportional to their size. Therefore, there is a competing process between carbides of differing sizes with fracture occurring at the highest stressed carbide, Curry and Knott (1979). The cleavage fracture toughness is then estimated by sampling the plastic zone for the presence of an eligible particle for which the fracture criteria can be satisfied. In the same manner that a failure probability for individual elements within the plastic zone based on microcrack lengths is achieved by Beremin (1983), Lin, Evans and Ritchie (1986) expressed in terms of a strength distribution. Where the total failure probability due to the propagation of the weakest particle is:

$$P_R = 1 - \exp\left\{ -\int_0^V \left[dV \int_0^\sigma g\,(S)\, dS \right] \right\} \qquad (3.68)$$

Where g(S)dS is the strength distribution and can be expressed in a three parameter Weibull model as:

$$\int_0^\sigma g(S)\, dS = \left(\frac{\sigma - S_u}{S_0}\right)^m f\, N \qquad (3.69)$$

S_0 is a scale parameter, S_u is the lower bound strength, m is a shape factor and N is the number of particles per unit volume. Whereas f is the number of eligible particles available to take place in the fracture process.

At low temperatures because the plastic zone is small the site of crack initiation is close to the elastic-plastic interface, whereas at higher temperatures this same site lies well within the plastic zone due to its increased size. Two idealisations are used to describe the stress field distributions, at low temperatures the far field linear elastic solution is used (1.12)

whereas at higher temperatures the near tip HRR solution is utilised. By defining active elements in which the stress is constant it is possible to express the elemental survival probability as a minimum at a characteristic distance r^* from the crack tip:

$$r^* = \left[\frac{1 - \nu^2}{I_n}\right]\left[\frac{2n + 3 - m}{2n + 3}\right]^{n+1} \left(\frac{K_I}{\sigma_0}\right)^2 \left(\frac{\sigma_0}{S_u}\right)^{n+1} \tilde{\sigma}^{n+1} \qquad (3.70)$$

Which occurred at the stress:

$$\sigma^* = \left[\frac{2n + 3}{2n + 3 - m}\right] S_u \qquad (3.71)$$

As shown in Figure 3.20. When cleavage occurs σ^* and r^* can be equated with the critical cleavage stress (σ_f) and the microstructurally significant distance of the Ritchie, Knott and Rice (1973) analysis. In statistical terms r^* represents the distance at which crack initiation is most liable to occur. For a sharp crack the local stresses progressively decrease with distance from the crack tip. The value of r^* reflects the competition between the far field, close to the elastic-plastic interface where the number of eligible particles is high but the stress level is low and the near tip field where the number of eligible particles is low but the stress level is high.

The statistical methodologies presented by both Beremin (1983) and Lin, Evans and Ritchie (1986) gave good agreement with experimental results however there are a number of important points that should be realised. These models rely on idealised stress field descriptions. The models are also only valid for the propagation of a microcrack from a carbide particle into the matrix. These are invalid if the controlling process is the propagation of a microcrack through the grain boundary which occurs near the transition temperature, Holtzman and Man (1971).

Anderson and Dodds (1991) have proposed an alternative approach which predicts the variation of fracture toughness with constraint changes by scaling in relation to the small scale yielding limiting solution. The probability of cleavage fracture is dependent on a *triggering microfeature*, which suggests that the volume of the material within the process

zone where the local stress exceeds the critical cleavage stress is the limiting feature. Therefore the probability of cleavage fracture in a cracked specimen is:

$$P_f = P\left[V(\sigma_1)\right] \qquad (3.72)$$

Where P_f is the failure probability, σ_1 is the maximum principal stress and $V(\sigma_1)$ is the total volume over which the principal stress is equal to or greater than σ_1. Anderson and Dodds (1991) attempt to predict the variation of fracture toughness with constraint changes by comparison with a reference solution, and not determine absolute toughness values. Anderson and Dodds (1991) utilise the stress field distribution of (3.58), in terms of the maximum principal stresses and then equate the stressed areas of the finite body to the Q=0 reference field. The area associated with the reference field (Q=0) enclosed by a principal stress level of $\left(\frac{\sigma_1}{\sigma_0}\right)$:

$$A_0 = \frac{J^2}{\sigma_0^2} h_0\left(\left(\frac{\sigma_1}{\sigma_0}\right); Q\right) \;,\; h_0 = \frac{1}{2}\int_{-\pi}^{\pi} g_1^2\left(\theta; \left(\frac{\sigma_1}{\sigma_0}\right); Q = 0\right) d\theta \qquad (3.73)$$

The area enclosed by this principal stress level depends on J as well as the level of stress triaxiality, therefore the area associated with Q≠0:

$$A_{FB} = \frac{J^2}{\sigma_0^2} h_{FB}\left(\left(\frac{\sigma_1}{\sigma_0}\right); Q\right) \;,\; h_{FB} = \frac{1}{2}\int_{-\pi}^{\pi} g_1^2\left(\theta; \left(\frac{\sigma_1}{\sigma_0}\right); Q\right) d\theta \qquad (3.74)$$

Therefore the level of fracture toughness can be expressed as:

$$\frac{J_{FB}}{J_0} = \sqrt{\frac{h_0\left(\frac{\sigma_1}{\sigma_0}\right)}{h_{FB}\left(\frac{\sigma_1}{\sigma_0}\right)}} \qquad (3.75)$$

Where J_{FB} is the toughness associated with a crack in a finite body with $Q \neq 0$. This toughness ratio quantifies the size and geometry dependence of cleavage fracture toughness and predicts the sharp increase in fracture toughness with a reduction in $\frac{a}{W}$.

3.11: Conclusions.

There is no unique method for quantifying crack tip constraint, the two principal methods espoused are, the elastic T-stress and the small strain difference term, Q. However the *validity* of both descriptions has been called into question.

The validity of the T-stress has been questioned at high levels of plasticity beyond limit load. However there is no doubt that the T-stress approach correctly identifies the plain strain geometries which lose constraint, and does so beyond the confines of small scale yielding. Whereas Q is *simply* a stress field difference term, therefore the accuracy of this approach cannot be questioned. However this theory is hindered by the lack of a simple engineering method for resolving Q, even the simplest engineering component would require a detailed full elastic-plastic analysis.

Two parameter fracture mechanics has the ability to expand radically present failure and defect assessment methodologies such as R6 Rev. 3 and PD6493. These methodologies presently rely upon a single parameter characterisation of stress fields and therefore do not take advantage of the enhanced toughness associated with unconstrained geometries.

Further advances based on utilising this enhanced toughness of unconstrained fields in relation to failure assessment diagrams are considered later in this work.

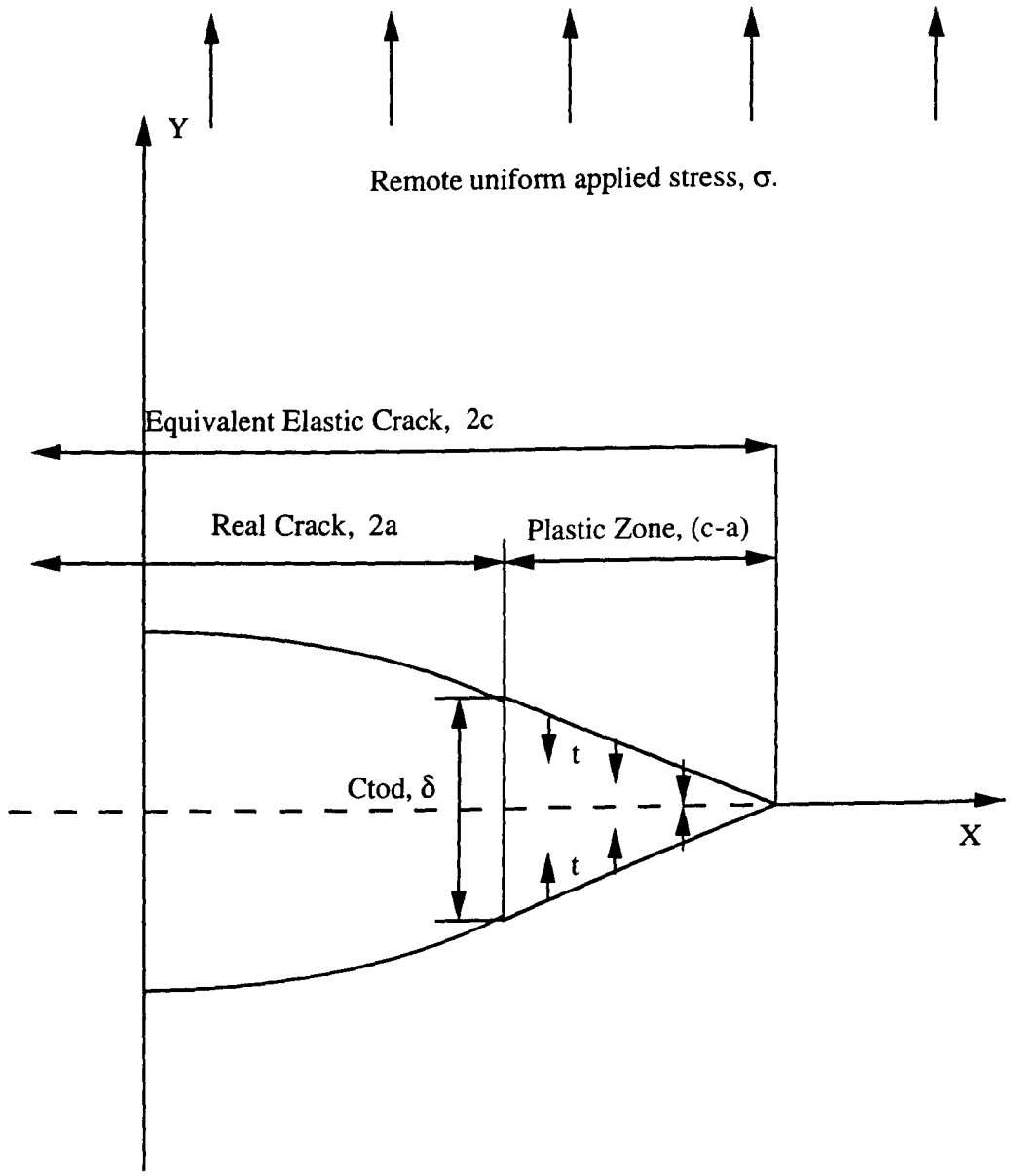

Figure 3.1: Dugdale 'Strip-Yield' Model for Crack Tip Plasticity.

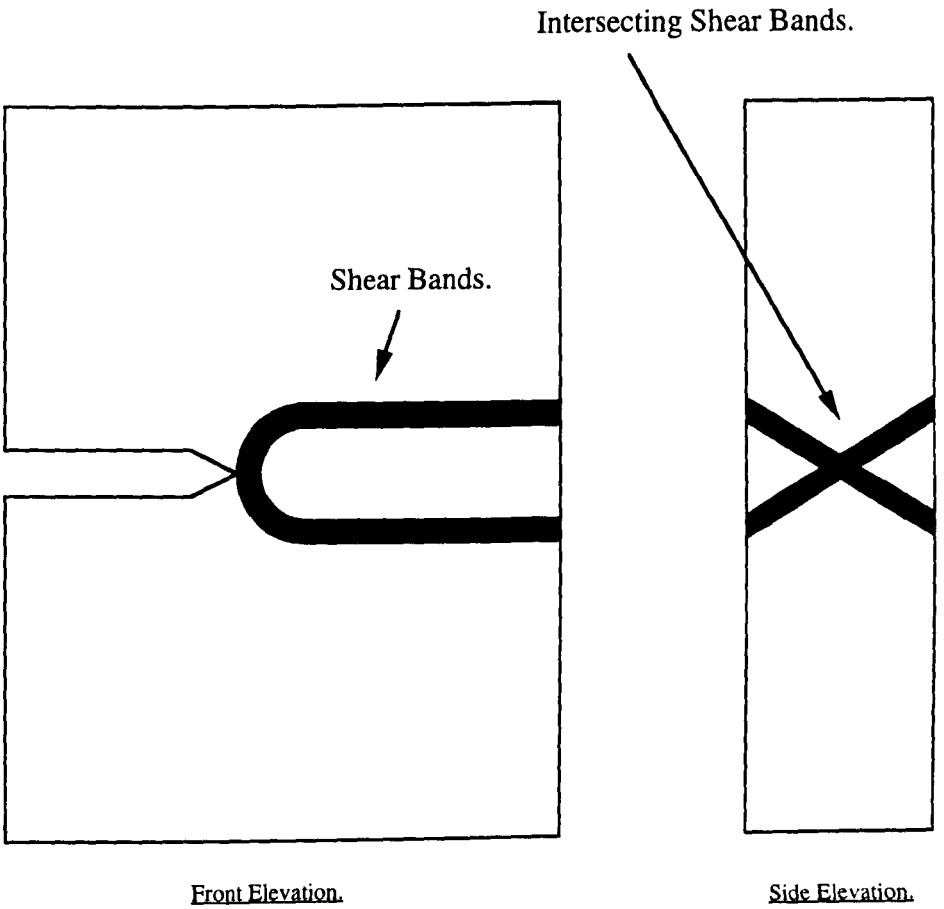

Figure 3.2: Idealised Schematic of the Results of Rosenfield et al Investigation.

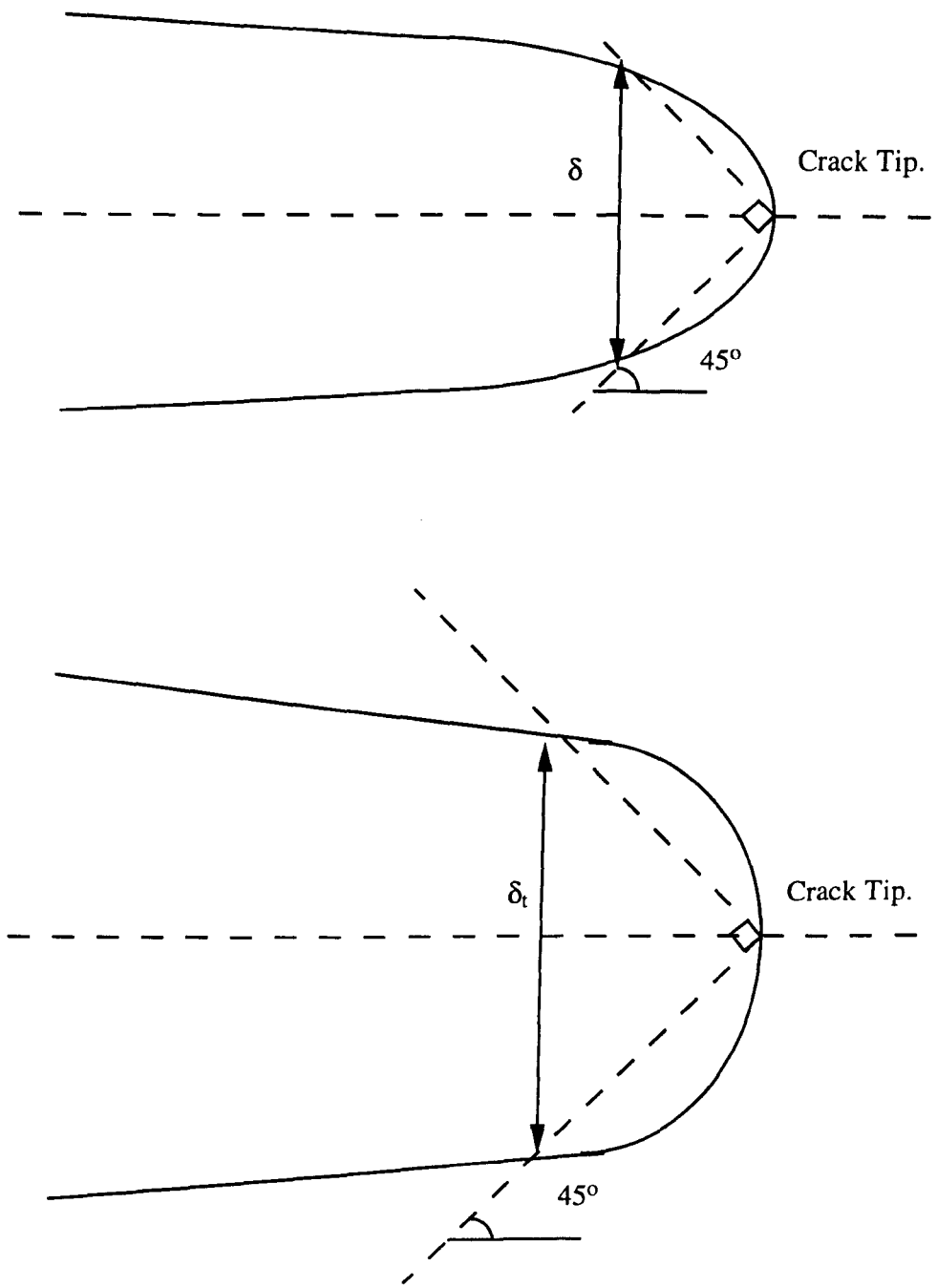

Figure 3.3: Definition of Crack Tip Opening Displacement (δ)

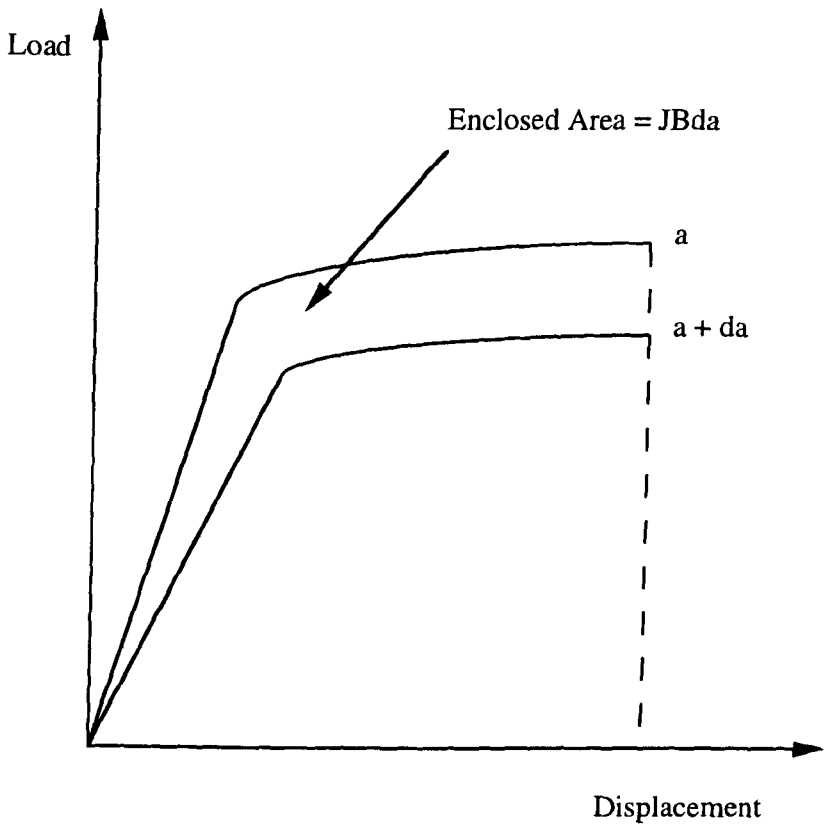

Figure 3.4: Determination of J by Potential Energy Difference.

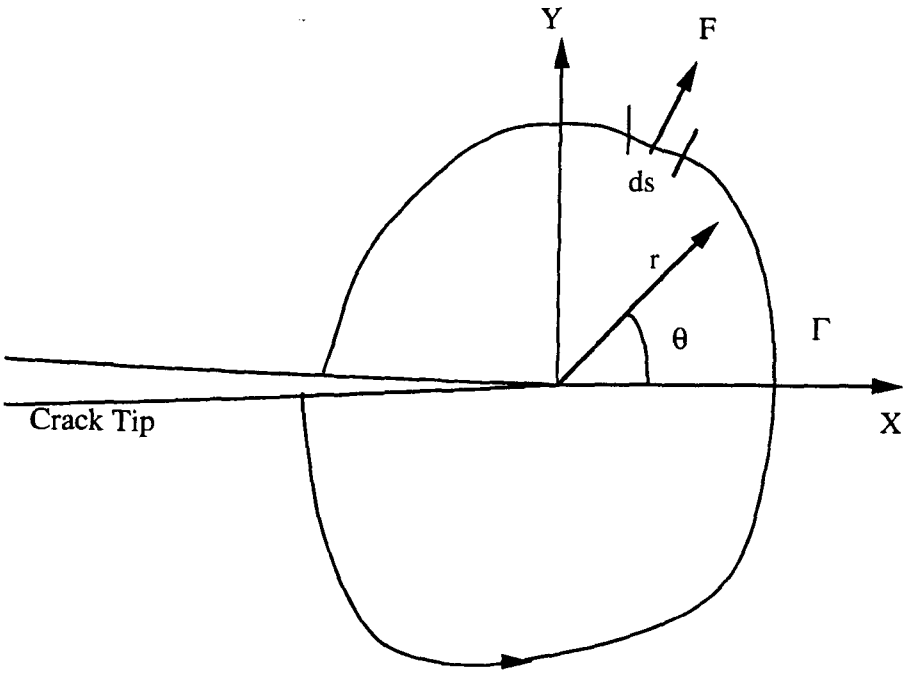

Figure 3.5: Definition of the J-Integral.

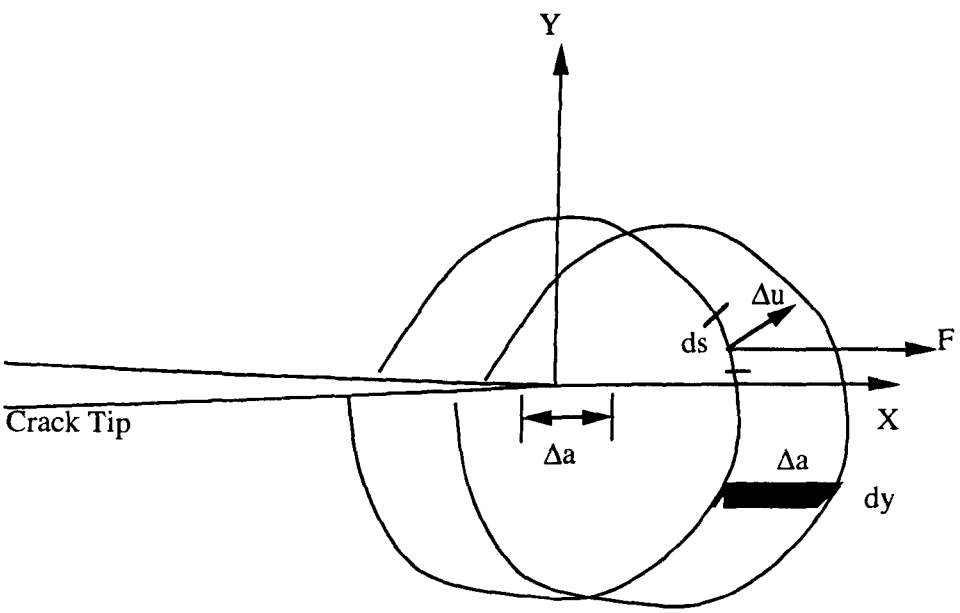

Figure 3.6: Crack Contour Integral and Crack Tip Coordinate System.

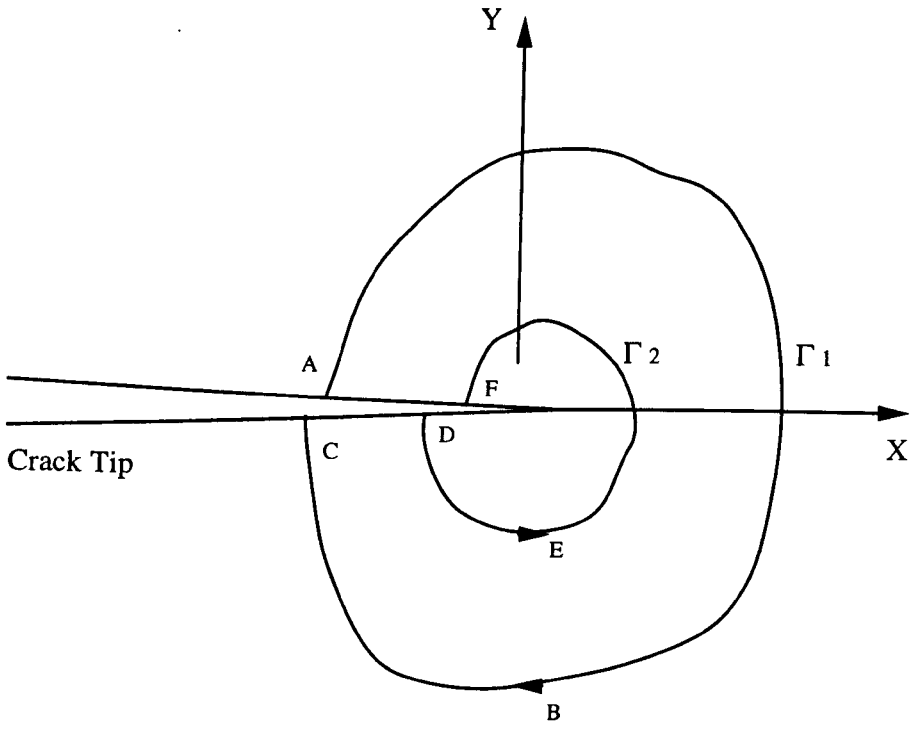

Figure 3.7: Path Independence of the J-Integral.

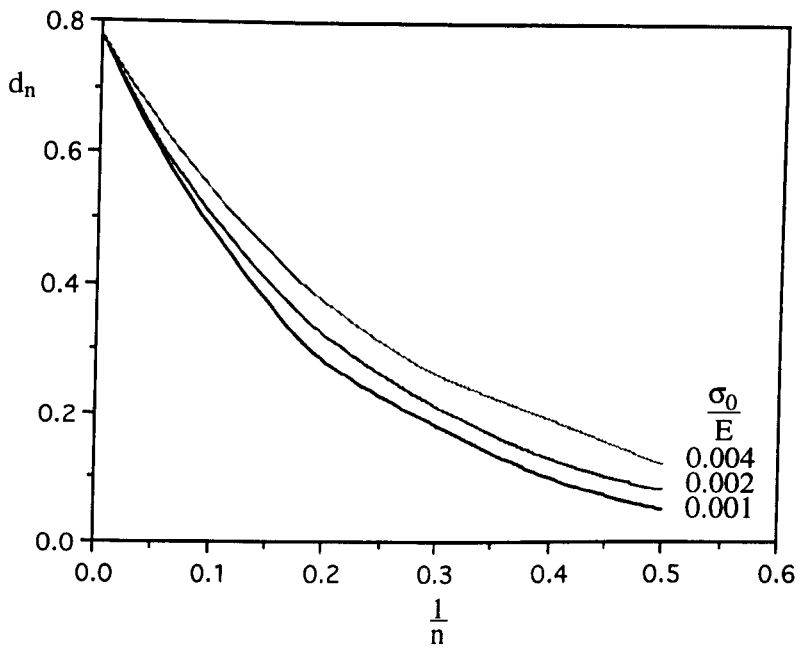

Figure 3.8: Variation of dn for Plane Strain (Shih et al 1981).

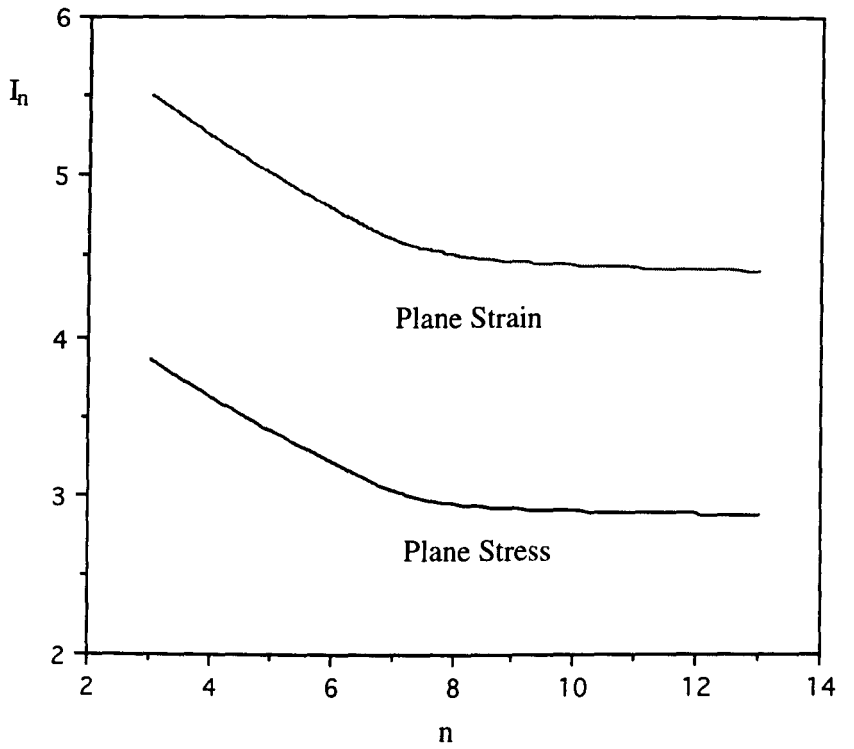

Figure 3.9: In for various Work Hardening Exponents.

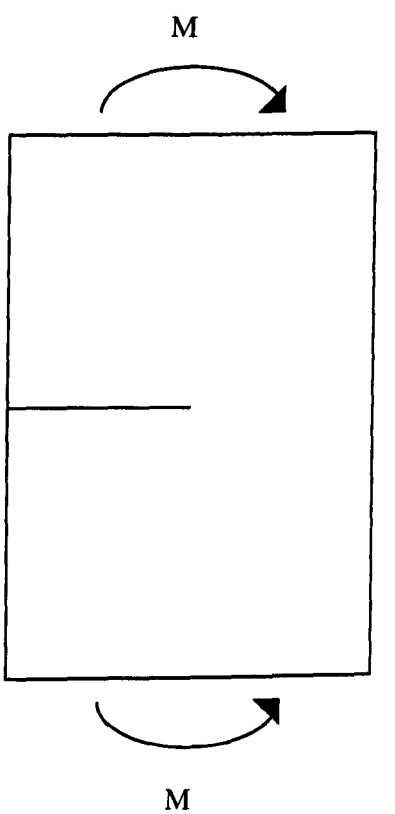

Figure 3.10: Deeply Cracked Bar in Pure Bending.

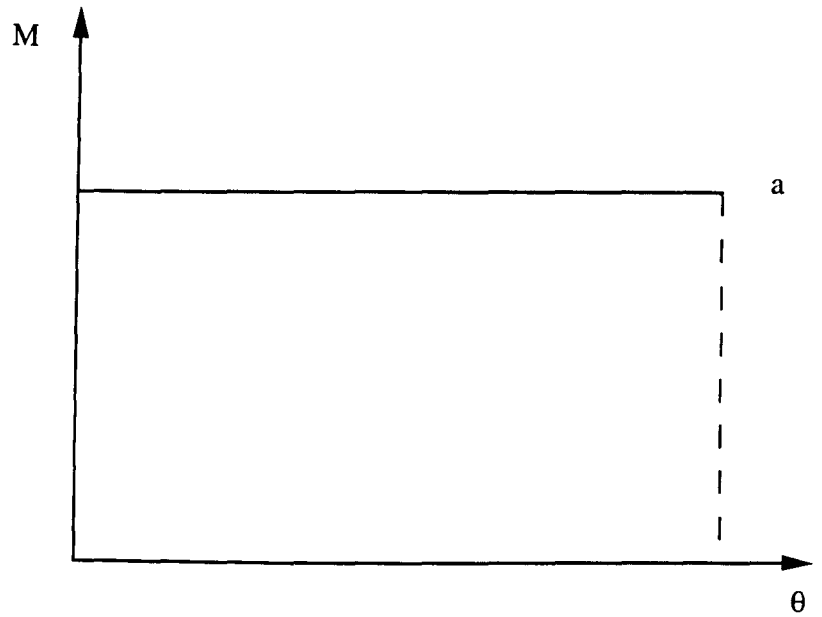

Figure 3.11: Moment-Rotation Diagram for a Non-Hardening Material.

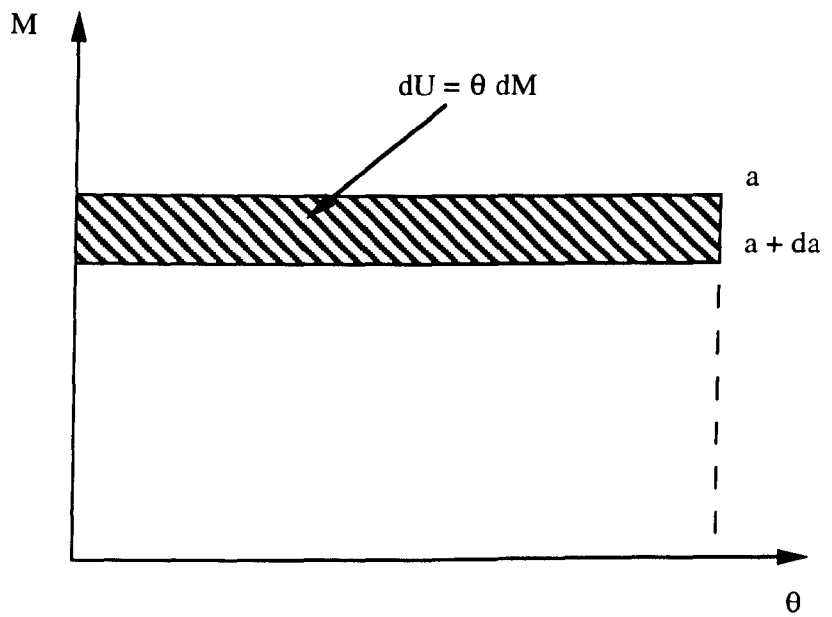

Figure 3.12: Change in Work Done for a Non-Hardening Material.

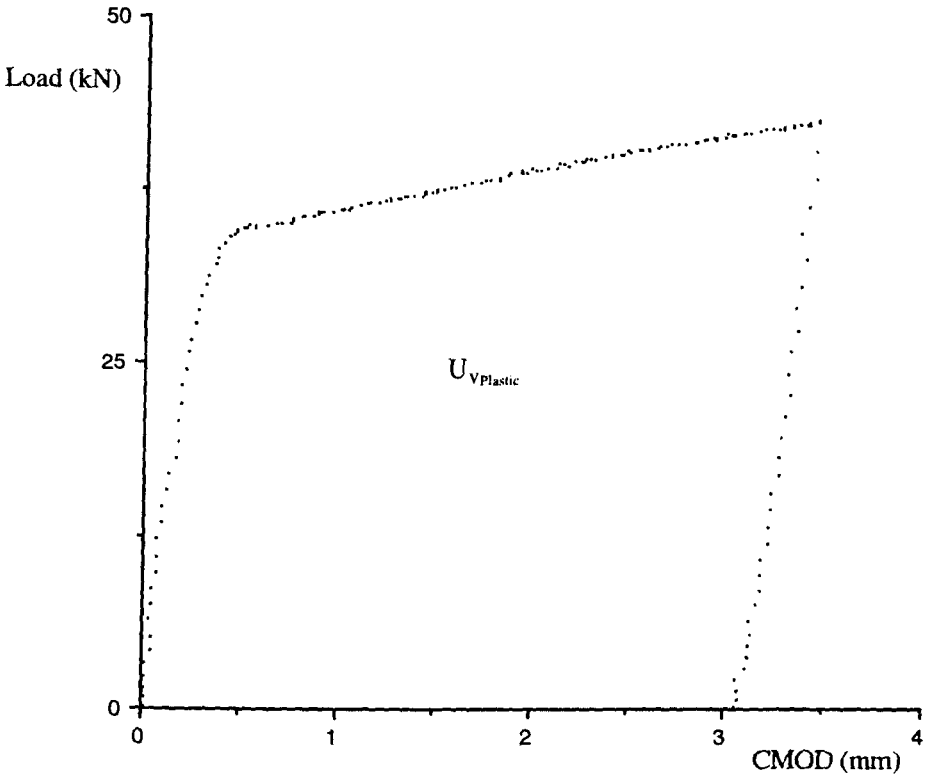

Figure 3.13: Load-CMOD Experimental Trace.

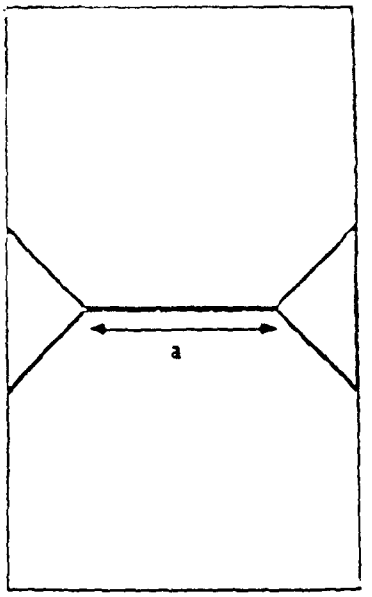

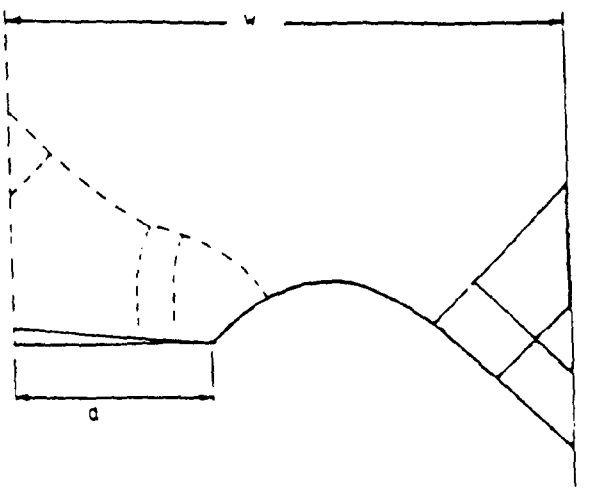

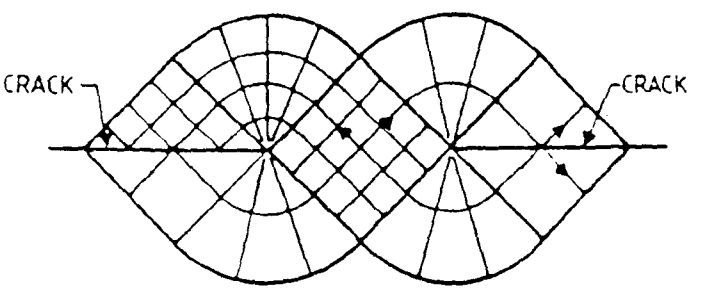

Figure 3.14: Slipline Fields for DECB, SEC3PB and CCP Geometries.

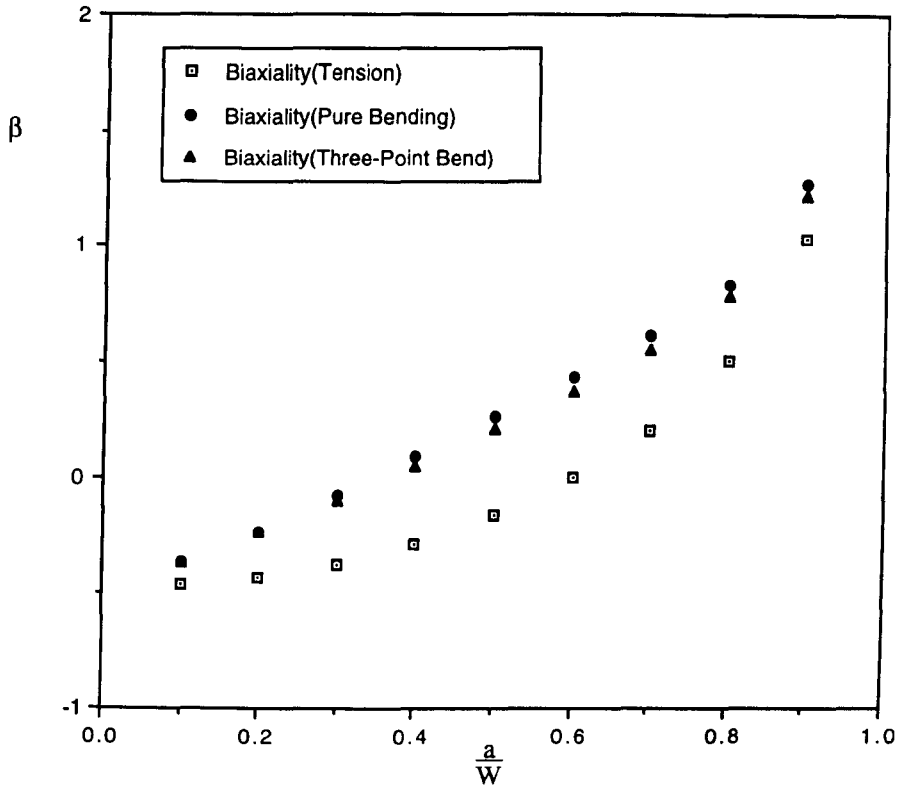

Figure 3.15: Biaxiality Parameters for Single Edge Cracked Specimens, Sham (1991).

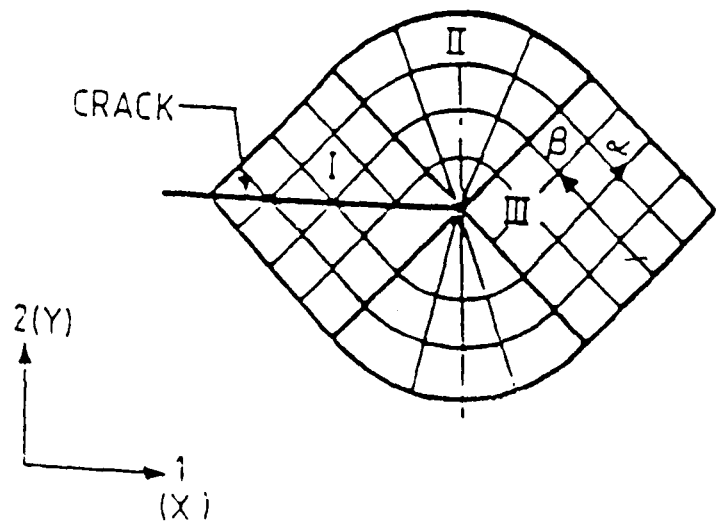

Figure 3.16: Full Prandtl Field.

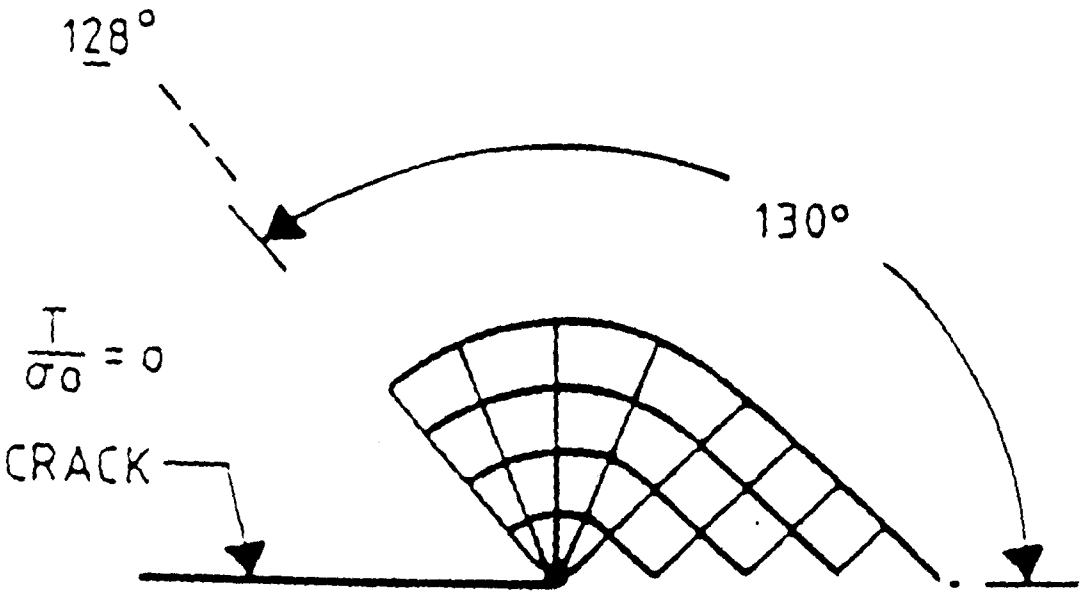

Figure 3.17: Plasticity around Crack Tip for $\frac{T}{\sigma_0} = 0$ Field.

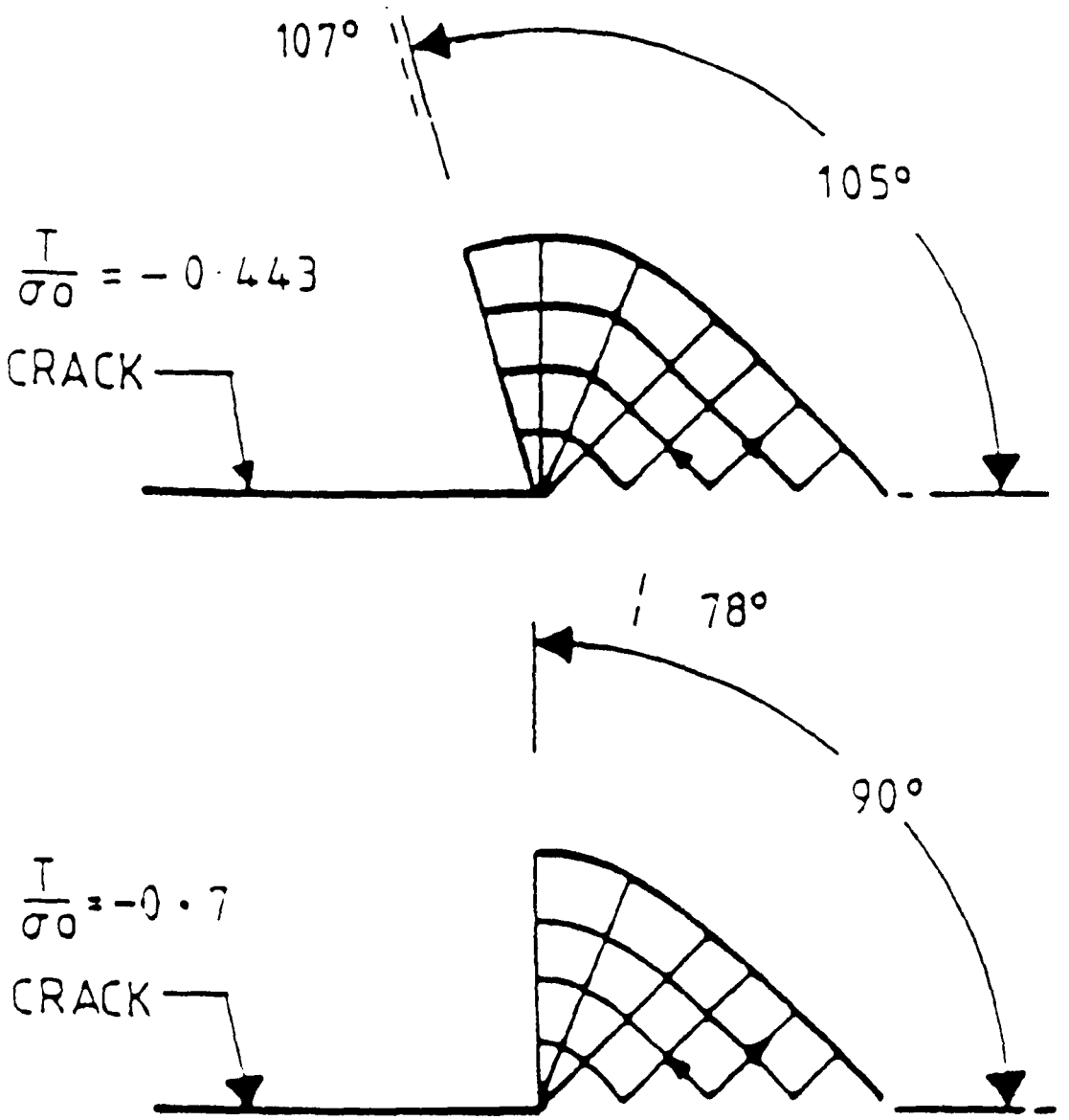

Figure 3.18: Plasticity around Crack Tip for -0.443 and -0.7 Fields.

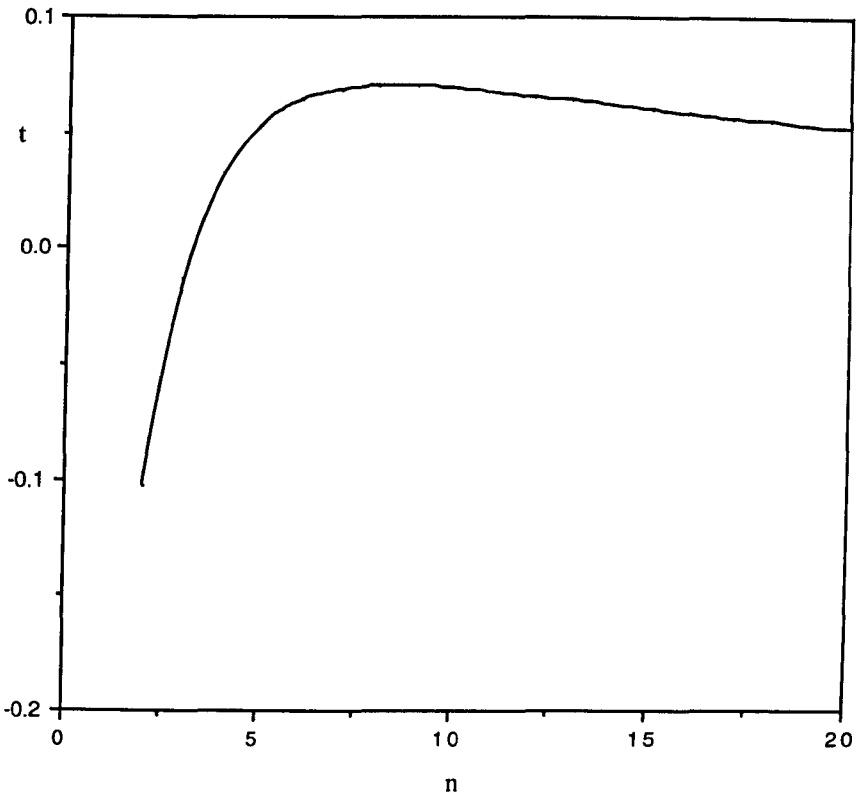

Figure 3.19: Graphed Value of the Power of the Second term in the Asymptotic Expansion of Sharma and Aravas (1991).

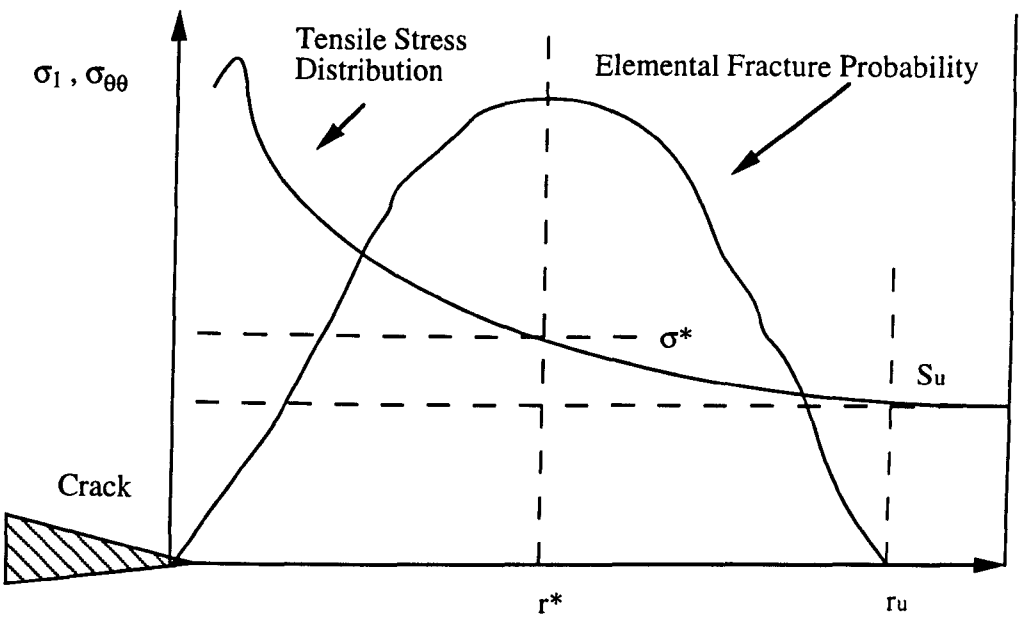

Figure 3.20: Site of Most Probable Crack Initiation.

4: Modified Boundary Layer Formulations.

4.1: Introduction.

In the present work the crack tip fields in small scale yielding have been determined using modified boundary layer formulations. The elastic displacements (u, v) associated with the leading two terms of the Williams expansion can be expressed as:

$$u = \frac{K}{2G}\left(\frac{r}{2\pi}\right)^{\frac{1}{2}} \cos\left(\frac{\theta}{2}\right)\left\{\kappa - 1 + 2\sin^2\left(\frac{\theta}{2}\right)\right\} + \frac{r\,T(1-\nu^2)\cos\theta}{E}$$

$$v = \frac{K}{2G}\left(\frac{r}{2\pi}\right)^{\frac{1}{2}} \sin\left(\frac{\theta}{2}\right)\left\{\kappa + 1 - 2\cos^2\left(\frac{\theta}{2}\right)\right\} - \frac{r\,T(\nu-\nu^2)\sin\theta}{E} \qquad (4.1)$$

Where (r, θ) are cylindrical coordinates centred at the crack tip and $\kappa = (3 - 4\nu)$ for plane strain. These displacement functions can then be applied as boundary conditions on a region surrounding the crack tip to govern the outer elastic field. This form of analysis removes the need to model the whole body when studying crack tip deformation.

Two types of analyses were considered, small and large strain solutions. Small geometry change solutions maintain a sharp crack tip as shown in Figure 4.1, this form of solution does not model the finite geometry changes associated with crack tip blunting and is therefore inherently a small strain solution, as exemplified by the HRR field. At the crack surface there is no free surface normal to the crack plane and as the crack tip is approached all the principal stresses become singular. In reality this is an impossibility since there will always be finite plastic deformation at the crack tip associated with the crack tip blunting and the formation of a real surface at the crack tip. The results of such an analysis are considered to be valid outwith the region of crack tip blunting which is usually taken to be of the order of $\frac{2J}{\sigma_0}$.

To investigate the influence of crack tip blunting on the stress fields large strain analyses were also carried out. This form of analysis allows blunting to occur at the crack tip. Numerical problems associated with strain singularities at the tip were avoided by the use of an initially blunt crack tip as illustrated in Figure 4.2. This technique gives a reasonable approximation to the blunting of a sharp tip after the diameter of the original crack tip has increased to two or three times its original opening as discussed by McMeeking (1977).

4.2: Numerical Method.

Plane strain boundary layer formulations were implemented in ABAQUS (1988a, b) using the focused mesh as shown in Figure 4.3. It was only necessary to model half of the body due to the symmetry associated with mode I loading. The mesh involved 360 hybrid second order reduced integration isoparametric elements arranged in 30 concentric rings of 12 elements. The radius of the first ring of elements was less than one millionth of the radius of the outer ring, to provide a suitably fine and detailed mesh. In the case of the small geometry change solutions 25 independent but coincident nodes were located at the crack tip. These nodes were arranged symmetrically around a key hole notch for the large strain solutions, displacement boundary conditions were then applied to the outer boundary of the mesh. Although this formulation gives no reference to geometric dimensions such as ligament length, a dimensional scale is introduced by the radius at which the elastic field is introduced. Solutions from these analyses were obtained for plastic zone radii very much less than the radius of the outer boundary, as described by Tracey (1976) and Parks and Wang (1988). These conditions therefore satisfy the requirements of small scale yielding, the stresses being self similar when normalised ahead of the crack by the yield stress (σ_0), while the distance ahead of the crack (r) was non-dimensionalised by $\frac{J}{\sigma_0}$. The amplitude of the stress triaxiality, thereby inferring the degree of crack tip constraint was measured by

normalising the mean stress (σ_m) by the Mises stress ($\bar{\sigma}$).

The crack driving force (J) was calculated from the displacement of a chosen node on the outer boundary of the model by calculating K from equation (4.1). The material response was linear elastic up to the yield stress while the subsequent response was matched with the plastic response by a Ramberg-Osgood relationship from 5% above the yield stress. Analyses were carried out for a number of strain hardening rates (n= 3, 6, 13 and infinity), ν= 0.3, α= 3/7 with E= 200GPa, ε_0= 0.001 and σ_0= 200MPa. The Ramberg-Osgood relationships for the hardening rates are illustrated in Figure 4.4. These analyses were based on small strain flow plasticity (ABAQUS, 1988a), adopting an incremental form of the Prandtl-Reuss flow rule. The large strain solutions allow the crack tip to blunt to 2δ, before they were considered to be valid, thereby negating any effect the original crack geometry may have had upon the crack tip fields.

In the case of non-zero T-stresses displacement boundary conditions were applied in a two step approach so as to ensure a constant T-Stress, by applying the full T-Stress displacement in the first step. The displacement due to the K+T field was then applied incrementally in the subsequent step. The non-zero T-stresses applied in the following analyses are compressive in nature and correspond to $\frac{T}{\sigma_0}$ = -0.3, -0.5, -0.7 and -0.9.

4.3: Results

Numerical solutions were compared with the HRR field, determined from the tabulated results of Hutchinson (1968) and Shih (1983). The hoop stresses directly ahead of the crack tip for a non-hardening material for both large and small strain analyses for a K field (T=0) are shown in Figure 4.5. The large strain solution differs from the HRR field outside the blunting region, $\frac{2J}{\sigma_0}$ by 4%, while as the small strain solution is extrapolated to the crack tip the HRR field was found to be recovered. Small and large strain solutions can be seen to match at distances in excess of $\frac{2J}{\sigma_0}$. The low comparable stress levels for the large strain solutions can be attributed to the loss of stress triaxiality which is associated with crack tip blunting. Figure 4.6 compares the stress triaxiality $\left(\frac{\sigma_m}{\sigma}\right)$ with the HRR field which differs by 7% at $\left(\frac{2J}{\sigma_0}\right)$.

The stress triaxiality was chosen as a test for the dominance of the HRR field since this parameter should be independent of radial distance, to the neglect of higher order terms. It can be clearly seen from this figure that this appears not to be the case. The existence of an HRR field can only be confirmed at the crack tip (r=0) and not at any significant finite radial distance from it.

The same comparisons are made for the hoop stress and triaxiality for a material with strain hardening exponent (n=3) as illustrated in Figures 4.7 and 4.8. Again it may be concluded that the HRR field is recovered as $r \rightarrow 0$ but significant discrepancies arise at finite distances from the crack tip.

A full range of compressive T-stresses have also been modelled. Figures 4.9-4.13 illustrate the stress fields for small and large strain solutions with a strain hardening exponent of six, directly ahead of the crack tip. The normalised hoop stresses are shown in Figures 4.9-4.10 for the full range of T-stresses while the stress triaxialities are shown in Figures 4.11-4.12. The equivalent plastic strain for the large strain analyses are shown in Figure 4.13, over the distances in which large strain effects are important. The stress fields

exhibited correspond to a range of T values. The highest stress levels are given by the T=0 field, the other T fields being, $\frac{T}{\sigma_0}$ = -0.3, -0.5, -0.7 and -0.9. Figures 4.14-4.18 consider a series of complementary analyses for a hardening rate of n=13. Presented again are the normalised hoop stresses and the amplitude of the stress triaxiality in the same order as the previous analyses for the full range of compressive T-stresses.

4.4: Discussion.

Sharma and Aravas (1991) describe stress fields in terms of higher order asymptotics in which the HRR field is recovered when interest is restricted to the first term. It is therefore possible to consider a similar functional form offered by Sharma and Aravas (1991) using the notation of O'Dowd and Shih (1991a) to define the amplitude of the second term as Q:

$$\left(\frac{\sigma_{ij}}{\sigma_0}\right)_{(T=0)} = \frac{\sigma_{ij}^{HRR}}{\sigma_0} + Q\left(\frac{r\sigma_0}{J}\right)^t \qquad r \to 0 \qquad (4.2)$$

Numerical values of the exponent t, the radial dependance of the second term are given by Sharma and Aravas (1991), while Q is the undefined amplitude of the second order term. It is possible to express the T=0 fields for a number of strain hardening rates in terms of the two term expansion as illustrated in Figures 4.19-4.22:

$$\left(\frac{\sigma_{ij}}{\sigma_0}\right)_{(T=0)} = \frac{\sigma_{ij}^{HRR}}{\sigma_0} - 0.18\left(\frac{r\sigma_0}{J}\right)^{0.05} \quad , n=\infty \qquad (4.3)$$

$$\left(\frac{\sigma_{ij}}{\sigma_0}\right)_{(T=0)} = \frac{\sigma_{ij}^{HRR}}{\sigma_0} - 1.4\left(\frac{r\sigma_0}{J}\right)^{-0.013} \quad , n=3 \qquad (4.4)$$

$$\left(\frac{\sigma_{ij}}{\sigma_0}\right)_{(T=0)} = \frac{\sigma_{ij}^{HRR}}{\sigma_0} - 0.65\left(\frac{r\sigma_0}{J}\right)^{0.065} \quad , n=6 \qquad (4.5)$$

$$\left(\frac{\sigma_{ij}}{\sigma_0}\right)_{(T=0)} = \frac{\sigma_{ij}^{HRR}}{\sigma_0} - 0.3\left(\frac{r\sigma_0}{J}\right)^{0.065} \quad , n=13 \qquad (4.6)$$

The radial dependence of the second term in the expansion (t) was taken from Sharma and Aravas (1991) while the amplitude Q was taken as an average of the stress field differences over the range graphed for each strain hardening rate.

4.5: Conclusion.

The use of unmodified boundary layer formulations (T=0) indicates that the HRR field exists only at the crack tip and not at any finite distance from it. This can be justified by considering the radial dependance of the stress triaxiality $\left(\frac{\sigma_m}{\bar{\sigma}}\right)$, which has been shown for a wide range of hardening rates. The HRR field can therefore be considered to be the first term of a series expansion, since at any finite distance from the crack tip the higher order terms of this series expansion become significant.

Large strain solutions can be matched with the small geometry change HRR field at distances of the order of two crack tip openings. Crack blunting causes a local loss of triaxiality which is recovered at this distance from the crack tip. This is not formally a rigorous comparison since the comparison is between a large strain solution and small strain solution, and appears to be more fortuitous rather than founded on any rigorous basis, especially when compared to the movement of the peak stress levels.

It appears from this series of analyses that the use of the HRR field as a generic reference field cannot be justified, especially when considering the effect of compressive T-stresses as shown in Figures 4.9-4.19. Single parameterisation of any form cannot possibly characterise these stress fields. This would argue the necessity for comparing stress fields with the small strain solution as an appropriate small scale yielding reference solution rather than with the single parameter characterisation of the HRR field used previously by Shih and

German (1981). The use of this small scale yielding field (T=0) is based on the observation that the second term is distance independent in relation to the small scale yielding.

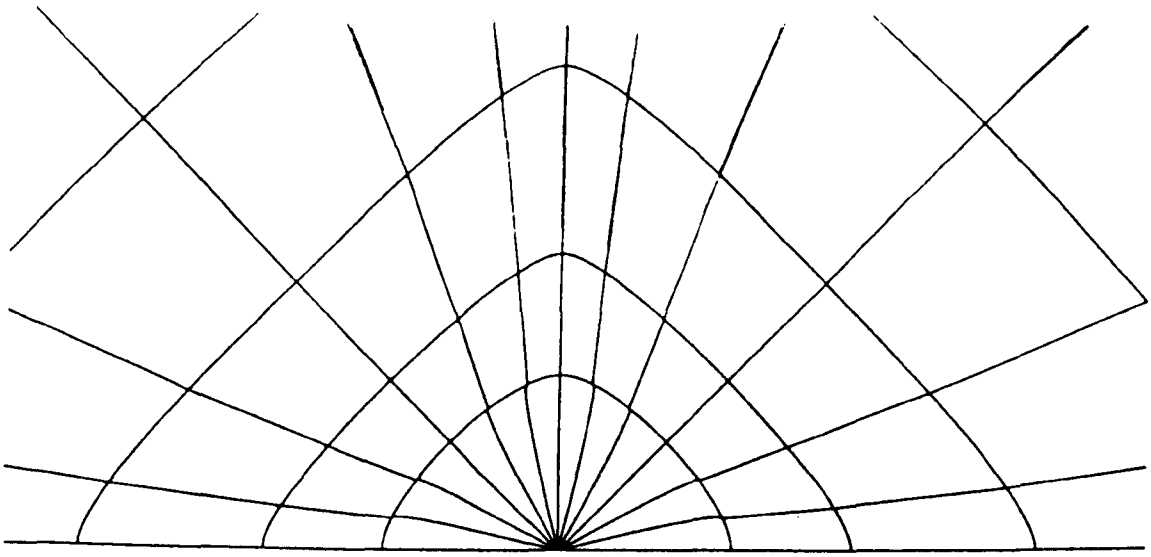

Figure 4.1: Small Strain Crack Tip Node Arrangement.

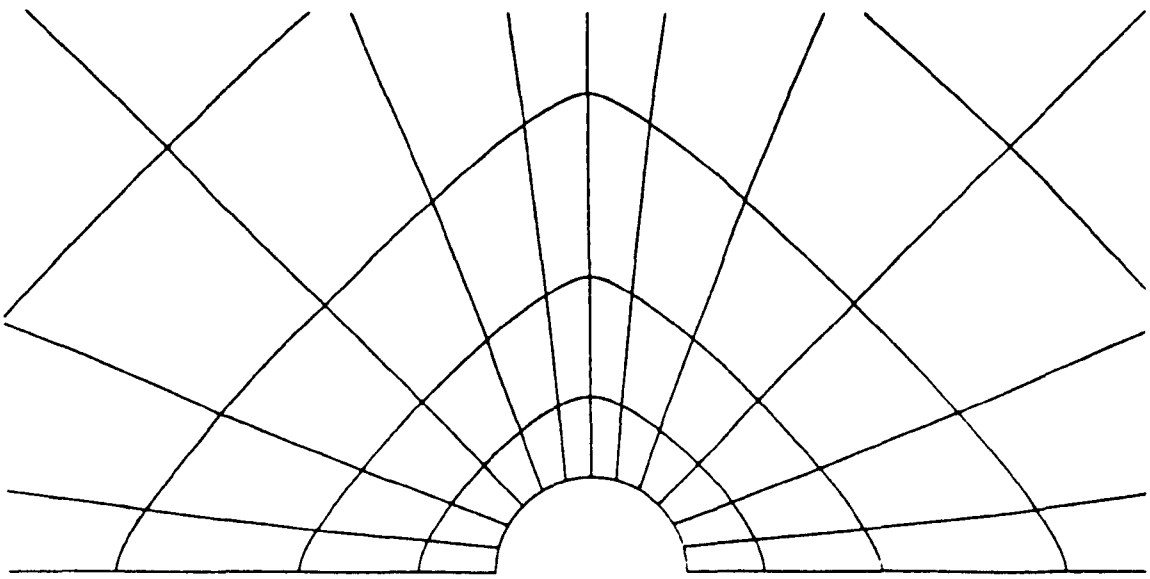

Figure 4.2: Large Strain Crack Tip Node Arrangement.

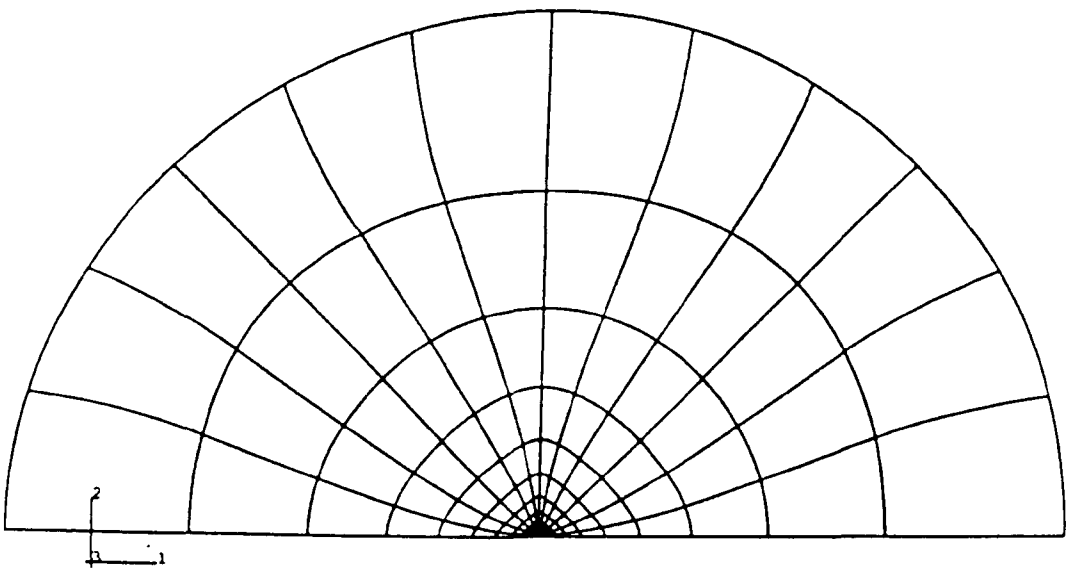

Figure 4.3: Boundary Layer Formulation Mesh.

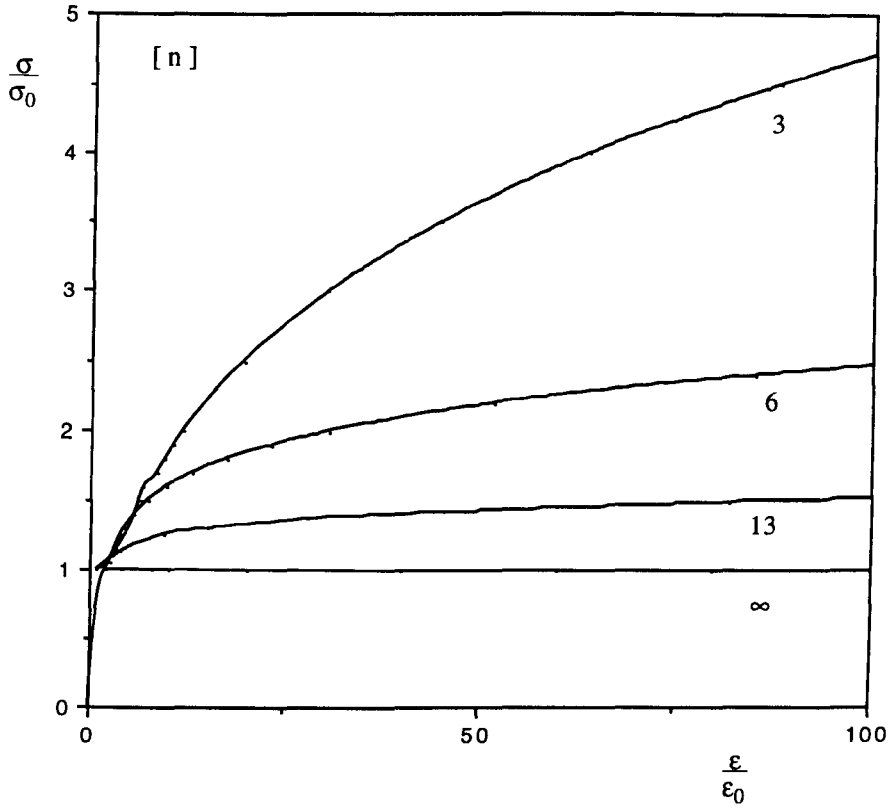

Figure 4.4: Ramberg-Osgood Stress-Strain Curves (n= 3, 6, 13 and ∞).

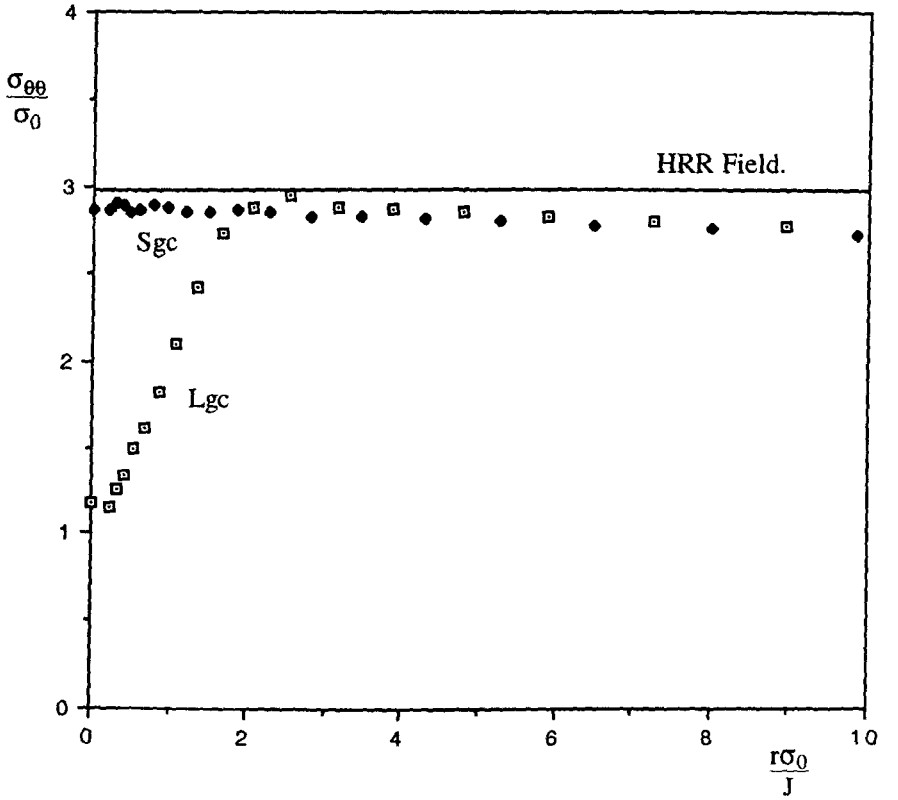

Figure 4.5: Hoop Stress Directly Ahead of the Crack Tip (n=∞, T=0).

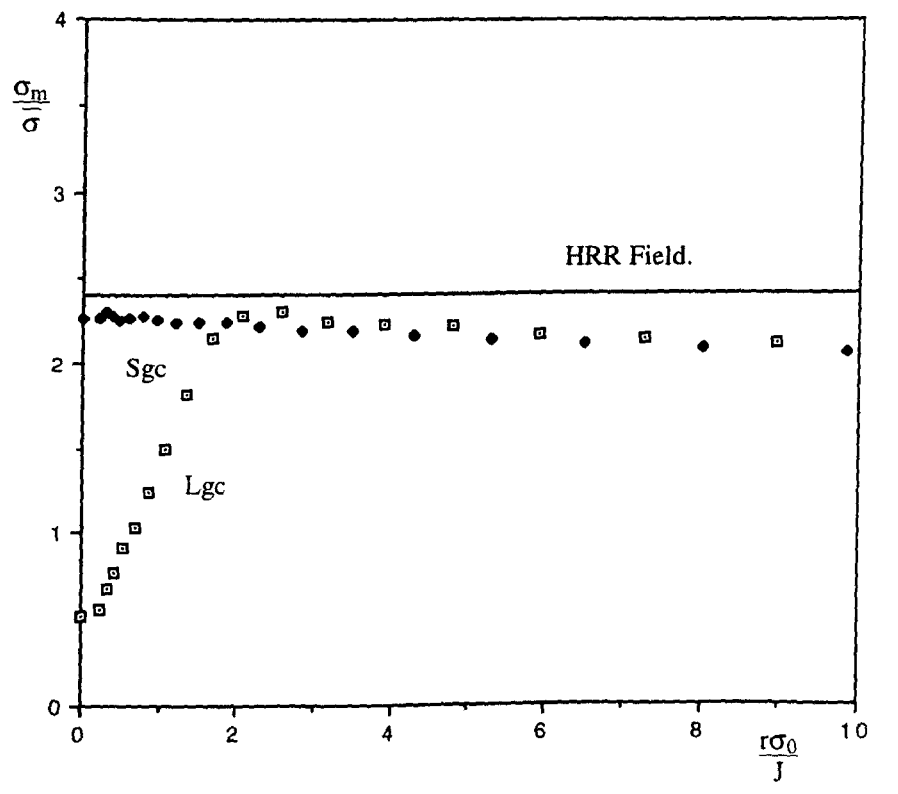

Figure 4.6: Normalised Mean Stress Directly Ahead of the Crack Tip (n=∞, T=0).

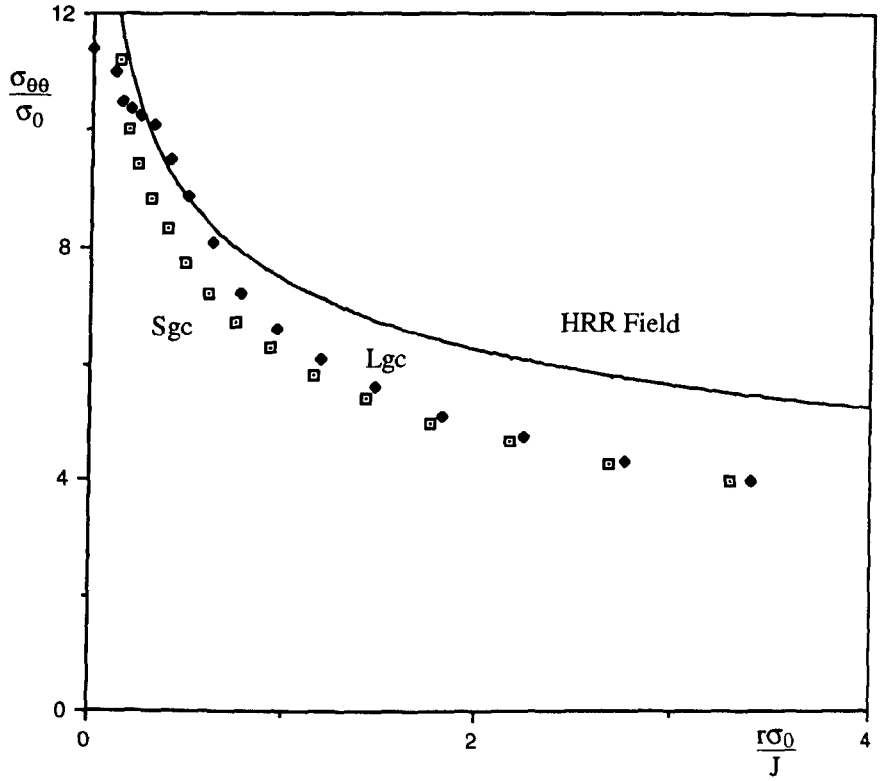

Figure 4.7: Hoop Stress Directly Ahead of the Crack Tip (n=3, T=0).

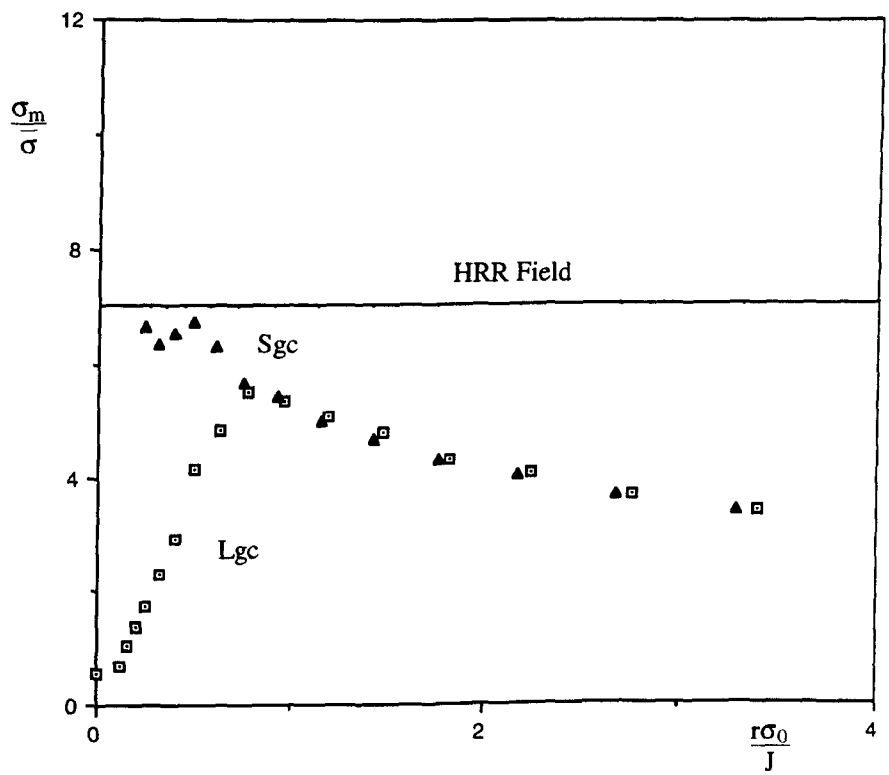

Figure 4.8: Normalised Mean Stress Directly Ahead of the Crack Tip (n=3, T=0).

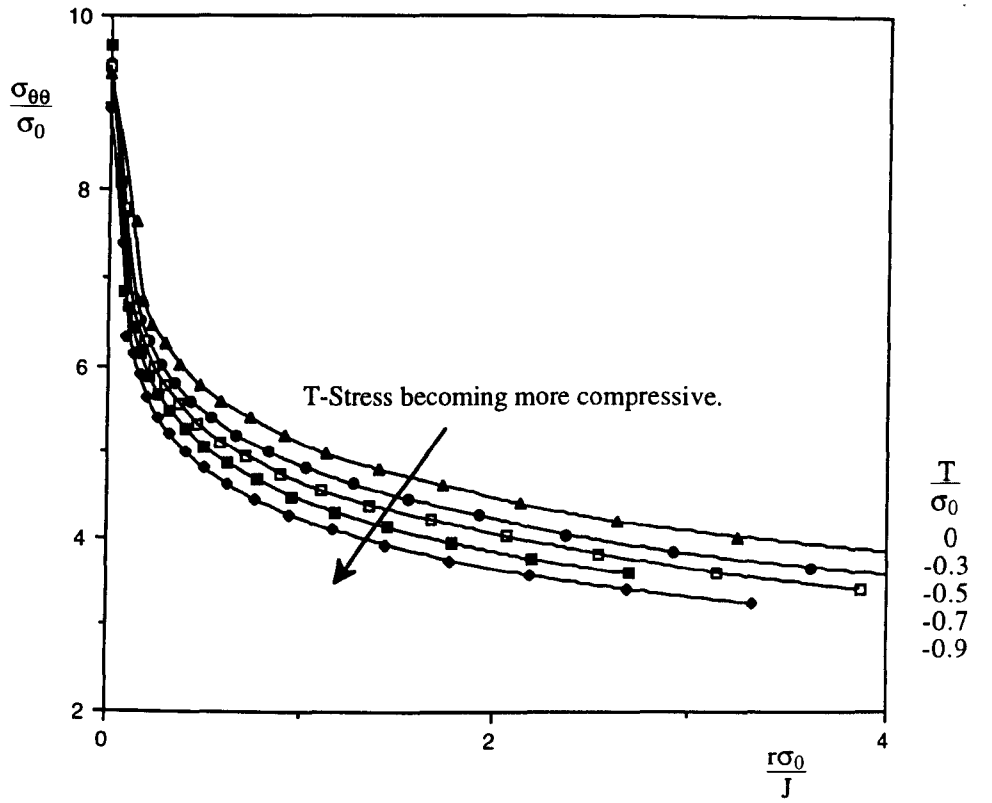

Figure 4.9: Small Strain Normalised Hoop Stresses (n=6).

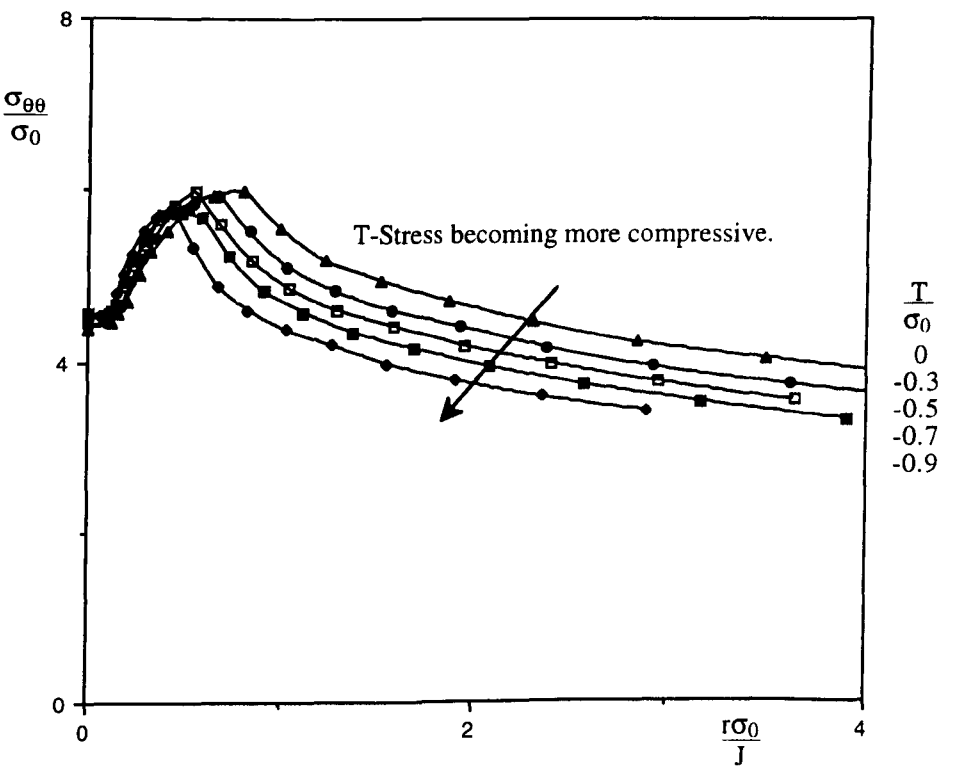

Figure 4.10: Large Strain Normalised Hoop Stresses (n=6).

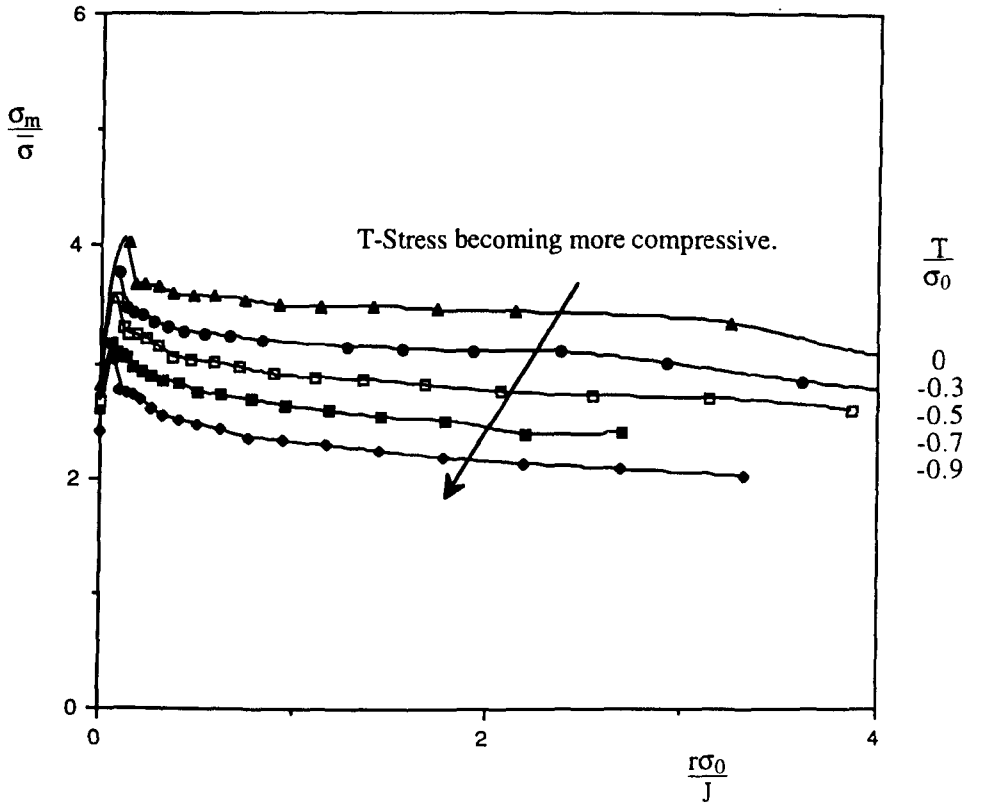

Figure 4.11: Small Strain Normalised Mean Stresses (n=6).

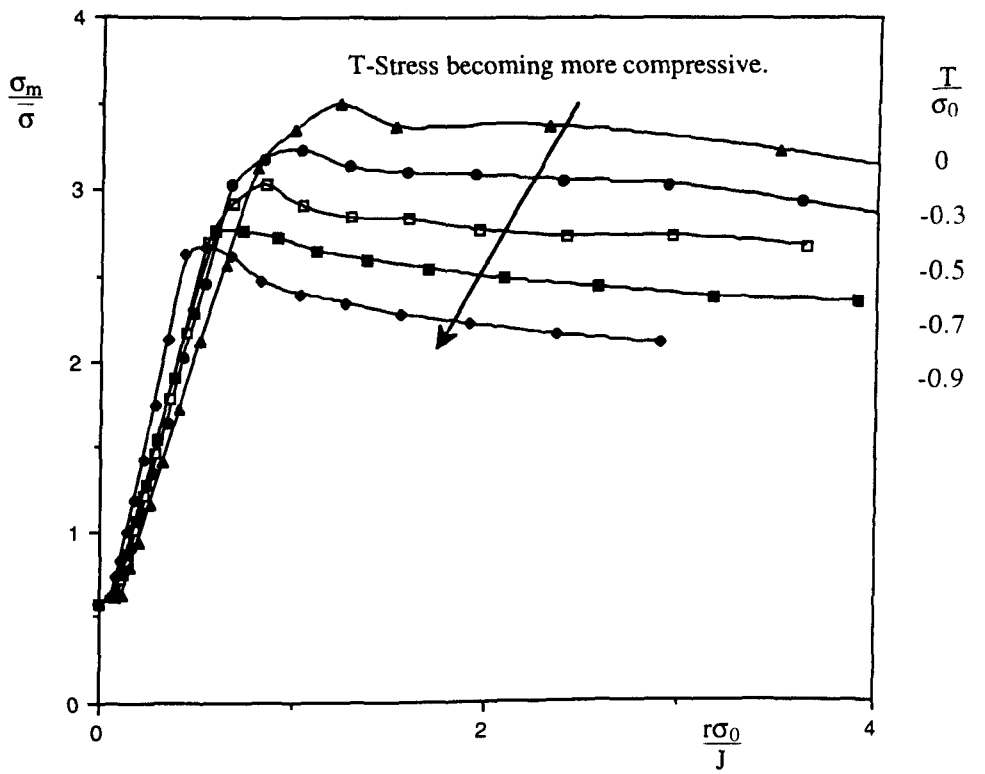

Figure 4.12: Large Strain Normalised Mean Stresses Directly Ahead of the Crack Tip (n=6).

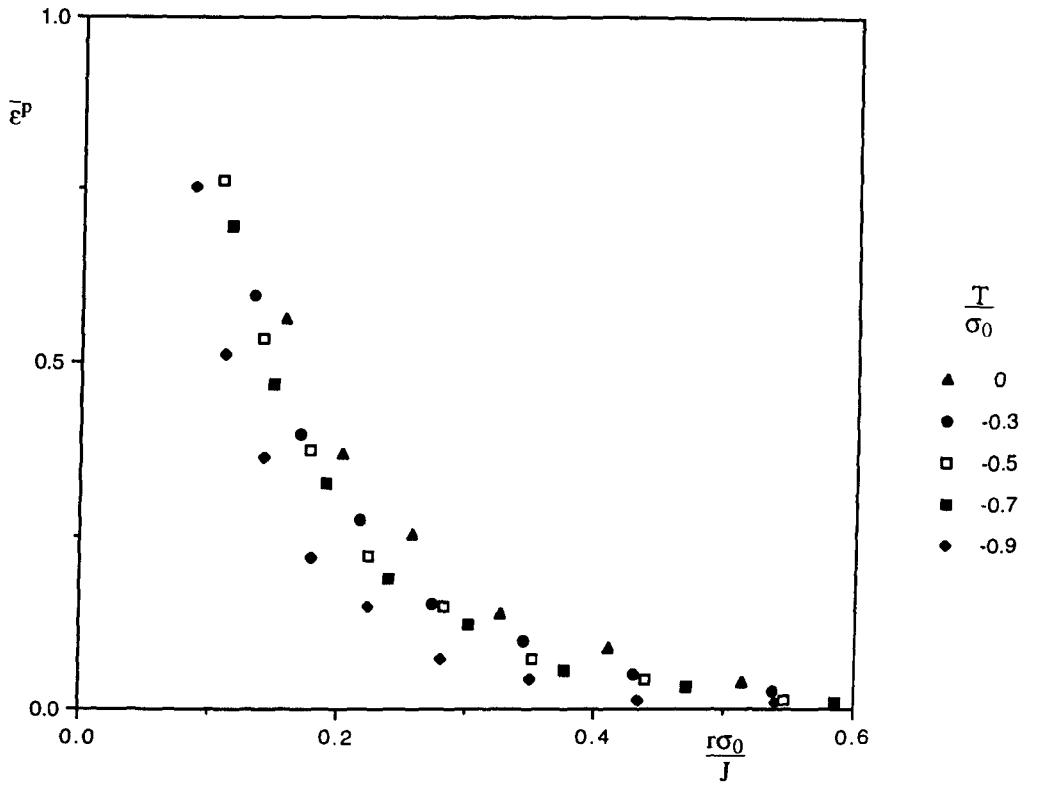

Figure 4.13: Plastic Eqivalent Strain Directly Ahead of the Crack Tip (n=6).

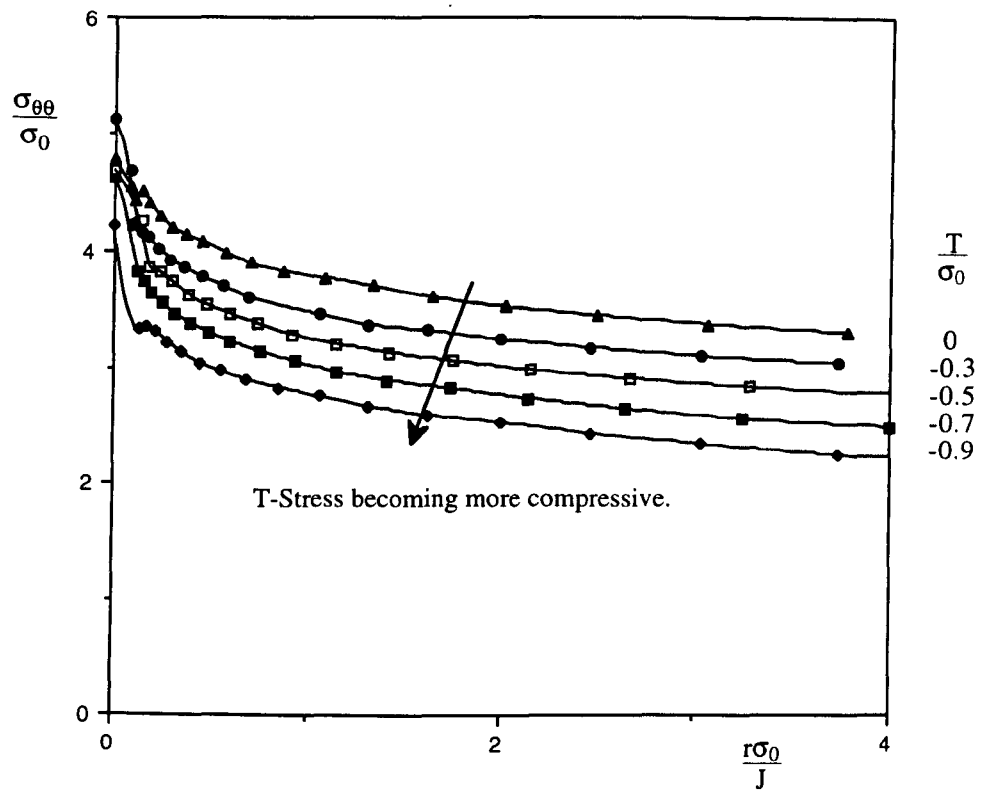

Figure 4.14: Small Strain Normalised Hoop Stress Directly Ahead of the Crack Tip (n=13).

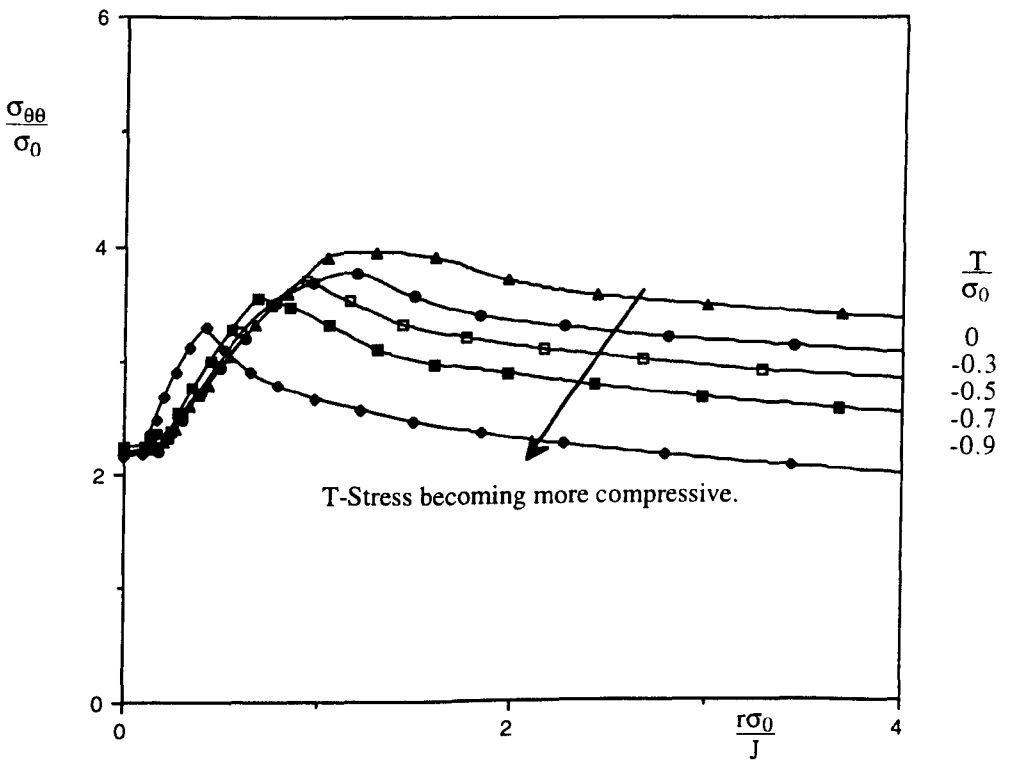

Figure 4.15: Large Strain Normalised Hoop Stress Directly Ahead of the Crack Tip (n=13).

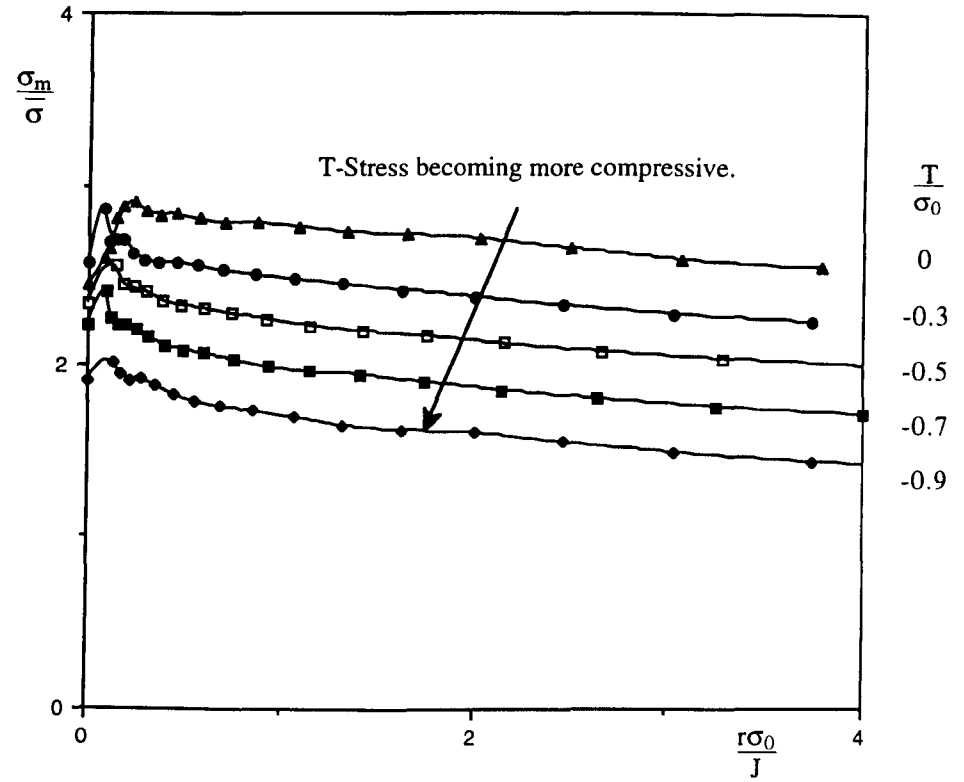

Figure 4.16: Small Strain Normalised Mean Stress Directly Ahead of the Crack Tip (n=13).

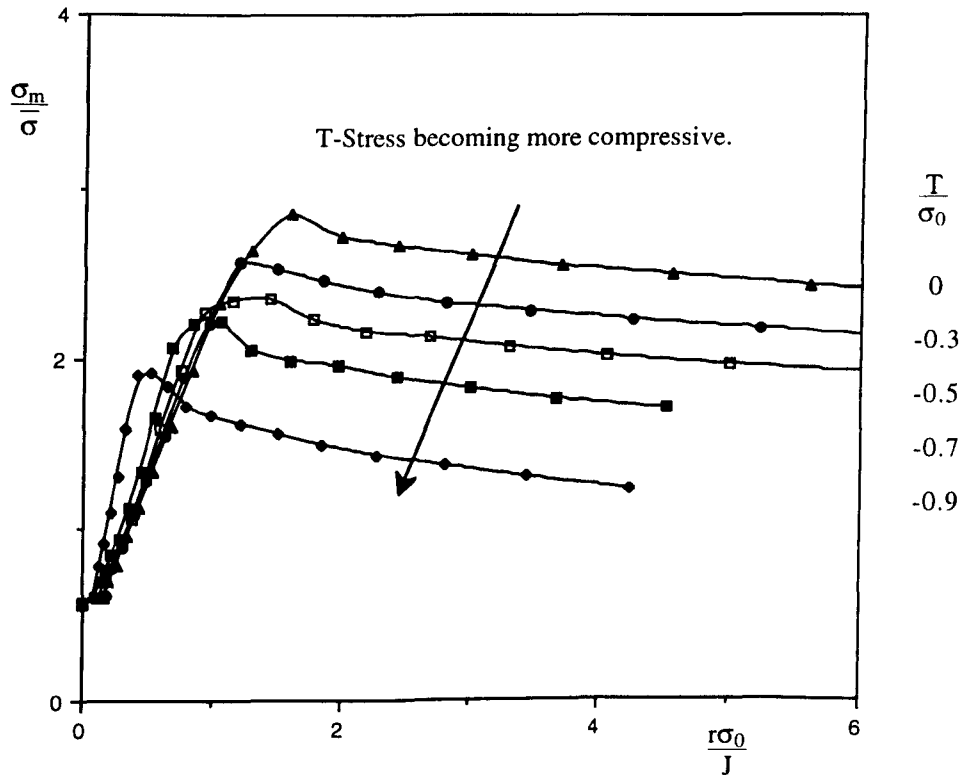

Figure 4.17: Large Strain Normalised Mean Stress Directly Ahead of the Crack Tip (n=13).

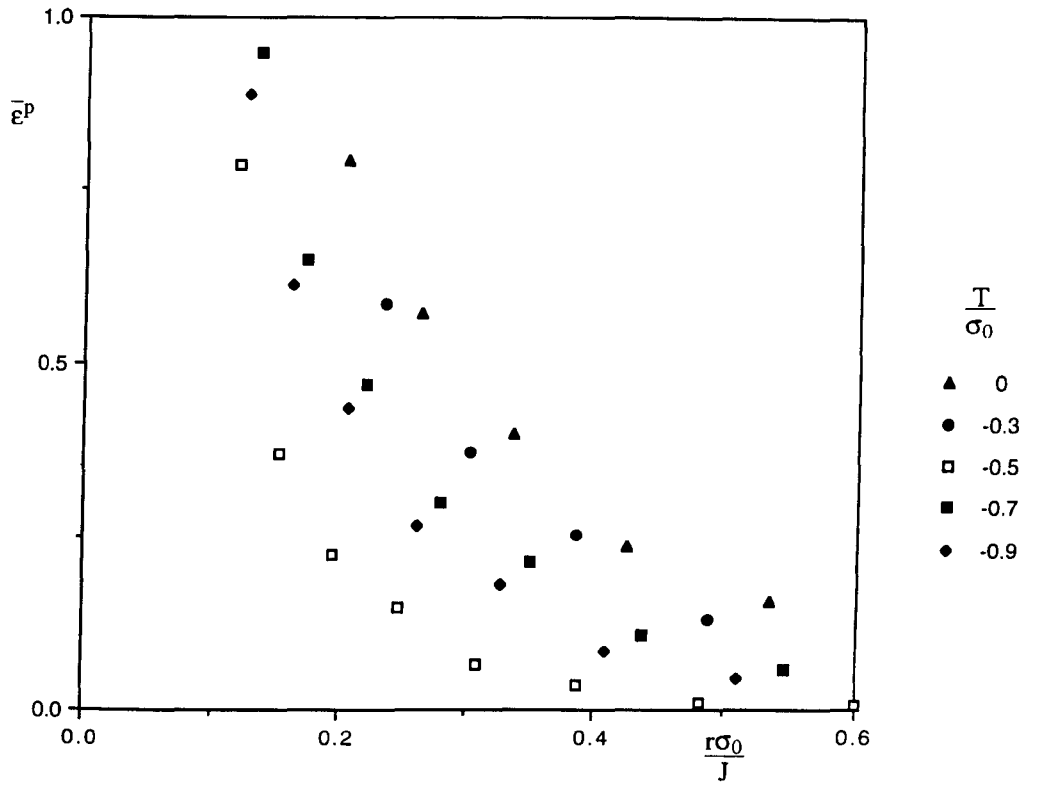

Figure 4.18: Plastic Eqivalent Strain Directly Ahead of the Crack Tip (n=13).

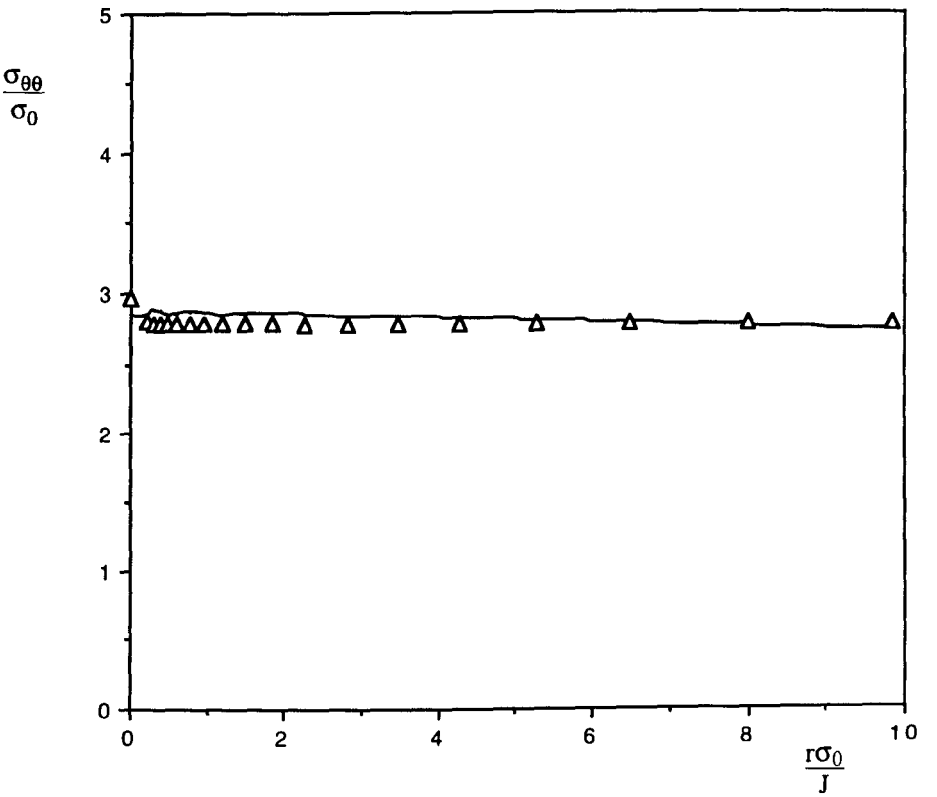

Figure 4.19: Curve fit for Boundary Layer Formulation of n=∞, T=0.

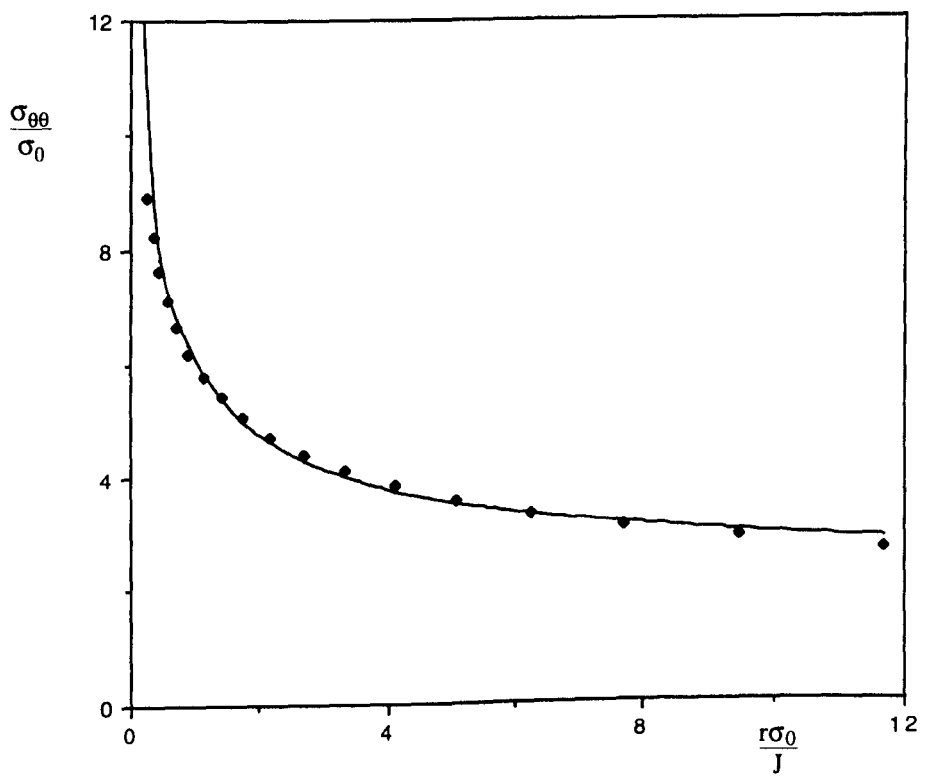

Figure 4.20: Curve fit for Boundary Layer Formulation of n=3, T=0.

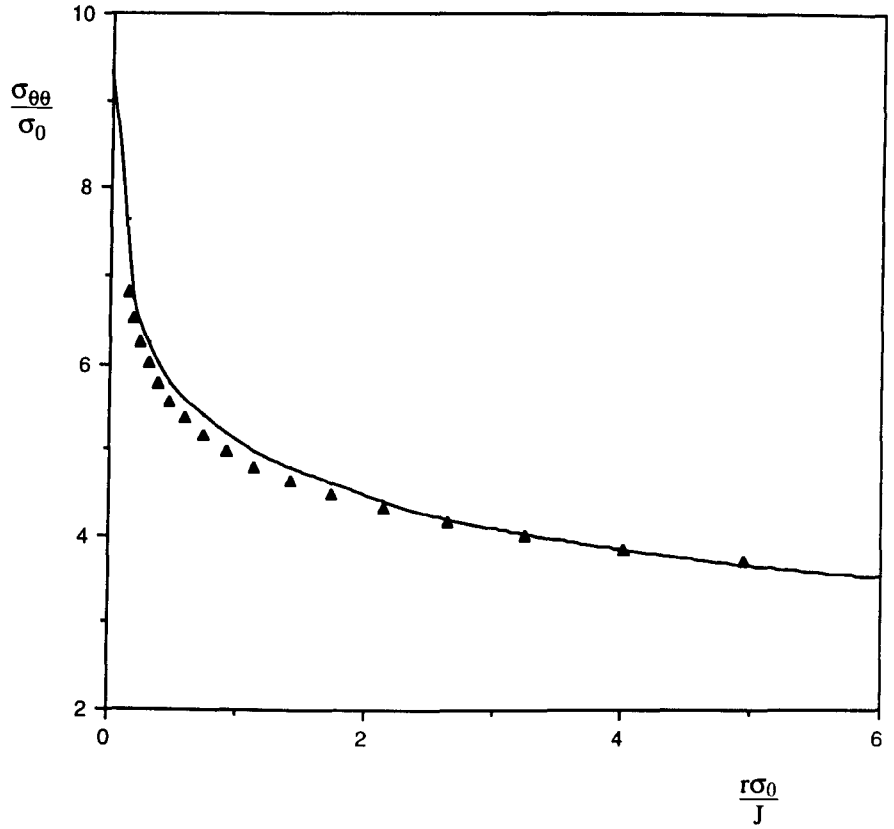

Figure 4.21 : Curve Fit for Boundary Layer Formulation of n=6, T=0.

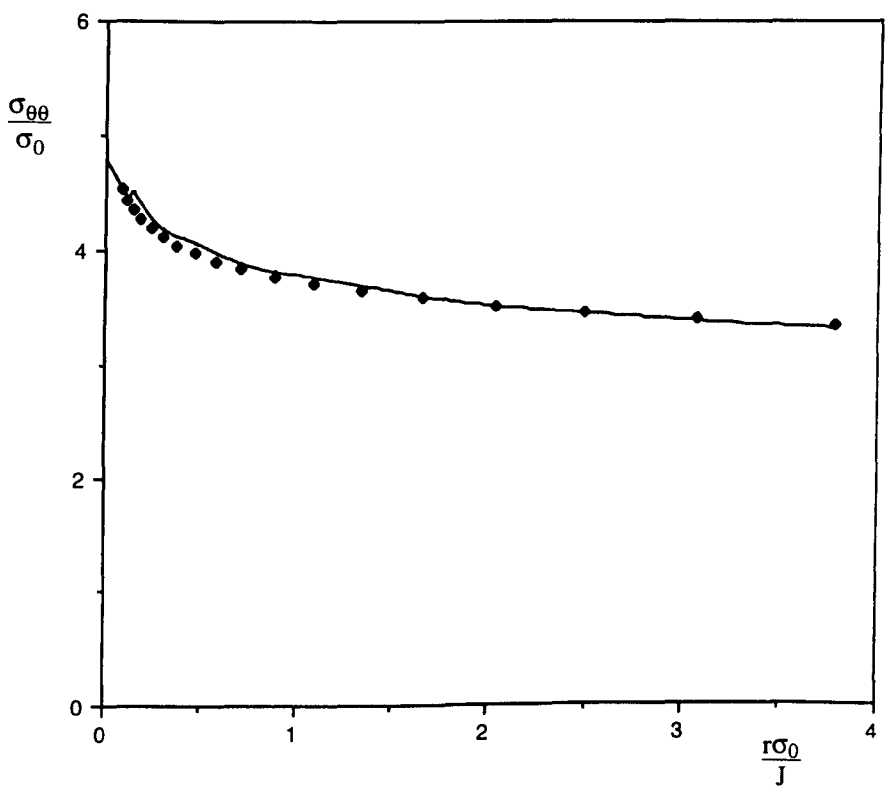

Figure 4.22: Curve fit for Boundary Layer Formulation of n=13, T=0.

5: Generalised Plane Strain.

5.1: Introduction.

The purpose of this series of analyses was to determine the effect of out of plane strain on elastic-plastic crack tip fields. This was accomplished by comparing results of full field solutions of geometries with positive (tensile) and negative (compressive) T-stresses, and compressive and tensile out of plane strains.

For comparison with these analyses two forms of reference field were utilised. In the case of the positive T, comparisons were made with the plane strain small scale yielding (T=0) boundary layer formulation. The reference fields for the negative T analyses were determined from modified boundary layer formulations.

The T-stress is a non-singular uniaxial in-plane stress, parallel to the crack flanks. A non-singular out of plane term (S) can be introduced following Rice (1974). In elastic plane strain conditions the three dimensional asymptotic stress fields can be expressed in the form:

$$[\sigma_{ij}] = \frac{K_I}{\sqrt{2\pi r}}[f_{ij}(\theta)] + \begin{bmatrix} T & 0 & 0 \\ 0 & 0 & 0 \\ 0 & 0 & S \end{bmatrix} \qquad (5.1)$$

The elastic stress-strain relation is:

$$\varepsilon_{zz} = \frac{1}{E}[\sigma_{zz} - \upsilon(\sigma_{xx} - \sigma_{yy})] \qquad (5.2)$$

Using the plane strain conditions (ε_{zz}=0) gives:

$$f_{zz}(\theta) = \upsilon(f_{xx}(\theta) + f_{yy}(\theta)) \qquad (5.3)$$

Also all the shear functions are zero, this allows the stress field to be expressed as:

$$[\sigma_{ij}] = \frac{K_I}{\sqrt{2\pi r}}[f_{ij}(\theta)] + \begin{bmatrix} T \\ 0 \\ S \end{bmatrix} \qquad (5.4)$$

Thus on the crack flanks $\sigma_{yy} = 0$, $\sigma_{xx} = T$ and $\sigma_{zz} = S$, where the out of plane non-zero singular term in the Williams (1957) expansion has been denoted S. In plane strain conditions the relation between S and T is established by the stress-strain relation:

$$\varepsilon_{zz} = \frac{1}{E}[S - \upsilon T] = 0$$

$$S = \upsilon T \qquad (5.5)$$

Hence in plane strain the non-zero stress field components can be expressed:

$$\sigma_{xx}(r, \theta) = \frac{K_I}{\sqrt{2\pi r}} f_{xx}(\theta) + T$$

$$\sigma_{yy}(r, \theta) = \frac{K_I}{\sqrt{2\pi r}} f_{yy}(\theta) \qquad (5.6)$$

$$\sigma_{zz}(r, \theta) = \frac{K_I}{\sqrt{2\pi r}} f_{zz}(\theta) + \upsilon T$$

In the present work generalised plane strain deformation has been imposed so that S is no longer simply equal to the plane strain value υT. Generalised plane strain analysis describes the deformation of bodies that have a constant curvature with respect to one axial material direction. The body may be visualised as lying between two planes which are orthogonal to the axial direction. These planes are allowed to move as rigid bodies with respect to each other and therefore cause an axial strain in the material direction. In these analyses the *bounding planes* were parallel to each other and prevented from rotation. The

elements used for these analyses had eight conventional nodes that determine the position and motion of the element in the two *bounding planes* as illustrated in Figure 5.1. The two additional out of plane nodes govern both the relative rotation of the planes and the change in axial length of the axial material fibre that connects these two nodes, these nodes are common to all the elements in the mesh.

5.2: Numerical Method.

Two series of elastic-plastic analyses were carried out on shallow and a deeply edge cracked bend bars (SECB). The shallow cracked bars had an $\frac{a}{W}$ ratio of 0.1, while the deeply cracked bar $\frac{a}{W}$=0.9. These particular ratios were chosen to generate a fully constrained fields in the case of the deeply cracked geometry, and unconstrained fields for the shallow cracked geometry. Both geometries had a height to width ratio of 3.

The meshes for these series of analyses were constructed using the commercial mesh generation program PATRAN (1990). These meshes contained 170 second order generalised plane strain elements, which are 10 noded quadrilateral elements with biquadratic displacement, linear pressure and reduced integration. Due to the symmetry of these analyses it was only necessary to model half of the body and it was necessary only to generate one mesh for both series of analyses. Both crack lengths could be defined by the application of appropriate boundary conditions to the same mesh as illustrated in Figure 5.2.

The models were subjected to a uniformly distributed load applied along the top node set. The elastic material constants, Youngs modulus and Poisson's ratio were set at 200 GPa and 0.3 respectively. Boundary conditions were such that the base of both meshes was fixed in the two direction with a single node also being fixed in the one direction to prevent rigid body motion. The two additional out of plane nodes have only limited degrees of freedom and their own coordinate system which prevents them from rotating. To generate the out of plane loading a displacement was applied to the second node to give an out of plane strain. Displaced meshes for both geometries are shown in Figures 5.3 and 5.4.

5.3: Results.

5.3.1: Positive T-Stress Analyses.

The positive T-stress analyses are compared with a reference field which is the small scale yielding solution (T=0). Figure 5.5 shows the normalised hoop stress $\left(\frac{\sigma_{\theta\theta}}{\sigma_0}\right)$ ahead of the crack as a function of normalised distance, $\left(\frac{r\sigma_0}{J}\right)$. In this series of analyses the body exhibiting a compressive out of plane strain appears to be the most sensitive of all the analyses in relation to the breakdown from the small scale yielding solution as shown in Figure 5.5. Breakdown from the chosen reference field is characterised by a deviation of ±10% from the specified reference field. The compressive out of plane strain appears to breakdown in relation to the reference field at a compressive strain of $-5\varepsilon_0$ and a corresponding deformation level $\left(\frac{c\sigma_0}{J}\right)$ of 18.5., where c is the remaining ligament.

In contrast the tensile plane strain analysis appears to be relatively insensitive to out of plane effects and does not exhibit a similar breakdown until the out of plane strain is of the order of $27\varepsilon_0$ as shown in Figure 5.6 for a deformation level $\left(\frac{c\sigma_0}{J}\right)$ of 11.6. When the same deeply cracked geometry subject to in plane loading effects only is considered at comparable levels of plasticity it has also deviated significantly from the small scale yielding solution due to the effect of the in plane bending stresses as shown in Figure 5.7.

5.3.2: Negative T-Stress Analyses.

In the short crack geometry the results are compared with modified boundary layer formulations. Compressive out of plane strains did not show any deviation from the chosen reference fields. The body exhibits behaviour consistent with that of modified boundary layer formulations to high values of deformation $\left(\frac{a\sigma_0}{J}\right)$ of 11.3 with a normalised out of plane strain $\left(\frac{\varepsilon_{33}}{\varepsilon_0}\right)$ of -4.81 as illustrated in Figure 5.8.

The tensile out of plane analysis exhibits the same form of behaviour, not deviating from the modified boundary layer formulation as shown in Figure 5.9 up to deformation levels $\left(\frac{a\sigma_0}{J}\right)$ of 8.7 when the normalised $\left(\frac{\varepsilon_{33}}{\varepsilon_0}\right)$ out of plane strain was 23.3. This same behaviour was found also to hold for the body loaded solely with in plane effects as shown in Figure 5.10.

5.4: Neutral Axis.

These series of analyses are not solely concerned with out of plane effects, but have also considered the in plane effect of the global bending field. The neutral axis is defined in this section as the point on the ligament (c) where the stress field directly ahead of the crack tip switches from a tensile to a compressive field.

Initially two geometries have been considered, a deeply cracked bar subjected to a tensile out of plane component. Two forms of analysis are carried out, one analysis considers the effect of a uniformly distributed applied tensile force and the other an applied bending moment. The effect of these two significantly different fields were then considered in relation to the development of the global bending field on the ligament.

The distance of the neutral axis from the crack tip is termed r_n and the ingress of the compression field which one naturally expects is tracked by the use of a second distance parameter (r) which relates directly to the crack tip blunting, where r is:

$$r = \frac{2J}{\sigma_0} \qquad (5.7)$$

It is therefore possible to illustrate the ingress of the compression field across the remaining ligament as a ratio of the two distance terms, $\left(\frac{r}{r_n}\right)$. The results of these analyses for tension and pure bending are illustrated in Figures 5.11 and 5.12 where the deformation levels are also shown. From these figures it is clear that the ingress of the compression field is more

pronounced in the bending field, than in the remotely applied tension.

Considering both series of analyses jointly in Figure 5.13, in both cases the fields exhibit the same trends. The loss of J-dominance in these analyses can be directly related to the ingress of the compression field towards the crack tip rather than out of plane effects.

5.5: Conclusion.

In near plastic strain conditions elastic plastic crack tip fields are dominated by in plane effects and not as may have first been supposed the out of plane strain. In general the loss of J-dominance due to the in plane effects was caused by the ingress of the remote compression field due to bending.

In bodies which exhibit positive T-stresses crack tip deformation is limited by the ingress of the compression field induced by the applied bending moment. In this case the in-plane effect has the greatest effect

Bodies which exhibit negative T-stresses again appear to be dominated by the in-plane effects, although the influence of the compression field was reduced due to the size of the ligament in a short crack problem.

The influence of out of plane effects in these series of analyses appears to be minimal since the most dominant effect has been the ingress of the in plane bending field.

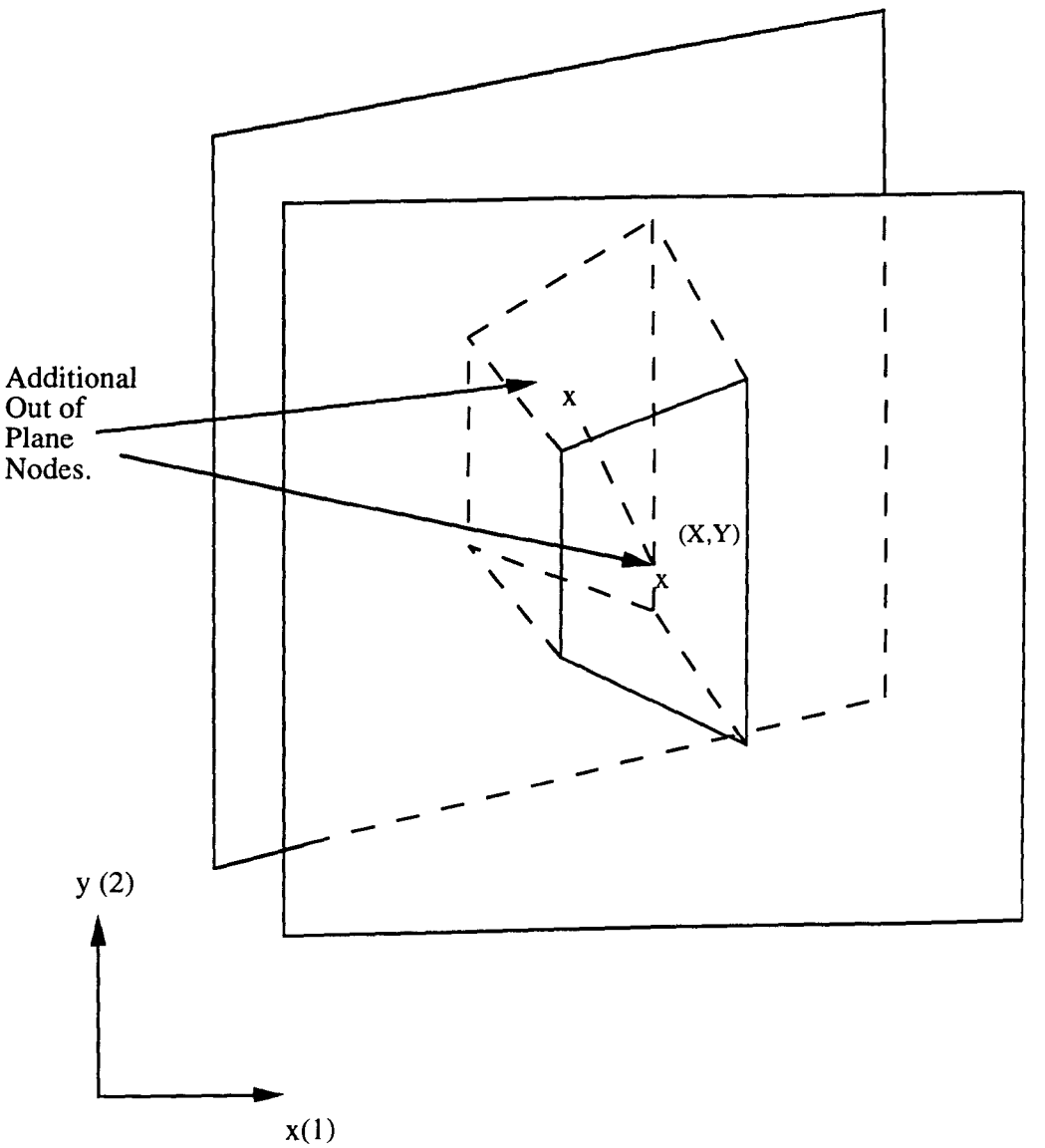

Figure 5.1: Bounded Planes Diagram.

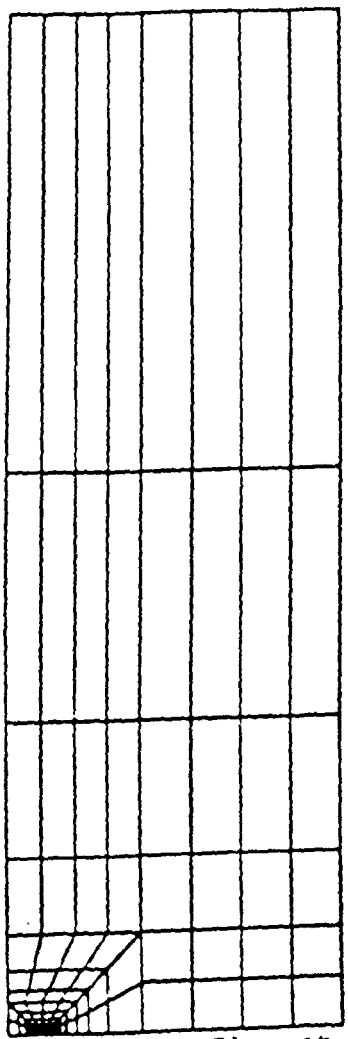

Figure 5.2: Finite Element Mesh.

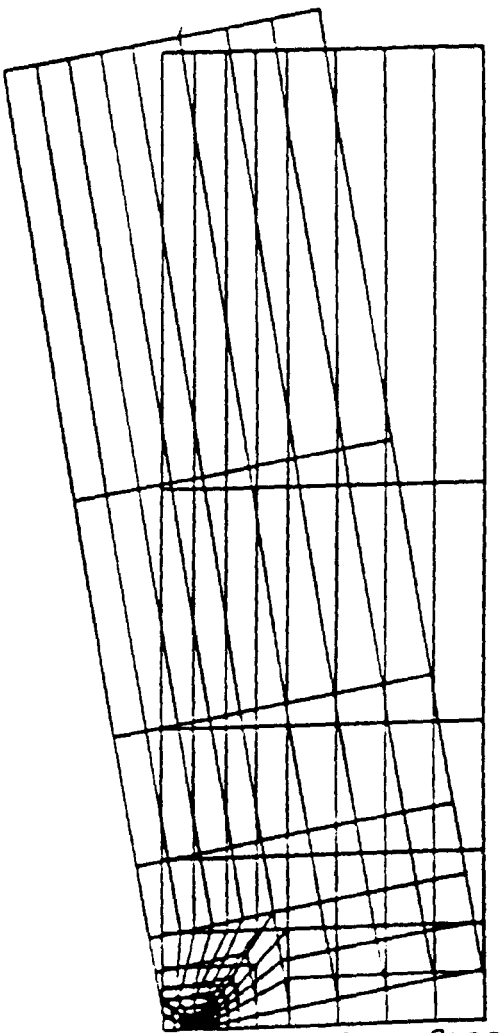

Figure 5.3: Displaced Mesh for Deep Crack Analysis.

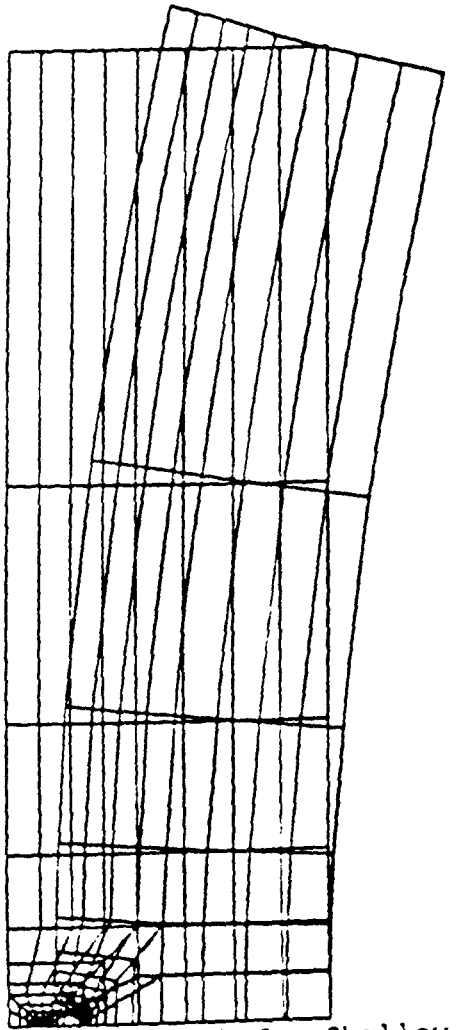

Figure 5.4: Displaced Mesh for Shallow Crack Analysis.

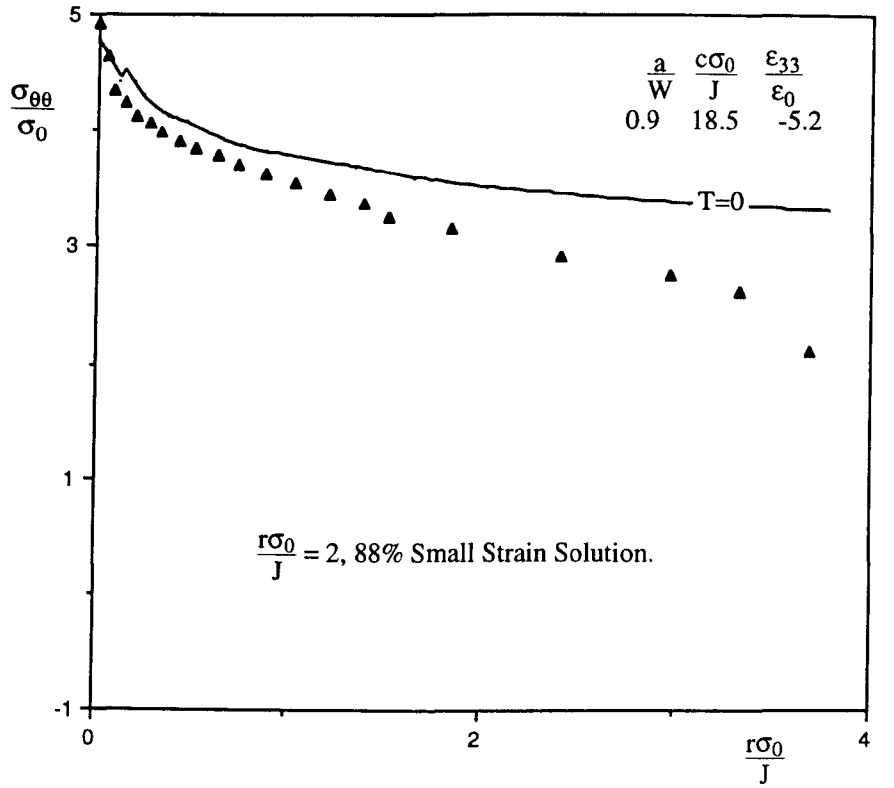

Figure 5.5 : Generalised Plane Strain Analysis of a body exhibiting +T and -S stresses.

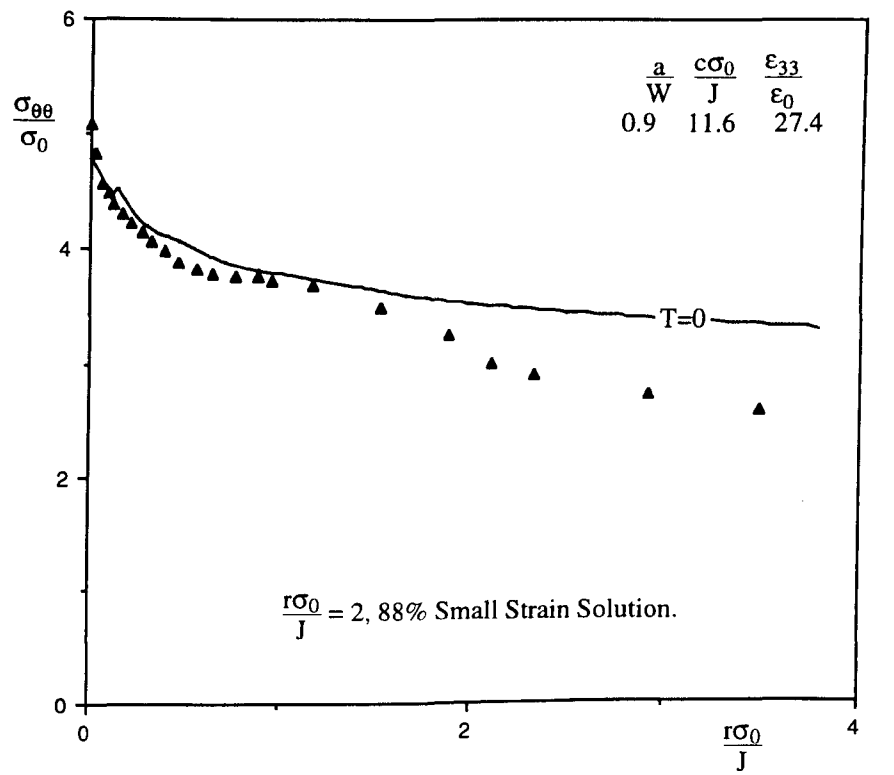

Figure 5.6 : Generalised Plane Strain Analysis of a body exhibiting +T and +S stresses.

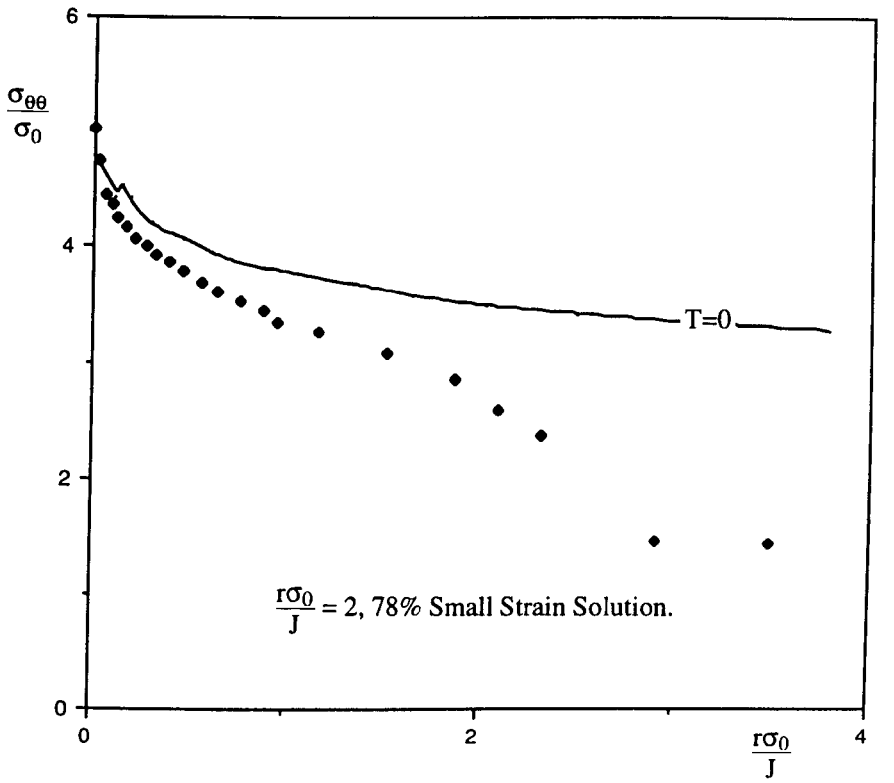

Figure 5.7: Plane Strain Analysis of a body exhibiting +T stress

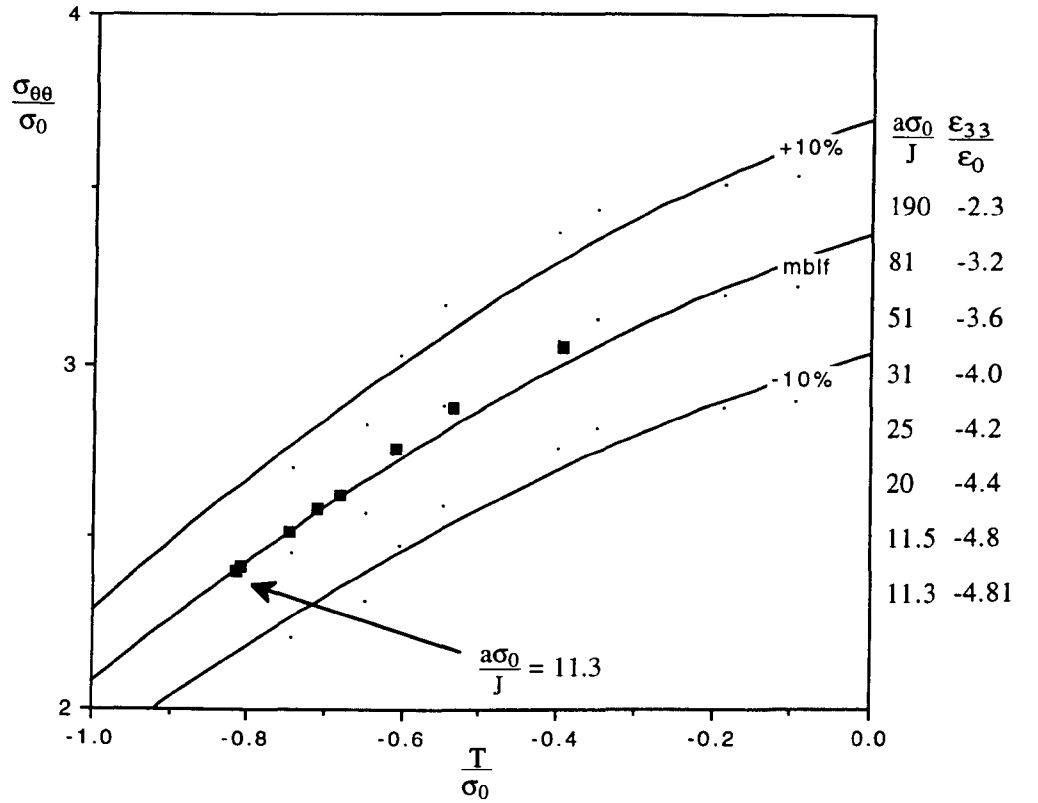

Figure 5.8 : Generalised Plane Strain Analysis of a body exhibiting -T and -S stresses.

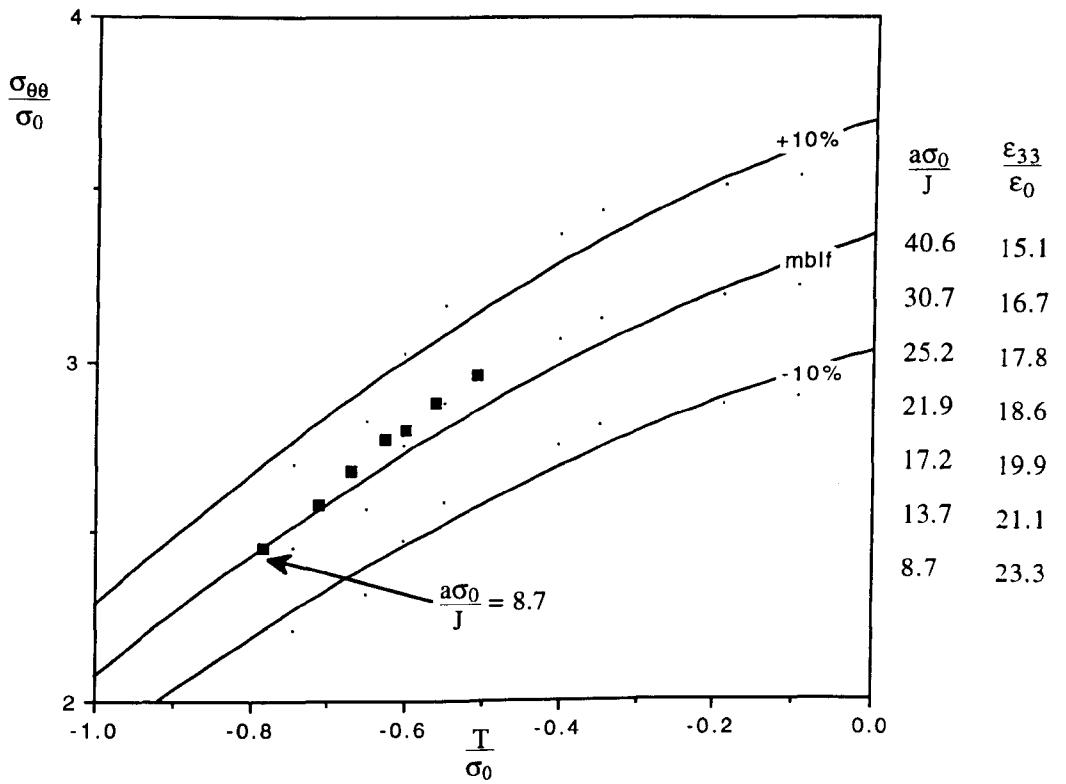

Figure 5.9: Generalised Plane Strain Analysis of a body exhibiting -T and +S stresses.

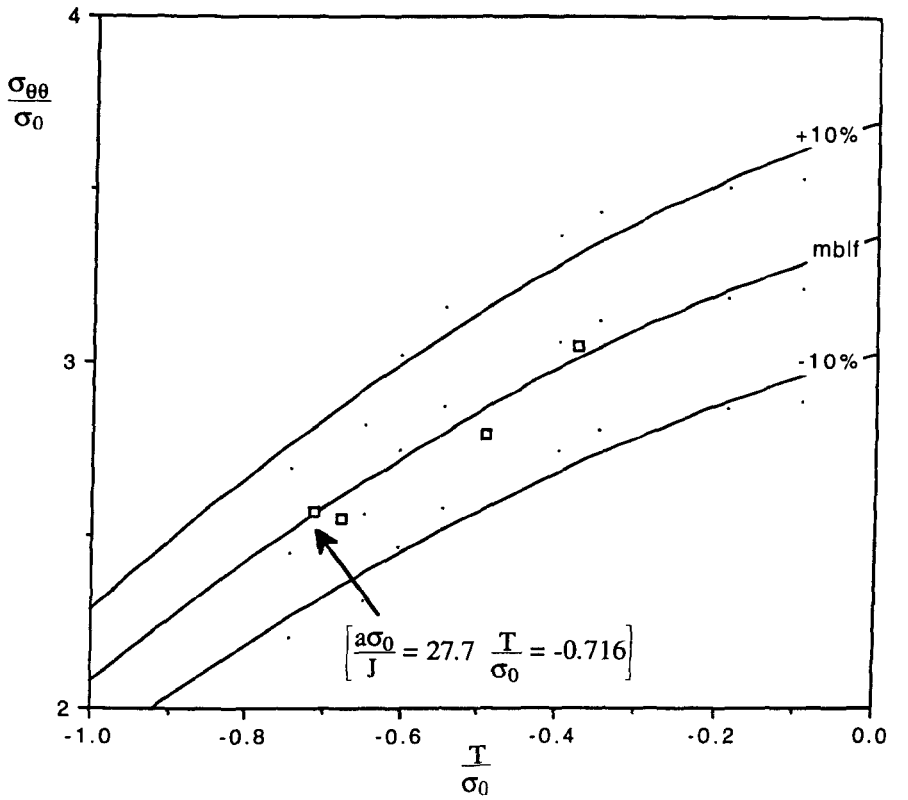

Figure 5.10: Plane Strain Analysis of a body exhibiting -T stress.

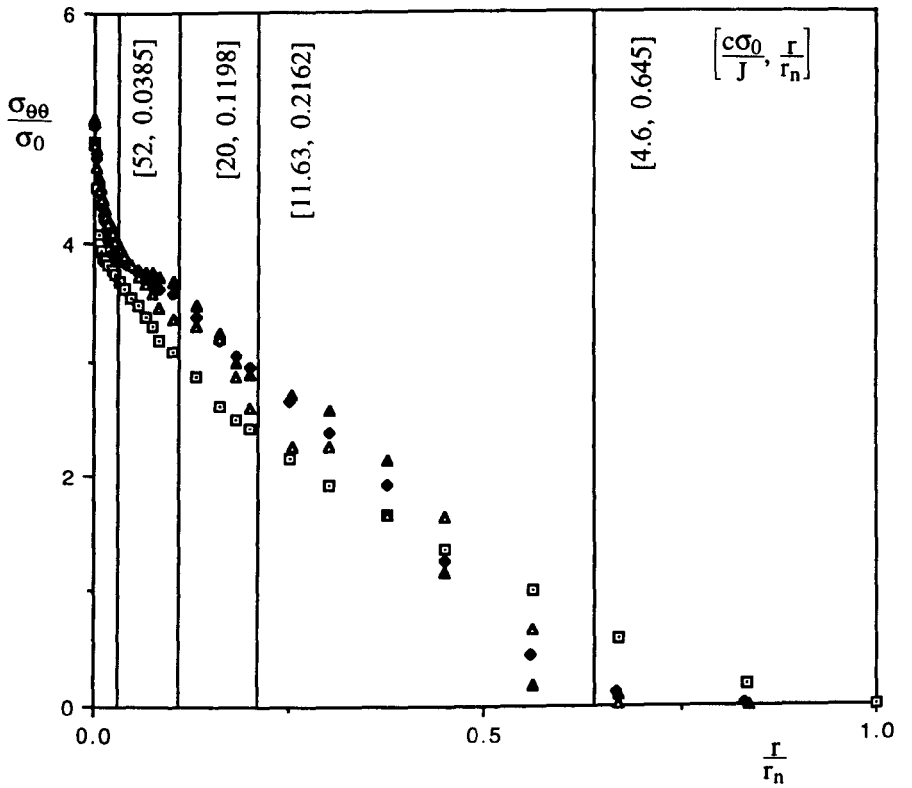

Figure 5.11: Neutral Axis graph for Tension Loading

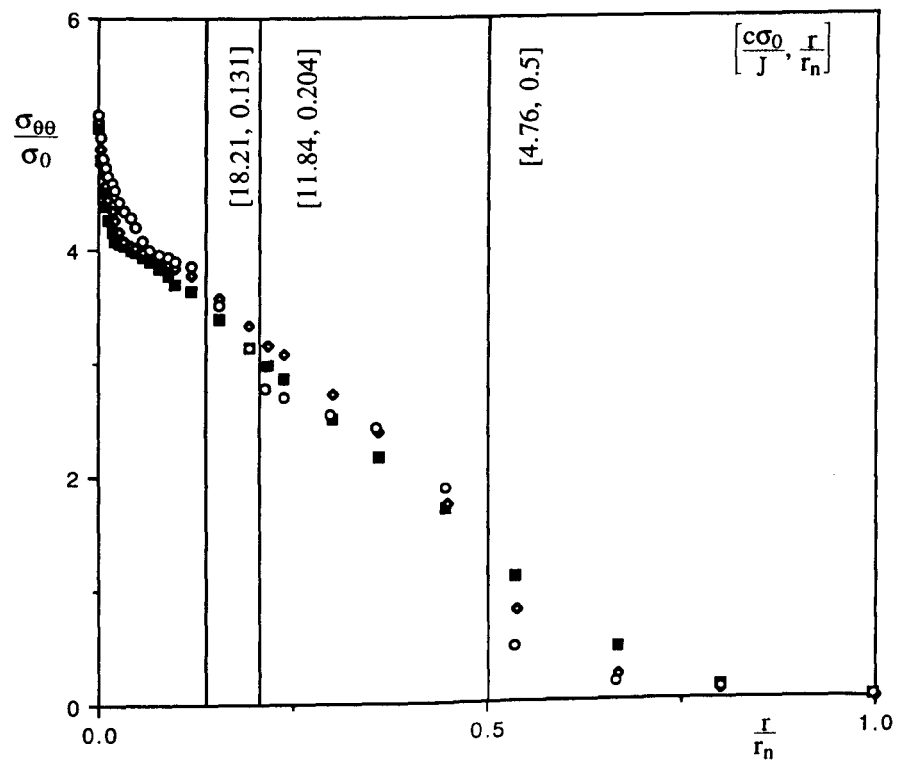

Figure 5.12 : Neutral Axis Graph for Pure Bending.

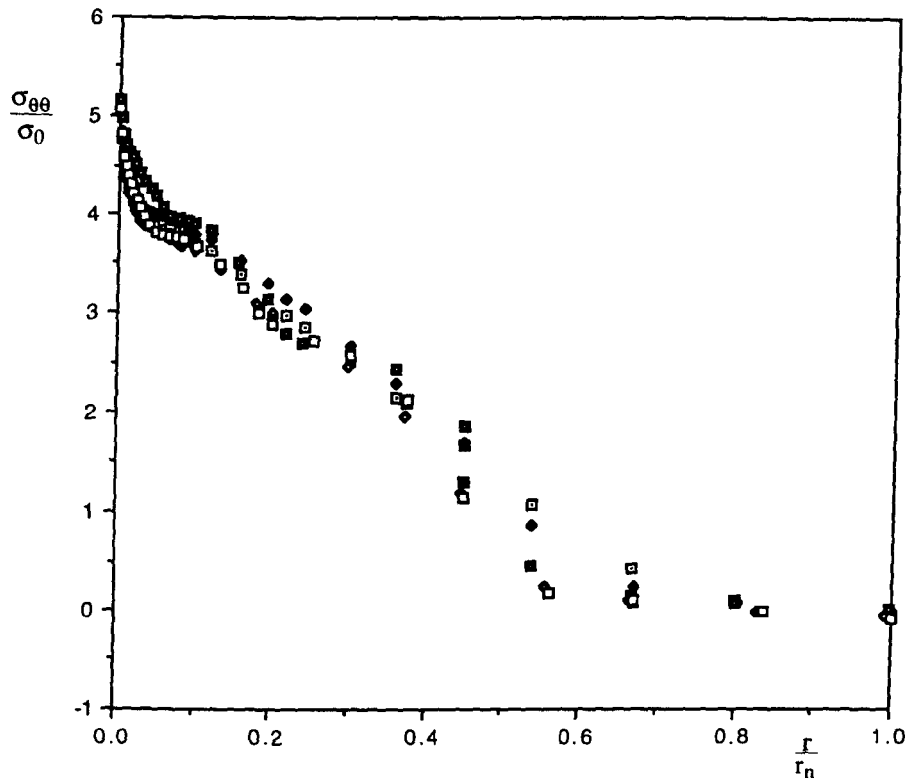

Figure 5.13 : Comparison of Tension and Bending fields.

6: Line-spring Analysis of Semi-elliptical cracks in a Tubular T-Joint.

6.1: Introduction.

The line-spring concept was introduced by Rice and Levy (1972) to determine the stress intensity factors for shells and plates containing part through thickness cracks. This particular form of defect is of interest in the design of reactor pressure vessels, pipelines and other thin walled structures. In the Rice and Levy (1972) model, as illustrated in Figure 6.1, the crack is idealised by the use of generalised line-spring elements which act across the discontinuity in a thin shell. The definition of a thin shell is such that the surface length of the crack is large in comparison to the thickness of the shell. Line-spring elements as defined in ABAQUS (1988) are computationally inexpensive tools, Rice (1972) and Parks and Wang (1988). A defect idealised by line-spring elements is a series of one dimensional finite elements placed along the part through flaw, this allows local flexibility at one side of the defect in respect to the other. At each point along the defect a local orthogonal axis system is defined (t, n, q) as shown in Figure 6.2, where A and B are points on opposing crack flanks. Here t is the tangent to the shell along the flaw, n is the normal to shell and q is given by the vector product:

$$q = t * n \qquad (6.1)$$

Rice and Levy (1972) proposed that a three dimensional body could be idealised as a two dimensional continuum which is subjected to both an axial force (F) and a moment per unit length (M). These conditions induce rotations and displacements of the mid-surface of the shells relative to each other. With the body idealised as a two dimensional continuum the crack can be regarded as a one dimensional discontinuity, as illustrated schematically in Figure 6.3. The force and bending moment carried by each section of the uncracked

ligament can be denoted F(x) and M(x) respectively, while the relative rotations and normal displacements of the plates are denoted $\delta(x)$ and $\theta(x)$ respectively. In linear elasticity the response of the crack to the loading is expressed as:

$$\begin{bmatrix} \delta(x) \\ \theta(x) \end{bmatrix} = \begin{bmatrix} C_{11}(x) & C_{12}(x) \\ C_{21}(x) & C_{22}(x) \end{bmatrix} \begin{bmatrix} F(x) \\ M(x) \end{bmatrix} \qquad (6.2)$$

Here the matrix [C] is the local elastic compliance of the body, which can be regarded as the response of a generalised linear spring. Rice and Tracey (1972) matched this response to that of a single edge cracked bar of crack depth a and width t in conditions of plane strain. Each section of the crack can be regarded as an edge cracked bar as illustrated in Figure 6.4 which also shows a model of the line-spring compliance.

The basic concept of the line-spring element is that an additional degree of freedom is introduced along the line of a crack in an uncracked geometry where the local solution is embedded to achieve the global response. This is achieved by the compliance generated by the additional degree of freedom within these elements. From the relative displacements and rotations coupled to the compliance ABAQUS (1988) determines the J-Integral and the stress intensity factor as a function of position along the crack. The relative opening displacements and rotations for mode I deformation are respectively:

$$\begin{aligned} \delta &= (\delta_B - \delta_A) \cdot q \\ \theta &= (\theta_B - \theta_A) \cdot t \end{aligned} \qquad (6.3)$$

The corresponding mode two and three relations are given by:

$$\begin{aligned} \delta_{II} &= (\delta_B - \delta_A) \cdot n \\ \delta_{III} &= (\delta_B - \delta_A) \cdot t \end{aligned} \qquad (6.4)$$

$$\theta_{III} = (\theta_B - \theta_A) . q$$

The term θ_{II} plays no part in the deformation of the body.

6.2: Determination of Non-dimensional Stress Intensity Factor.

The stress intensity factor K is calculated through the relative displacements and rotations of the line-spring elements for every integration point in the elements used to represent the flaw. The results of this series of analyses were then normalised by K_0 which in tension is defined as:

$$K_0 = \sigma \sqrt{\pi a} \qquad (6.5)$$

Now let $\left(\frac{K}{K_0}\right)$ be denoted λ_t for the tensile loading component. For a crack subjected to a bending moment per unit thickness the normalising parameter is defined as:

$$K_0 = \frac{6M \sqrt{\pi a}}{t^2} \qquad (6.6)$$

Similarly $\left(\frac{K}{K_0}\right)$ is denoted λ_b for the bending component. In combined tension and bending K can be expressed separately in terms of tension and bending components and then superimposed to find K as exemplified in Chapter Two's benchmarking of Lefm.

6.3: Determination of T Stress.

Following Levers and Radon(1983) the T stress can be defined through a biaxiality parameter β:

$$T = \frac{K\beta}{\sqrt{\pi a}} \qquad (6.8)$$

Following from equation (6.5) T can now be written in the non-dimensional form:

$$\frac{T}{\sigma} = \lambda\,\beta \qquad (6.9)$$

Where

$$\sigma = \sigma_t \quad \text{(tension)}$$
$$\sigma = \sigma_b \quad \text{(bending)}$$

In a linear elastic analysis K and the T stress components for tension and bending can be resolved separately and then recombined. Superimposing solutions for tension and bending allows T to be expressed for the full solution as:

$$T = \lambda_t\beta_t\sigma_t + \lambda_b\beta_b\sigma_b \qquad (6.10)$$

Where the subscripts t and b represent tension and bending respectively. In the case of tension the nominal tensile force acting upon each section is given from the numerical analysis as a force gradient denoted S_{11}:

$$S_{11} = \frac{\partial F}{\partial x} \qquad (6.11)$$

Which when combined with the thickness of the body represents a *stress* term:

$$\sigma_t = \frac{1}{t}\frac{\partial F}{\partial x} = \frac{S_{11}}{t} \qquad (6.12)$$

For the tension component of the analysis T can be expressed as:

$$T_t = \beta_t \lambda_t \frac{S_{11}}{t} \qquad (6.13)$$

For the bending component of the analysis:

$$T_b = \lambda_b \beta_b \sigma_b \qquad (6.14)$$

From the analysis the moment gradient at each section of the line-spring is given by:

$$S_{22} = \frac{\partial M}{\partial X} \qquad (6.15)$$

Therefore the bending component T_b can be defined as :

$$T_b = \beta_b \lambda_b \frac{6S_{22}}{t^2} \qquad (6.16)$$

The values for both $\beta_b\lambda_b$ and $\beta_t\lambda_t$ are given by Sham (1991) illustrated in Figure 6.5, the full solution is given:

$$T = \beta_t \lambda_t \frac{S_{11}}{t} + \beta_b \lambda_b \frac{6S_{22}}{t^2} \qquad (6.17)$$

6.4: Numerical Method.

6.4.1: Benchmarking.

The benchmark analyses consider a series of flat plate geometries with a range of geometries through shallow to deeply cracked where through cracks are modelled, $\left(0.1 \leq \frac{a}{W} \leq 0.9\right)$. These benchmark models contain 181 nodes with 60 elements, of which 10 are line spring elements (LS3S) with the remainder being second order shell elements (S8R). Only half of the mesh was modelled due to conditions of symmetry, plane strain conditions were imposed by displacement boundary conditions on the right hand node set of the model.

6.4.2: Tubular T-Joint analysis.

The second mesh under consideration was a tubular T-joint discussed by Huang and Hancock (1986) and Du and Hancock (1989), a schematic of which is shown in Figure 6.6, with the actual geometry being shown in Figure 6.7. This joint was subjected to uniaxial tension with a uniformly distributed force applied to the brace, while the ends of the chord were fixed. Due to the symmetry of the geometry the problem can be reduced to one quarter of the actual structure under analysis. The cracks were located at the site of maximum stress concentration, which under these loading conditions is situated at the toe of the weld adjacent to the saddle point. The cracks are on the chord side of the chord-brace intersection which is the site of maximum stress concentration with the cracks being one brace wall thickness from the centreline intersection. Three crack geometries were analysed. Semi-elliptical cracks with a maximum crack depth to thickness ratio a/T=0.2, 0.6 and 0.9, with a surface length ratio of 2c/T=4 were modelled.

In this model a total of 210 eight noded double curved shell elements were used to represent the T-joint, thus giving a system with 4000 degrees of freedom. The semi-elliptical cracks were represented by the line-spring concept of Rice and Levy(1972) as implemented

in ABAQUS(1988).

6.5 : Results.

6.5.1 : Benchmarking.

Figures 6.8 and 6.9 show the results of the series of plate analyses as well as the previous results of Sham (1991). The biaxiality results are compared with the values given by Sham (1991) for a body subject to pure tension, these values can be matched up to a certain level but differ from these values for very deep cracks, a/W> 0.7. The discrepancies between the two series of results can be explained by the differing loading mechanisms used in the analyses, Shams (1991) results are achieved through force loading as opposed to the displacement loading for these analyses

6.5.2 : Tubular T-Joint analysis.

The results in this series of analyses mirror the work of Du and Hancock (1989) who originally calculated the stress intensity factor for the geometry as shown in Figure 6.10. The two deeper analyses, a/T=0.6 and 0.9 exhibit positive or tensile T stresses which maintain J dominance of the geometries in question. While the a/T ratio of 0.2 exhibits a negative or compressive T stress which necessitates the use of a two parameter characterisation. The purpose of the T-joint analysis was to demonstrate the computational simplicity with which T can be obtained for semi-elliptical cracks in complicated three dimensional engineering structures. The results of the T stress calculations are shown in Figure 6.11.

6.6: Discussion.

The tubular T-joint the line spring analysis mirrors the full three dimensional analyses of Du and Hancock (1989). The difference associated with the stress intensity factors for the shallowest crack arises from the different stress concentrations produced by the shell and continuum analyses, this arises from the modelling of the weld profile in the three dimensional analysis, this influence is negated as the crack depth is increased. Another point to be noted on the utilisation of the line-spring is that as the crack front approaches the free surface the physics of the line spring breaks down since the material moves from conditions of plane strain to plane stress.

6.7: Conclusion.

Line-spring analysis allows the determination of the first and second terms of the Williams (1957) expansion. As examples, line-spring analyses of tubular T-joints and the internally pressurised cylinders show good agreement with the results of continuum models. This agreement confirms the observation that the line-spring method is an accurate and computationally inexpensive method for the calculation of the non-singular term T, and thereby infer the degree of crack tip constraint.

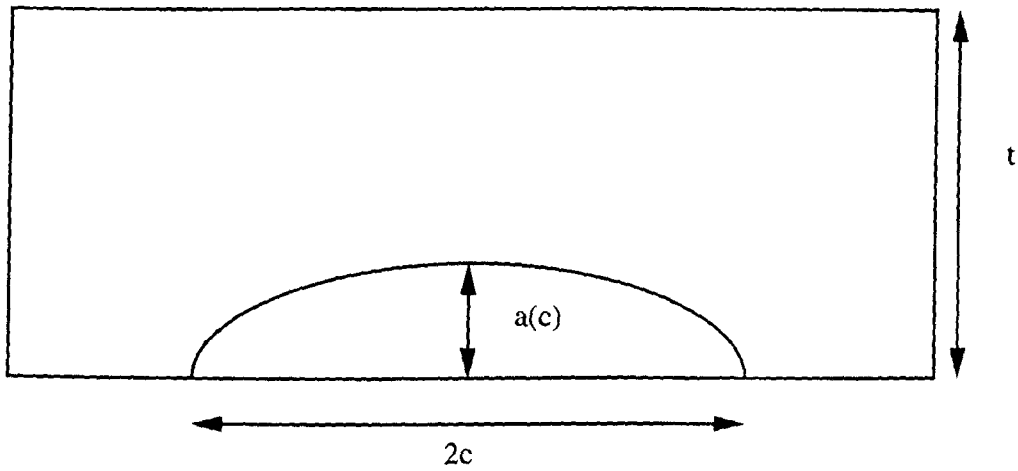

Figure 6.1: Part Through Surface Crack.

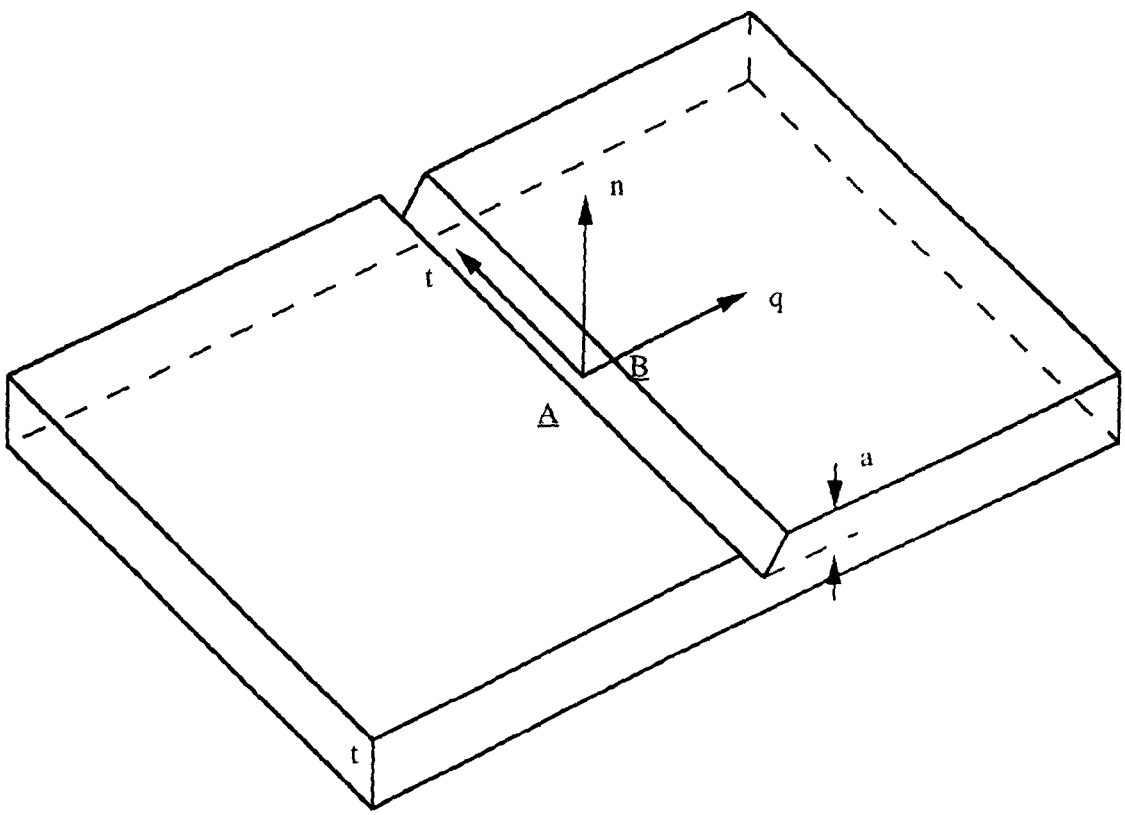

6.2: Line Spring Modelling.

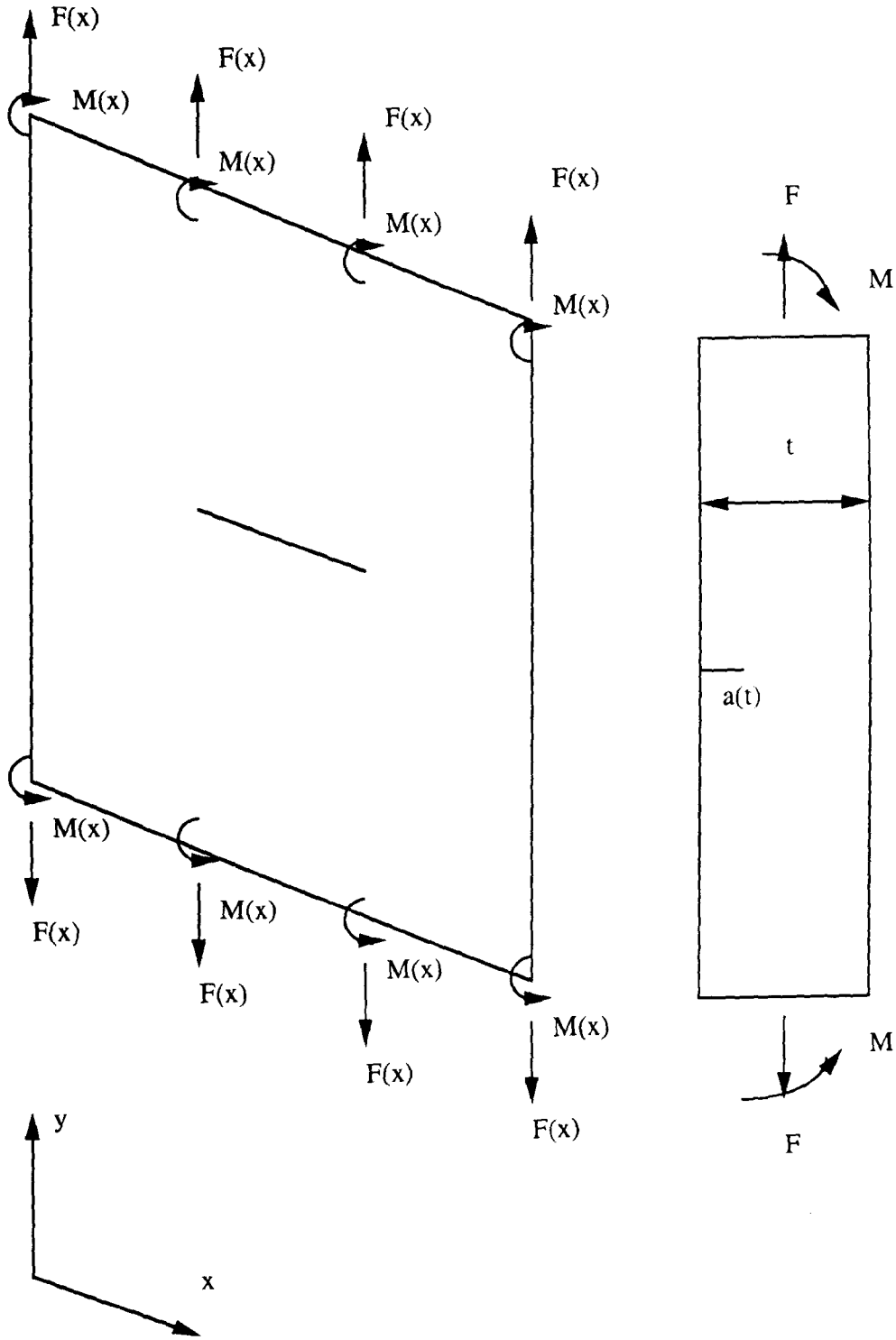

Figure 6.3: Idealised Model of Linespring Concept.

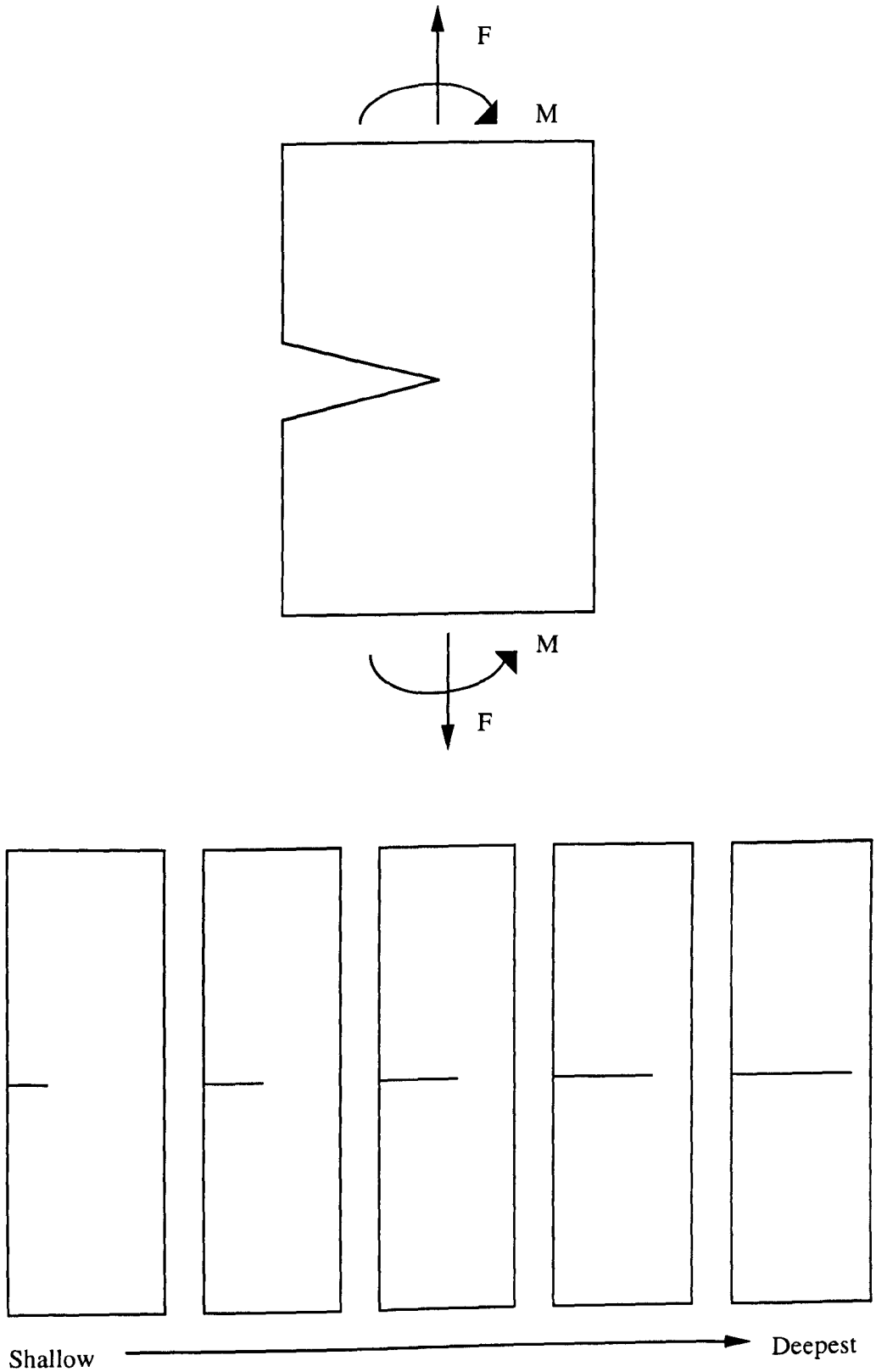

Figure 6.4: Idealisation of Semi-Elliptical Crack.

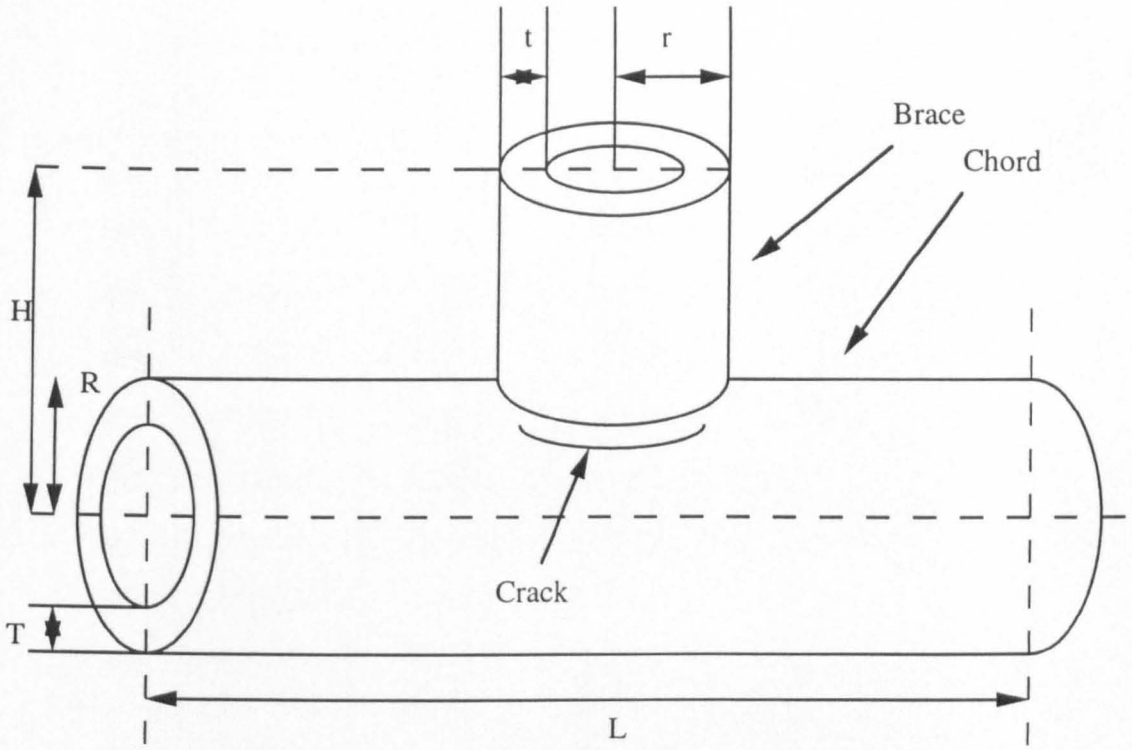

Figure 6.6: Schematic of Tubular Welded Joint Geometry

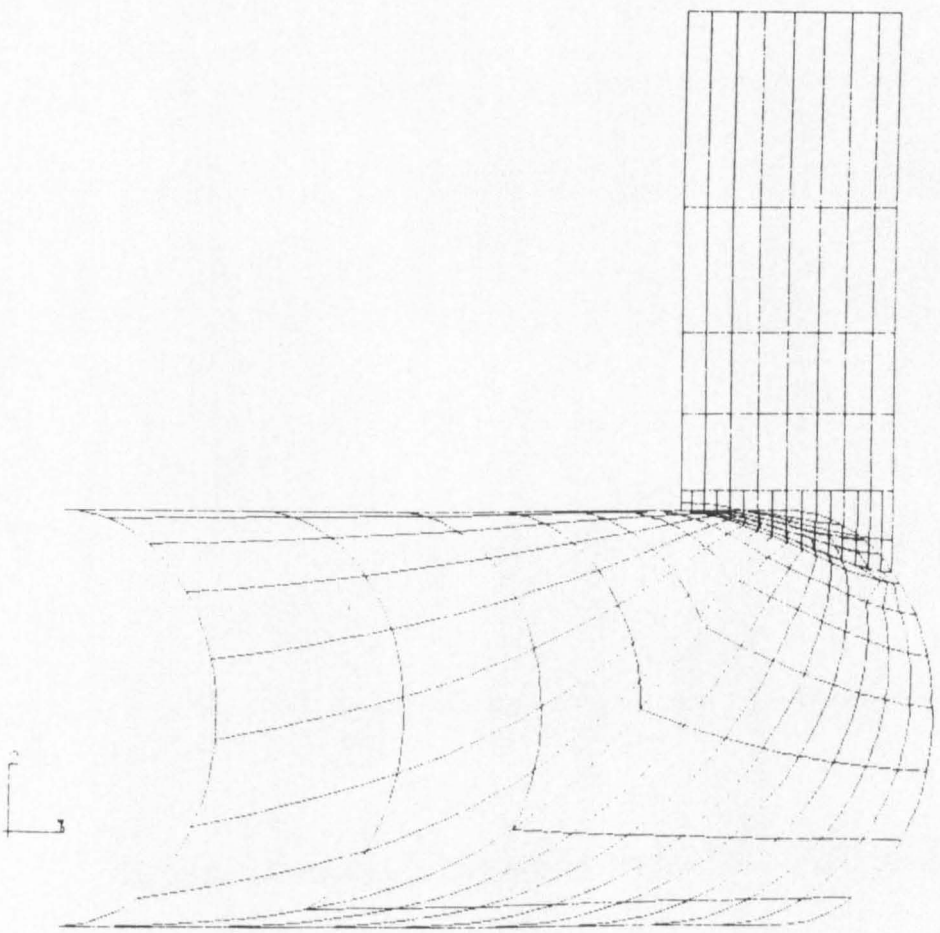

Figure 6.7: Geometry of Tubular Welded Joint. (Huang and Hancock (1986)).

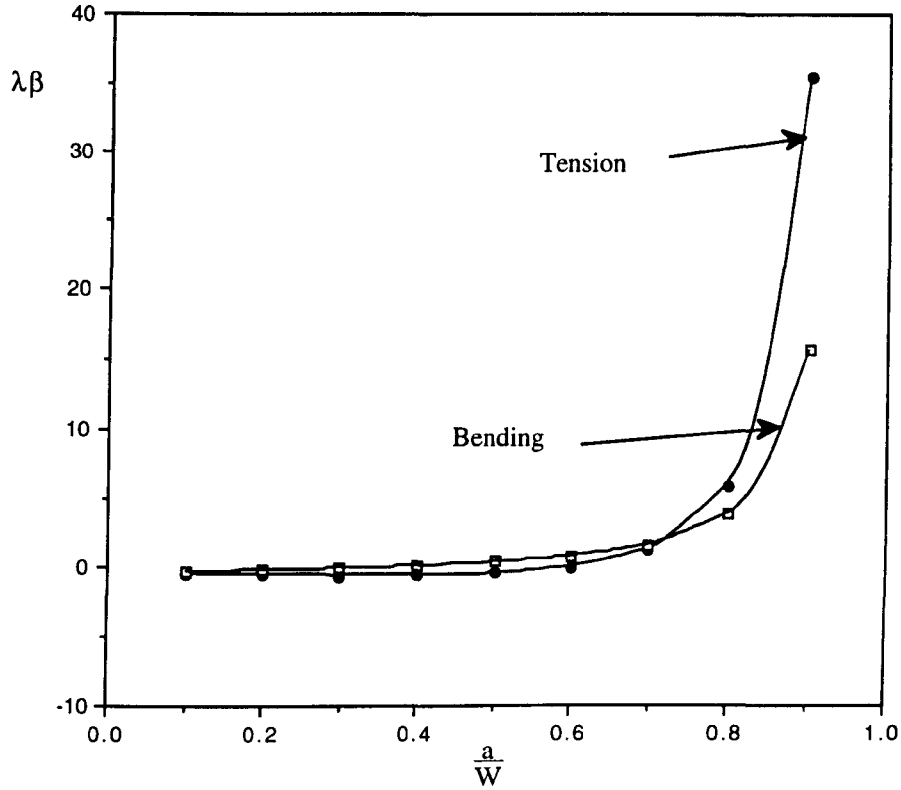

Figure 6.5: Geometry and Load Dependent Parameters after Sham (1991).

$\frac{a}{t}$	0.2	0.6	0.9
Du and Hancock (1989) $\frac{K_I}{K_0}$ where $K_0 = \sigma\sqrt{a}$	11.96	8.42	2.71
Analyses (1991) $\frac{K_I}{K_0}$ where $K_0 = \sigma\sqrt{\pi a}$	6.75	4.76	1.53

Figure 6.10: Comparison of Stress Intensity Ratios for T-Joint Analyses.

$\frac{a}{T}$	0.2	0.6	0.9
S_{11}	4.564e6	4.368e10	-1.489e10
S_{22}	3.679e7	2.598e11	1.355e11
T	-3.793e5	5.134e9	1.03e10
β	-0.2958	0.2272	1.4135

$\sigma = 4.75e9$
$T = 16$

Figure 6.11: T-Joint Analysis Results.

7: The Effect of Constraint on the Micro-mechanics of the Ductile-Brittle Transition.

7.1: Introduction.

Temperature dependent transitions in the failure modes of steels are of vital importance to the integrity of engineering structures. Within the context of plain carbon structural steels three principal modes of failure have been distinguished.

At low temperatures failure occurs by cleavage instability by the direct separation of the low index crystallographic planes as shown in Figure 7.1. As the temperature increases the failure mode passes through a transition region where initial crack extension is by void growth and coalescence but the final failure occurs by cleavage instability. Whereas at higher temperatures the toughness reaches the *upper shelf,* where crack extension occurs solely by ductile mechanisms, as illustrated in Figure 7.2.

As the temperature increases there is not only a change in the fracture mode but also in the material toughness, where the *upper shelf* is ductile in nature with high toughness levels. Brittle failure (cleavage) mechanisms are associated with low toughness levels as exemplified in the transition curve shown in Figure 7.3. It is obviously desirable to operate engineering structures on the *upper shelf,* due to the increased toughness and the possibility of crack growth. The transition temperature between brittle and ductile modes has therefore particular significance for materials and structures that operate at or near this temperature. Attempting to specify a transition temperature can be subjective since the temperature will occur within the transition region where the two failure modes are competing to satisfy their individual failure criteria. In reality the onset of the *upper shelf* is characterised by significant amounts of stable crack growth .

In this chapter interest is centred on the effect of geometry and size on the *lower shelf* toughness and transition temperature. Failure loci are interpreted in terms of the effect of

specimen size and temperature on the *lower shelf* toughness in terms of the second parameter in the Williams expansion (1957). Finally the shift in transition temperature associated with the change in geometry from deep to shallow cracked bars is predicted.

7.2: Cleavage Fracture.

The lowest energy absorbent form of fracture exhibited by engineering materials is cleavage, where this form of fracture is termed brittle. In ferritic steels the main mode of failure is by transgranular cleavage. Cleavage is the most dramatic form of failure and in a significant way contributed to the development of engineering fracture mechanics. The likelihood of cleavage failure occurring is increased by higher strain rates and low temperatures as exemplified in a toughness transition curve.

Cleavage occurs by the direct separation of low index crystallographic planes, such as the cube planes {100} in b.c.c. metals. As a result the fracture surface is highly reflective because of the facets associated with each grain orientation. Features common in cleavage failure include steps and tongues. Steps are achieved when two parallel cracks simultaneously pass through a material grain, when these cracks intersect they form a step as shown in Figure 7.4. Tongues are formed at twin matrix intersects as illustrated in Figure 7.5.

Brittle materials have high yield strengths but a reduced ductility and are therefore unable to accommodate significant plastic deformation. In such materials despite the localised plastic flow associated with crack tip blunting the local stress levels are still high enough to break interatomic bonds. Within this analysis a critical stress criterion based on the Ritchie, Knott and Rice (1973), (henceforth RKR) criterion was used as defined in Chapter 3. Cleavage failure is associated with the cracking of grain boundary carbides, this necessitates that the RKR approach is applied over some characteristic distance (Rice and Johnson (1970)), which is a multiple of the grain diameter as illustrated in Figure 7.6.

7.3: Ductile Failure.

Ductile failure is a strain induced process where failure occurs in the form of void nucleation and coalescence. Failure of this form will occur when the strain reaches a critical value which is dependent on the stress state, (MacKenzie, Hancock and Brown (1977)). Despite design to the contrary many engineering structures contain stress concentrations, these cause localised yield and plastic flow which reduce the stress levels. Although yield and plastic flow cause a reduction in the stress levels it also replaces the stress concentration with a strain concentration. Ductile failure will occur when a critical strain is reached which is a function of the stress state. Therefore the ductility of the body is highly dependent on the stress triaxiality of the body, (Hancock and MacKenzie (1976)). It is necessary to make sure that the material can sustain this level of strain, where the ductility of the material is highly dependent upon the stress triaxiality $\left(\frac{\sigma_m}{\bar{\sigma}}\right)$. The triaxiality is defined in terms of σ_m the hydrostatic or mean stress and $\bar{\sigma}$ the Mises stress which can be expressed in terms of the principal stresses:

$$\sigma_m = \frac{\sigma_1 + \sigma_2 + \sigma_3}{3} \qquad (7.1)$$

$$\bar{\sigma} = \sqrt{\frac{1}{2}\left\{(\sigma_1 - \sigma_2)^2 + (\sigma_2 - \sigma_3)^2 + (\sigma_3 - \sigma_1)^2\right\}} \qquad (7.2)$$

Ductility is vitally important in forming processes, which involve plastic deformation and the ability to withstand stress concentrations by localised plastic flow due to yielding. Ductile failure is caused by void coalescence which is due to void growth which in turn is controlled by the level of stress triaxiality. Void growth models have been considered by Berg (1962), McClintock (1968) and Rice and Tracey (1972). Rice and Tracey (1972) expressed conditions for failure initiation in global parameters in terms of the stress triaxiality and a critical volume fraction of voids. Favoured sites for void growth are second phase particles and inclusions which are formed during the manufacturing processes. These are

favoured because they are sites of stress and strain concentration, (Argon, Im and Safoglu (1975), Thomson and Hancock (1984)). The largest of these particles cannot accommodate significant plastic deformation due to the brittle nature of second phase particles and therefore fail early in the loading process forming voids within the matrix.

Ductile failure is caused by void coalescence and growth which is controlled by the level of stress triaxiality . Void growth models have been considered by Berg (1962), McClintock (1968) and Rice and Tracey (1972). Rice and Tracey expressed conditions for failure initiation in global parameters such as the volume fraction of voids. They considered an initially spherical void within a rigid non-hardening plasticity model where the rate of change of the mean void radius (R) with the plastic strain at high values of the triaxiality parameter was found to be well approximated by:

$$\frac{dR}{R} = 0.28\, d\bar{\varepsilon}^{p} \exp \frac{3\sigma_m}{2\bar{\sigma}} \qquad (7.3)$$

If failure occurs at a critical void radius or volume fraction, the failure initiation strain ($\bar{\varepsilon}^{f}$) is inversely proportional to the void growth rate:

$$\bar{\varepsilon}^{f} = \alpha \exp\left(\frac{-3\sigma_m}{2\bar{\sigma}}\right) \qquad (7.4)$$

Where α is a material constant.

7.4: Temperature Effects on Material Properties.

At low temperatures both b.c.c. and h.c.p. metals fail by cleavage whereas the failure modes of f.c.c. structures are unaffected by temperature. This temperature dependency is reflected in the yield stress of b.c.c. metals which increases markedly as the temperature reduces as illustrated in Figure 7.7 after Bennett and Sinclair (1966). At low temperatures the resistance to thermally activated processes inhibits slip and plastic flow the effect of

which is to raise the yield strength and thereby reduce the ductility of plain carbon structural steels:

$$\sigma_y = 745.6 - 0.056\ T \ln\left(\frac{a}{\sqrt{2\dot{\varepsilon}}}\right) \qquad (7.5)$$

Here T is the temperature in Kelvin, a is a constant equal to $10^8\ s^{-1}$, $\dot{\varepsilon}$ is the strain rate, taken to be 1.6×10^3 and σ_y is the yield stress in MPa.

7.5: Numerical Methods.

Local failure criteria have been applied to elastic-plastic crack tip fields, based on the ability to describe the crack tip fields of shallow cracks with modified boundary layer formulations. The work expresses the critical value of J for shallow cracked bend bars to that of the small scale yielding solution, as a function of T thereby defining a failure locus as shown in Figure 7.8. Crack tip deformation under small scale yielding has previously been modelled by modified boundary layer formulations, where the boundary conditions are specified by the first two parameters of the Williams (1957) expansion, K and T. Betegón and Hancock (1991) considered this problem where the crack tip plasticity was modelled by a Ramberg-Osgood stress-strain relation with a power law hardening exponent, n=13. Given the framework of small strain theory the stress fields directly ahead of the crack tip can be described by the family of solutions as shown in Figure 7.9. Betegón and Hancock (1991) have expressed the stress field in terms of higher asymptotics based on the small scale yielding field:

$$\frac{\sigma_{\theta\theta}}{\sigma_0} = \frac{\sigma_{SSY}}{\sigma_0} + 0.64\left(\frac{T}{\sigma_0}\right) - 0.4\left(\frac{T}{\sigma_0}\right)^2 \qquad (7.6)$$

The stress field may be written:

$$\frac{\sigma_{\theta\theta}}{\sigma_0} = 4.03\left(\frac{r\sigma_0}{J}\right)^{-0.07143} - 0.3\left(\frac{r\sigma_0}{J}\right)^{0.065} + 0.64\left(\frac{T}{\sigma_0}\right) - 0.4\left(\frac{T}{\sigma_0}\right)^2 \qquad (7.7)$$

Small strain solutions, as exemplified by the HRR field exhibit stress singularities at the crack tip whereas large strain solutions define finite maximum stress level as shown in Figure 7.9. This maximum finite stress level occurs at a distance which is approximately two crack tip openings from the tip. As the T-stress becomes more negative the maximum finite stress achievable reduces and the distance at which it is achieved approaches the crack tip.

As discussed in Chapter 3, the RKR analysis postulates that brittle failure will occur when a critical cleavage stress (σ_f) is attained over some microstructurally significant distance (r^*) from the crack tip. However it is possible to remove this dependency on distance by comparing the family of stress fields with a reference T=0, field, at a given stress level, it is possible to remove the distance term, r^*:

$$\frac{J_{(T)_k}}{J_{(T=0)_k}} = \frac{\dfrac{r^*\sigma_0}{J_{(T=0)_k}}}{\dfrac{r^*\sigma_0}{J_{(T)_k}}} \qquad (7.8)$$

The T=0 field is the limiting field which applies at infinitesimally small applied loads, and is hence identified as the small scale yielding field (SSY). The ratio $\frac{J_{(T)_k}}{J_{(T=0)_k}}$ is shown in Figure 7.10 as a function of $\frac{T}{\sigma_0}$ for a range of critical stress levels. The form of the failure locus is clearly captured in comparison with the experimental loci as illustrated in Figure 7.11, while an exact fit depends on the critical cleavage stress level. Supplying dimensional values of σ_f and r^* allows the temperature dependence of J to be modelled, as shown in Figure 7.12-7.13. In these Figures r^* was taken to be 100 μm combined with a critical cleavage stress of 1400 MPa, which is an appropriate value for a plain carbon steel described by BS 4360 Grade 50D. The chemical composition of this structural carbon steel is given in

Table 1. For the purpose of a sensitivity study the results of an analysis with a fracture stress of 1800 MPa are also shown. The data are truncated at the maximum temperature at which cleavage initiation can occur.

The J-T loci shown in Figures 7.14 and 7.15 unify the geometry dependence of toughness by quantifying the associated constraint of the crack tip fields by T. It is possible to reinterpret this information in terms of a range of specific geometries, in this case interest is restricted to edge cracked three point bend bars. J is related to the applied load by the engineering approach as defined in Chapter 3, where J is expressed as elastic and plastic components and then combined. The T-stress is defined through the biaxiality parameter and the stress intensity factor.

For any given specimen, geometry and size the J-T history can be determined, allowing failure to be predicted at the intersection with the J-T failure locus. On this basis it is possible to determine the effect of temperature, size and geometry on the *lower shelf* toughness of the material as shown in Figure 7.16. The maximum temperatures at which cleavage initiation can occur are also shown in Figures 7.17 and 7.18 as a function of geometry and size.

7.6: Discussion.

The RKR analysis and its refinements provide a foundation for modelling the temperature dependent cleavage of deeply cracked bend bars. The ability to describe the crack tip fields of unconstrained specimens, such as edge cracked bend or tension bars with short cracks allows the method to be extended to a wide range of geometries. A particular difficulty with the RKR analysis, and a source of much discussion, Curry and Knott (1976) has been the size of microstructural distance, r^*. Fortunately this can be removed by comparing the effect of constraint on cleavage toughness, as shown in Figure 7.10, and presenting data in the non-dimensional form $\frac{J_{T_c}}{J_{(T=0)_k}}$. Dimensional values can be supplied by using the RKR method to determine $J_{(T=0)_k}$. The experimentally determined temperature dependence of the yield stress, Bennet and Sinclair (1966) now allows the temperature dependence of J to be determined as shown in Figures 7.12 and 7.13. Such results can be compared with those of Anderson and Dodds (1991) who use an amplitude parameter to scale the HRR field to fit the fields of bend bars. This also leads to the ratio of the toughness of short and deeply cracked bars, and like the present method the ratio is independent of the micro-structural distance. However unlike the present analysis of weakly hardening boundary layer formulations, Anderson and Dodds (1991) analysis appears to be independent of the critical stress, σ_f.

It is now appropriate to turn to the conditions under which cleavage cannot initiate ahead of a crack tip. Here it is necessary to recognise that the large strain solutions indicate that there is a maximum stress achievable at finite distances ahead of a blunting crack tip, as shown in Figure 7.9. In small scale yielding $J_{(T=0)_k}$ this is approximately 3.96 times the yield stress. At elevated temperatures cleavage initiation is prevented by the fact that the yield stress is too low to allow the local stress to reach the critical cleavage stress. The maximum temperature at which cleavage is possible is given by the temperature at which the maximum principal stress can just reach σ_f. The maximum stress that can be achieved ahead of the crack decreases with constraint, as shown in Figure 7.9. This implies that the highest

temperature at which cleavage can initiate failure is lower in short crack geometries than in deeply cracked configurations as shown in Figures 7.17 and 7.18. This is in accord with experimental observations Li (1985), Li, Zhou and Li (1986) and Al-Ani (1991) that the transition temperature decreases with (a/W) ratio.

The effect of size on the transition temperature, ϕ_c, for specific geometries is shown in Figure 7.17 . Size independence is exhibited by the deep cracked geometries, for which T is positive or close to zero, given $(W\text{-}a) \geq \frac{25J}{\sigma_0}$. The transition temperature of the shallow cracked configurations is however geometry dependent until a critical size is reached. Figure 7.18 shows the effect of specimen size on the transition temperature for a range of geometries. Geometry and size independence occur only in very large specimens. This temperature shift associated with specific geometries can then be compared with experimental observations of Al-Ani (1991), Sumpter (1982) and MacLennan shown respectively in Figures 7.19-7.21.

7.7: Conclusions.

A J-T description of elastic plastic crack tip fields has been combined with local fracture criteria to indicate the effect of constraint on toughness, as measured by a J-T failure locus. An identical approach is possible in terms of Q. Such failure loci can be interpreted in terms of the effect of size and geometry on both the *lower shelf* toughness and the ductile-brittle transition temperature as measured by the maximum temperature at which cleavage initiation can occur. The analysis indicates that the transition temperature decreases with crack tip constraint in accord with experimental data. The model also predicts the size dependence of the transition temperature for short and deeply cracked geometries.

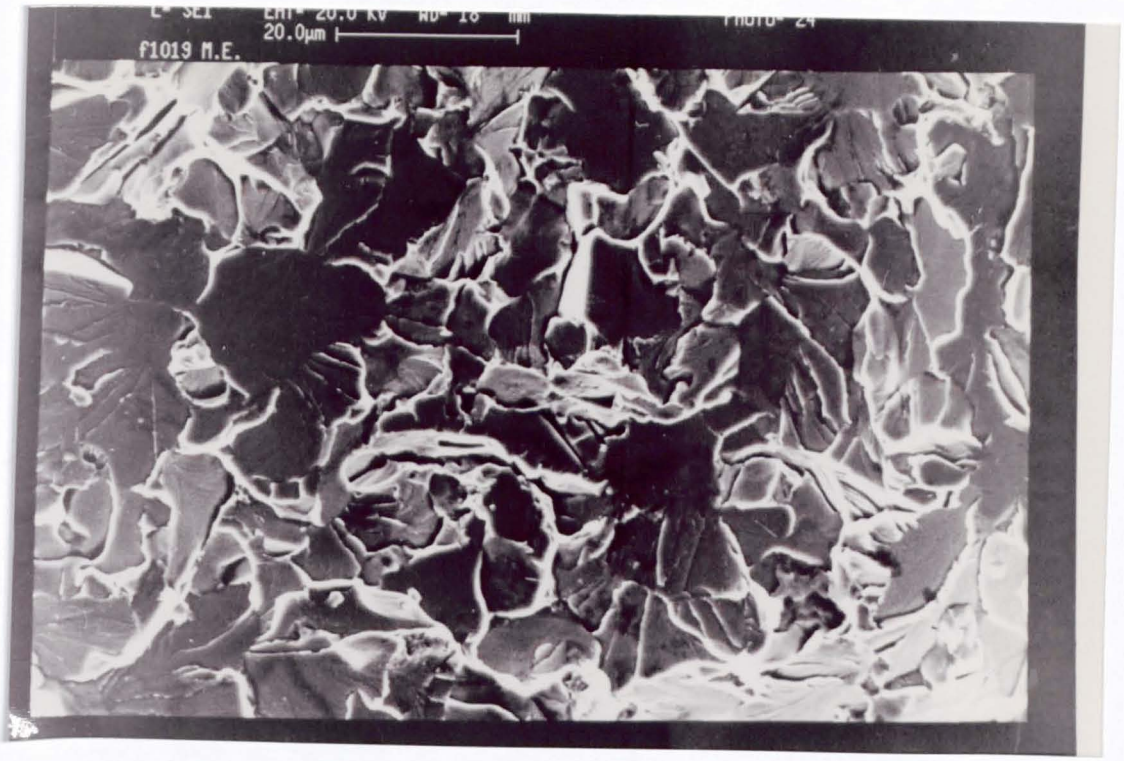

7.1: Transgranular Cleavage.

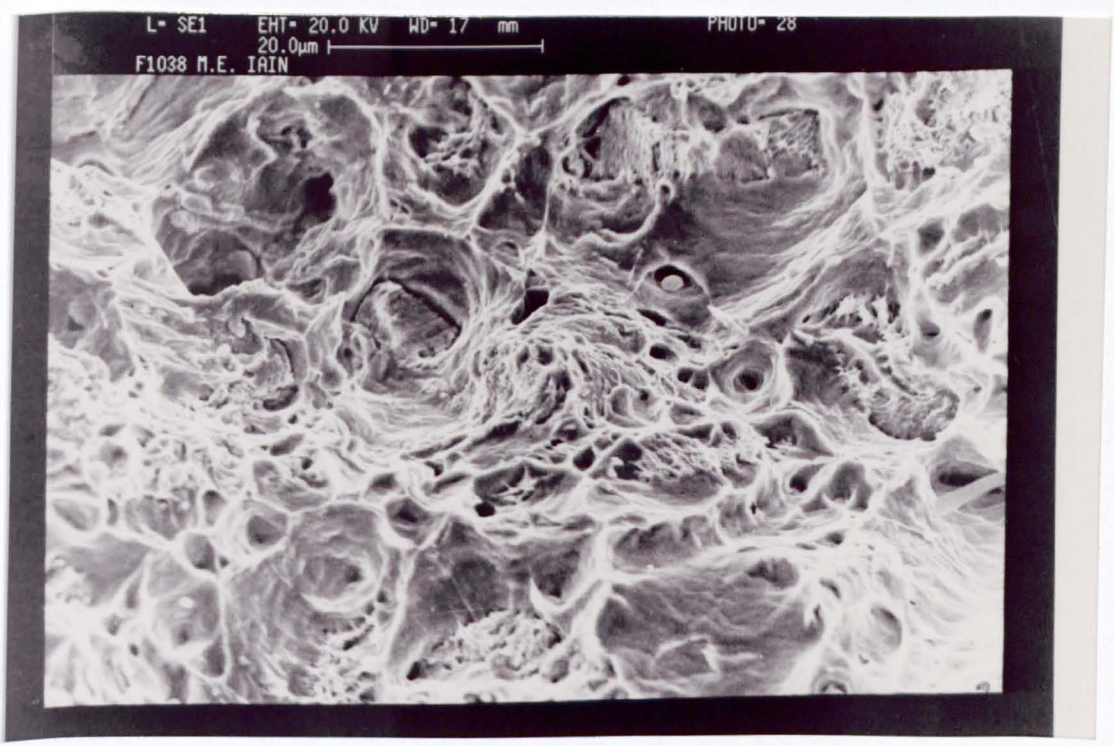

7.2: Ductile Failure.

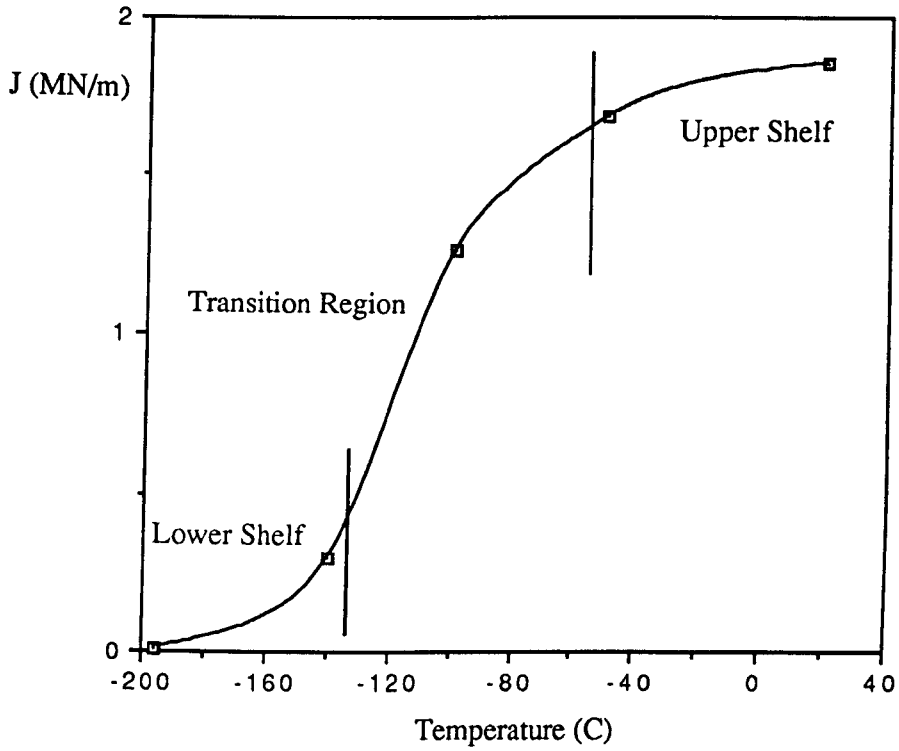

Figure 7.3: Ductile-Brittle Transition.

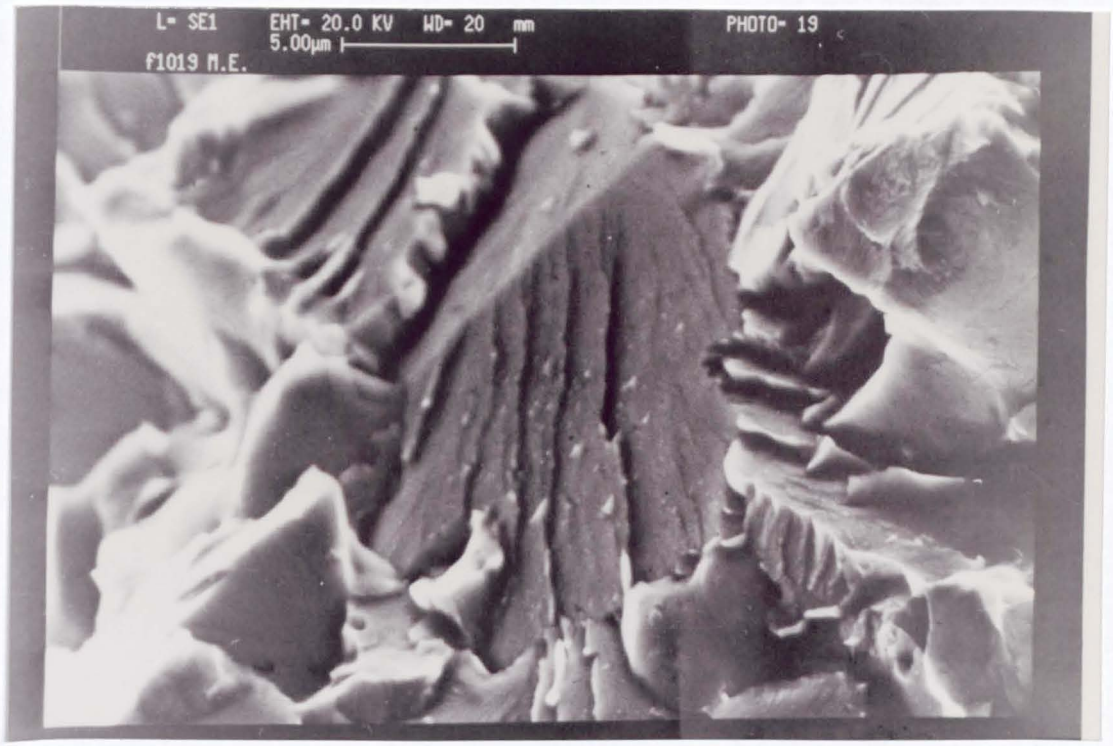

7.4: Cleavage Steps.

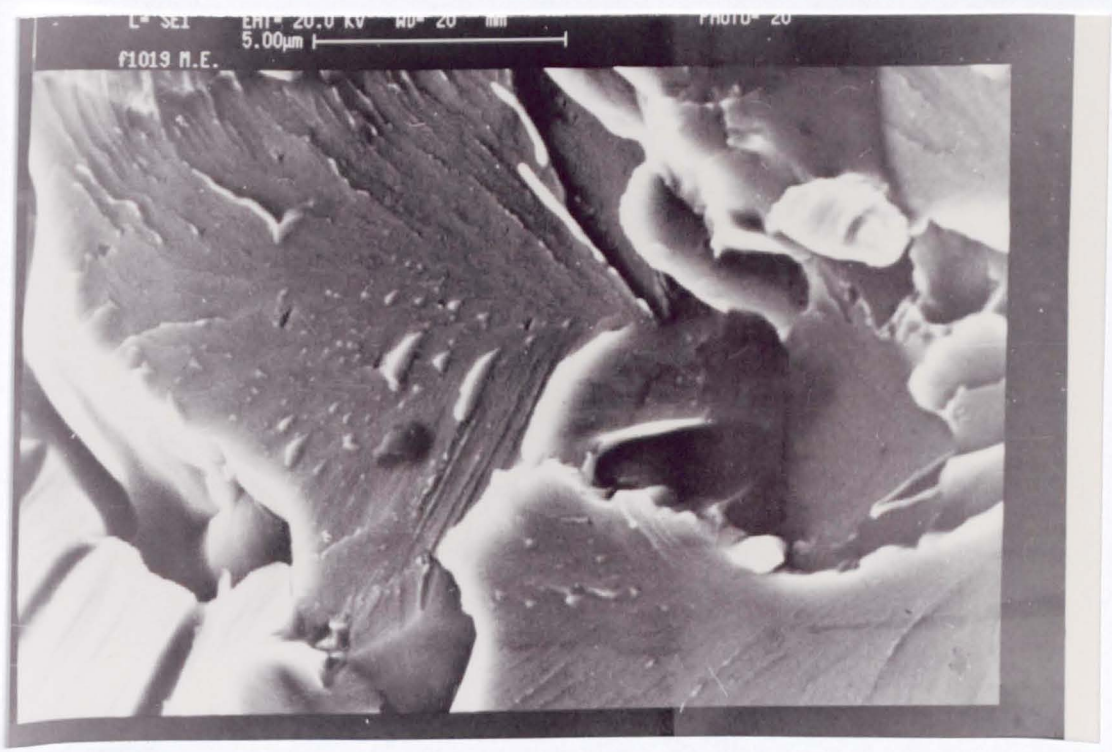

7.5: Cleavage Tongues.

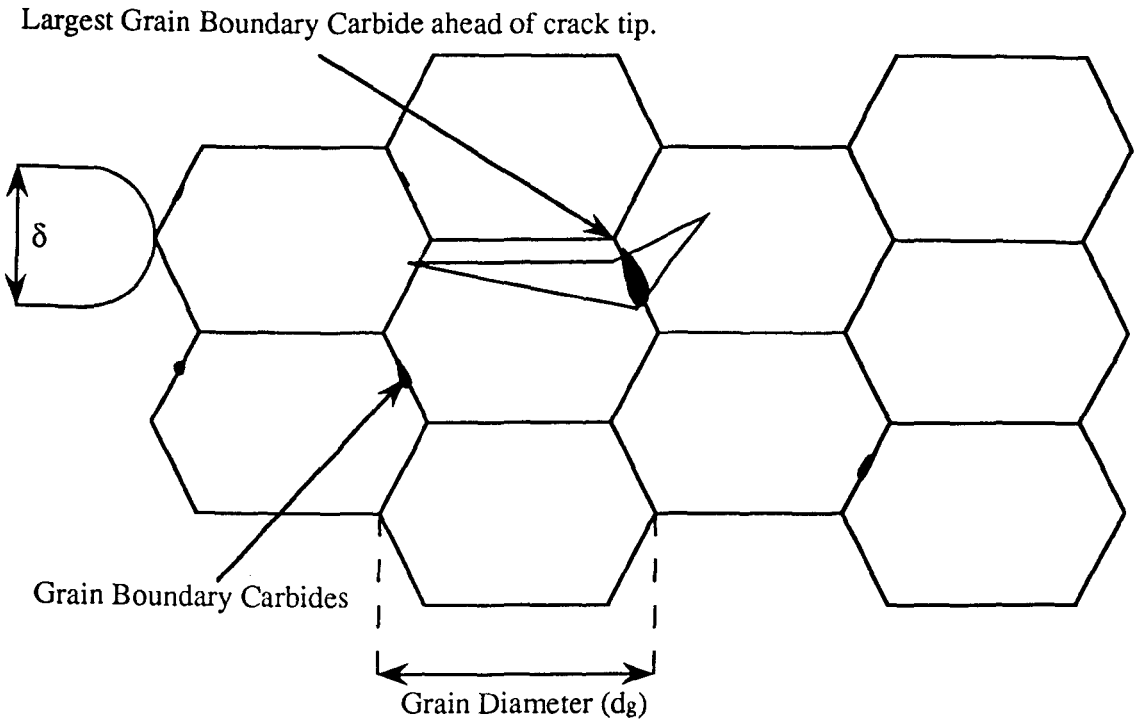

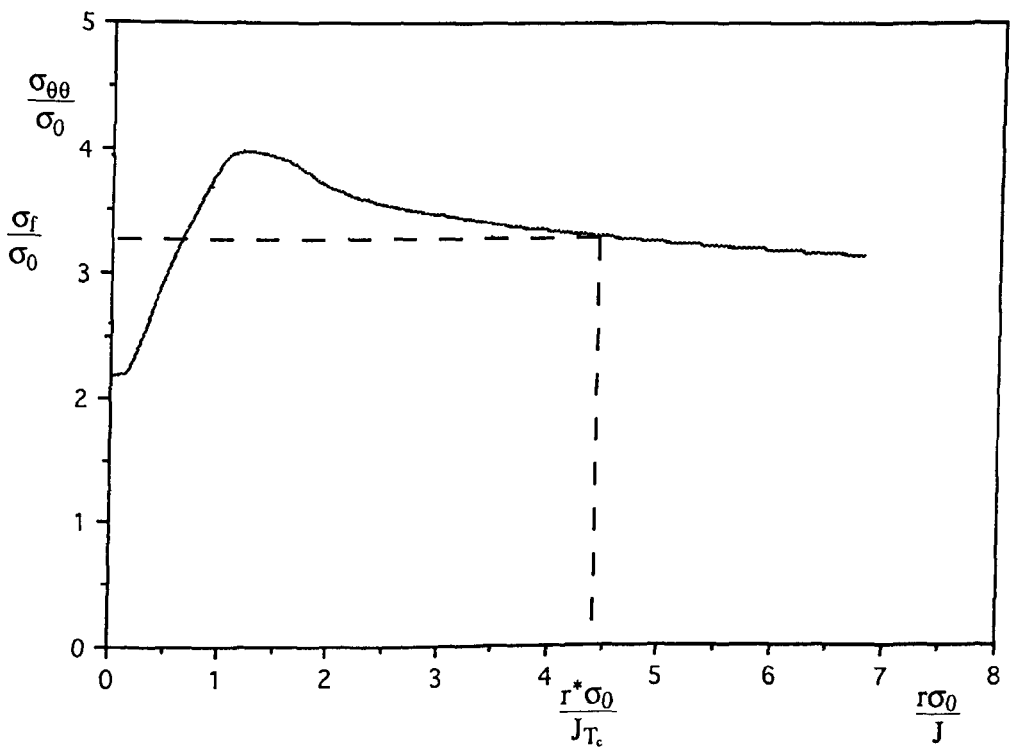

Figure 7.6: Ritchie, Knott and Rice Stress Controlled Cleavage Model.

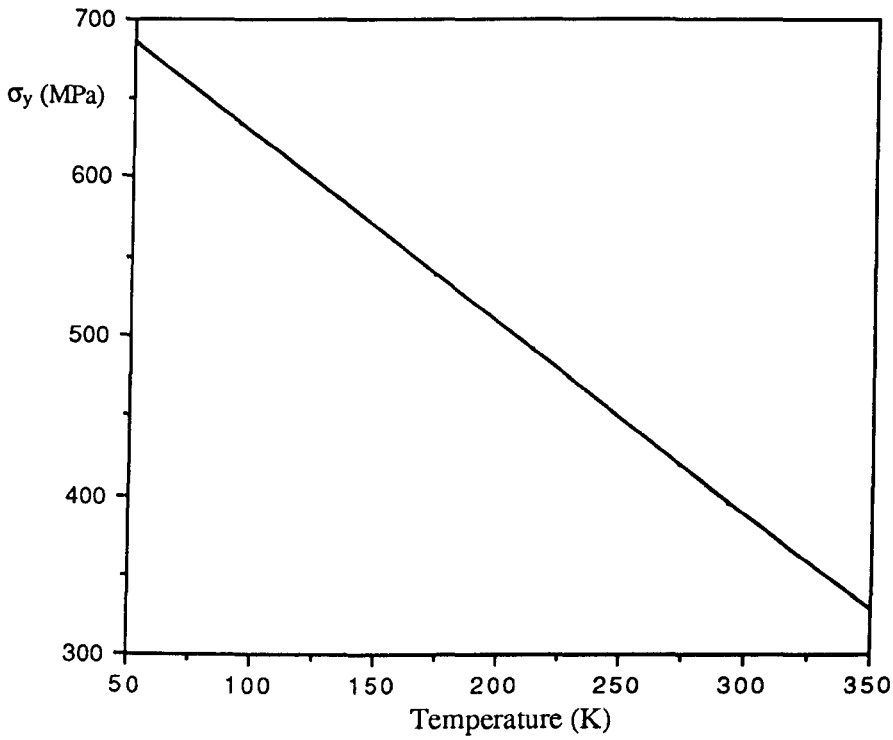

Figure 7.7 : Temperature Dependent Yield Stress after Bennett and Sinclair (1966).

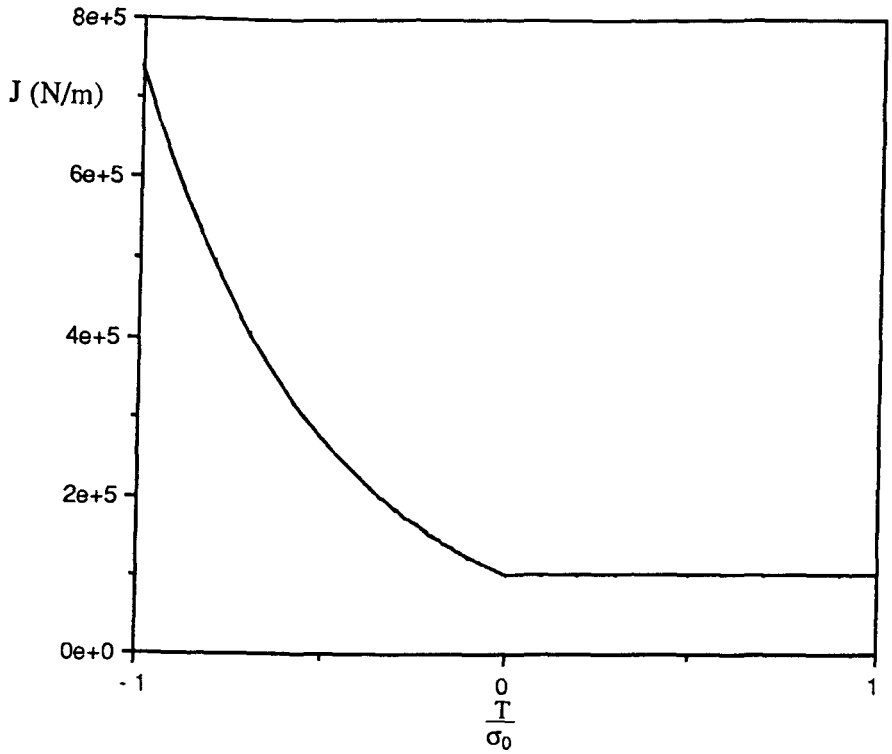

Figure 7.8: Idealised Failure Loci.

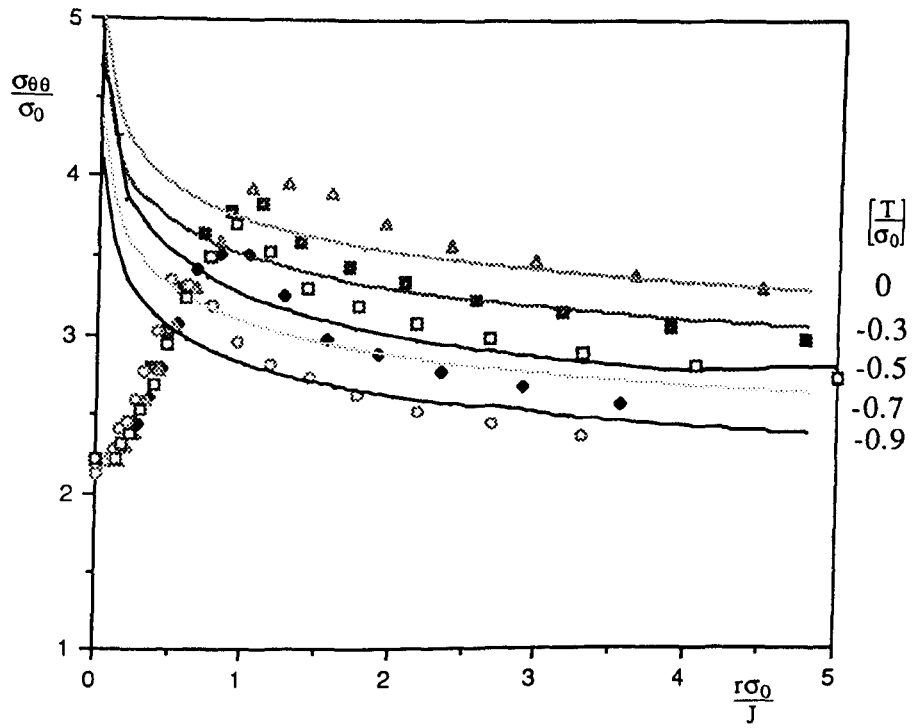

Figure 7.9: Family of Small and Large Strain Solutions for n=13.

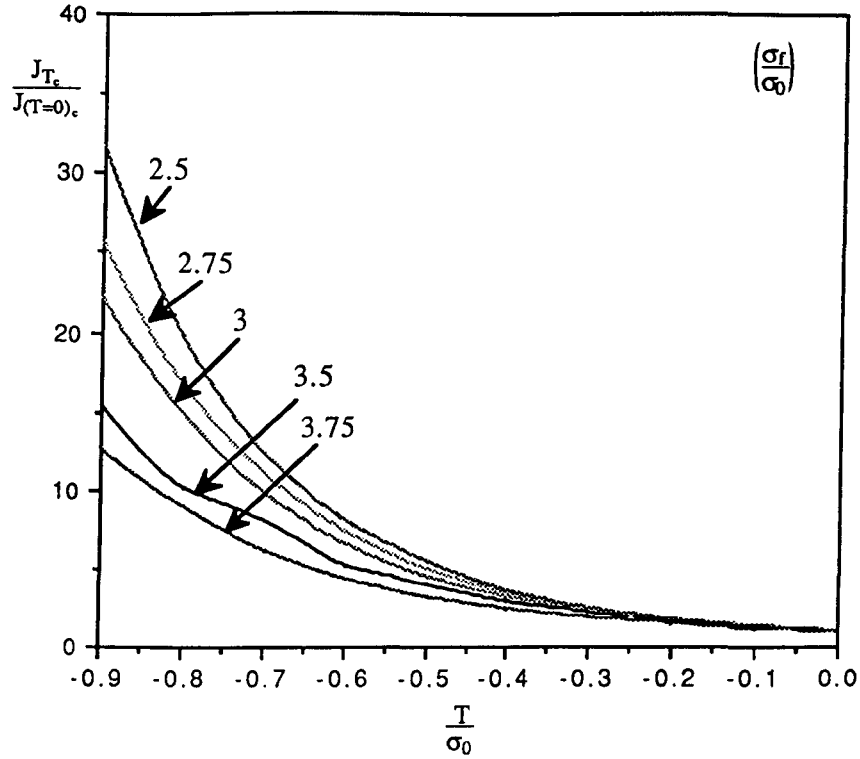

Figure 7.10: Non-dimensionalised J-T loci for Cleavage at a Range of Fracture Stresses for n=13.

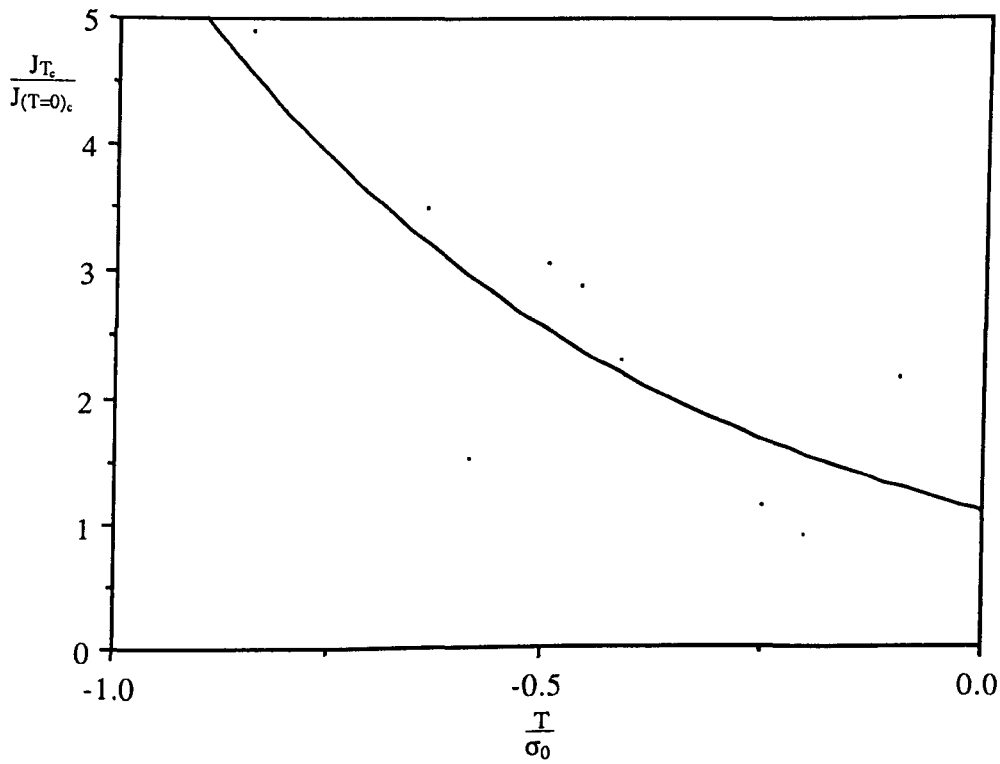

Figure 7.11: Normalised Experimental J-T loci, after Betegón (1990)

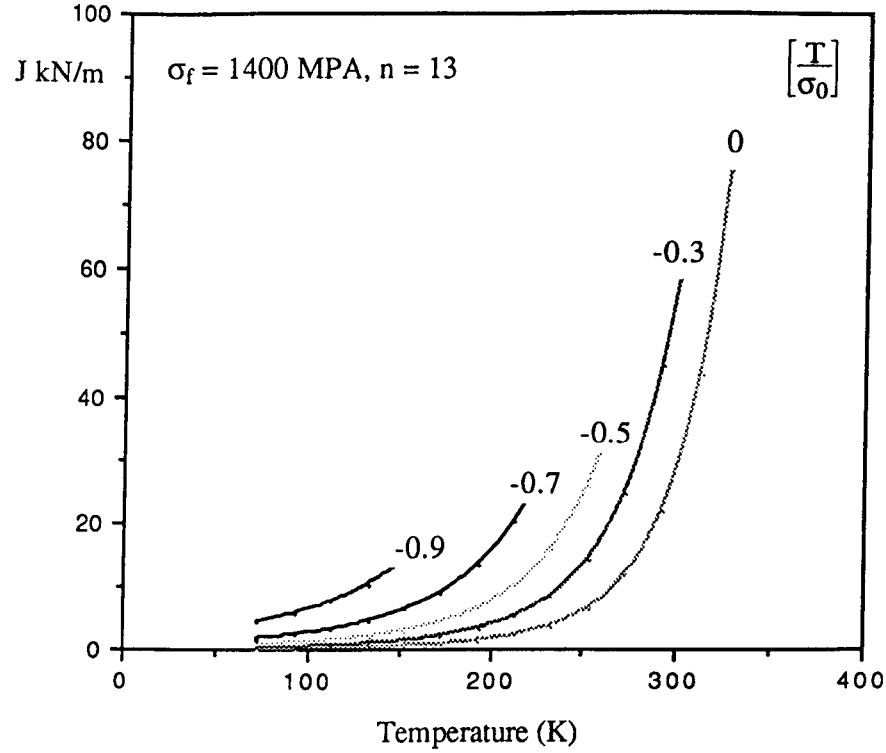

Figure 7.12: Effect of Temperature on Toughness with varying degrees of Constraint.

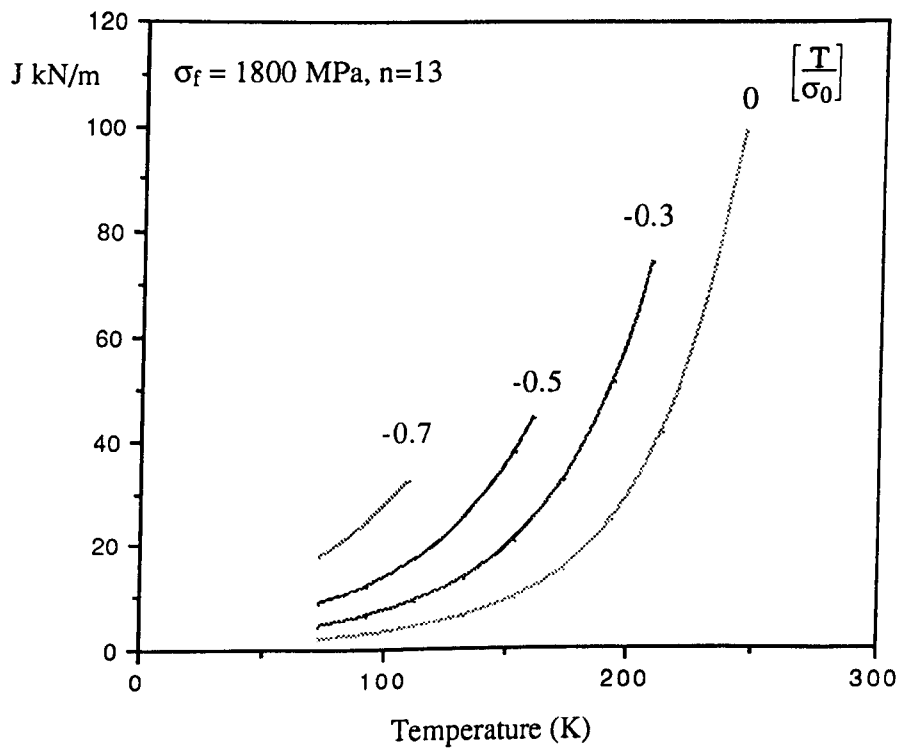

Figure 7.13: Effect of Temperature on Toughness with varying degrees of Constraint.

Chemical Composition (Wt%).								
C	Si	Mn	P	S	Cr	Mo	Cu	Nb
0.17	0.29	1.3	0.01	0.008	0.09	0.01	0.11	0.045

Table 1: Chemical Composition of BS4360 grade 50D Steel.

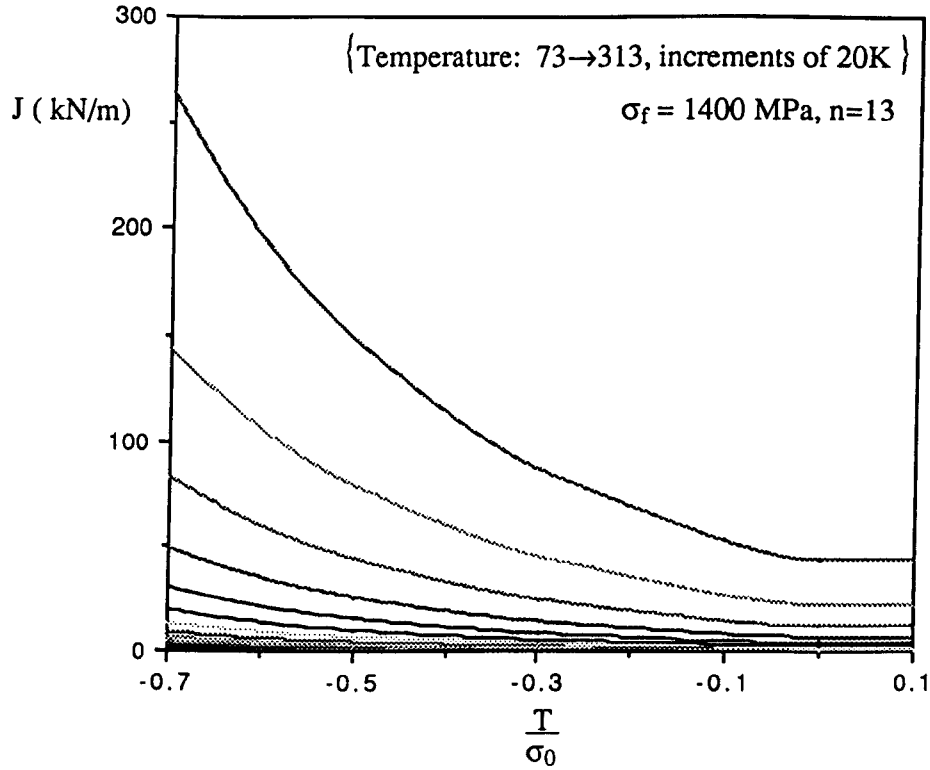

Figure 7.14:Temperature Dependence of J-T Loci for a Critical Cleavage Stress of 1400MPa

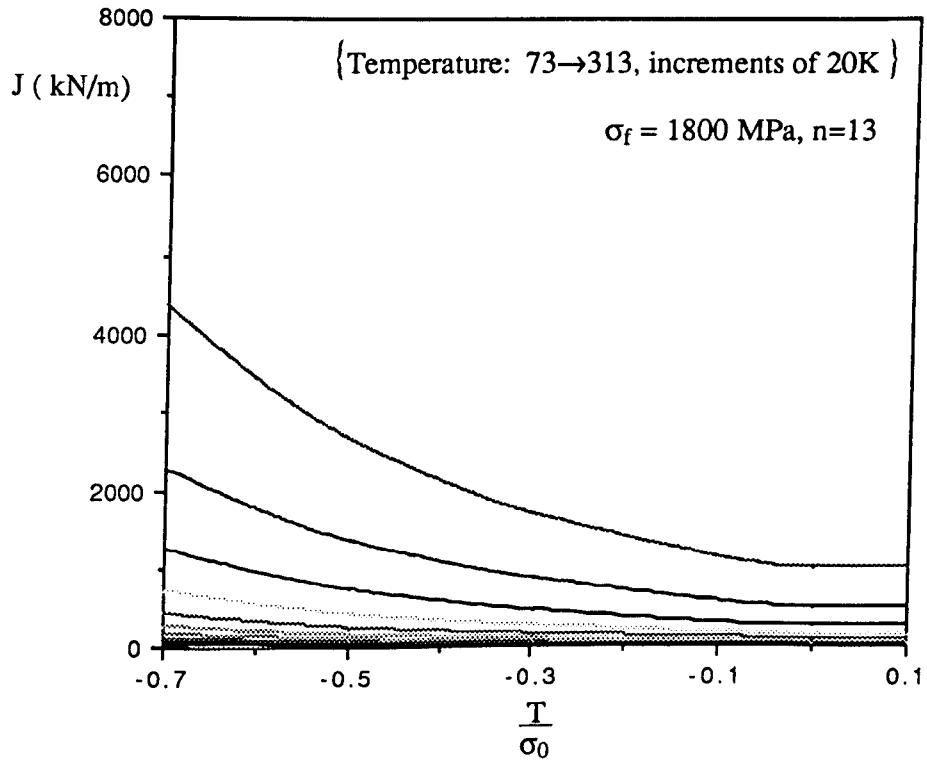

Figure 7.15: Temperature Dependence of J-T Loci for a Critical Cleavage Stress of 1800MPa

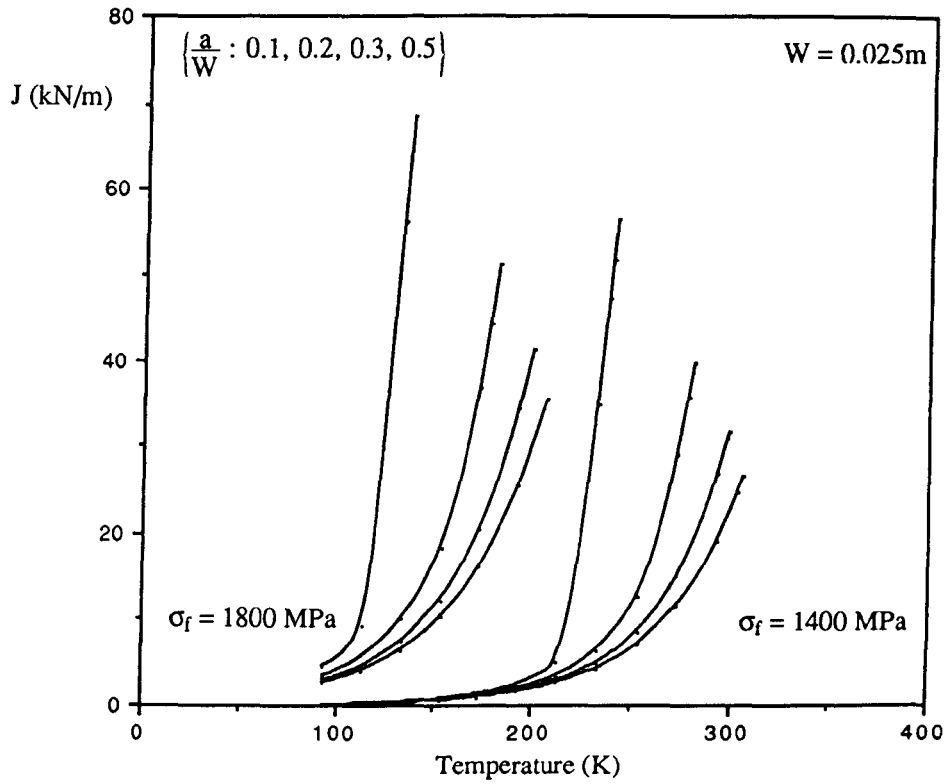

Figure 7.16: The Influence of Geometry on Toughness.

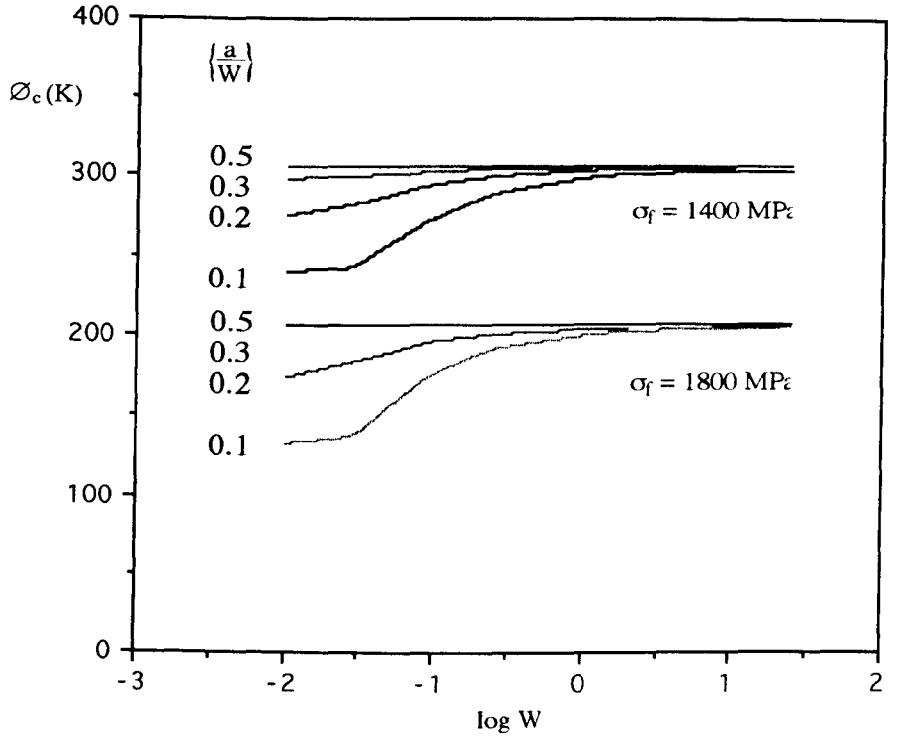

Figure 7.17: The Effect of a/W on the Transition Temperature for a Range of Specimen Widths.

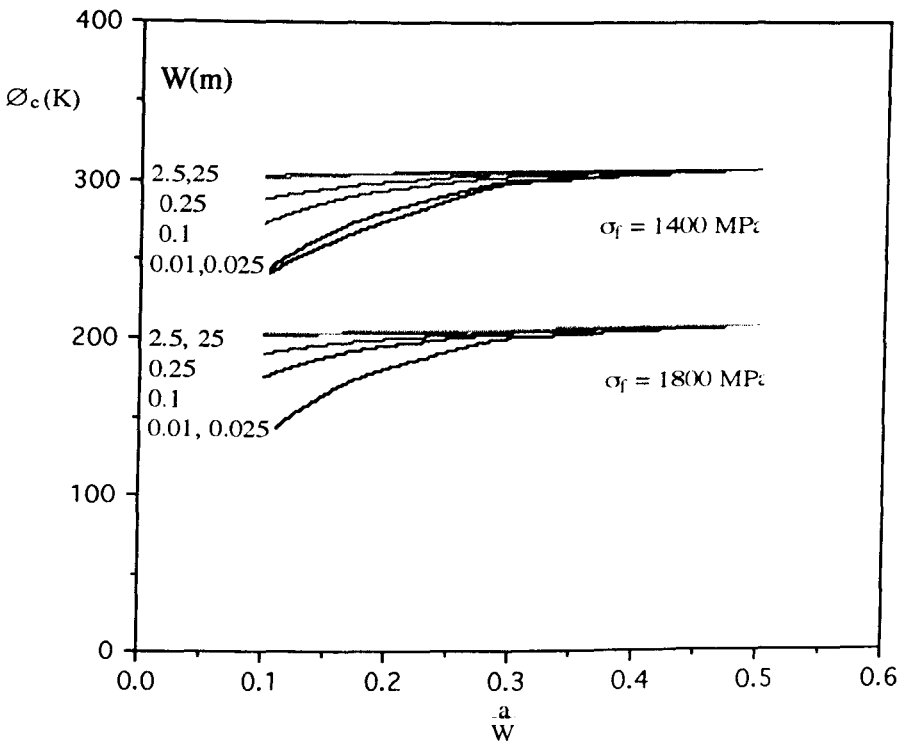

Figure 7.18: The Effect of Size on the Transition Temperature for a Range of Geometries.

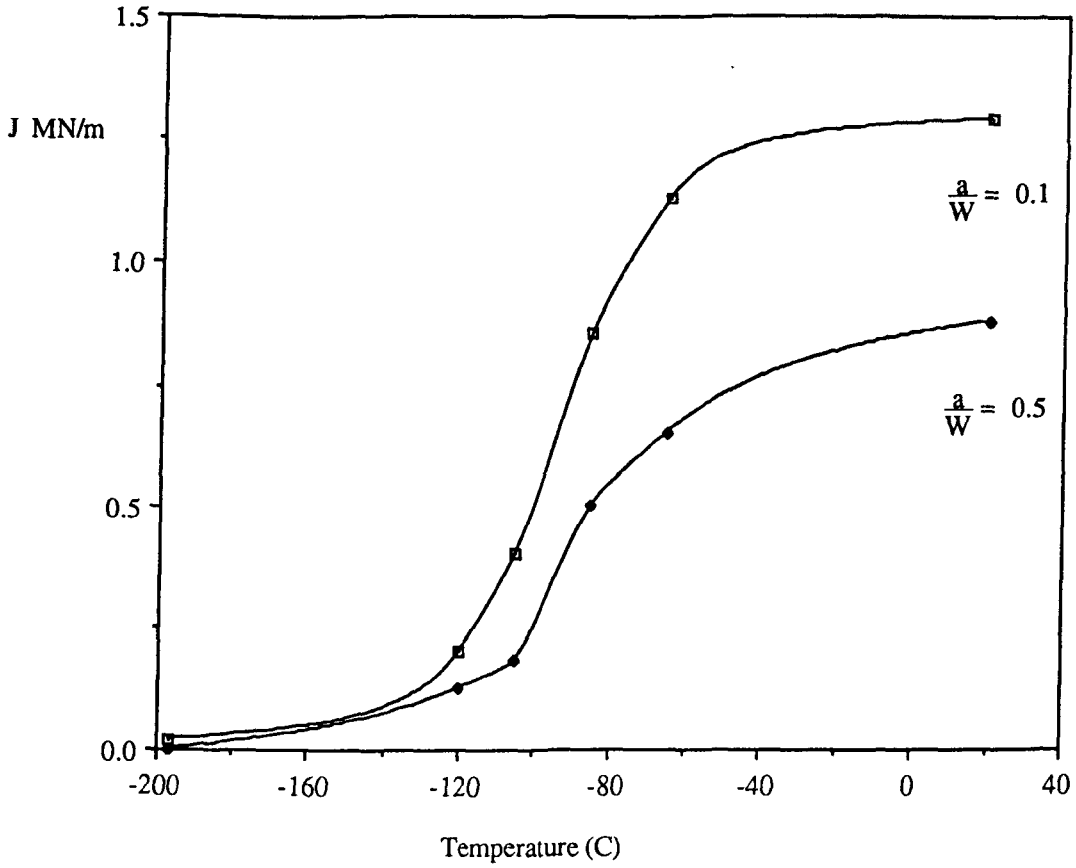

Figure 7.19: Variation of Initiation J as a Function of Temperature, after Al-Ani (1991)

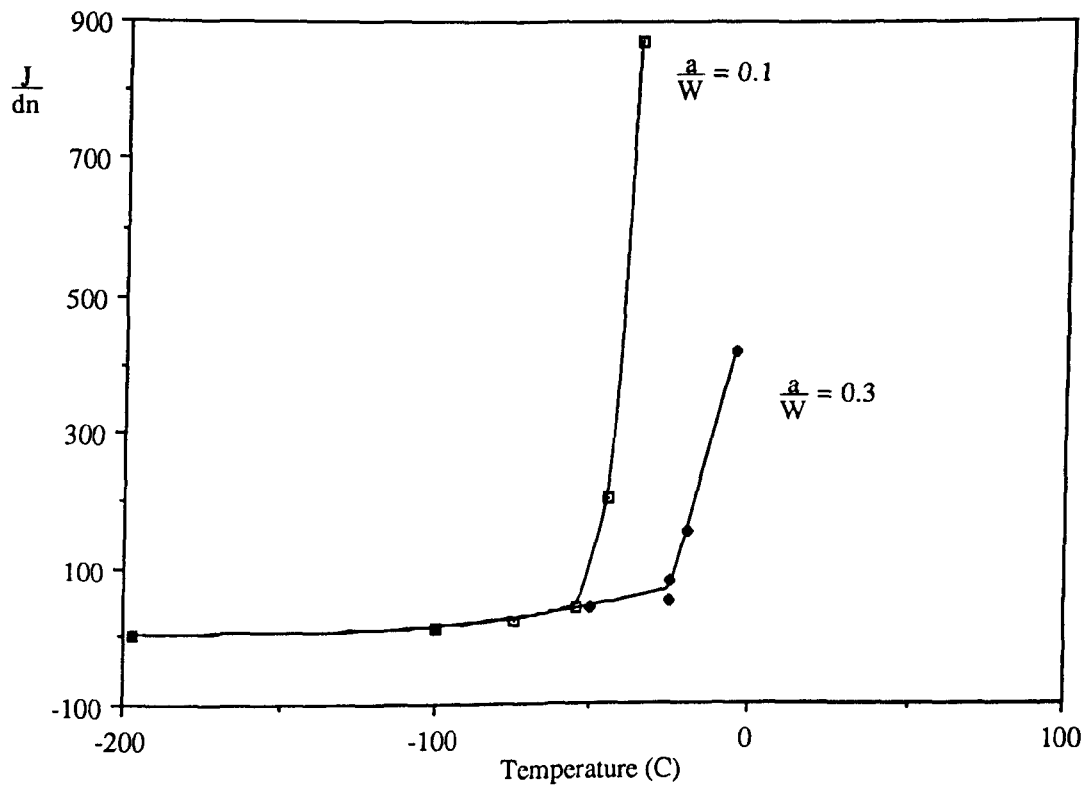

Figure 7.20: Experimental Results for Deep and Shallow cracks after Sumpter (1982)

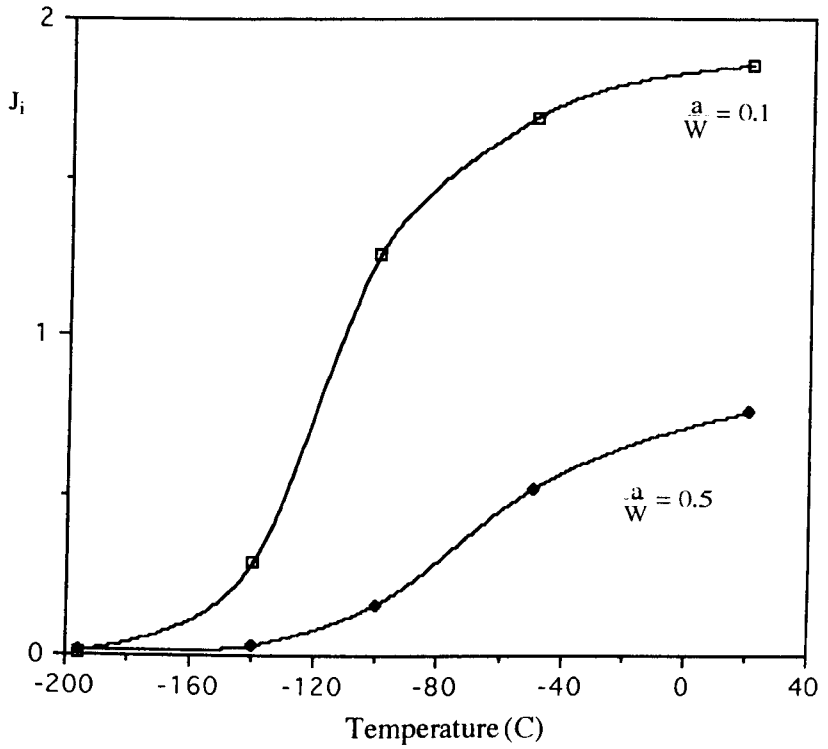

Figure 7.21: Variation of Initiation J as a function of Temperature for BS4360 Grade 50D.

8: Constraint Based Failure Assessment Diagrams.

8.1: Introduction.

Engineering structures invariably contain defects and imperfections which compromise their structural integrity. It is necessary therefore to have a clear design and failure assessment methodology for critical components, especially in petrochemical and nuclear industries. In the first instance structural design is based on an assumption that defects are not present. Plastic collapse is avoided by limiting the nominal stresses to a fraction of the yield or ultimate tensile strength.

Such design methodologies are not intended to take account of defects and inhomogeneities present within structural materials. It is therefore necessary to derive a simple applicable engineering method to ensure structural integrity in the presence of material defects. Fracture mechanics offers a way to relate the relevant loading, material properties and defects which will lead to failure.

Several methodologies have been developed worldwide for determining structural integrity. The two principal methods are the J estimation methodology as provided by EPRI (1981) and the R6, Rev. 3 (1986) approach developed originally by the Central Electricity Generating Board (CEGB). Further methodologies developed either in Europe or America are based on linear elastic fracture mechanic methods. For example, ASME XI is applicable to the collapse of austenitic steel piping whereas in Germany KTA rules are utilised and have many similarities to the ASME validification procedures.

The J estimation approach evaluates elastic-plastic parameters in terms of J for a range of geometries and materials responses. The British approach which has been codified in both R6, Rev. 3 (1986) and PD6493 (1991) has a number of similarities to these procedures. In the linear elastic regime it incorporates both the ASME and KTA approach although modifications made in Revision 3 are based on the J estimation scheme derived by EPRI

(1981).

8.2: R6 Failure Assessment Diagrams.

Within the United Kingdom the major method for ensuring structural integrity is the Failure Assessment Diagram as formulated in R6 (1976) and PD6493 (1991) which defines a failure assessment curve. R6 evolved from research carried out originally by the then CEGB, principally from the 'Two Criteria' approach of Dowling and Townley (1975). R6 was originally introduced in 1976, and has subsequently been revised twice, presently being in its third revision, R6, Rev. 3 (1986). In its simplest form R6 assumes that failure will occur when the applied load reaches the lower of, either a load to cause a LEFM failure or a load capable of causing plastic collapse.

The Failure Assessment Diagram is a graphical representation of a transition between two distinctly separate failure mechanisms, LEFM and plastic collapse. The area enclosed by the axes and the conservatively drawn failure line is termed the safe region. The vertical axis represents the normalised stress intensity factor whereas the horizontal axis represents the normalised limit load. Any combination of geometry and loading that falls outwith this region may lead to failure of the structure. A given load case depends on the yield strength, toughness and the geometry of the structure or component and is represented graphically as a single point on a Failure Assessment Diagram.

In its original form the Failure Assessment Diagram was a simple square box, as illustrated in Figure 8.1. The problem with this form was that all the important structural cases were found to occur in the top right corner of the diagram. This therefore demands a more accurate analysis of the transition from brittle failure to plastic collapse.

Three methods for deriving a Failure Assessment Diagram are offered in Revision 3 of R6 (1986): a general curve, a material specific curve, and a J integral analysis method. The general curve is recommended for materials that do not exhibit a yield discontinuity in the

stress-strain relationship and is the result of applying the EPRI J estimation procedure. The failure locus is described by the relationship;

$$\frac{K_I}{K_{IC}} = \left(1 - 0.14\left(\frac{P}{P_0}\right)^2\right)\left(0.3 + 0.7\exp\left(-0.65\left(\frac{P}{P_0}\right)^6\right)\right) \quad \left(\frac{P}{P_0}\right) \le \left(\frac{P}{P_0}\right)_{max} \qquad (8.1)$$

Where P_0 is the limit load. The code allows a material specific curve to be generated for any metal regardless of its stress-strain relationship or yield discontinuities, through the relation;

$$\frac{K_I}{K_{IC}} = \sqrt{\frac{E\varepsilon_{true}}{\frac{P}{P_0}\sigma_0} + \frac{\left(\frac{P}{P_0}\right)^3\sigma_0}{2E\varepsilon_{true}}} \qquad \left(\frac{P}{P_0}\right) \le \left(\frac{P}{P_0}\right)_{max} \qquad (8.2)$$

Here ε_{true} is the true strain for a stress equal to UTS. this method is felt to offer a more acceptable approximation to the flaw tolerance than the general curve especially for materials operating in the strain hardening regime.

Finally the code allows a Failure Assessment Diagram to be generated through a J-Integral analysis, for a specific material and geometry. This analysis requires that the elastic ($J_{elastic}$) and plastic ($J_{plastic}$) components of J have to be calculated. The abscissa of the Failure Assessment Diagram is therefore now described as;

$$\frac{K_I}{K_{IC}} = \sqrt{\frac{J_{(elastic)_k}}{J_{(T=0)_k}}} \qquad (8.3)$$

Where $J_{(T=0)_k}$ denotes fully constrained deformation identified with the T=0 field. The abscissa is still given by the ratio of the applied to limit load. In practice the material specific and the J-analysis methods are rarely used in the United Kingdom, as the general curve as illustrated in Figure 8.2 is widely believed to give satisfactory results for materials in common use. All three forms of curve are truncated at an abscissa value $\left(\frac{P}{P_0}\right)_{max}$;

$$\left(\frac{P}{P_0}\right)_{max} = \left[\frac{\sigma_0 + \bar{\sigma}}{2\sigma_0}\right] \qquad (8.4)$$

Here σ_0 is the yield stress and $\bar{\sigma}$ is the ultimate tensile strength, this cut off occurs at 1.64 for a strain hardening exponent of 6 and 1.19 for 13. In the Failure Assessment Diagrams the load to limit load ratio is termed L_r and the cut-off is defined L_r^{max} to maintain consistency with R6 Rev. 3, where the normalised stress intensity factor is termed K_r.

The nature of present Failure Assessment Diagrams and defect schemes can be considered to be inherently pessimistic, thereby ensuring structural integrity. However the pressure to minimise 'downtime' by avoiding unnecessary repairs is increasing. Unneccesary levels of conservatism must therefore be avoided in the assessment of defects.

The purpose of fracture mechanics is to determine the 'fitness for purpose' of structures and components which contain defects. Current international approaches attempt to ensure the integrity of structures through the measure of a single parameter, such as J. A lower bound fracture toughness is obtained from deeply cracked bend specimens, which develop a high degree of constraint and when applied to structural defects ensure a conservative approach . Although this approach is 'safe' it is ultra conservative when applied to cracks which develop unconstrained flow fields, such as short edge cracks in bending or tension and centre cracked panels. Therefore this conservative approach penalises unconstrained flow fields.

The current defect assessment methods also deny a fundamental objective of fracture mechanics, that data should be transferrable from one geometry to another. This is now addressed by the concept of constraint matching which has been discussed by Sumpter and Hancock (1991) in the context of J-T, but is a philosophy which can also be advanced in terms of J-Q.

The motive of the present work is to incorporate the effect of constraint on the Failure Assessment Diagrams and allow the advantage of constraint enhanced toughness effects. This has been achieved for a wide range of size scales and for geometries including centre-

cracked plates in tension (CCP) and single edge cracked bars in three point bending (SEC3PB) for a number of strain hardening exponents. A methodology has been derived that allows constraint dependent and also modified Failure Assessment Diagrams to be derived, this methodology is then compared with available experimental results.

8.3: Classical Failure Assessment Diagrams.

Failure Assessment Diagrams can be derived by making use of the J estimation scheme of Kumar, German and Shih (1981). The crack driving force J is taken for the purpose of these series of results to be the sum of the elastic and plastic components;

$$J_{(total)} = J_{(elastic)} + J_{(plastic)} \qquad (8.5)$$

In the present analysis these parameters are determined on the basis of the original crack length rather than the effective crack length as proposed by Irwin (1951) and described in (3.41). Analyses were carried out for the SEC3PB and CCP geometries as shown in Figures 8.3 and 8.4. The elastic component of the crack driving force has been expressed by Kumar, German and Shih (1981) as a function of the applied load such that;

$$\frac{J_{(elastic)}}{\sigma_0 \varepsilon_0 c h_1\left(\frac{a}{W}, n=1\right)} = \left(\frac{P}{P_r}\right)^2 \qquad (8.6)$$

Here P is the applied load, P_r is a suitably defined reference load, σ_0 is the yield stress, c is the remaining ligament, ε_0 is a reference strain usually taken to be $\frac{\sigma_0}{E}$ and $h_1\left(\frac{a}{W}, n=1\right)$ is a strain hardening and geometry dependent variable. Kumar, German and Shih (1981) define the reference load (P_r) for a SEC3PB as;

$$P_r = \frac{1.456\, Bc^2\sigma_0}{s} \qquad (8.7)$$

Here s is the span of the specimen. In contrast the limit load of an edge cracked bar has been given by Millar (1966) as;

$$P_0 = m\frac{BW^2\sigma_0}{s} \qquad (8.8)$$

Where m is a geometric parameter defined as;

$$m = 1 - 0.33\frac{a}{W} - 6\left(\frac{a}{W}\right)^2 + 15.5\left(\frac{a}{W}\right)^3 - 19.8\left(\frac{a}{W}\right)^4 \qquad \frac{a}{W} \le 0.295$$

$$m = 1.26\left(1 - \frac{a}{W}\right)^2 \qquad \frac{a}{W} \ge 0.295 \qquad (8.9)$$

In the case of three point bending the reference and limit load differ as illustrated in Figure 8.5. In the case of the CCP the limit load (P_0) and the reference load (P_r) are one and the same;

$$P_0 = P_r = \frac{4Bc\sigma_0}{\sqrt{3}} \qquad (8.10)$$

The plastic component of J can be expressed in the following form;

$$\frac{J_{(plastic)}}{\alpha\sigma_0\varepsilon_0 ch_1\left(\frac{a}{W}, n\right)} = \left(\frac{P}{P_r}\right)^{n+1} \qquad (8.11)$$

Here α is a material constant which features in the Ramberg-Osgood stress-strain relation (3.15). This has a similar functional form as the solution for the elastic portion of the crack driving force. The full solution for SEC3PB is then expressed as the sum of the elastic and plastic components as follows;

$$J_{(total)} = \sigma_0\varepsilon_0 ch_1\left(\frac{a}{W}, n=1\right)\left(\frac{P}{P_r}\right)^2 + \alpha\sigma_0\varepsilon_0 ch_1\left(\frac{a}{W}, n\right)\left(\frac{P}{P_r}\right)^{n+1} \qquad (8.12)$$

In this functional form the geometric size scale is introduced by using the remaining ligament (c) as the relevant dimension. However for the CCP geometry the size scale is introduced in terms of half the crack length (a);

$$J_{(total)} = \sigma_0 \varepsilon_0 a h_1\left(\frac{a}{W}, n=1\right)\left(\frac{P}{P_r}\right)^2 + \alpha\sigma_0\varepsilon_0 a h_1\left(\frac{a}{W}, n\right)\left(\frac{P}{P_r}\right)^{n+1} \qquad (8.13)$$

In these expressions $h_1\left(\frac{a}{W}, n\right)$ is a tabulated function of geometry and strain hardening exponent (n) given by Kumar, German and Shih (1981) and illustrated in Figure 8.6. From such expressions J can be calculated for any relevant geometry and material for a given applied load.

8.4: Constraint Based Failure Assessment Diagrams.

EPRI and R6 are single parameter fracture mechanics approaches and constraint independent failure based on a critical value of J. It is proposed to introduce the effect of constraint into this failure methodology and thereby expand the applicability of R6. For this series of analyses to determine the effect of constraint on the Failure Assessment Diagrams, idealised J-T failure loci have been described by a relation of the form;

$$\frac{J_{(T)_c}}{J_{(T=0)_c}} = \left[\frac{1}{\exp\left(\frac{T}{\sigma_0}\right)}\right]^m \qquad \left(\frac{T}{\sigma_0} < 0\right)$$

$$\frac{J_{(T)_c}}{J_{(T=0)_c}} = 1 \qquad \left(\frac{T}{\sigma_0} \geq 0\right) \qquad (8.14)$$

A constraint independent failure locus (m=0) was used to show the inherent geometry dependence of failure as illustrated in Figure 8.7. As the load is incremented J increases as is

described in the form of a J-T history as shown in Figure 8.8, where this history intercepts the failure locus defines a failure condition which can be represented as a single point on a Failure Assessment Diagram. Therefore by carrying out a number of these analyses over different size scales it is possible to construct a Failure Assessment Diagram.

To construct the R6 Failure Assessment Diagram the stress intensity factor was determined from the applied load using the relevant K calibration given by Murakami (1987) and Rooke and Cartwright (1976);

$$K_I = \sigma\sqrt{\pi a}\left(1 - 0.025\left(\frac{2a}{W}\right)^2 + 0.06\left(\frac{2a}{W}\right)^4\right)\sqrt{SEC\left(\frac{2a}{W}\frac{\pi}{2}\right)} \qquad \boxed{\text{CCP}\ \begin{matrix}\text{Remote}\\ \text{Tension}\end{matrix}}$$

(8.15)

$$K_I = \frac{6M\sqrt{\pi a}}{2}\left(1.11 - 1.55\left(\frac{a}{W}\right) + 7.71\left(\frac{a}{W}\right)^2 - 13.5\left(\frac{a}{W}\right)^3 + 14.2\left(\frac{a}{W}\right)^4\right) \qquad \boxed{\text{SEC 3PB}}$$

The elastic component of J, $J_{elastic}$ was related to K for plane strain conditions by;

$$J_{(elastic)} = \frac{K^2(1-\nu^2)}{E} \qquad (8.16)$$

The vertical axis of the R6 Failure Assessment Diagram is taken to be;

$$\frac{K_I}{K_{IC}} = \sqrt{\frac{J_{(elastic)_e}}{J_{(T=0)_e}}} = K_r \qquad (8.17)$$

Where $J_{(T=0)_e}$ is used to define geometry independent failure in highly constrained J dominated loading conditions characterised by non-negative values of T, in the Failure Assessment Diagrams K_r is again used to maintain consistency with R6 Revision 3 (1986). This leads to a geometry dependent Failure Assessment Diagram. It is possible to carry out a normalisation taking account of the associated degree of constraint at the intersection J-T history with the locus. Instead of normalising by the small scale yielding solution the normalisation is carried out by the associated value of J, dependent upon the crack tip constraint. This is achieved by matching the constraint of the structure or component under

test to the appropriate value within a J-T locus ($J_{(T)_c}$);

$$\sqrt{\frac{J_{(elastic)_c}}{J_{(T)_c}}} \qquad (8.18)$$

The unifying constraint dependent failure of the modified failure assessment approach can be seen when considering the original decomposition of J, (8.5) rearranging gives;

$$\sqrt{\frac{J_{(elastic)_c}}{J_{(T)_c}}} = \sqrt{1 - \frac{J_{(plastic)_c}}{J_{(T)_c}}} \qquad (8.19)$$

For any specific geometry this can be further expressed in terms of the applied loads and a relevant dimension;

$$\sqrt{\frac{J_{(elastic)_c}}{J_{(T)_c}}} = \sqrt{1 - \frac{\alpha\sigma_0\varepsilon_0 c h_1\left(\frac{a}{W}, n\right)\left(\frac{P}{P_r}\right)^{n+1}}{\sigma_0\varepsilon_0 c h_1\left(\frac{a}{W}, n=1\right)\left(\frac{P}{P_r}\right)^2 + \alpha\sigma_0\varepsilon_0 c h_1\left(\frac{a}{W}, n\right)\left(\frac{P}{P_r}\right)^{n+1}}} \qquad (8.20)$$

Which can be reduced to;

$$\sqrt{\frac{J_{(elastic)_c}}{J_{(T)_c}}} = \sqrt{1 - \frac{h_1\left(\frac{a}{W}, n\right)\left(\frac{P}{P_r}\right)^{n+1}}{\frac{1}{\alpha}h_1\left(\frac{a}{W}, n=1\right)\left(\frac{P}{P_r}\right)^2 + h_1\left(\frac{a}{W}, n\right)\left(\frac{P}{P_r}\right)^{n+1}}} \qquad (8.21)$$

This can be further reduced and the Failure Assessment Diagram given by option three in Revision 3 of R6 is thus independent of $\frac{J}{\sigma_0\varepsilon_0 c}$;

$$\sqrt{\frac{J_{(elastic)_c}}{J_{(T)_c}}} = \sqrt{1 - \frac{1}{\frac{1}{\alpha}\frac{h_1\left(\frac{a}{W}, n=1\right)}{h_1\left(\frac{a}{W}, n\right)}\left(\frac{P}{P_r}\right)^{1-n} + 1}} \qquad (8.22)$$

Where the ratio $\sqrt{\frac{J_{(elastic)_c}}{J_{(T)_c}}} = K_r^{modified}$ based on the previous notation defined by R6 Rev. 3. Therefore following Ainsworth (1984) it is clear that the strain hardening and the inherent geometry dependence depends on the ratio:

$$\frac{\alpha\, h_1\left(\frac{a}{W}, n\right)}{h_1\left(\frac{a}{W}, n=1\right)} \qquad (8.23)$$

This dependence is illustrated in Figures 8.9-8.12 with the abscissa being represented in relation to load ratio in respect to the limit load. These figures illustrate the inherent geometry dependence for two geometries (SEC3PB, CCP) and strain hardening rates (6, 13). It is therefore possible to derive an upper and lower failure curve due to geometry and thereby set up an envelope of operation in which the structure results have to be defined in both cases of normalisation. In the analyses of Kumar, German and Shih (1981) and the above figures α is set to unity.

Although the geometry and hardening rate sensitivity can be minimised by a suitable choice of reference load, rather than the limit load, this loses part of the appeal of Failure Assessment Diagrams. The general failure assessment line lies below the material specific load for loads less than L_r^{max} for the cases considered and indeed the general curve proposed is deliberately intended to be pessimistic. However this is not a universal result and combinations of factors in 8.23 can lead to the material specific curve lying below the general curve. This point has been raised by Ainsworth (1992). The point which is being emphasised here, is that in the Failure Assessment Diagram there is an inherent geometry and hardening sensitivity which is not connected in anyway with constraint effects. This arises from the terms in 8.23 even when failure occurs at a critical value of J or COD and the material is constraint insensitive. This issue will reoccur in considering the experimental data in relation to the first option in R6 Rev.3, and is a cogent argument for the lower bound toughness data.

8.5: Analytical Results.

A series of classical and modified R6 Failure Assessment Diagrams have been generated for materials which exhibit constraint dependent failure as described by failure loci given by 8.14. Specific calculations were performed for SEC3PB with crack length to width ratios $\left(\frac{a}{W}\right)$ of 0.1, 0.2 and 0.3. The ratios were chosen to exhibit a wide range of constraint from very negative to slightly positive T-stresses, for $\frac{a}{W} > 0.3$ toughness values are taken to be identical and constraint independent consistent with the experimental evidence of Betegón and Hancock (1991).

The stress-strain relationship is described by the Ramberg-Osgood equation where the material constant α has been set to unity. The first series of results shown in Figures 8.13-8.14 are for the constraint independent locus (m=0), showing both classic and modified Failure Assessment Diagrams for strain hardening exponents, 6 and 13. In this and the following idealised cases the abscissa is the applied load normalised by the limit load as defined by Millar (1966). The strain hardening dependence is illustrated for a shallow crack SEC3PB in Figure 8.15.

Figures 8.16-8.19 show the effect of constraint on the classic form of Failure Assessment Diagram. These results are also mirrored in the remaining loci (m=2 and 3) with the effect of constraint becoming more pronounced as the slope of the respective locus becomes more severe as illustrated in Figures 8.20-8.27, with Figures 8.24-8.27 showing the most constraint dependent failure loci (m=3). As the slope of the locus becomes more severe geometries with high negative T stresses can be seen to reach higher normalised values of K at the corresponding intersection points with the failure locus.

8.6: Experimental Validification.

This failure methodology is then applied to the experimental results of Sumpter and Forbes (1992), Sumpter (1993), Betegón and Hancock (1991), Hancock, Reuter and Parks (1991) and MacLennan. These experimental results are tabulated in Figures 8.28-8.33 where the steels are plain carbon manganese with varying hardening rates (n), given in the experimental tables. Failure modes for the majority of these experiments are cleavage instability, although Hancock, Reuter and Parks (1991) experiments are ductile in nature with the structural limitation relating to crack growth of two hundred microns being employed. The chemical composition and material properties are given in Figures 8.34-8.36 with the chemical composition of BS 4360 Grade 50D being given previously in Chapter 7. Experimental results in the form of Failure Assessment Diagrams are presented in the form of the abscissa being applied load normalised by the appropriate limit load. The failure loci (J-T) for these materials are illustrated in Figures 8.37-8.38.

The data from these series of experiments are presented in the form of classic and modified Failure Assessment Diagrams for each series of test results. Figures 8.39-8.42 show the results for Sumpter and Forbes (1992) for both the SEC3PB and CCP results. The mild steel plate SEC3PB data of Sumpter and Forbes (1992) end data points from the shallow cracks fall around the cut-off point as specified by R6, Revision 3. While the experimental results are clearly shown to be above the universal failure curve. With the material specific curves following the same form as the universal failure curve. In the modified diagram the majority of these results collapse onto a single line. This is compared with a lower material specific curve corresponding to a SEC3PB $\left(\frac{a}{W} = 0.875\right)$ and the upper line being SEC3PB $\left(\frac{a}{W} = 0.125\right)$. These forms of results are again mirrored in the plate data for CCP after Sumpter and Forbes (1992) with the upper line of the modified envelope corresponding to CCP $\left(\frac{2a}{W} = 0.125\right)$. Within the classic diagram the CCP exhibits higher toughness levels than the corresponding SEC3PB results.

Figures 8.43-8.44 shows the weld plate results of Sumpter (1993) clearly showing a

high constraint effect in the classic diagram and the expected collapsed effect in the modified Failure Assessment Diagram. In the modified SEC3PB diagram the experimental results are compared with material specific results corresponding to a SEC3PB $\left(\frac{a}{W} = 0.875\right)$ and the upper line being SEC3PB $\left(\frac{a}{W} = 0.125\right)$.

Betegón (1991) results are illustrated in Figures 8.45 and 8.46 and exhibit clearly well defined behaviour in both the classic and modified Failure Assessment Diagrams where the envelope lines are again defined as SEC3PB $\left(\frac{a}{W} = 0.125\right)$ and SEC3PB $\left(\frac{a}{W} = 0.875\right)$.

Where the very low temperature results of Maclennan are shown in Figures 8.47 and 8.48 which again in both cases exhibit the previously defined behaviour. In the modified Failure Assessment Diagram the envelope is defined for SEC3PB $\left(\frac{a}{W} = 0.1\right)$ and SEC3PB $\left(\frac{a}{W} = 0.5\right)$. The experiments of Hancock, Reuter and Parks (1991) are shown in Figure 8.49 and 8.50 with the modified envelope defined as SEC3PB $\left(\frac{a}{W} = 0.1\right)$ and SEC3PB $\left(\frac{a}{W} = 0.3\right)$.

8.7: Discussion.

The loss of crack tip constraint results in an increased resistance to both cleavage and ductile tearing. There are therefore major structural advantages to be gained by utilising the enhanced toughness of low constraint configurations in plane strain.

The universal failure curve as offered by R6 Rev. 3 general curve has been shown to be ultra-conservative in the case of constraint dependent failures as illustrated for example in Figure 8.22. Proposed in this chapter is a form of normalisation that allows the degree of crack tip constraint to be incorporated into the integrity analysis by matching the constraint dependent toughness. This allows a form of modified Failure Assessment Diagram to be generated which relates a particular structure to a specific failure curve or if necessary a family of curve, as exemplified in the modified Failure Assessment Diagrams given for available experimental data.

In the approach proposed, an inherent geometry dependence has been found for the analyses considered which prevents a single failure curve being defined. This inherent

geometry effect has been considered by Ainsworth (1984) who believes that by matching the reference load parameters it is possible to eliminate this geometry dependence. Combined classic and modified Failure Assessment Diagrams are shown grouped in Figures 8.51-8.52 for all hardening rates. Within the modified Failure Assessment Diagrams it is possible to find a trend for the SEC3PB specimens of similar hardening rates even though they have significantly dissimilar material parameters.

The general failure assessment curve in most cases is found to lie below those of the material specific curves although this is not a universal rule and a combinations of factors in (8.13) can lead to the material specific curve falling below that of the general curve. This point has also been raised by Ainsworth (1992) therefore in the Failure Assessment Diagram there is an inherent geometry and hardening sensitivity which is not connected in anyway with constraint effects.

The simplicity of this constraint (T) based structural engineering approach is underlined by the fact that no plasticity analyses have to be undertaken to complete a structural integrity case. There is however controversy over the limitation of J-T theory in this description. there can be little doubt that the T stress approach correctly identifies the plane strain geometries which lose constraint and it does so beyond the strict confines of LEFM. Karstensen, Nekkal and Hancock (1994) argue that T effectively quantifies constraint for edge cracked bars up to the cut off at L_r^{max}. Further, the deviations from the J-T description at higher load levels are such that the loss of constraint is underestimated. This results in a conservative description of the toughness enhancement, and argues strongly for the relevance of the J-T approach in the context of surface flaws. In the case of centre cracked panels the J-T description breaks down close to limit load but is still conservative for a/W ratios greater than 0.3 in uniaxial tension at all loads.

No matter how constraint matching is achieved, Figures 8.13-8.27 show that there are major structural advantages to be gained by utilising the enhanced toughness of low constraint plane configurations in plane strain below the cut off at L_r^{max}. However the enhanced toughness results in points on a FAD which depend both on the geometry and the

constraint sensitivity of the material. This is a major difficulty, which can be resolved by using a modified Failure Assessment Diagram in which the toughness used to normalise the applied stress intensity factor K_r is the constraint matched value. This procedure recovers the original FAD curves using simply modified axes.

The proposed defect assessment procedure is to construct a failure locus in which the toughness is quantified by measuring the toughness of shallow and deeply cracked bend bars as a function of T. This is used to match the constraint of the defect in the structure with an appropriate toughness by determining T for the structure. The Failure Assessment Diagram is then plotted using the constraint matched toughness instead of K_{IC}. Theses development of constraint modified Failure Assessment Diagrams development have been supported by the analysis of a large number of plane strain toughness experiments.

In a real engineering structure it is desirable to use a lower bound failure locus to quantify the material behaviour due to effect of scatter associated with any experimental or structural results. The results of such an application to the experimental material data is given in Figures 8.53-8.54.

8.8: Conclusion.

A practical engineering approach to determine structural integrity has been presented. This methodology accounts for significant constraint effects associated with shallow crack geometries, allowing enhanced material toughnesses to be taken into account. It is therefore possible to provide in the form of a modified failure diagram a structural integrity assessment which has resolved the constraint and geometry sensitivity of previous methodologies.

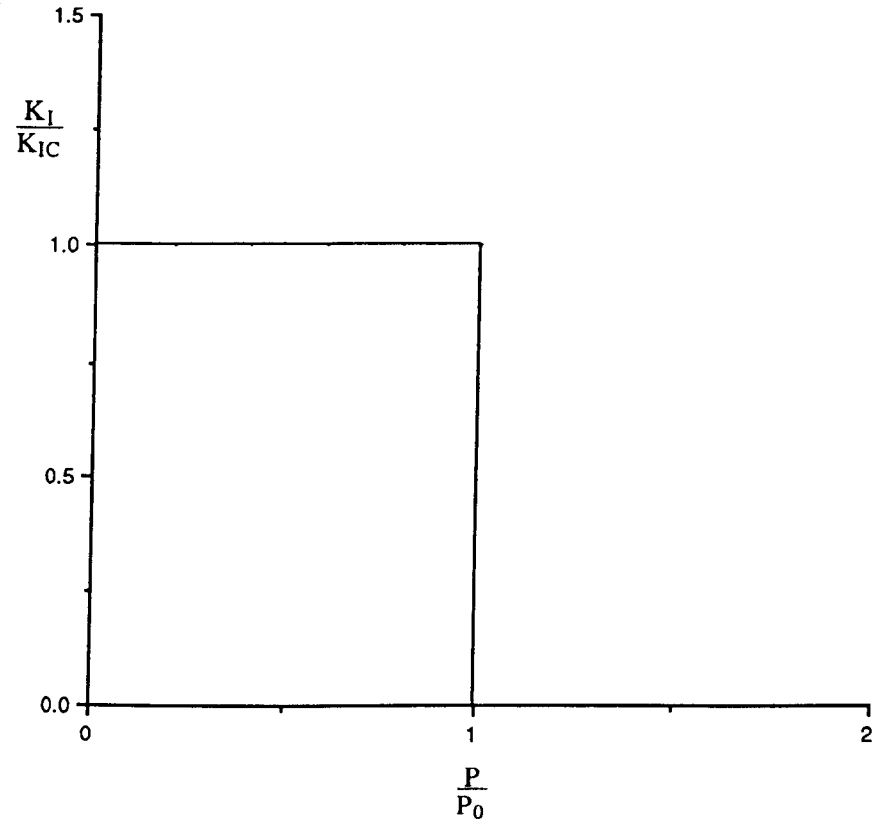

Figure 8.1: Original and Simplest Form of a Failure Assessment Diagram.

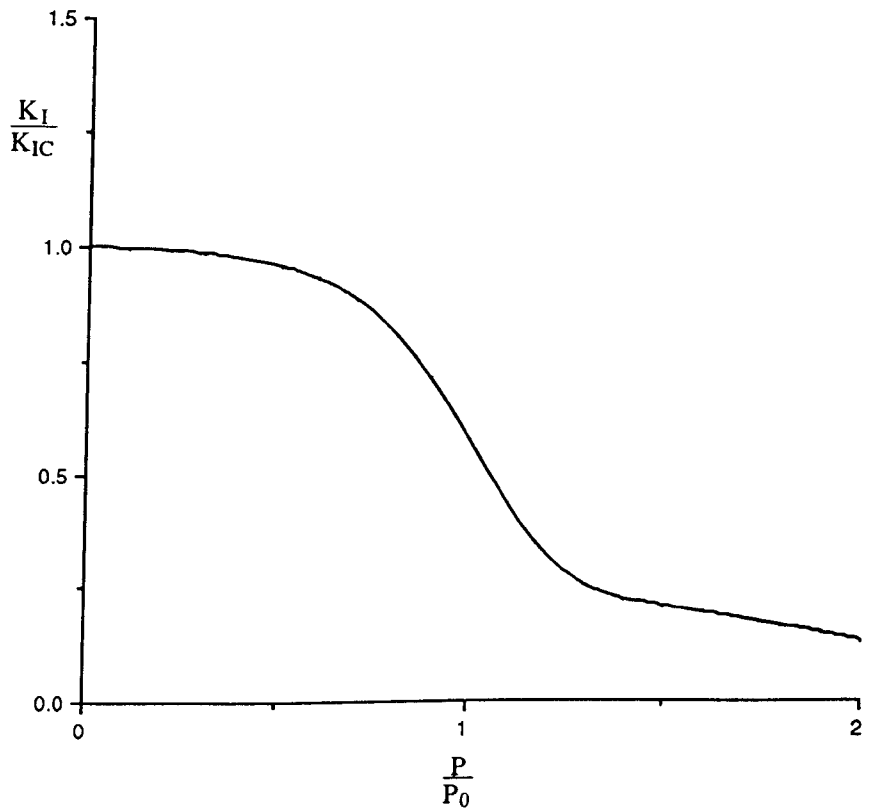

Figure 8.2: The General Failure Line as given by R6 Revision 3.

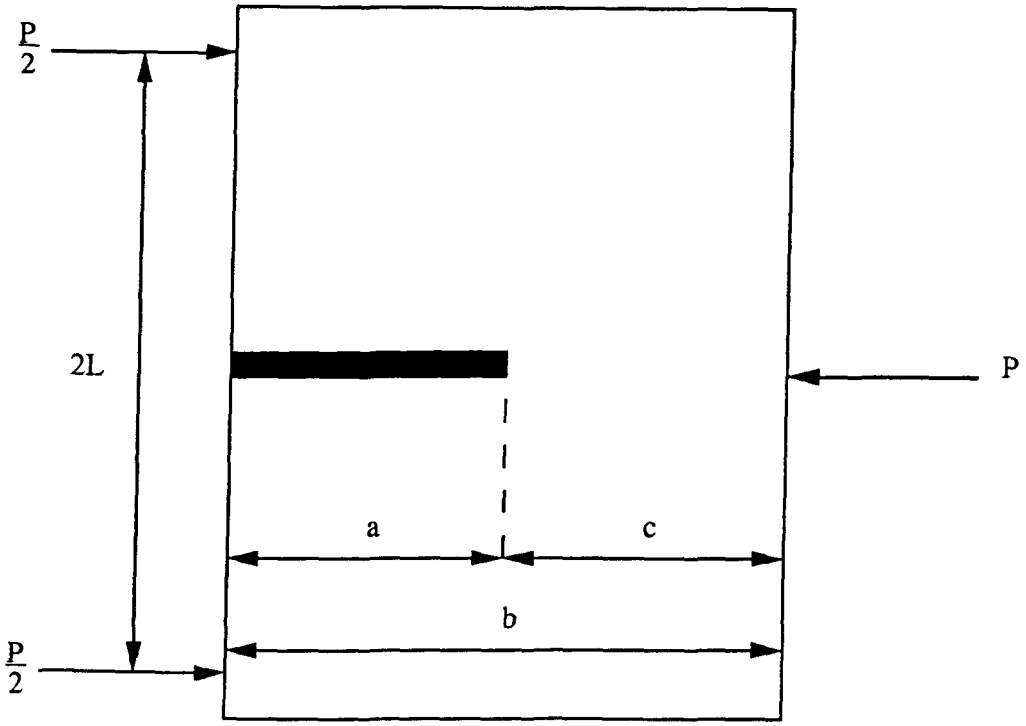

Figure 8.3: Single Edge Cracked Bar under ThreePoint Bending (SEC3PB).

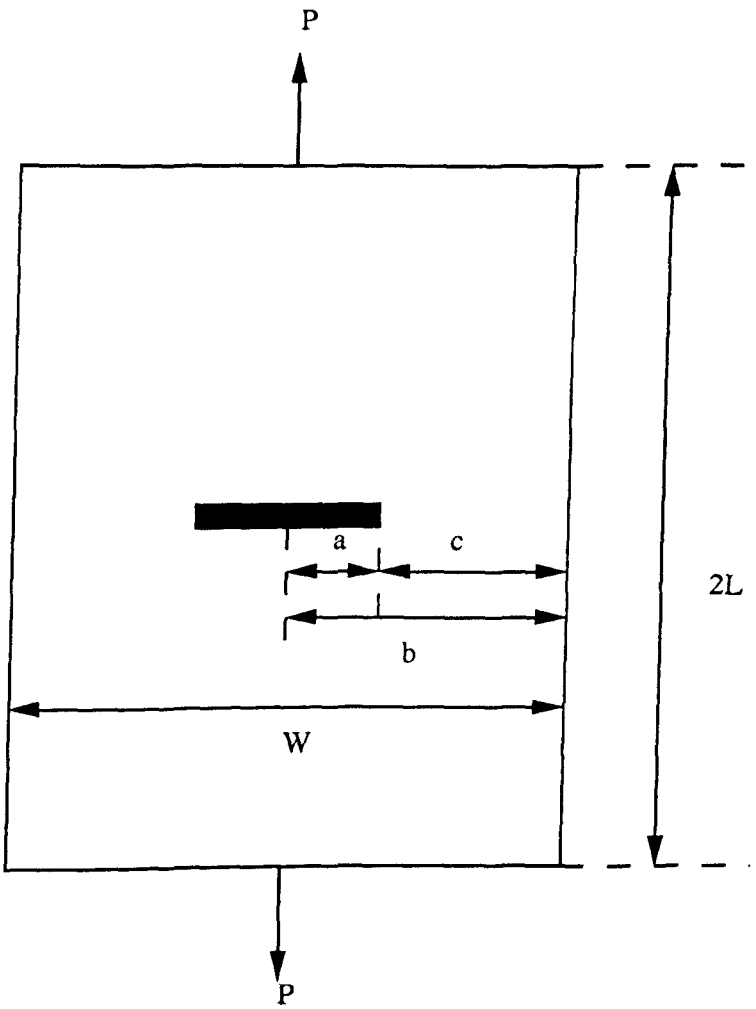

Figure 8.4: Centre Cracked Plate under Remote Tension (CCP).

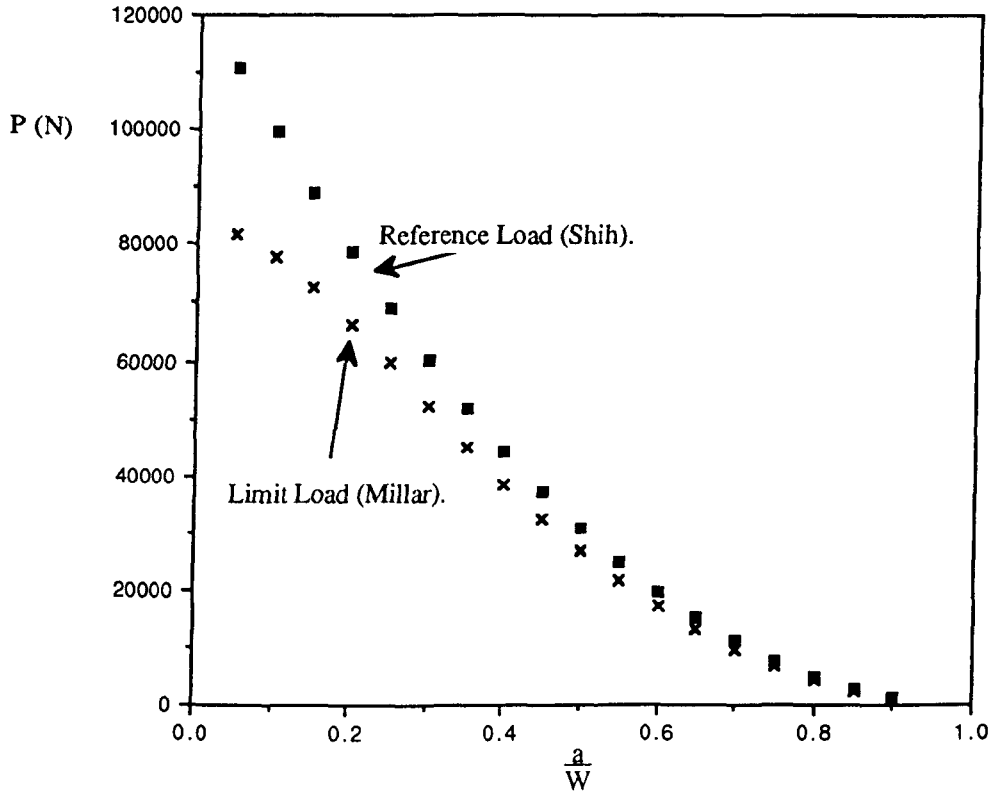

Figure 8.5:Reference and Limit Loads as Derived by Shih and Millar.

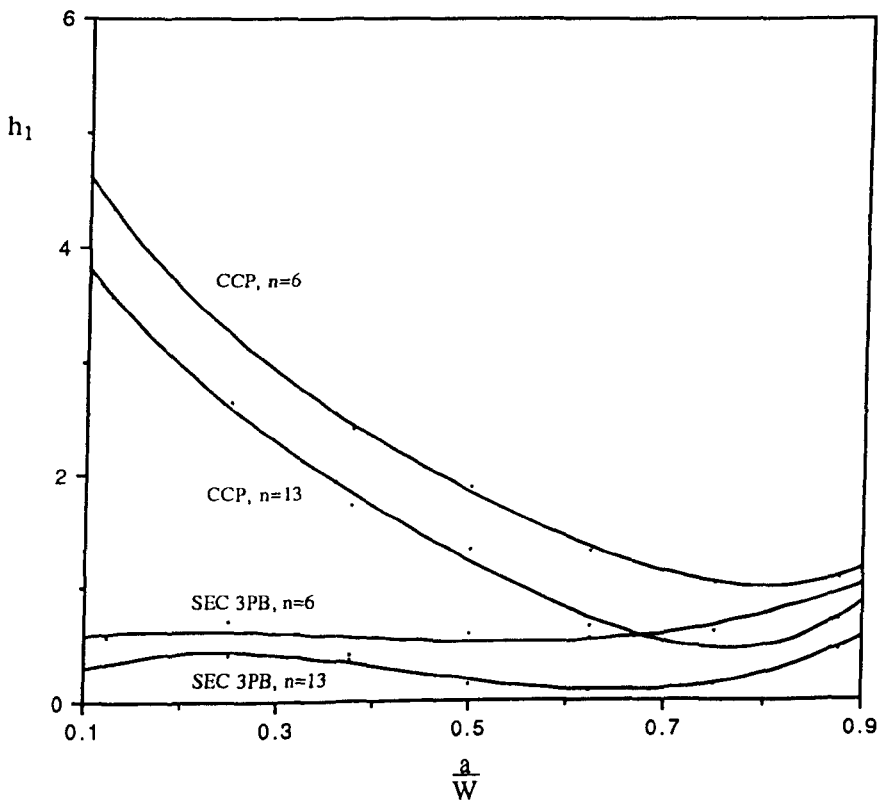

Figure 8.6: h_1 factors for CCP and SEC3PB.

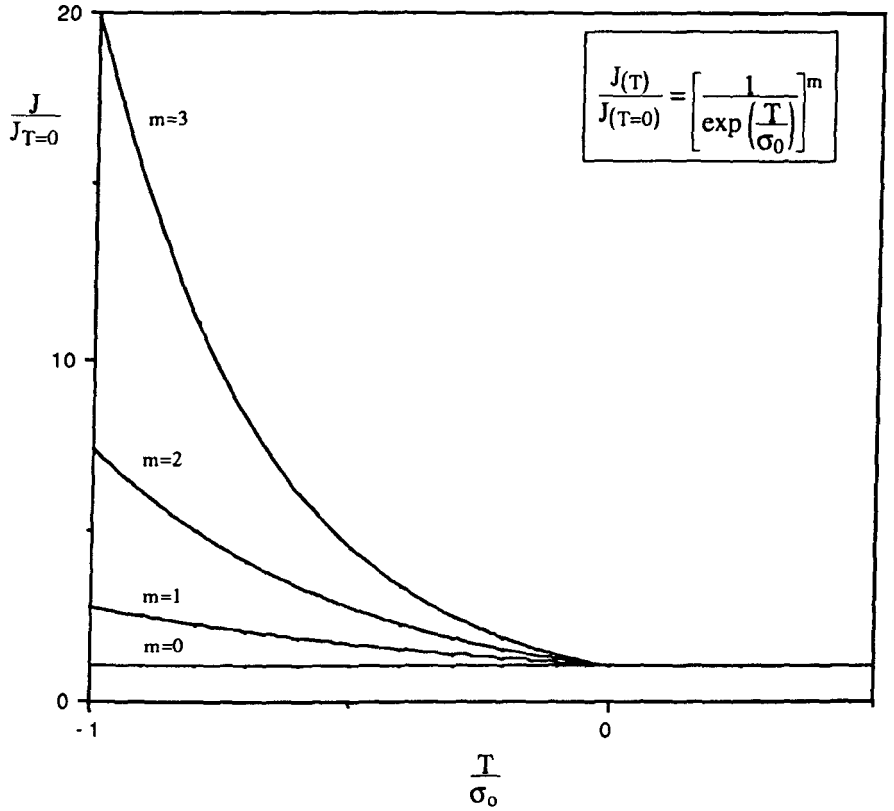

Figure 8.7: Idealised Failure Loci.

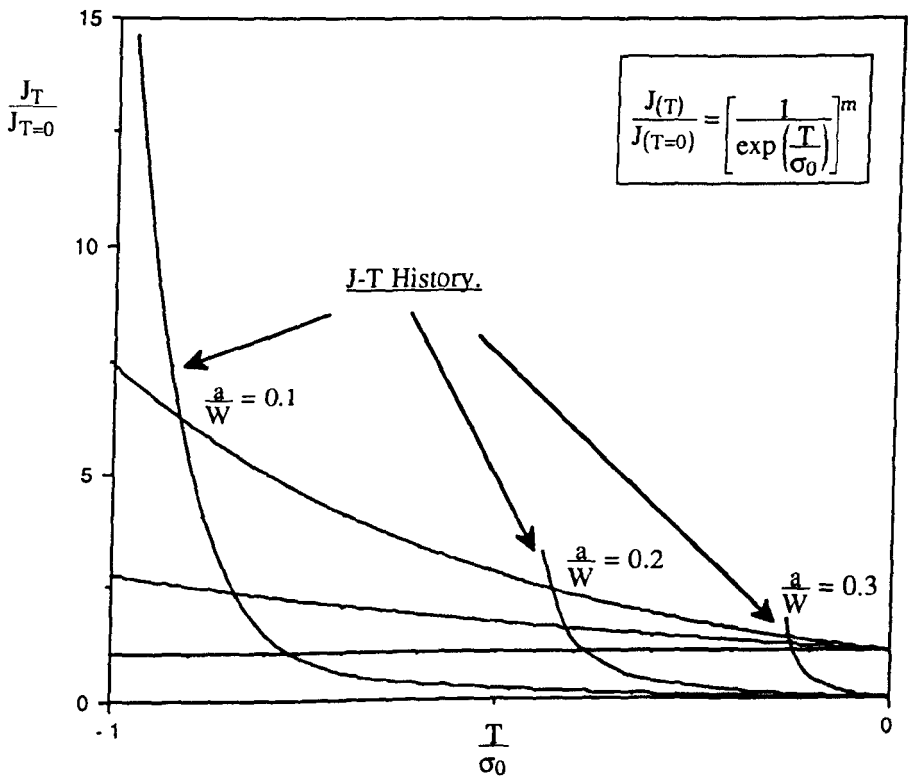

Figure 8.8: J-T History, showing the Intersection Point for Loci, described by m=0, 1, 2, n=13.

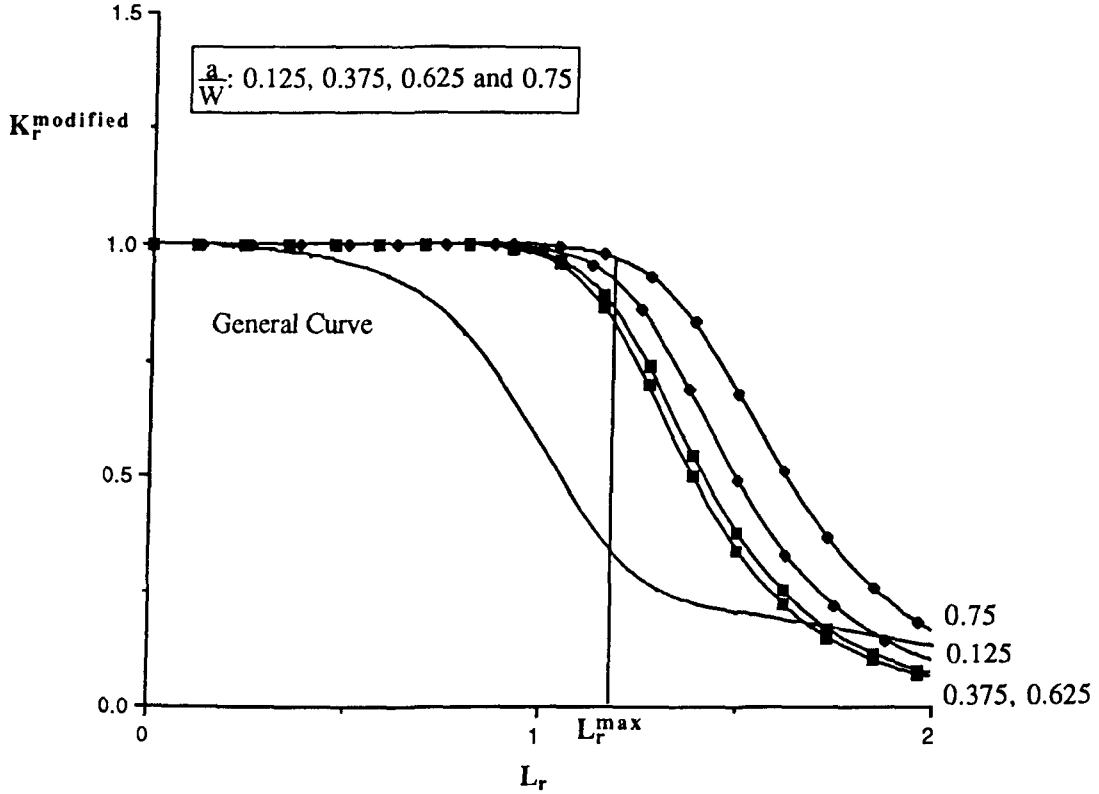

Figure 8.9: Geometry Specific Failure Assessment Diagram, SEC3PB, n=13.

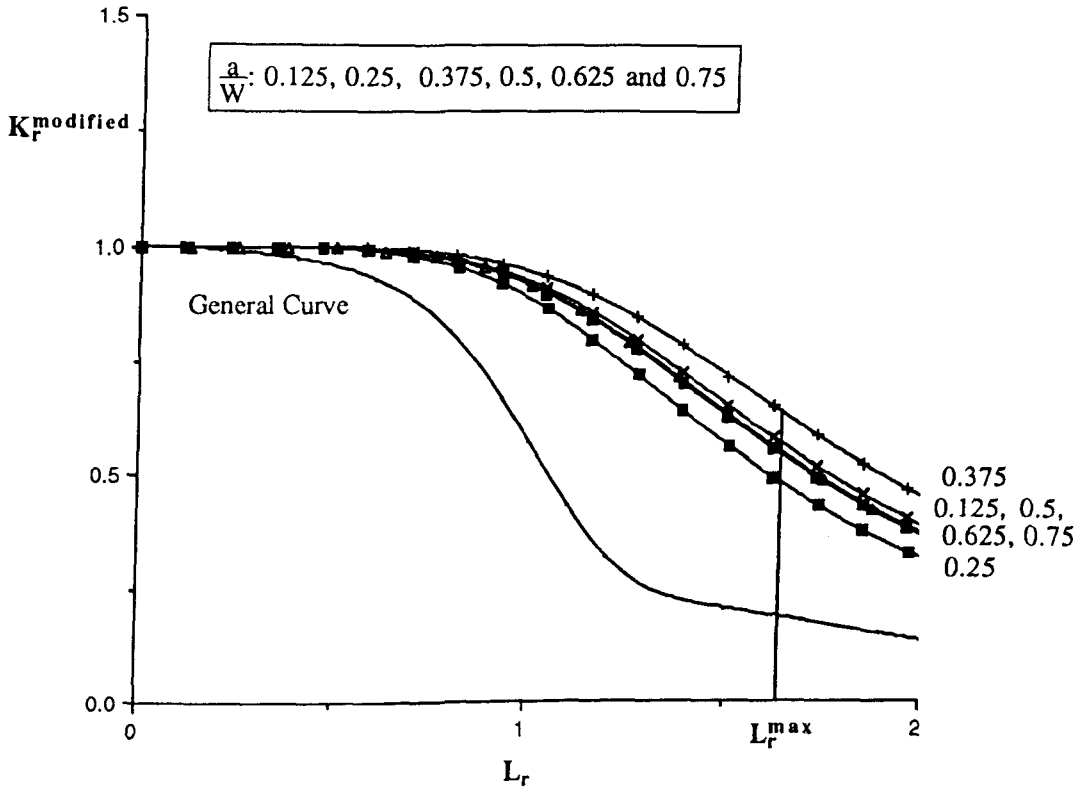

Figure 8.10: Geometry Specific Failure Assessment Diagram, SEC3PB, n=6.

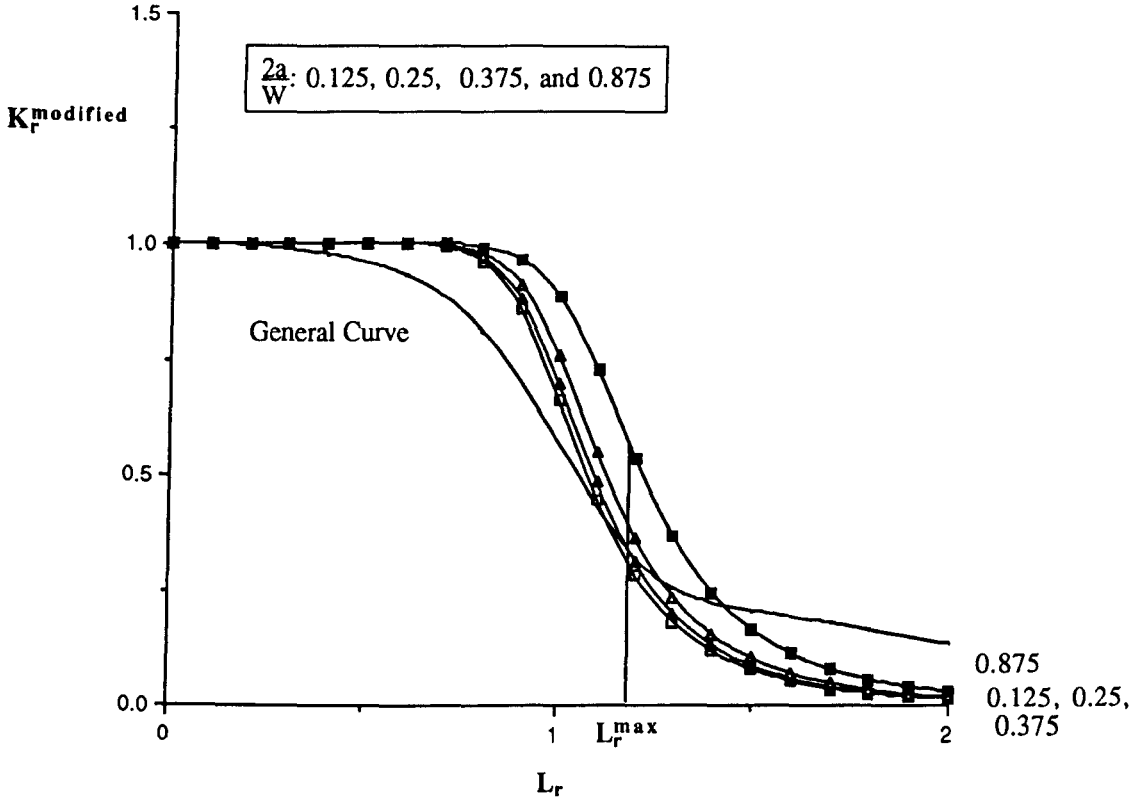

Figure 8.11: Geometry Specific Failure Assessment Diagram, CCP, n=13.

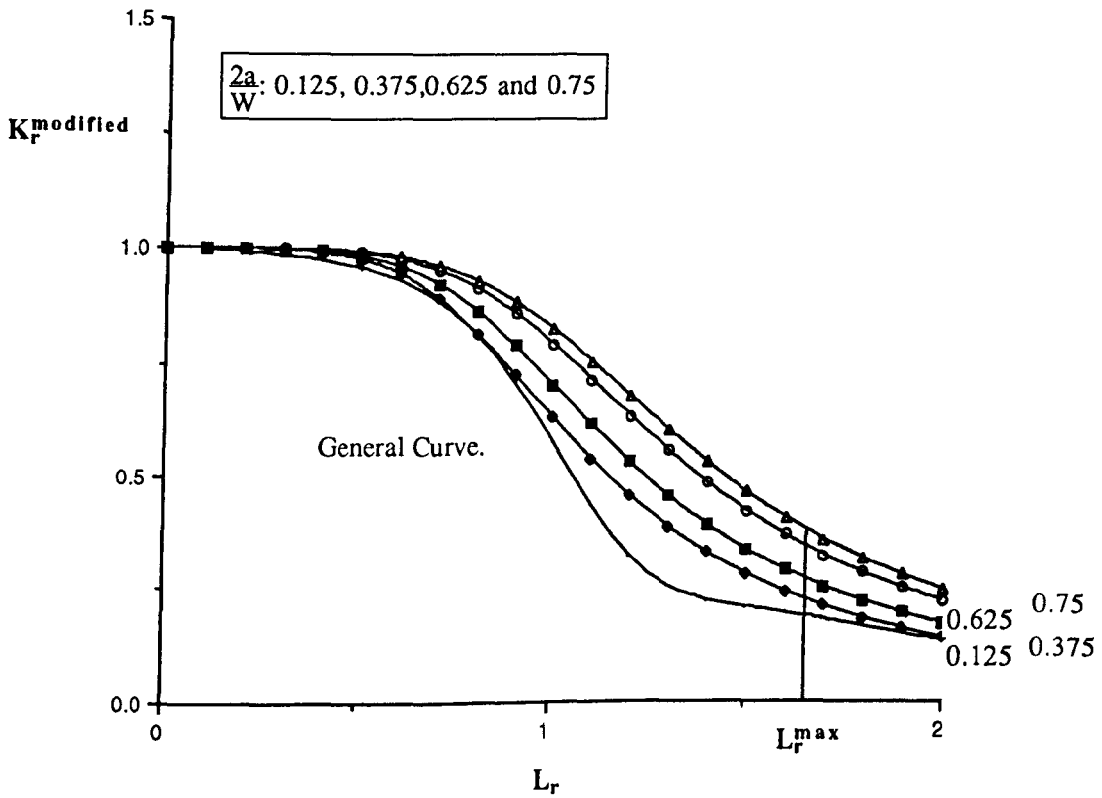

Figure 8.12: Geometry Specific Failure Assessment Diagram, CCP, n=6.

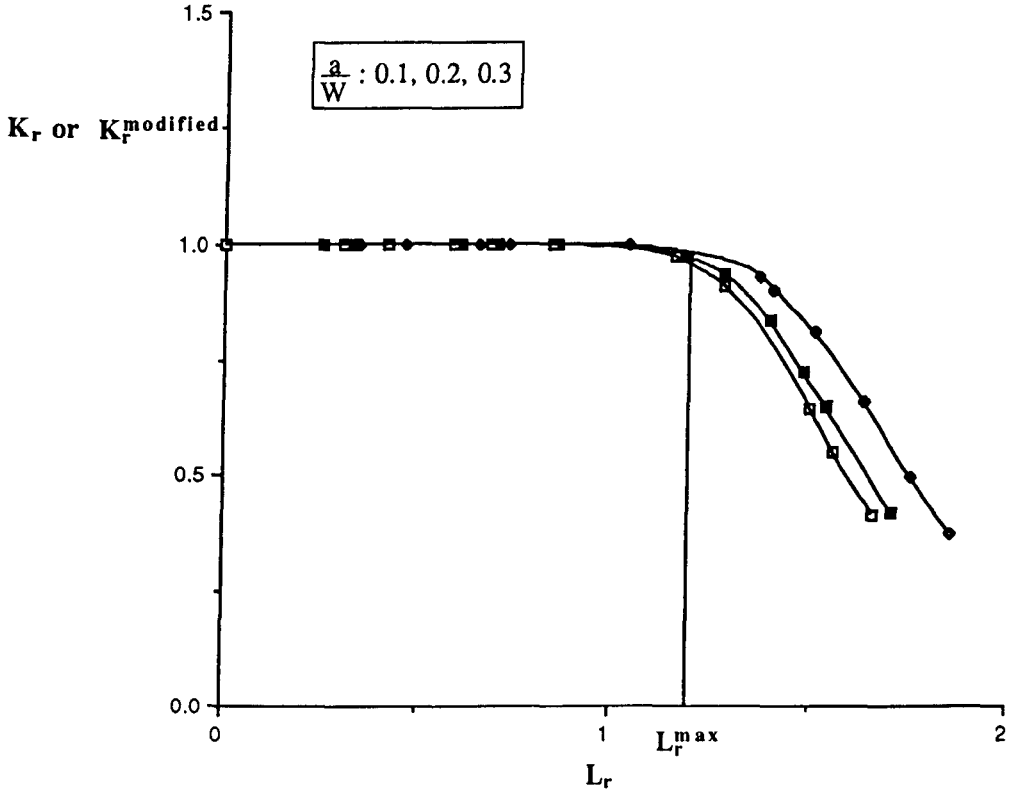

Figure 8.13: Failure Assessment Diagram, SEC3PB, n=13, m=0.

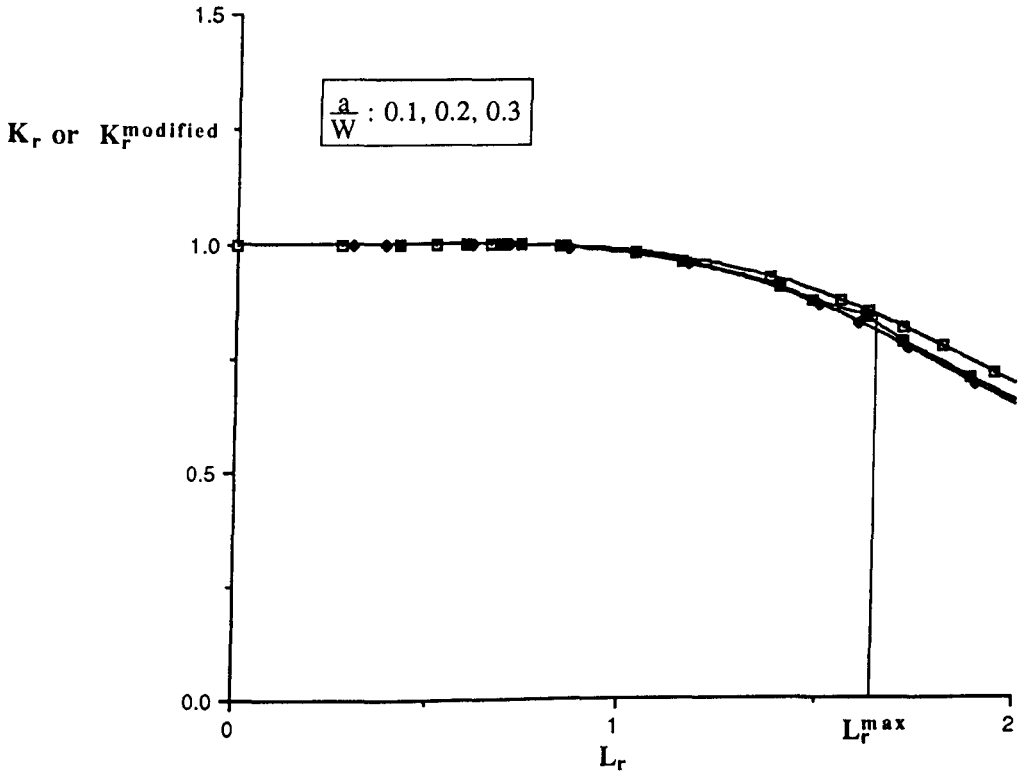

Figure 8.14: Failure Assessment Diagram, SEC3PB, n=6, m=0.

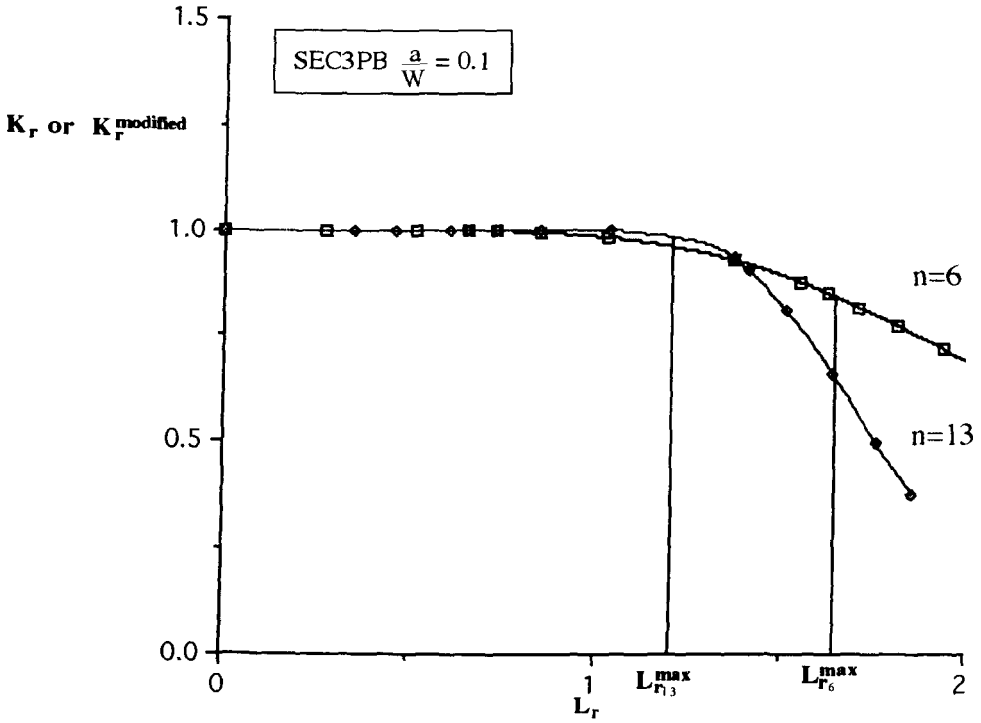

Figure 8.15: Effect of Strain Hardening Rate (m=0).

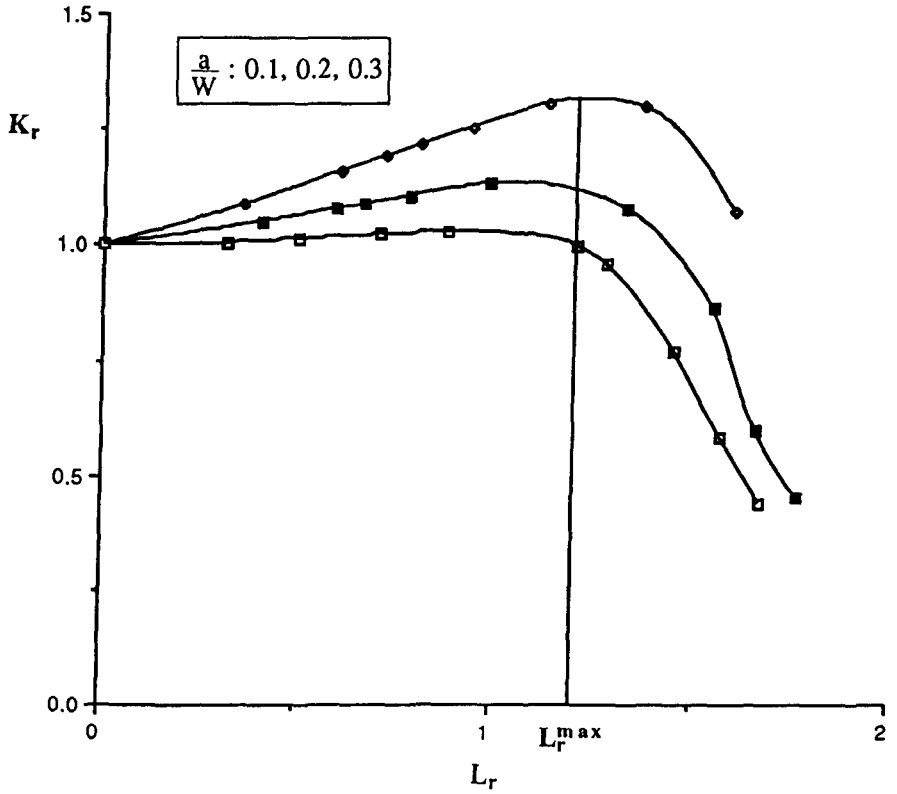

Figure 8.16: Failure Assessment Diagram, SEC3PB, n=13, m=1.

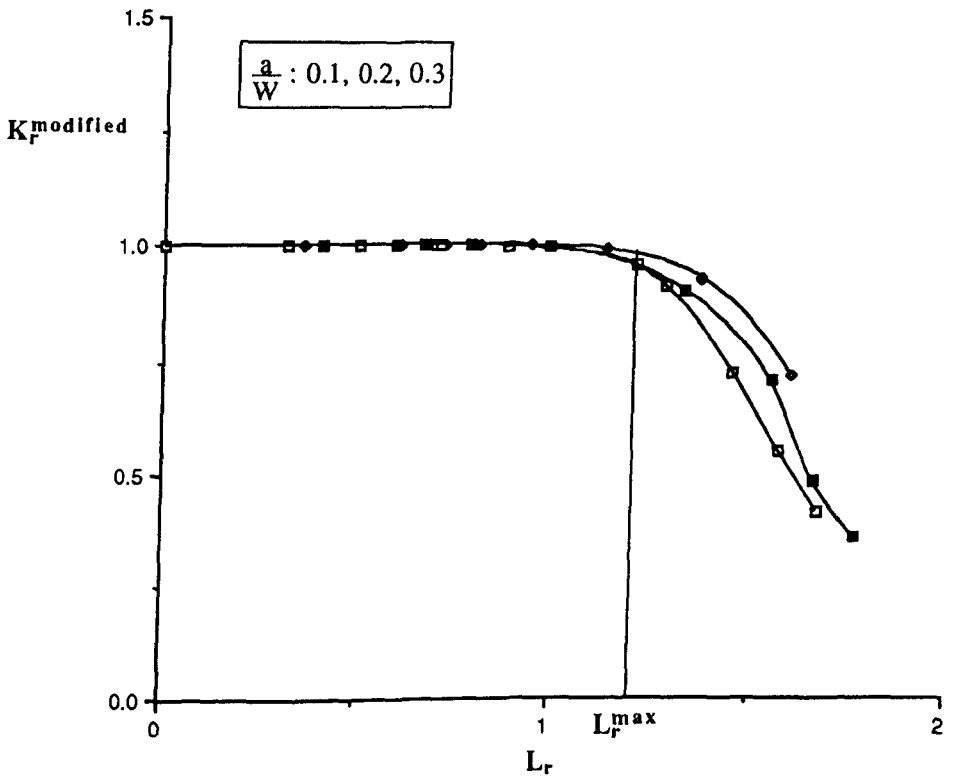

Figure 8.17: Modified Failure Assessment Diagram, SEC3PB, n=13, m=1.

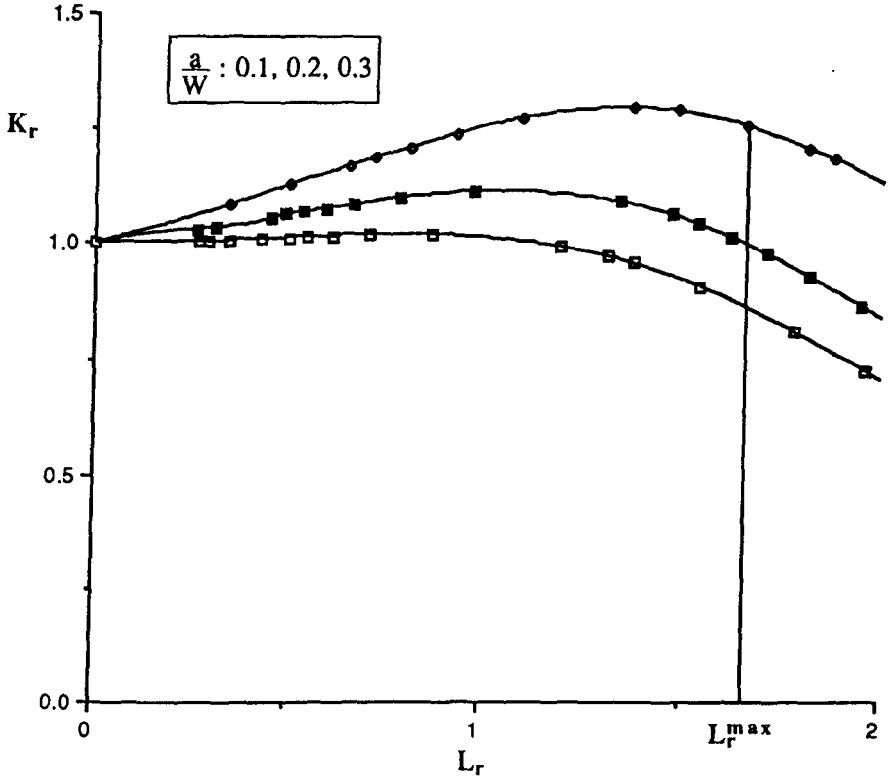

Figure 8.18: Failure Assessment Diagram, SEC3PB, n=6, m=1.

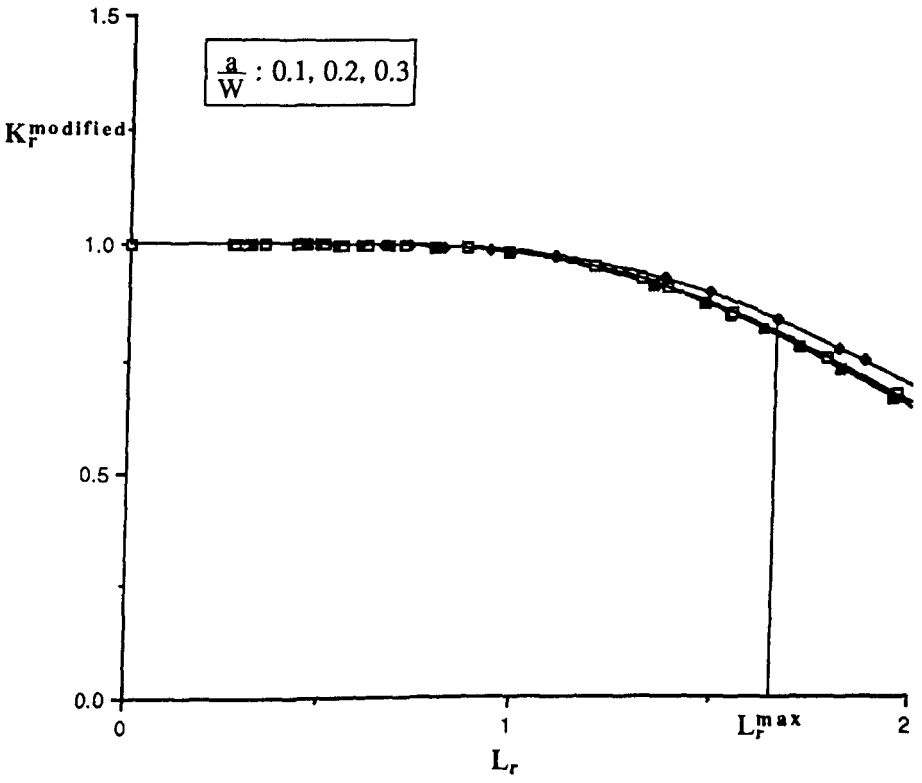

Figure 8.19: Modified Failure Assessment Diagram, SEC3PB, n=6, m=1.

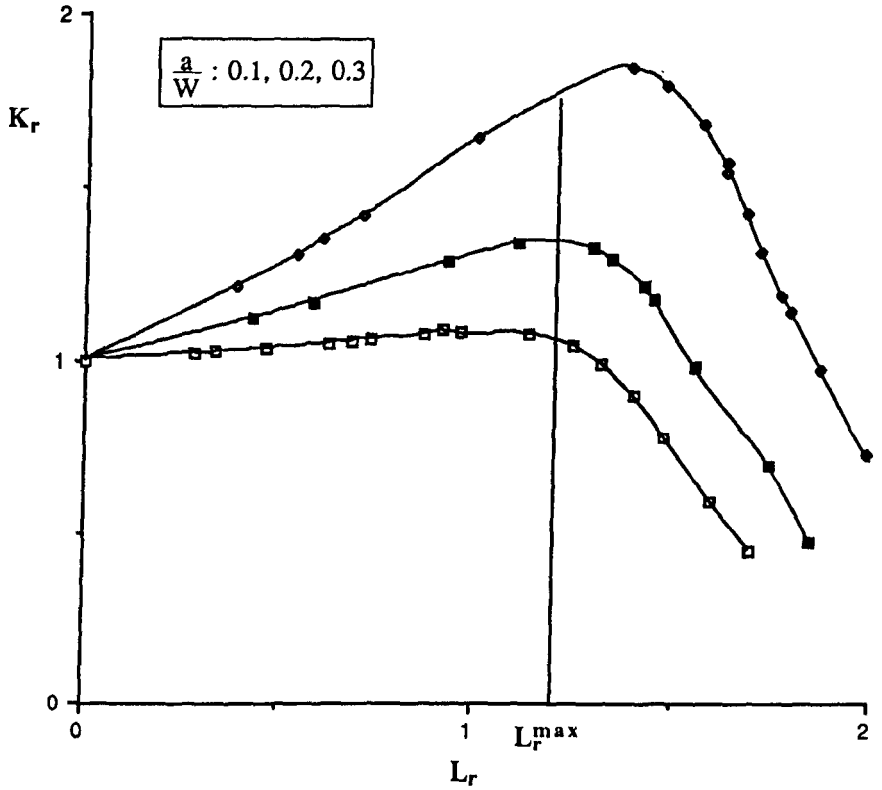

Figure 8.20: Failure Assessment Diagram, SEC3PB, n=13, m=2.

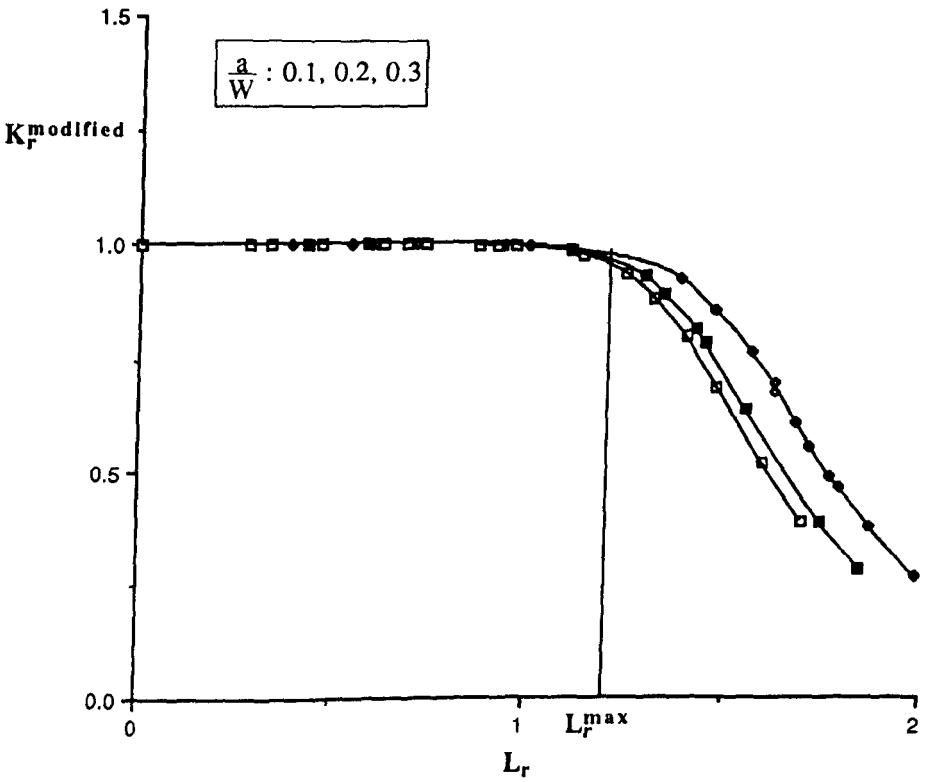

Figure 8.21: Modified Failure Assessment Diagram, SEC3PB, n=13, m=2.

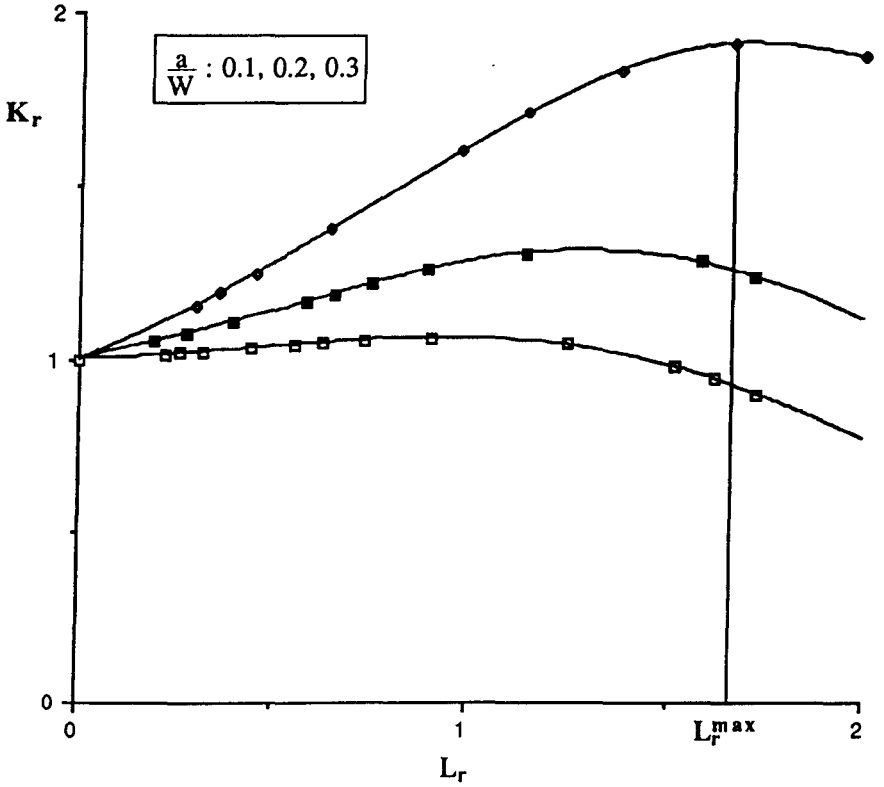

Figure 8.22: Failure Assessment Diagram, SEC3PB, n=6, m=2.

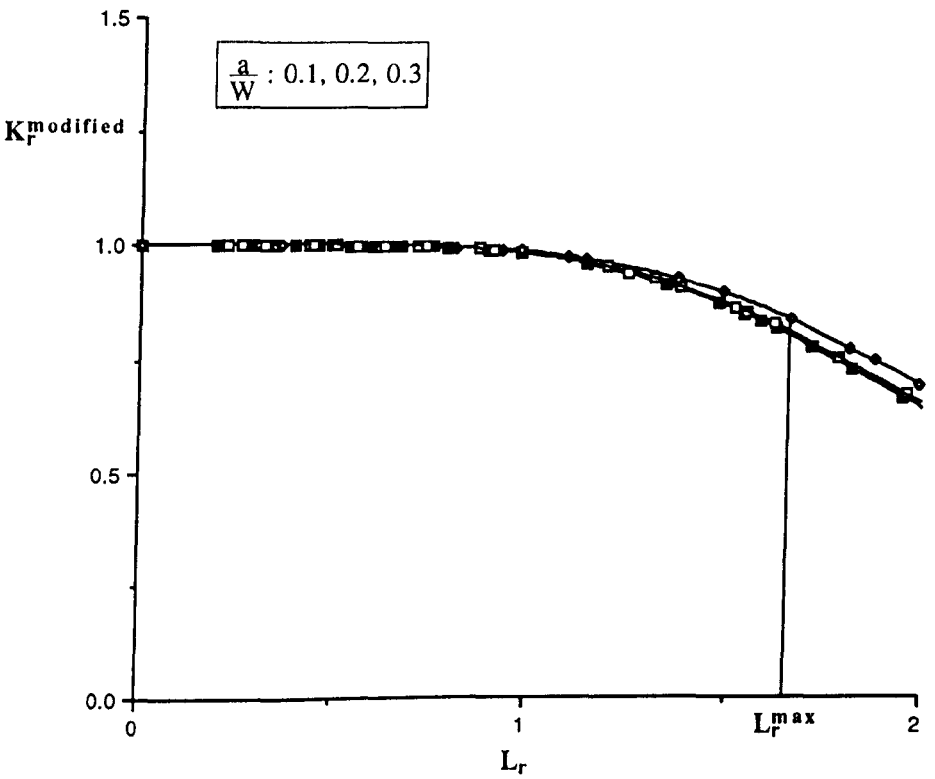

Figure 8.23: Modified Failure Assessment Diagram, SEC3PB, n=6, m=2.

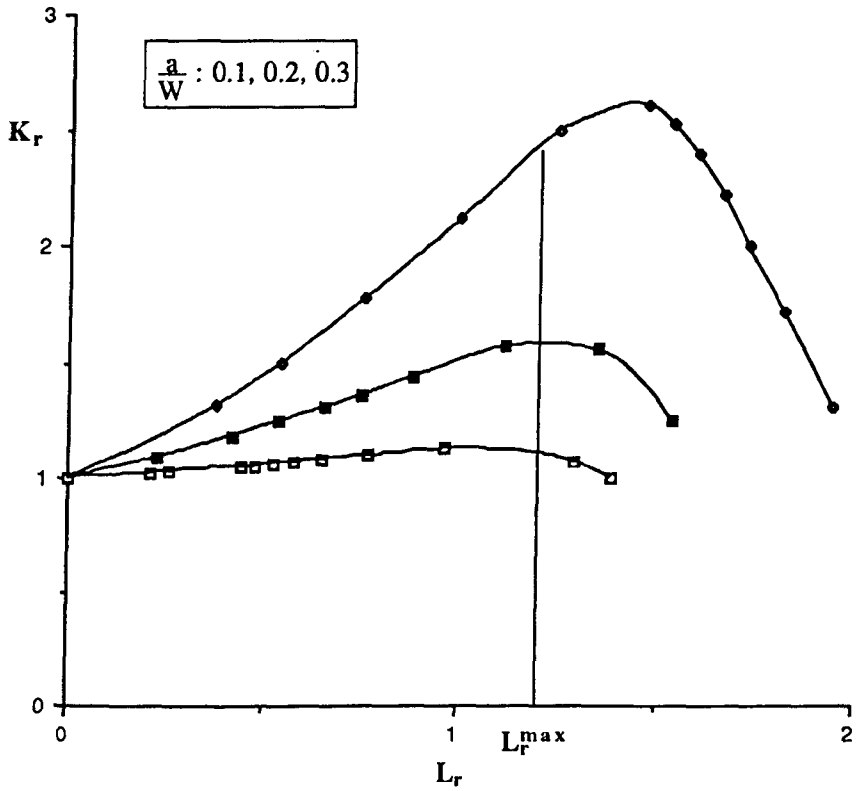

Figure 8.24: Failure Assessment Diagram, SEC3PB, n=13, m=3.

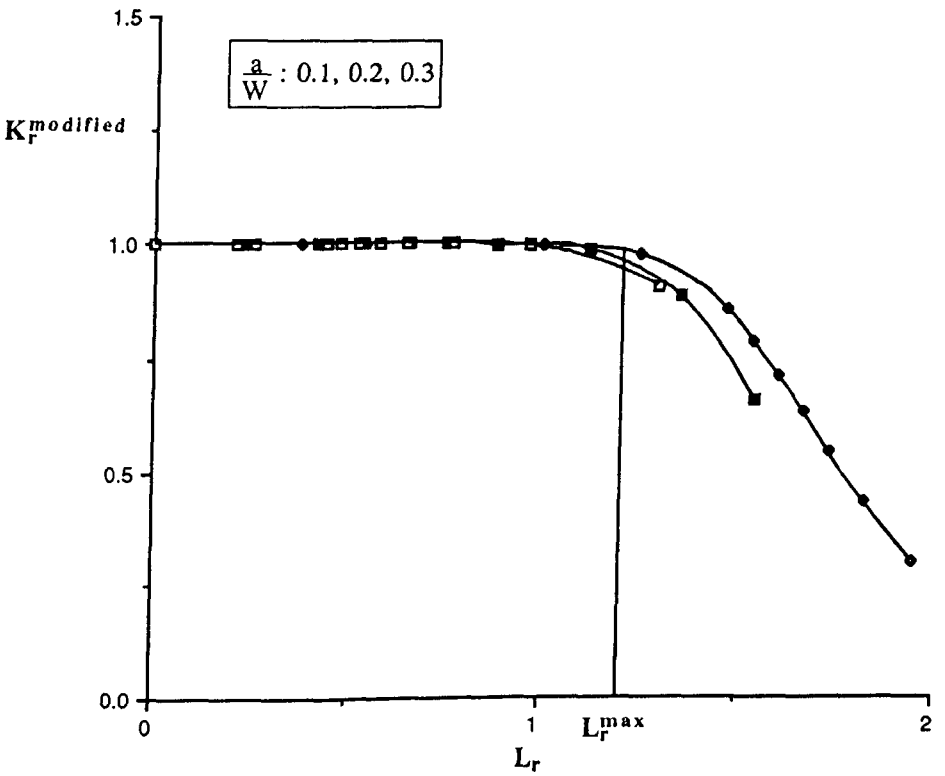

Figure 8.25: Modified Failure Assessment Diagram, SEC3PB, n=13, m=3.

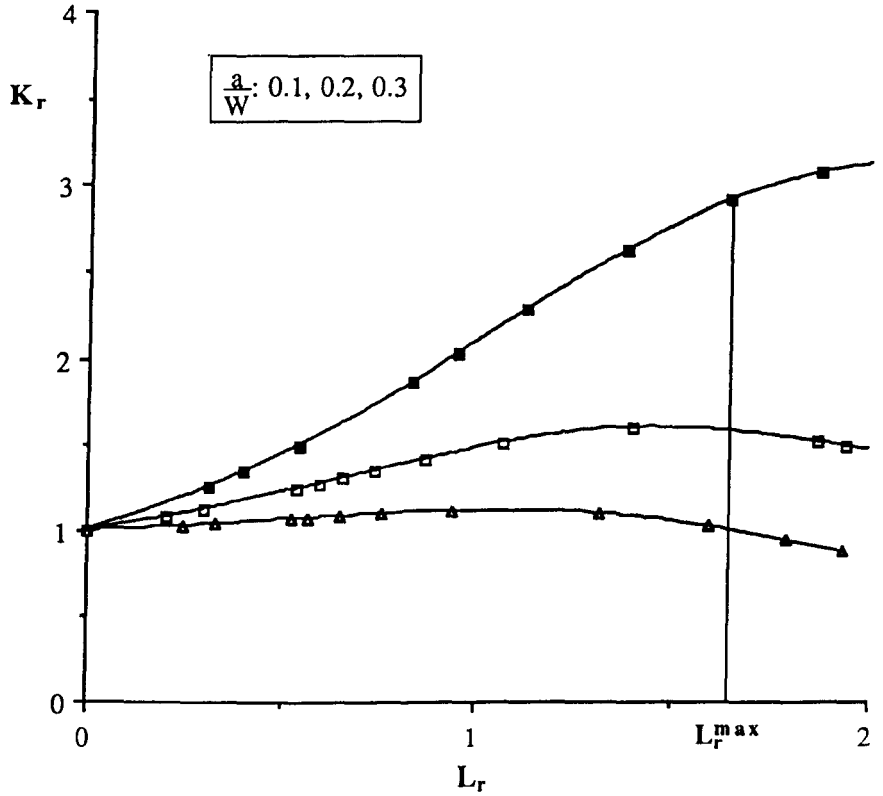

Figure 8.26: Failure Assessment Diagram, SEC3PB, n=6,m=3.

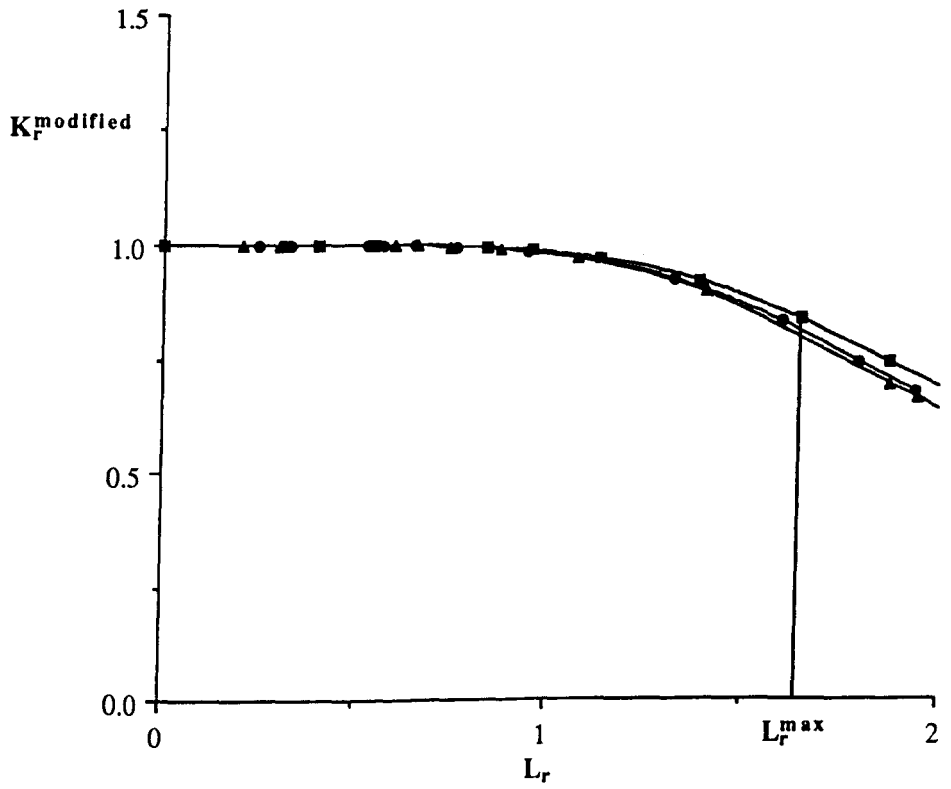

Figure 8.27: Modified Failure Assessment Diagram, SEC3PB, n=6, m=3.

Test Number	W(m)	B(m)	S(m)	$\frac{a}{W}$	P_f (kN)	$J_c^{elastic}$ (kJ/m^2)	J_c^{total} (kJ/m^2)	$\frac{T}{\sigma_0}$
1	0.029	0.024	0.120	0.057	62.3	7.316	132.0	-0.858
2	0.029	0.024	0.120	0.043	74.0	7.798	268.0	-1.049
3	0.029	0.024	0.120	0.028	77.0	5.734	245.0	-1.143
7	0.029	0.023	0.120	0.095	54.8	9.711	124.0	-0.695
8	0.029	0.023	0.120	0.060	62.0	8.141	166.0	-0.878
9	0.029	0.023	0.120	0.135	45.0	9.312	62.0	-0.492
10	0.029	0.024	0.120	0.075	61.3	8.929	134.0	-0.789
11	0.031	0.024	0.124	0.075	61.3	8.102	120.0	-0.733
12	0.031	0.024	0.124	0.074	62.1	8.110	122.0	-0.745
13	0.031	0.024	0.124	0.085	57.9	8.064	91.0	-0.672
17	0.031	0.024	0.124	0.100	53.9	8.412	134.0	-0.603
18	0.031	0.024	0.124	0.086	57.9	8.296	95.0	-0.676
19	0.031	0.024	0.124	0.071	66.4	9.050	102.0	-0.804
20	0.031	0.024	0.124	0.090	57.0	8.295	144.0	-0.649
21	0.033	0.024	0.132	0.209	43.0	10.136	89.0	-0.269
22	0.033	0.024	0.132	0.120	54.1	9.172	37.0	-0.521
23	0.033	0.024	0.132	0.145	51.0	9.627	74.0	-0.441
25	0.033	0.024	0.132	0.214	44.3	9.050	58.0	-0.271
26	0.035	0.024	0.140	0.222	44.3	11.013	50.0	-0.243
27	0.035	0.024	0.140	0.246	41.4	11.058	33.0	-0.192
28	0.035	0.024	0.140	0.392	28.1	10.702	32.0	0.044
30	0.035	0.024	0.140	0.226	43.5	10.791	26.0	-0.230
37	0.030	0.024	0.120	0.131	49.8	9.050	91.0	-0.498
38	0.030	0.024	0.120	0.048	72.3	7.685	194.0	-0.972
39	0.030	0.024	0.120	0.066	62.0	7.611	106.0	-0.787

Test Temperature = -50°C $\alpha = 6.65$
Yield Stress (-50°C) = 245 MPa. $n = 5$

Table 8.28: Mild Steel Plate Three Point Bend Tests (Sumpter and Forbes (1992)).

Test Number	W(m)	B(m)	$\frac{2a}{W}$	P_f (kN)	$J_c^{elastic}$ (kJ/m^2)	J_c^{total} (kJ/m^2)	$\frac{T}{\sigma_0}$
1	0.140	0.023	0.088	368.0	14.97	107.0	-0.602
2	0.140	0.023	0.089	348.0	13.94	100.0	-0.578
3	0.140	0.023	0.088	341.0	12.85	72.0	-0.558
4	0.140	0.023	0.088	346.0	13.23	122.0	-0.566
5	0.140	0.023	0.087	354.0	13.29	125.0	-0.570
6	0.140	0.023	0.088	380.0	15.96	155.0	-0.622
7	0.140	0.023	0.088	366.0	14.81	132.0	-0.599
9	0.140	0.023	0.088	355.0	13.93	131.0	-0.581
10	0.140	0.023	0.088	379.0	15.88	133.0	-0.620
11	0.140	0.023	0.108	254.0	14.05	143.0	-0.532
12	0.140	0.023	0.109	238.0	13.03	107.0	-0.511
13	0.140	0.023	0.109	239.0	13.15	147.0	-0.513
14	0.140	0.023	0.11	224.0	12.19	158.0	-0.492
15	0.140	0.023	0.108	238.0	12.33	156.0	-0.499
16	0.140	0.023	0.107	244.0	12.54	151.0	-0.505
20	0.140	0.023	0.108	248.0	13.39	134.0	-0.520

Test Temperature = -50°C
Yield Stress (-50°C) = 245 MPa.

$\alpha = 6.65$
$n = 5$

Table 8.29: Mild Steel Plate Centre Crack Tension Tests (Sumpter and Forbes (1992)).

Test Number	W(m)	B(m)	S(m)	$\frac{a}{W}$	P_f (kN)	$J_c^{elastic}$ (kJ/m^2)	J_c^{total} (kJ/m^2)
4537/15	0.0265	0.0242	0.106	0.08	159	70.286	900
4538/29	0.0264	0.0248	0.1056	0.086	155	67.712	750
4538/31	0.0283	0.0248	0.1132	0.119	140	70.631	410
4537/22	0.028	0.0248	0.112	0.131	133	68.442	300
4536/10	0.028	0.0245	0.112	0.134	117	55.061	100
4538/32	0.0297	0.0243	0.1188	0.188	127.5	87.167	240
4537/19	0.0297	0.0248	0.1188	0.207	114.5	74.772	110
4538/34	0.0313	0.0248	0.1252	0.233	102.5	65.437	100
4537/20	0.0313	0.0247	0.1252	0.240	98.5	63.084	90
4538/35	0.0358	0.0244	0.1432	0.319	59	30.248	31
4537/21	0.0362	0.0247	0.1448	0.341	65	40.162	41
4536/14	0.050	0.0247	0.20	0.518	28.5	15.431	16
4538/41	0.050	0.0246	0.20	0.534	55	64.426	82

Figure 8.30: Weld Data Three Point Bend Tests, Sumpter (1993)

Test Number	W(m)	B(m)	S(m)	$\frac{a}{W}$	P_f (kN)	$J_c^{elastic}$ (kJ/m^2)	J_c^{total} (kJ/m^2)	$\frac{T}{\sigma_0}$
1	0.022	0.022	0.088	0.044	136.4	44.26	827.8	-0.845
2	0.022	0.022	0.088	0.059	144.4	64.43	1018.6	-0.832
3	0.022	0.022	0.088	0.094	125.7	73.39	586.5	-0.641
4	0.022	0.022	0.088	0.099	117.2	66.73	254.7	-0.587
5	0.022	0.022	0.088	0.117	98.7	54.85	483.2	-0.46
6	0.022	0.022	0.088	0.138	116.9	89.43	512.5	-0.498
7	0.022	0.022	0.088	0.151	100.5	71.89	387.0	-0.412
8	0.022	0.022	0.088	0.213	84.4	72.12	192.6	-0.249
9	0.022	0.022	0.088	0.218	80.7	67.61	149.8	-0.203
10	0.022	0.022	0.088	0.3	75.3	89.69	363.8	-0.095
11	0.022	0.022	0.088	0.41	50.9	73.5	168.6	0.063
12	0.022	0.022	0.088	0.48	42.2	76.07	208.3	0.139

Test Temperature =20°C
Yield Stress (20°C) = 760 MPa

$\alpha = 1.4$
$n = 14$

Figure 8.31: Plate Steel Three Point Bend Tests (Betegón (1991)).

Test No.	W(m)	B(m)	S(m)	$\frac{a}{W}$	P_f (kN)	J_c^{total} (kJ/m^2)	Temperature (°C)	σ_0 (MPa)
2	0.05	0.025	0.203	0.5	27.5	12.74	-196	654
4	0.05	0.025	0.203	0.5	27.7	12.93	-196	654
7	0.0278	0.025	0.203	0.1	33.8	11.33	-196	654
8	0.0278	0.025	0.203	0.1	28.9	10.16	-196	654
18	0.05	0.025	0.203	0.5	42.5	29.72	-142	589
19	0.0278	0.025	0.203	0.1	51.5	294.6	-142	589

$\alpha = 8.08$
$n = 6$

Figure 8.32: BS 4360 Grade 50D Steel Three Point Bend Tests (MacLennan).

Test Number	$\frac{a}{W}$	B(m)	W(m)	a (m)	P_f(kN)	$J_c^{elastic}$ (kJ/m^2)	J_c^{total} (MJ/m^2
T3	0.1	0.016	0.0141	0.0014	18.6	31.194	1.06
T5	0.1	0.016	0.0141	0.0014	18.0	29.214	1.13
T7	0.1	0.016	0.0141	0.0014	17.8	28.568	0.648
T9	0.1	0.016	0.0141	0.0014	17.5	27.613	0.506
T0	0.1	0.016	0.0141	0.0014	18.4	30.526	0.602
T13	0.1	0.016	0.0141	0.0014	18.3	30.196	0.976
T1	0.2	0.016	0.016	0.0032	17.6	37.656	0.814
T2	0.2	0.016	0.016	0.0032	18.2	40.268	0.492
T10	0.2	0.016	0.016	0.0032	18.2	40.268	0.354
T12	0.2	0.016	0.016	0.0032	18.8	42.966	0.675
T4	0.3	0.016	0.018	0.0544	18.6	47.259	0.610
T6	0.3	0.016	0.018	0.0544	18.9	48.796	1.09
T8	0.3	0.016	0.018	0.0544	18.4	46.248	0.50
T11	0.3	0.016	0.018	0.0544	17.8	43.281	0.374

Test Temperature = 20 C $\quad\quad$ $\alpha = 0.85$

Yield Stress = 470 MPa $\quad\quad$ n = 10

Figure 8.33: A710 Three Point Bend Tests (Hancock, Reuter and Parks (1991)).

Chemical Composition (Wt%).					
C	Si	Mn	P	S	Cr
0.19	0.04	0.59	0.01	0.032	0.09

Figure 8.34: Chemical Composition of low grade Mild Steel.

Chemical Composition (Wt%).							
C	Si	Mn	P	S	Al	Ni	Nb
0.11	0.176	1.14	0.018	0.003	0.031	0.692	0.03

Figure 8.35: Chemical Composition of Betegón Test Plate.

Chemical Composition (Wt%).									
C	Si	Mn	P	S	Cr	Mo	Cu	Ni	Ti
0.05	0.25	0.47	0.01	0.04	0.74	0.21	1.2	0.85	0.038

Figure 8.36: Chemical Composition of A710 Steel.

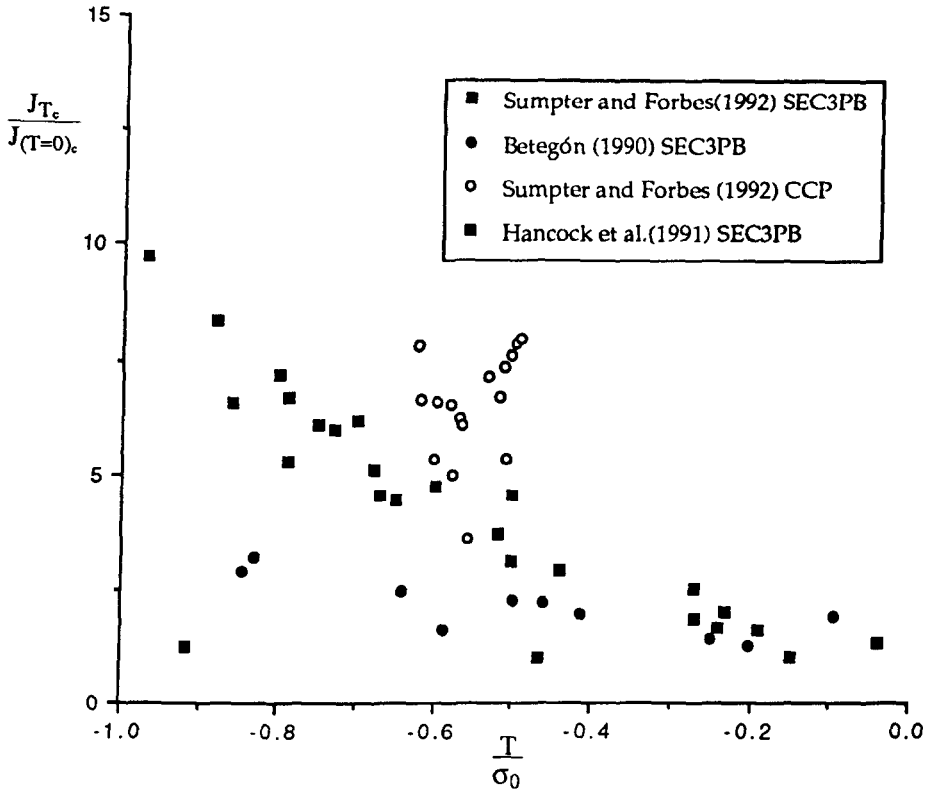

Figure 8.37: Experimental Material Loci.

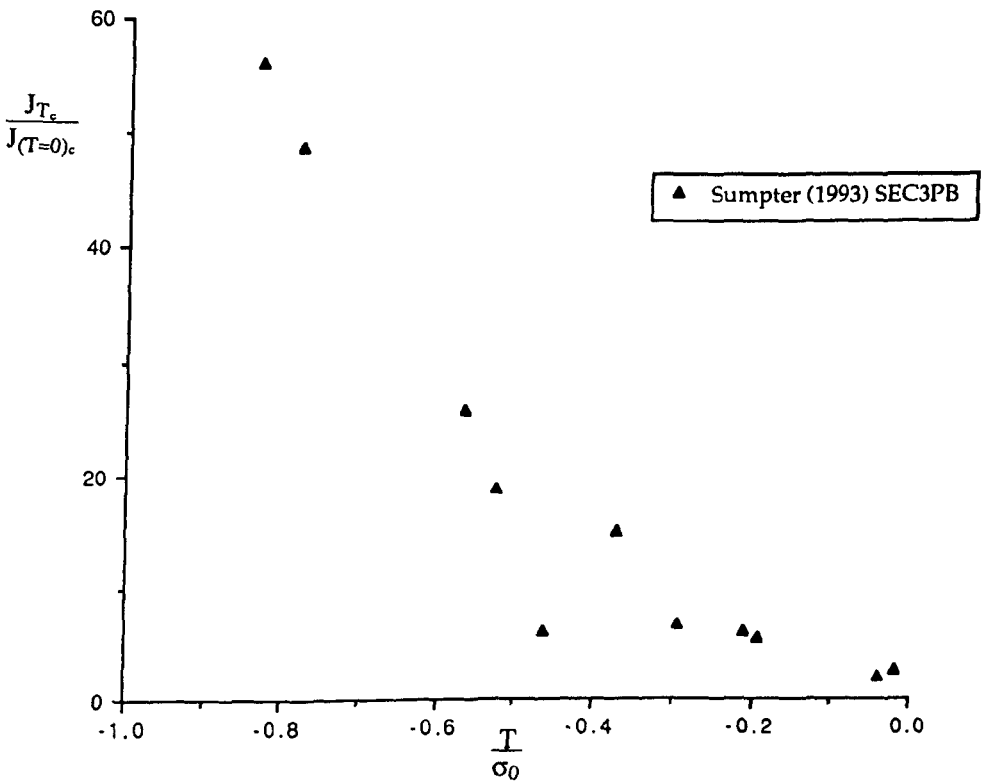

Figure 8.38: Experimental Material Loci.

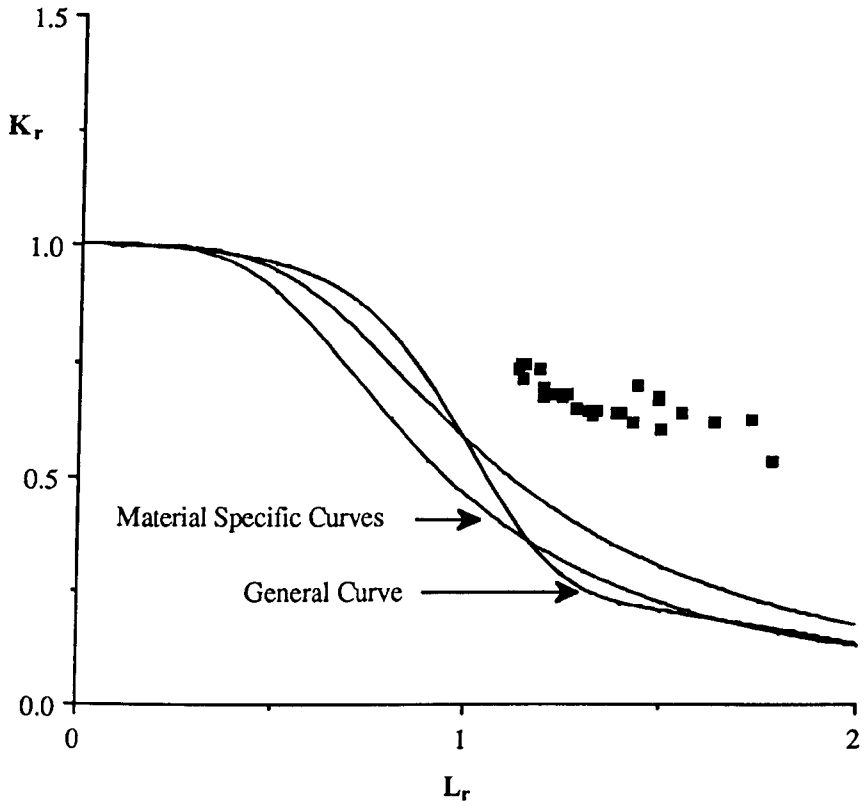

Figure 8.39: Failure Assessment Diagram, Sumpter and Forbes (1992), SEC3PB, n=5.

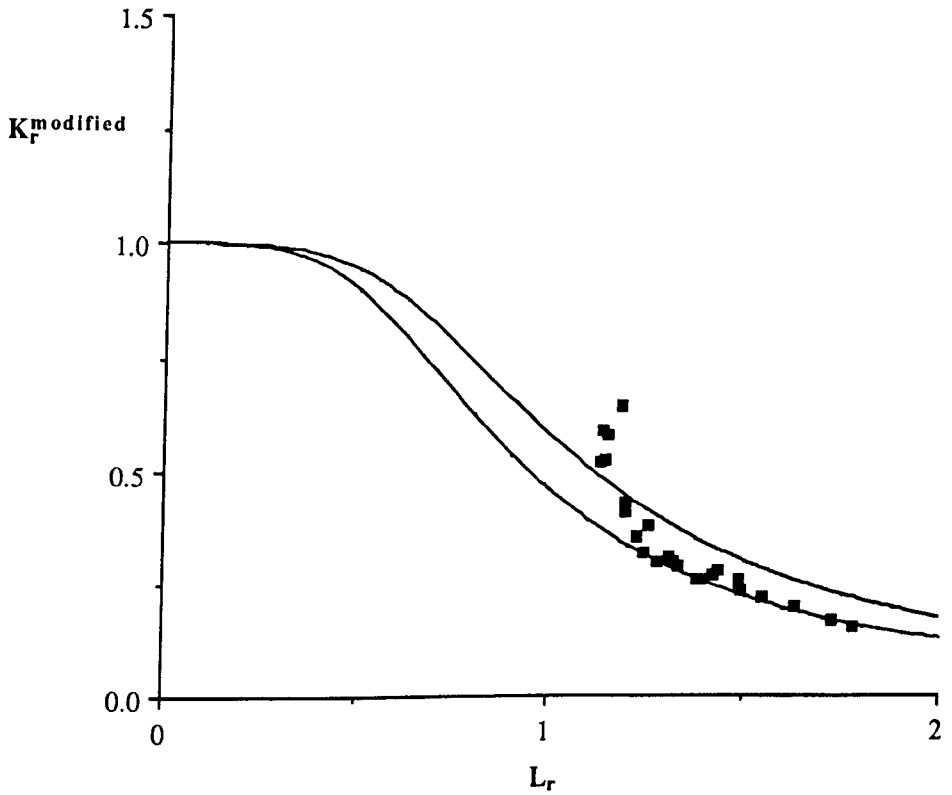

Figure 8.40: Modified Failure Assessment Diagram, Sumpter and Forbes (1992), SEC3PB, n=5.

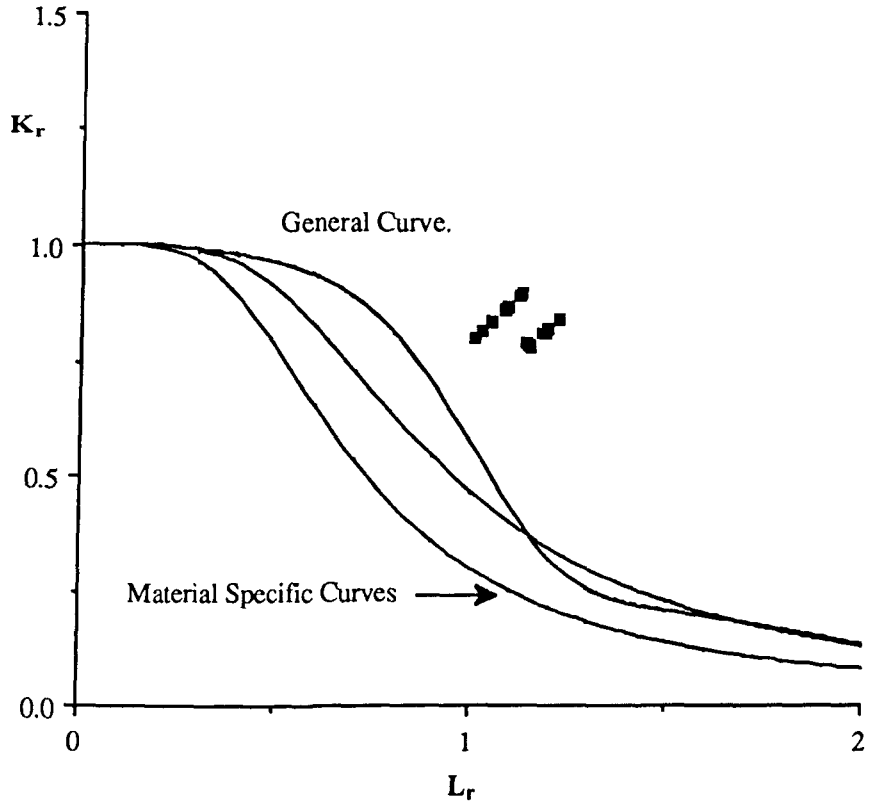

Figure 8.41: Failure Assessment Diagram, Sumpter and Forbes (1992), CCP, n=5.

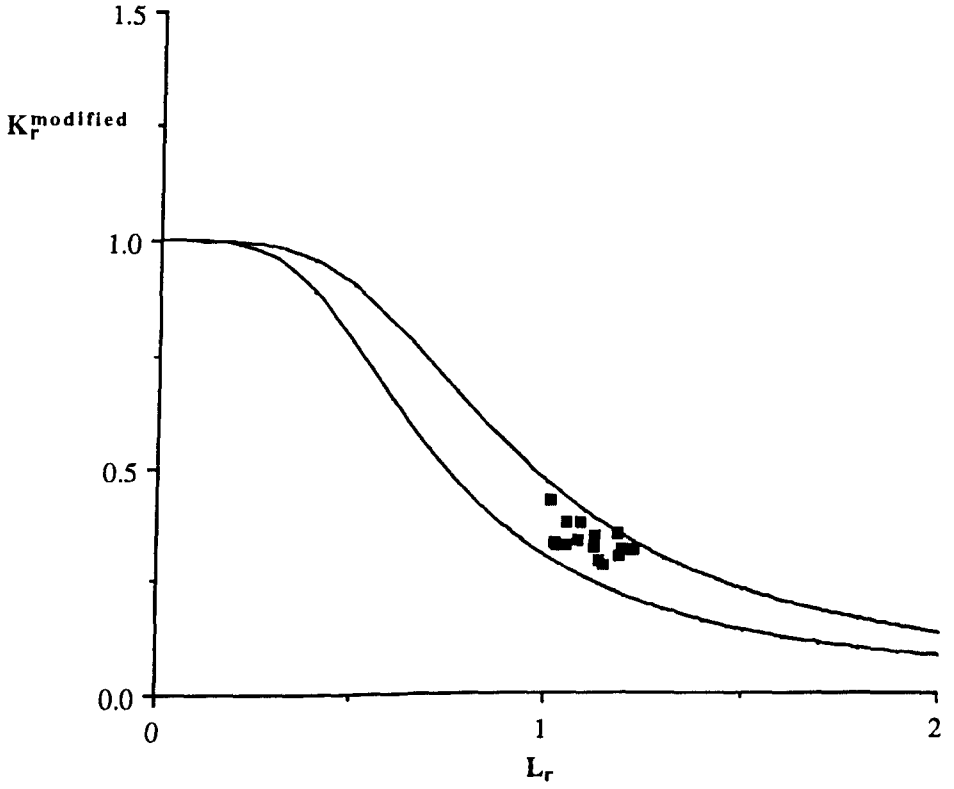

Figure 8.42: Modified Failure Assessment Diagram, Sumpter and Forbes (1992), CCP, n=5.

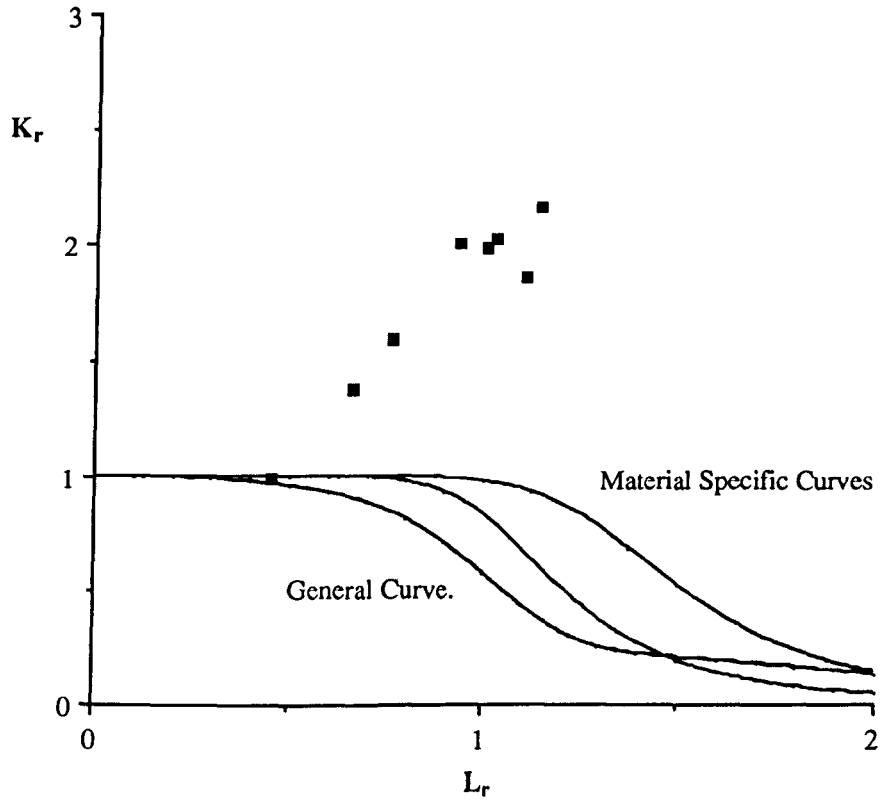

Figure 8.43: Failure Assessment Diagram, Sumpter Weld Data, SEC3PB, n=10.

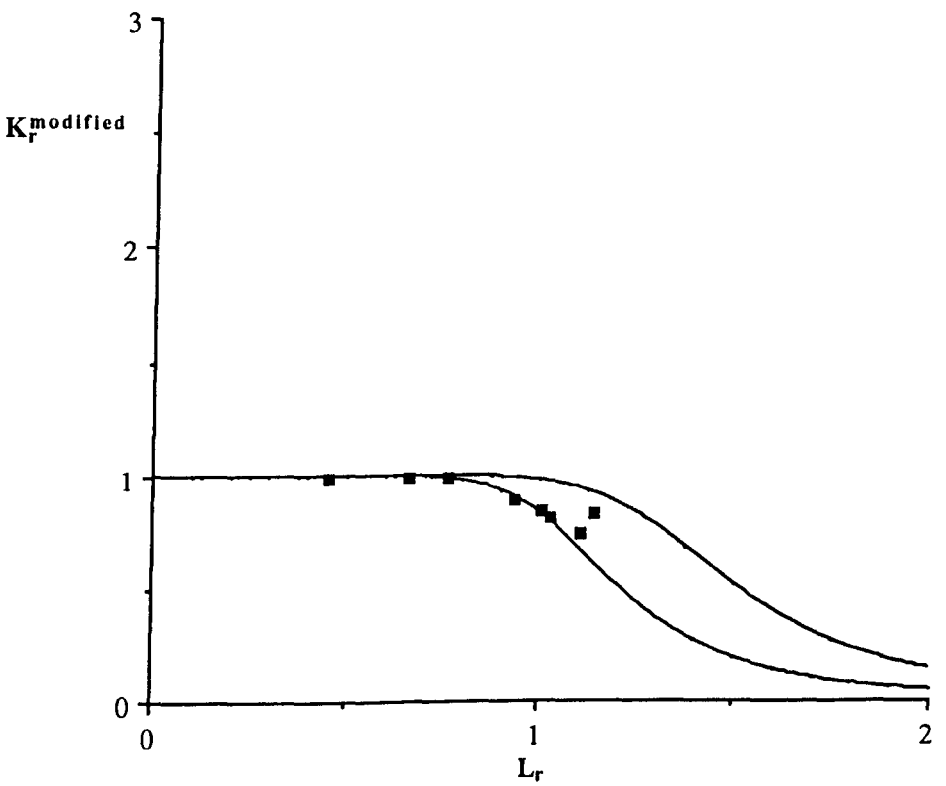

Figure 8.44: Modified Failure Assessment Diagram, Sumpter Weld Data, SEC3PB, n=10.

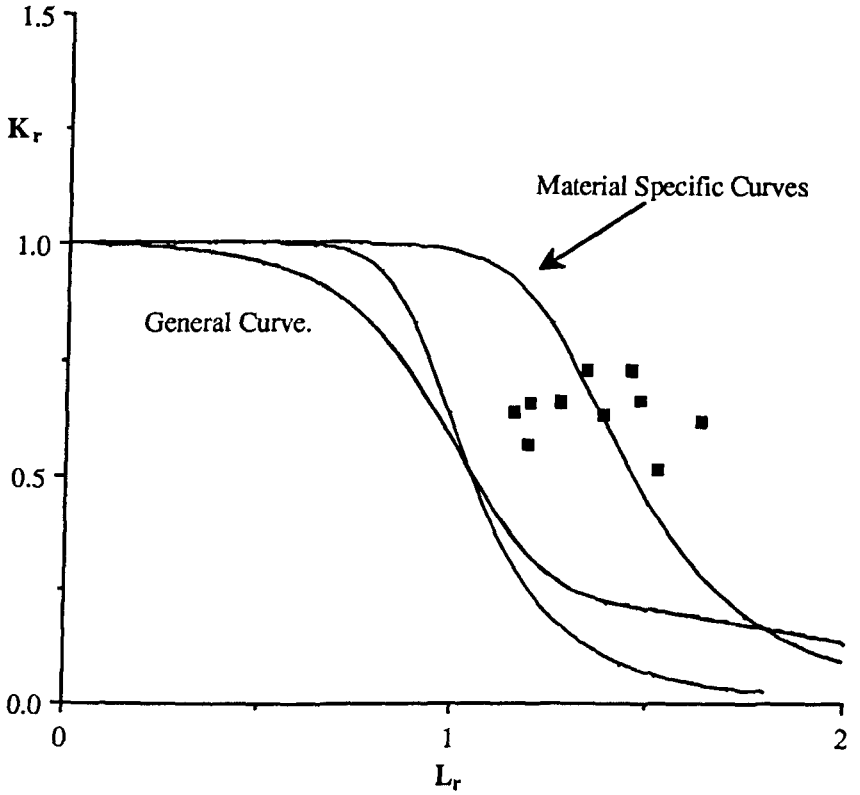

Figure 8.45: Failure Assessment Diagram, Betegón (1991), SEC3PB, n=14.

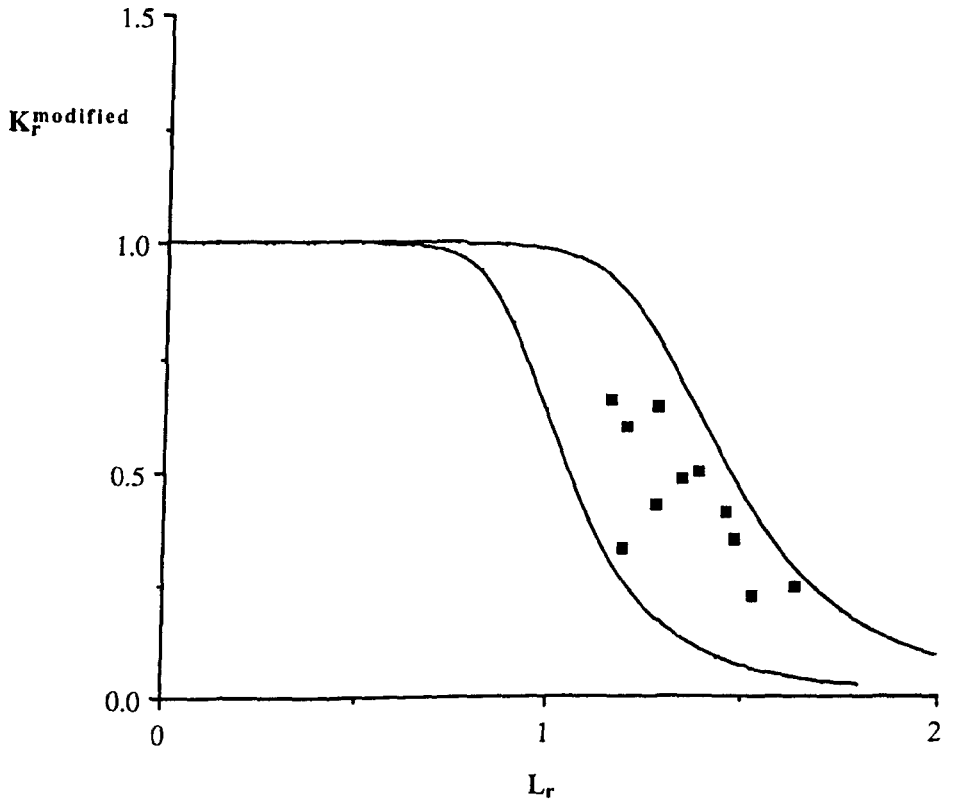

Figure 8.46: Modified Failure Assessment Diagram, Betegón (1991), SEC3PB, n=14.

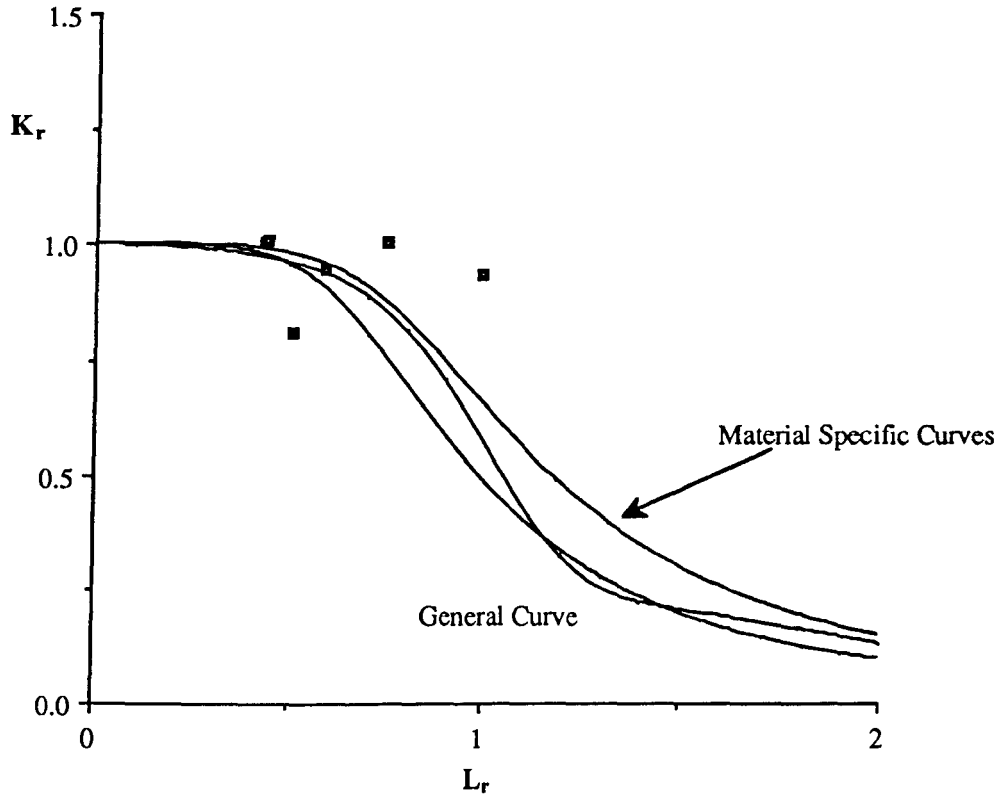

Figure 8.47: Failure Assessment Diagram, MacLennan, SEC3PB, n=6.

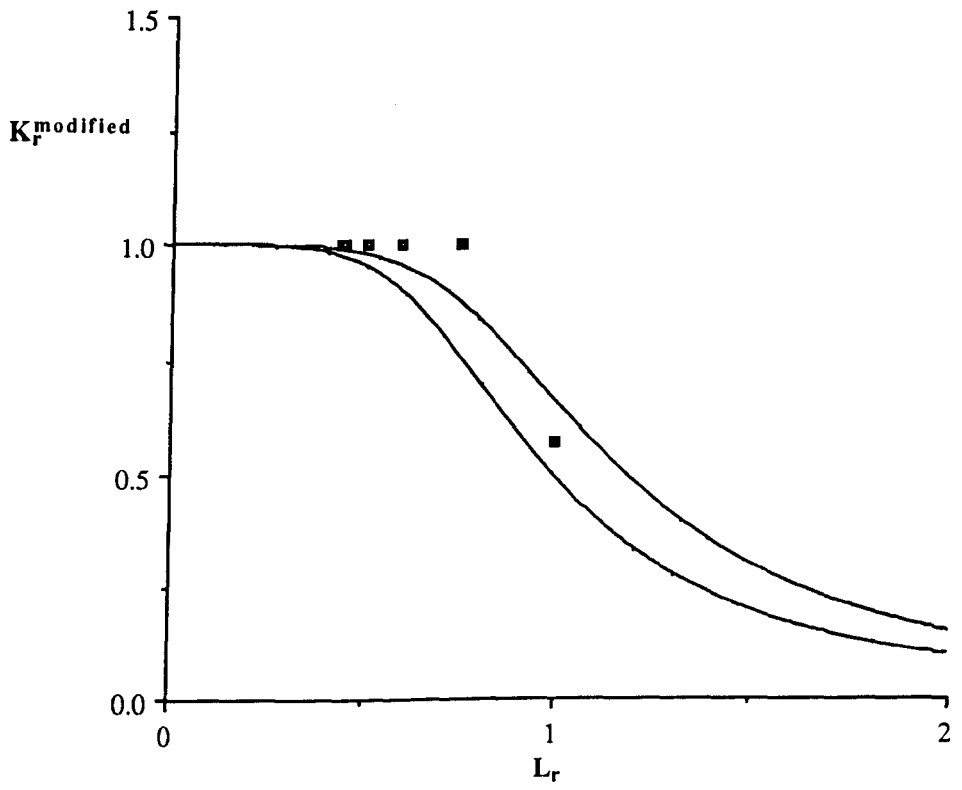

Figure 8.48: Modified Failure Assessment Diagram, MacLennan, SEC3PB, n=6.

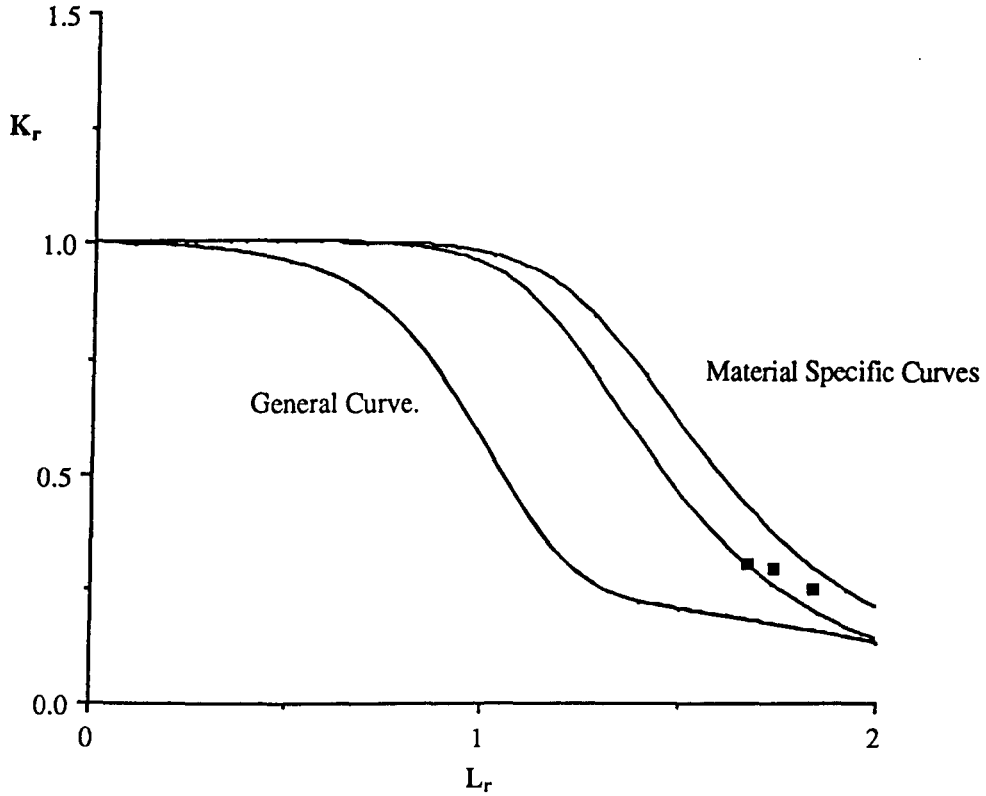

Figure 8.49: Failure Assessment Diagram, Hancock, Reuter and Parks (1991), n=10.

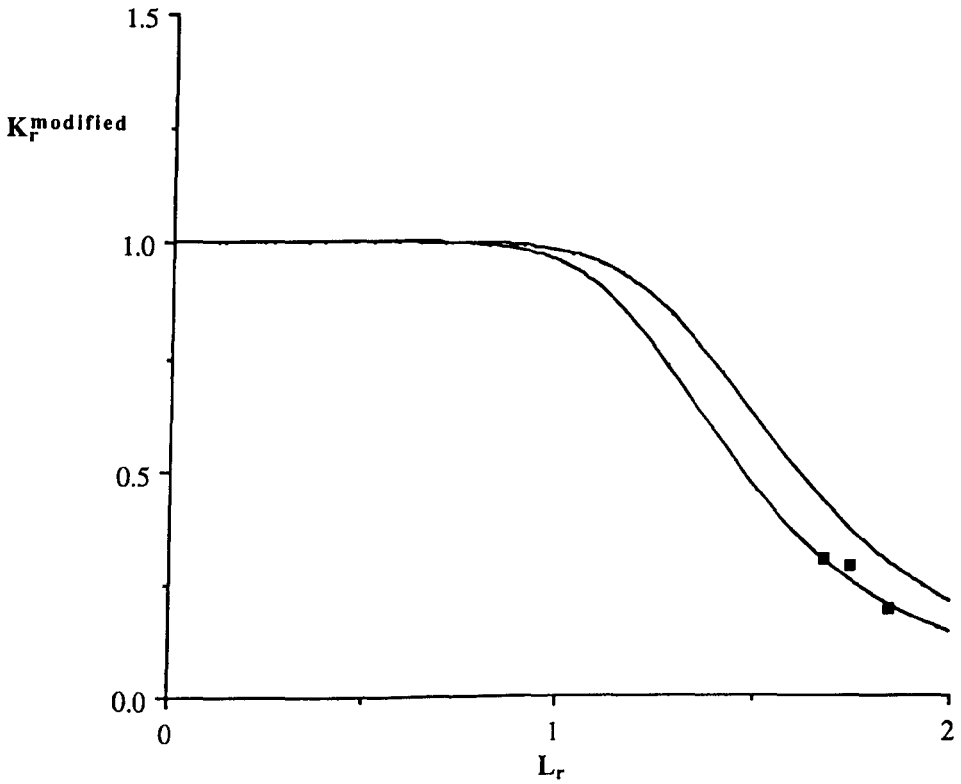

Figure 8.50: Modified Failure Assessment Diagram, Hancock, Reuter and Parks (1991), n=10.

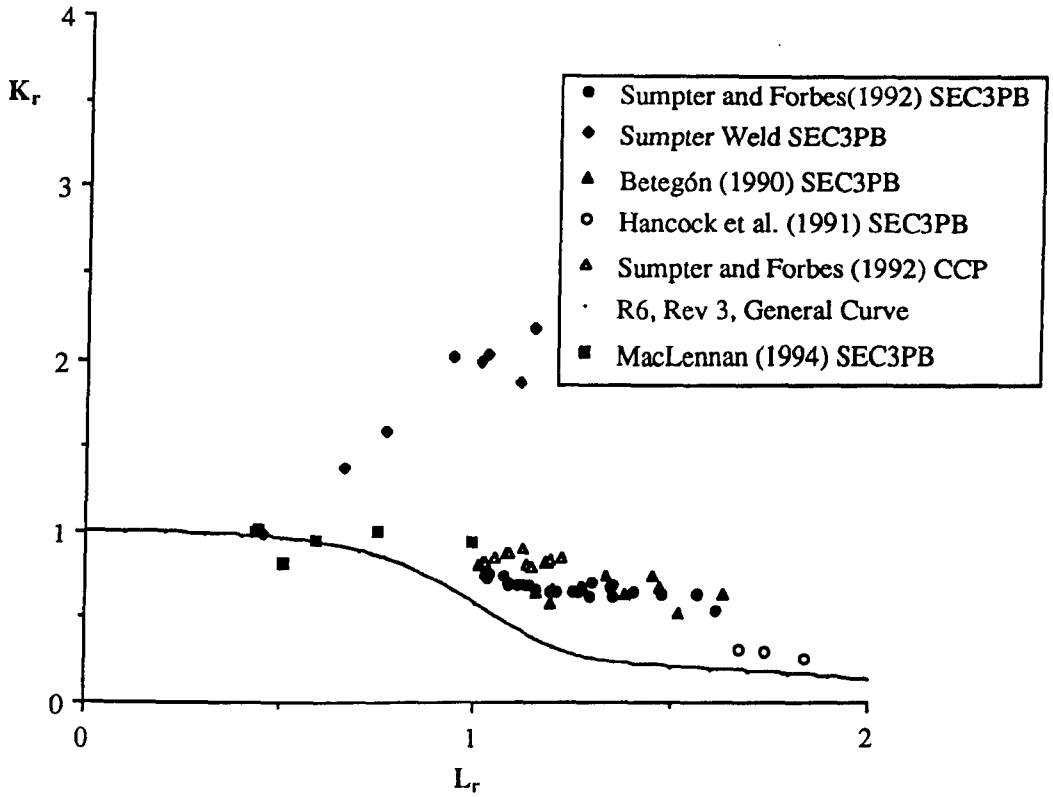

Figure 8.51: Combined Failure Assessment Diagram.

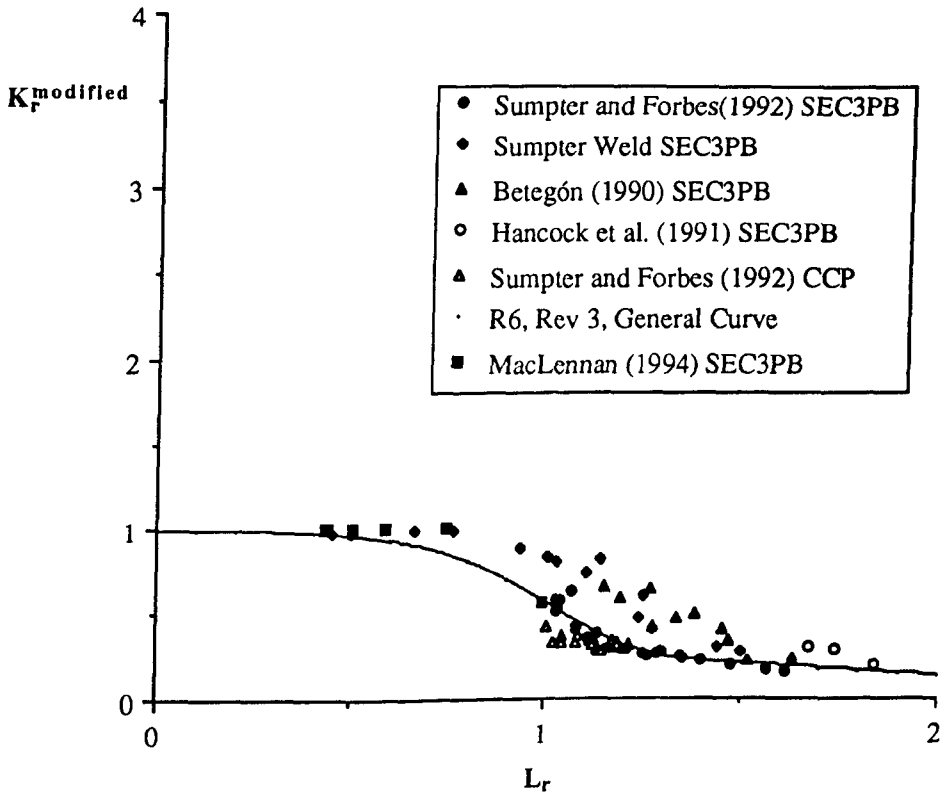

Figure 8.52: Combined Modified Failure Assessment Diagram.

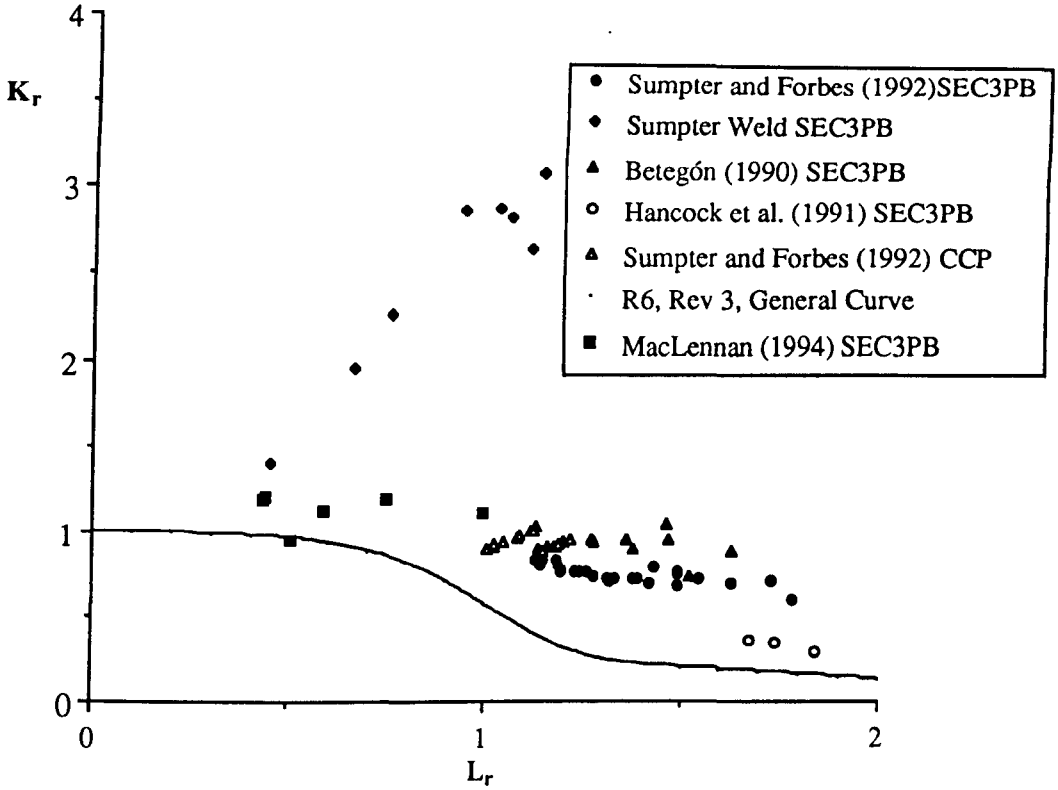

Figure 8.53: Lower Bound Failure Assessment Diagram.

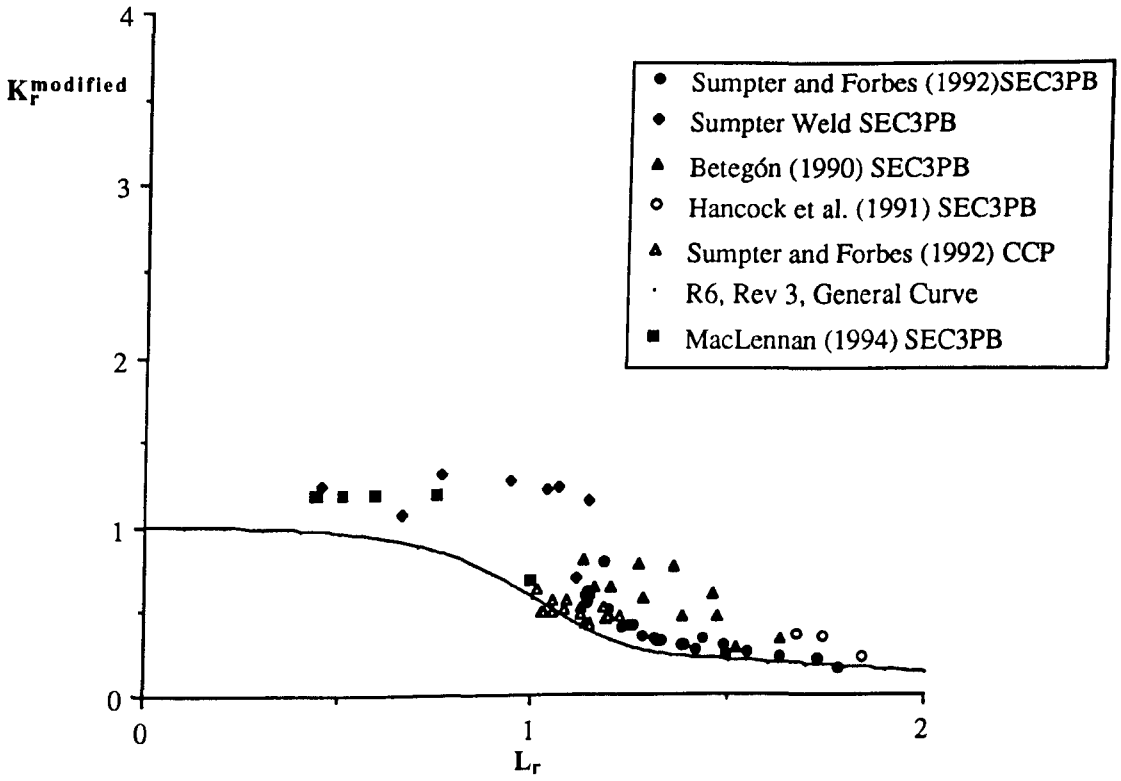

Figure 8.54: Modified Lower Bound Failure Assessment Diagram.

9: Experimental Fracture Mechanics.

9.1: Introduction.

Tests have been carried out on shallow and deeply cracked three point bend bars (SEC3PB) to show the effect of constraint on toughness and in particular its effect on the ductile-brittle transition as illustrated in Figure 9.1. To complement these experiments tests have also been carried out on torsion and notched tensile specimens. In the case of notch tensile geometries control of the notch geometry allows constraint to be varied in a systematic manner (Bridgman (1952) and Hancock and MacKenzie (1976)).

9.2: Notch Tensile Experiments.

Following Bridgman (1952) it is possible to generate different degrees of constraint by varying the notch profiles of axisymmetric circumferentially notched specimens, illustrated in Figure 9.2. The influence of notches on fracture behaviour has been known since its first utilisation in structural concepts by Kircaldy (1860), although its early formulation into fracture theory is attributed to Ludwik and Scheu (1923) and Haigh (1923).

9.2.1: Experimental Notch Theory.

The triaxiality of a stress state can be quantified by a dimensionless parameter in which the mean stress is normalised by the effective stress $\left(\frac{\sigma_m}{\bar{\sigma}}\right)$. Where the mean and the effective stress have previously been defined in terms of the principal stresses. The extent of plastic flow can be expressed in a similar functional form, involving the principal plastic shear strain increments;

$$d\bar{\varepsilon}^p = \sqrt{\frac{2}{9}\left\{\left(d\bar{\varepsilon}_1^p - d\bar{\varepsilon}_2^p\right)^2 + \left(d\bar{\varepsilon}_2^p - d\bar{\varepsilon}_3^p\right)^2 + \left(d\bar{\varepsilon}_3^p - d\bar{\varepsilon}_1^p\right)^2\right\}} \qquad (9.1)$$

$$\bar{\varepsilon}^p = \int_0^{\bar{\varepsilon}^p} d\bar{\varepsilon}^p \qquad (9.2)$$

The average effective plastic strain across the neck of the specimen is given by;

$$\bar{\varepsilon}^p = 2 \ln\left(\frac{d_0}{d}\right) \qquad (9.3)$$

Here d_0 is the original and d is the current value specimen diameter. The effective plastic strain across the section of the specimen is constant while the axial (σ_z), hoop (σ_θ) and radial (σ_r) stresses vary across this section as shown in Figure 9.3 after Bridgman (1952). The value of $\left(\frac{\sigma_m}{\bar{\sigma}}\right)$ rises from $\frac{1}{3}$ at the surface to a maximum on the axis of the specimen;

$$\frac{\sigma_m}{\bar{\sigma}} = \frac{1}{3} + \ln\left(\frac{a}{2R} + 1\right) \qquad (9.4)$$

Here R is the external notch radius. In these specimens the maximum triaxiality occurs at the centre of the specimen. Failure initiation can be detected experimentally by examining the average axial stress as a function plastic strain which rises as the material work hardens and then drops suddenly. The drop in the average axial stress level corresponds to the formation of a distinct crack in the centre of the specimen by void coalescence this causes a reduction in load bearing cross sectional area as illustrated in Figure 9.4. The strain at which this drop occurs has been defined as the plastic strain for failure initiation, $(\bar{\varepsilon}^f)$. At strain levels below that of failure initiation discrete holes are found across the cross section of the specimen, Hancock and MacKenzie (1976).

9.2.2: Experimental Results.

Three specimen geometries were considered in this part of the experimental program. These are denoted D-notch, A-notch and Plane geometries following Hancock and MacKenzie (1976) and Hancock, Mackenzie and Brown (1977). The Plane geometry is slightly waisted around the centreline to ensure that necking begins in the central notch region.

The steel under consideration in these experiments was a normalised Carbon-Manganese structural steel, commonly used in offshore applications and designated Grade 50D, under BS4360 (Chemical composition of this steel is given in Chapter 7). The yield stress at room temperature is 390 MPa, temperature and strain dependence of the yield stress of similar steels has been described by Bennett and Sinclair (1966).

The machine used for all experimental analyses was a 250 kN Instron test frame under strain control. Test temperatures were measured using a Copper-Constantan thermocouple attached to the specimens by a silicon sealant. Tests were carried out to determine ductility as a function of triaxiality, at temperatures of -196 C, -80 C, 20 C and 200 C. In these experiments -196 C was attained by utilising a tank filled with liquid nitrogen as illustrated in Figure 9.5. For the other temperatures below ambient, a brass tank was used with liquid nitrogen circulated around the tank to maintain the desired temperature, shown in Figure 9.6. The high temperature test (200 C) was achieved using a furnace as shown in Figure 9.7.

The results of one series of room temperature tests (20 C) are shown in Figures 9.8 and 9.9. These figures show the load and the average axial stress (kN/mm^2) against both the diameter reduction and the nominal effective plastic strain respectively for the three form of specimens tested. The stress state triaxialities are shown graphically in the next section combined with the torsion results for the five series of notch tests, two series of tests were carried out at room temperature.

9.3: Torsion Experiments.

Torsion experiments were attempted at three separate temperatures, 200 C, 20 C and -80 C, these were carried out in an attempt to cover the full range of possible constraint or triaxial stress states, within a torsion experiment there is no triaxiality $\left(\frac{\sigma_m}{\sigma} = 0\right)$. The design of the specimens used in these experiments is illustrated in Figure 9.10.

Experiments were carried out on an Avery reverse torsion test rig at a constant twist rate of thirty degrees per minute. The furnace and cooling arrangements was similar to the axisymmetric tensile experiments with the orientation of the furnace and cooling apparatus being along the horizontal Plane as opposed to the vertical. Specimen twist was determined from a scribe line along the specimen length, where the scribe line was not of a sufficient depth to influence the stress fields.

9.3.1: Torsion Theory.

For a cylindrical bar of sufficient length subjected to a uniform twisting moment then similar conditions along the length of the specimen as well as symmetry conditions lead to a linearly varying strain distribution from the centre of the specimen, Crandall and Dahl (1959). Symmetry and isotropic conditions mean that direction of twist is unimportant since twist and elongation in one direction will be consequently mirrored in the opposite possible direction.

As illustrated in Figure 9.11 the angle of twist can be directly related to the angle of the scribe line:

$$\gamma = \tan \theta \qquad (9.5)$$

Where γ is the maximum shear strain and θ is the rotation of the scribe line. The shear strain can be written in terms of the equivalent strain by the relation:

$$\bar{\varepsilon}^p = \frac{\gamma^p}{\sqrt{3}} \qquad (9.6)$$

9.3.2: Torsion and Tension Experimental Results.

The results for the torsion experiments are given in Table 1, while the notch and torsion experiment results are represented graphically in Figure 9.12. From this series of experiments it would appear that there is a temperature dependent trend in ductility for these torsion experiments. Although the specimens have comparable twist angles the small differences between each of these angles is magnified due to the nature of (9.5) therefore the equivalent plastic strain $(\bar{\varepsilon}^p)$ varies approximately between 1.3 and 1.8 for these experiments. With the highest degree of ductility being exhibited unsurprisingly by the high temperature experiment.

In the case of the tensile experiments the ductility is almost temperature independent for the experiments in the range between 80 C and 200 C as shown in Figure 9.12, Aboutorabi (1985). The liquid nitrogen experiments exhibited significantly reduced ductility and a micromechanical examination by scanning electron microscope showed failure by cleavage instability as illustrated for these experiments in Figure 9.13. In all the experiments the specimens followed the rule that the higher the triaxiality of the system then the lower the final ductility of the specimen. For the experiments carried out at -80 C micromechanical examination reveals that the Plane and A notch specimens showed ductile initiation leading to cleavage instability as illustrated in Figure 9.14(a-b).

9.4: Finite Element Analysis of Notched Tensile Specimens.

Finite element analyses were carried out on the three axisymmetric specimens to provide better estimates of the triaxiality. Three axisymmetric analyses were implemented in ABAQUS (1993) with the specimens being modelled as illustrated in Figures 9.15 - 9.17. Due to symmetry conditions it was only necessary to model a quarter of the body. These meshes were constructed using the commercial mesh generator PATRAN (1990) from axisymmetric eight noded biquadratic, hybrid, linear pressure reduced integration elements. The Plane geometry was slightly waisted around the centreline to ensure that necking begins in the central notch region.

The specimens were subjected to a remote uniform axial displacement with Youngs modulus and Poisson's ratio were set at 200 GPa and 0.3 respectively. Analyses were carried out for a strain hardening exponent (n) of 6 with σ_0 = 400 MPa corresponding to BS4360 Grade 50D steel.

9.4.1: Notch Tensile Finite Element Results.

The stress state is most severe in axisymmetric notches at the centre of the specimen, Hancock and Mackenzie (1976) and the results presented here relate purely to the centre of these specimens. All the parameters are plotted against the logarithmic diameter change, Figure 9.18 illustrates the change of the measure of stress state triaxiality $\left(\frac{\sigma_m}{\sigma}\right)$, where the deepest notch (D notch) has the most severe stress state for all specimens. Figure 9.19 illustrates the normalised axial stress where again the deep notch exhibits the higher stress levels with the Plane specimen exhibiting the least severe of the fields. Figure 9.20 shows the equivalent plastic strain with comparable levels of ductility necessitating a larger relative diameter change in the deep D notch as opposed to the Plane specimen. These results are consistent with the previous analysis of Hancock and Brown (1983).

9.5: Three Point Bend Experiments.

Three point bend experiments reported in the literature have shown that the level of fracture toughness was significantly affected by crack depth, Aboutorabi (1985), Sumpter (1986), Sorem et. al (1989) Betegón (1991) and Al-Ani and Hancock (1991).

The purpose of the current experiments was to monitor the effect of crack depth on fracture toughness and model the ductile-brittle transition for both shallow and deep cracks, from the lower shelf (-196 C) through to room temperature (20 C). The experimental methods are based upon the work of Sumpter (1987).

In the present investigation, two $\left(\frac{a}{W}\right)$ ratios, 0.1 and 0.5 were considered. Both bars had the same uncracked ligament (c=W-a=25mm). It was possible to generate both negative $\left(\frac{a}{W} = 0.1\right)$ and positive $\left(\frac{a}{W} = 0.5\right)$ T-stresses with these geometries and thereby study the effect the degree of crack tip constraint has upon the ductile-brittle transition

Specimens were machined from 25mm thick plate with the orientation of the specimen being in the rolling direction of the steel as illustrated in Figure 9.21. The specimens were fatigue cracked from 5mm notches machined at the mid-point of the specimens. Fatigue precracking was carried out on 100kN Dartec three point bend test rigs. Fatigue cracks were grown halfway through the specimens and then machined to the appropriate $\frac{a}{W}$ ratio. These specimens were tested on the same experimental test frame as the notched tensile specimens. The SEC3PB were tested under displacement control, at a displacement rate of no more than 0.5mm/min. For low temperature experiments the specimens were contained in a bath of liquid nitrogen as shown in Figure 9.22. Due the low temperatures involved in this test it was impossible to utilise a clip gauge, due to the embrittlement of the connecting wires on contact with the liquid nitrogen. In these low temperature tests it was possible only to record the movement of the crosshead and the load applied to the specimen. Specimens tested at liquid nitrogen temperatures were allowed to soak in liquid nitrogen to eliminate temperature gradients through the specimens.

At room temperature it was possible to attach a clip gauge using knife edges attached to

the specimen to measure the crack mouth opening displacement (CMOD), the method of attachment is shown in Figure 9.23. Temperatures between ambient and -140 C were achieved by attaching brass tanks to both sides of the specimen around the crack tip and pumping liquid nitrogen through these at varying flow rates to reach the desired temperature as shown in Figure 9.24. Additional Kaowool insulation also surrounded the experimental specimens to prevent temperature gain.

9.5.1: Three Point Bend Theory.

The experimental analysis of the SEC3PB tests follows that of Sumpter and Turner (1976) and Sumpter (1987). The critical stress intensity factor was determined through the calibration given by Tada, Paris and Irwin (1973);

$$K = \frac{3PS}{2BW^2}\sqrt{\pi a}\, f_I\left(\frac{a}{W}\right) \qquad (9.7)$$

Here S is the span of the specimen, $f_I\left(\frac{a}{W}\right)$ is a geometry, W is the width and P is the applied load. The geometric function is defined as;

$$f_I\left(\frac{a}{W}\right) = 1.090 - 1.735\left(\frac{a}{W}\right) + 8.2\left(\frac{a}{W}\right)^2 - 14.18\left(\frac{a}{W}\right)^3 + 14.57\left(\frac{a}{W}\right)^4 \qquad \frac{S}{W} = 4$$

$$f_I\left(\frac{a}{W}\right) = 1.07 - 2.120\left(\frac{a}{W}\right) + 7.71\left(\frac{a}{W}\right)^2 - 13.55\left(\frac{a}{W}\right)^3 + 14.25\left(\frac{a}{W}\right)^4 \qquad \frac{S}{W} = 8 \qquad (9.8)$$

It is now possible to express the stress intensity factor K in the form;

$$K = \frac{P\lambda}{B\sqrt{W^3}} \qquad (9.9)$$

Where λ is defined as;

$$\lambda = 6\sqrt{\frac{a}{W}}\, f_I\left(\frac{a}{W}\right) \qquad (9.10)$$

When the failure is not governed by purely elastic terms the elastic and plastic components of J can be resolved separately as discussed in Chapter 3, (3.21). Sumpter and Turner (1976) expressed the fracture toughness of a specimen in terms of the area under a load-displacement trace, this allows J to be related directly to the plastic component of crack mouth opening displacement (CMOD).

$$J = \frac{K^2(1-\nu^2)}{E} + \frac{\eta_{plastic} U_{V_{plastic}}}{B(W-a)} \cdot \frac{W}{a_t + r(W-a)} \qquad (9.11)$$

Here a_t must incorporate the crack depth plus the height of knife edges if used, while r is a rotational constant defined in (3.35). The constant $\eta_{plastic}$ is given in (3.30) and $U_{V_{plastic}}$ is the plastic area under the load-CMOD trace.

9.5.2: Three Point Bend Experimental Results.

The results of this series of experiments are tabulated in Figure 9.25, with the fracture toughness of the specimens expressed in terms of both J_c and δ_t where possible. Figures 9.26-9.29 show these fracture toughness in relation to the amount of crack growth (Δa) at room temperature (20 C) and at -50C. The crack growth (Δa) and crack tip opening displacement (δ_t) are determined from detailed scaled crack tip photographs as shown in Figure 9.30.

At room temperature (20 C) and -50 C the J - Resistance and δ_t - Resistance curves show that at both temperatures the toughness of the shallow crack markedly exceeds that of the deeply cracked geometry, no matter which characterising parameter is used (J, δ). The failure mechanism for these tests was ductile tearing which is consistent with the experimental observations of Aboutorabi (1985) and Sumpter (1987).

In the case of the limited number of experiments at -100 C, two shallow and one deeply cracked geometries were tested. For both types of geometries failure initiation was ductile in nature whereas the final failure was due to cleavage instability, this can be explained in terms of competing processes. Ductile failure is stress and strain state sensitive whereas cleavage is controlled by the maximum principal stress. Failure initiation is controlled by whichever mechanism is satisfied first. Again the shallow crack toughness significantly exceeds that of the deeply cracked geometry.

Experiments carried out below -138 C all failed by cleavage instabilities for both geometries, with the shallow crack exhibiting a higher degree of fracture toughness than the deeply cracked geometry. Experiments carried out at liquid nitrogen temperatures (-196 C) produced geometry independent results. Figure 9.31 expresses the variation of J initiation (J_i) as a function of temperature, for geometries subject to ductile tearing. J_i is measured at a crack extension of 200μm as interpolated from Figures 9.26-9.29. The corresponding cleavage experiments are taken at maximum load even when small amounts of ductile tearing preceded Experiment 15 being regarded as somewhat dubious and subsequently ignored.

9.6. Conclusions.

The experimental programme has attempted to demonstrated the effect of constraint on the ductile-brittle transition. The central result is given in Figure 9.30 and may be compared with the micro-mechanical modelling shown in Figure 7.16. On the upper shelf crack extension occurs by ductile tearing the shallow cracked geometry is markedly tougher than the deeply cracked configuration. This is due to the loss of constraint associated with the negative T stress, which decreases the void growth rate as a function of plastic strain (Rice and Tracey 1969). This effect is also clearly shown in comparing the ductility of constrained and unconstrained notched tensile bars, where the ductility decreases markedly with constraint(triaxiality). The notched tensile bars also demonstrate that ductile failure is only weakly temperature sensitive, and experiments on cracked structures usually support this observation in showing little or no temperature dependence on the upper shelf in the absence of time dependent creep effects.

On the lower shelf the failure mechanism is by cleavage, at very low absolute values of toughness. At these levels the dimension of the ligament and crack length meets the size criterion proposed by McMeeking and Parks (1979), and in addition the small applied loads result in very small(negative) values of the T stress. As a consequence there is very little geometry dependence of the toughness. This effect was correctly modelled in Chapter 7 where a local approach based on a Ritchie Knott and Rice model was used. Thus Figure 7.16 shows geometry independent toughness being recovered on the lower shelf, which is also shown by the experimental data of Al-Ani in Figure 7.19 and that of Sumpter in Figure 7.20.

The micro-mechanical modelling predicts that with increasing levels of plasticity a geometry dependent constraint effect should appear and the transition curve for deep and shallow cracked specimens should diverge as they are correctly observed to do in Figure 9.31. The analysis also predicts that the onset of ductile tearing should occur at higher temperatures in constrained than in unconstrained specimens. However experimentally this effect occurs at temperatures between -100C and -150C where the difficulty of consistent and accurate temperature control has prevented there being sufficient data to check the prediction.

The computational modelling resulting in Figure 7.17. suggests that the shift in the ductile-brittle transition should be approximately equal to 60 C between geometries with a

25mm ligament and a/W ratios of 0.1 and 0.5. This is broadly consistent with the data of Al-Ani and Sumpter. The present experimental results do not exhibit such a sharp shift in transition temperatures, and although the shift in the ductile brittle transition temperature is more subjective, the trend is correctly predicted. Ideally it would have been desirable to have carried out more experiments as cleavage failure in particular is well known to exhibit high levels of scatter. The modelling has been based on critical local cleavage stresses of 1400 and 1800 mPa. The toughness and the transition temperature are particularly sensitive to the exact value of the cleavage stress. The data is more appropriately described using a cleavage stress close to 1800MPa. This limited experimental program has demonstrated the capacity to model geometry and constraint effects, however it is clear that the number of free variables (cleavage stress and the critical micro-structural distance) make the method very flexible in terms of fitting data, but more problematic in terms of predicting the geometry and constraint dependence of toughness.

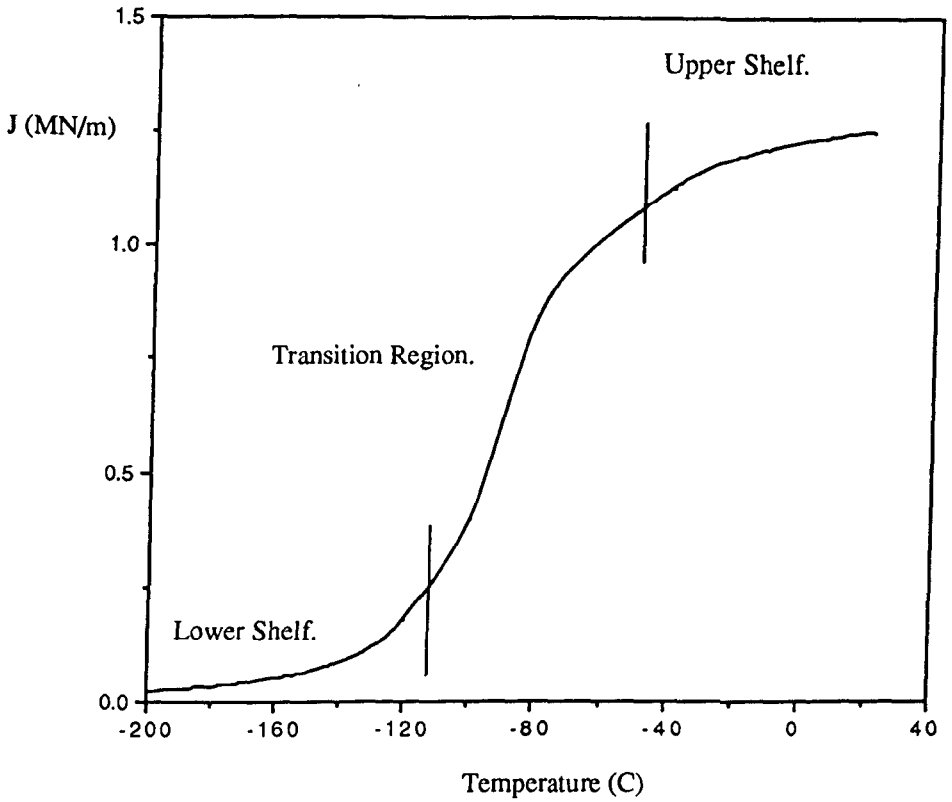

Figure 9.1: Schematic Ductile Brittle Transition.

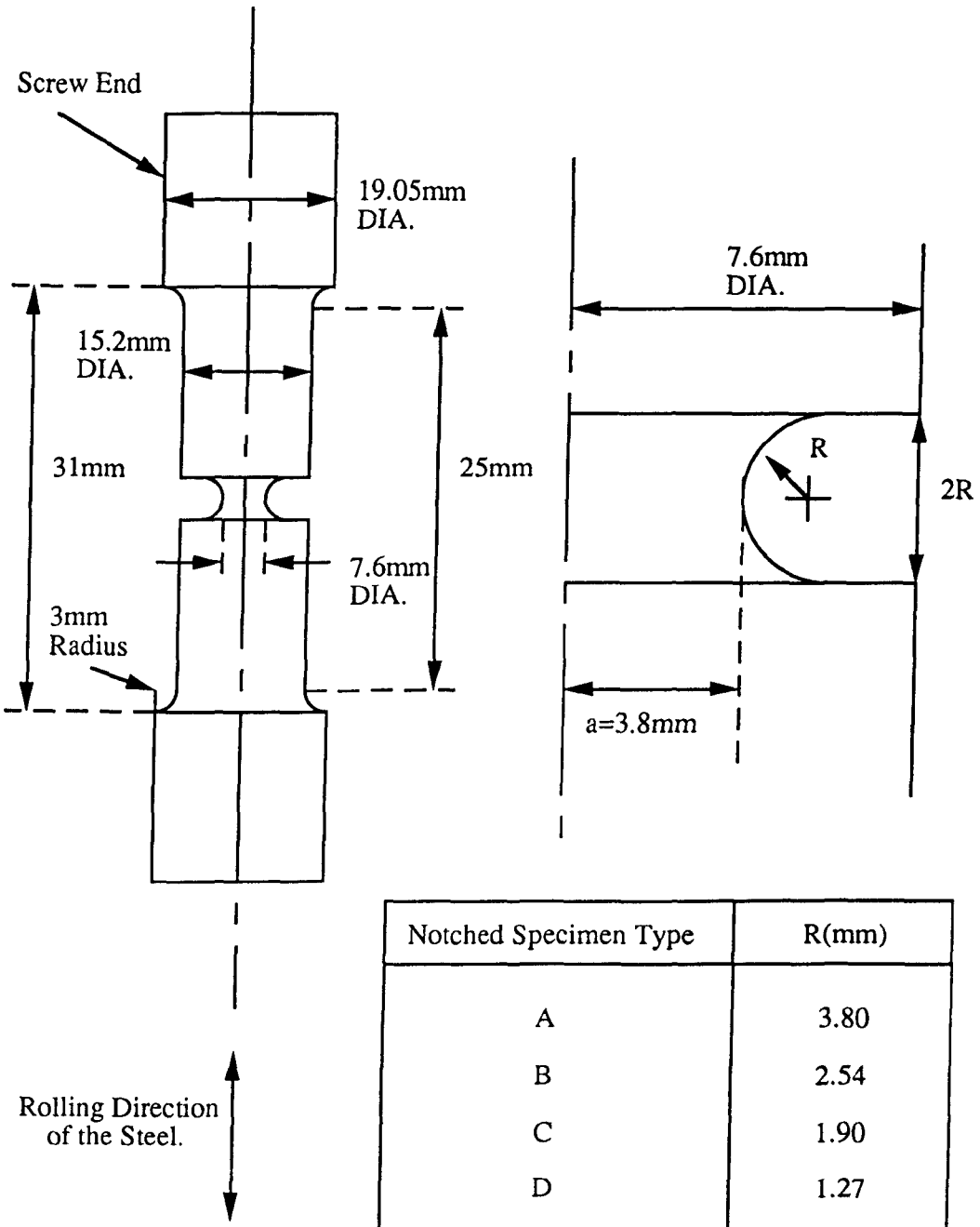

Notched Specimen Type	R(mm)
A	3.80
B	2.54
C	1.90
D	1.27
E	6.34

Figure 9.2: Notch Tension Specimens.

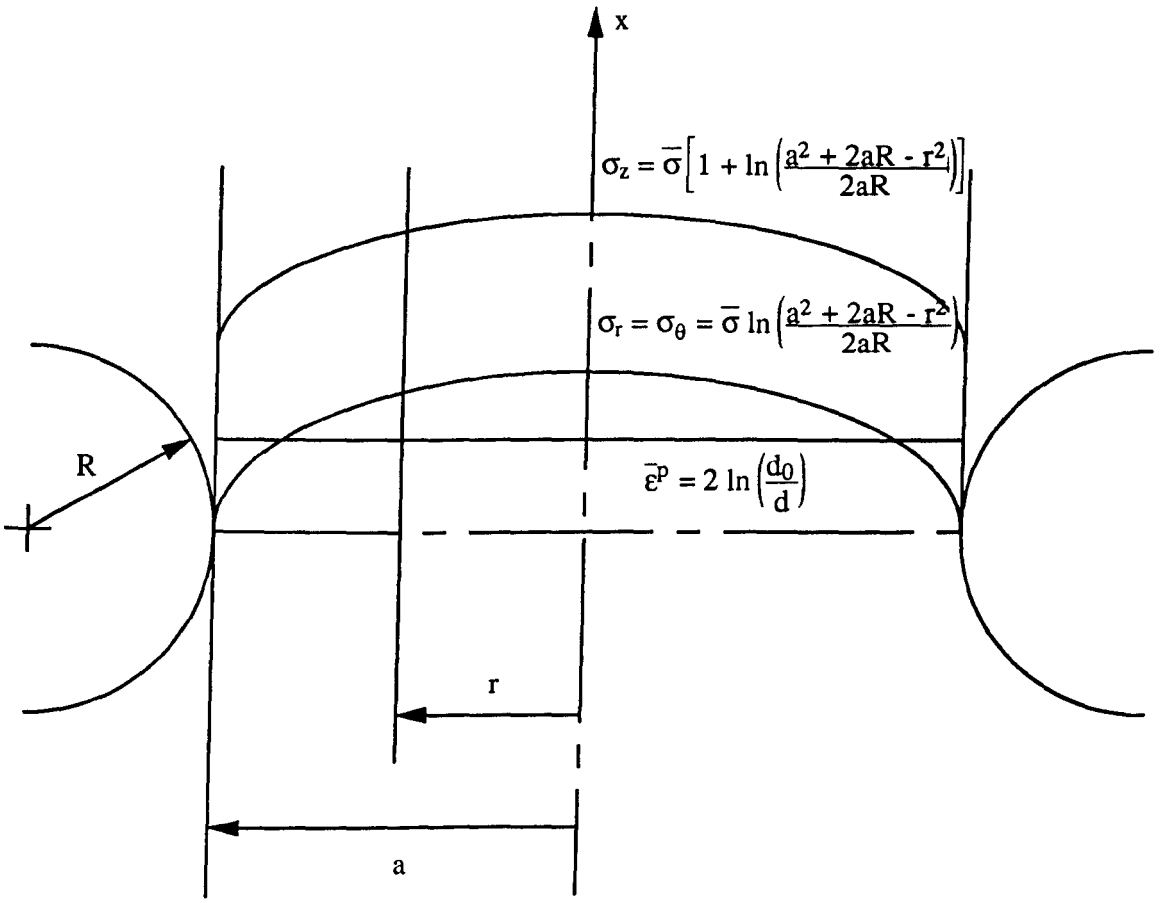

9.3: Stress Distribution (after Bridgman (1952)).

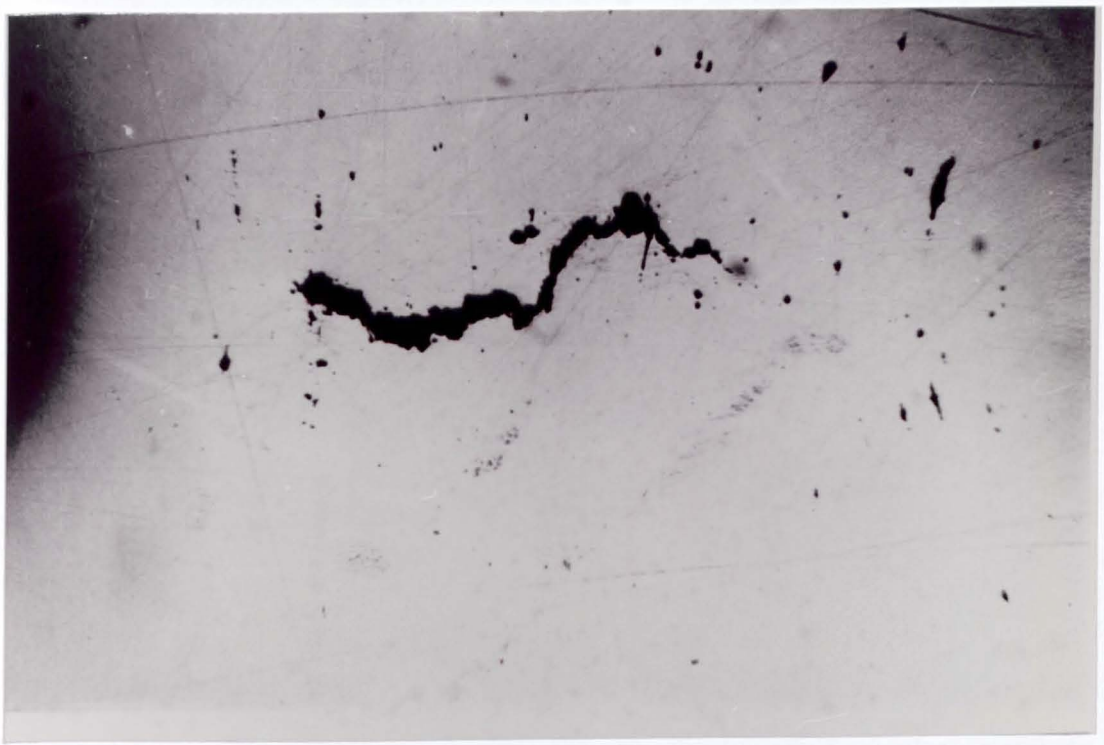

Figure 9.4: Crack in Centre of Notch Tensile Specimen.

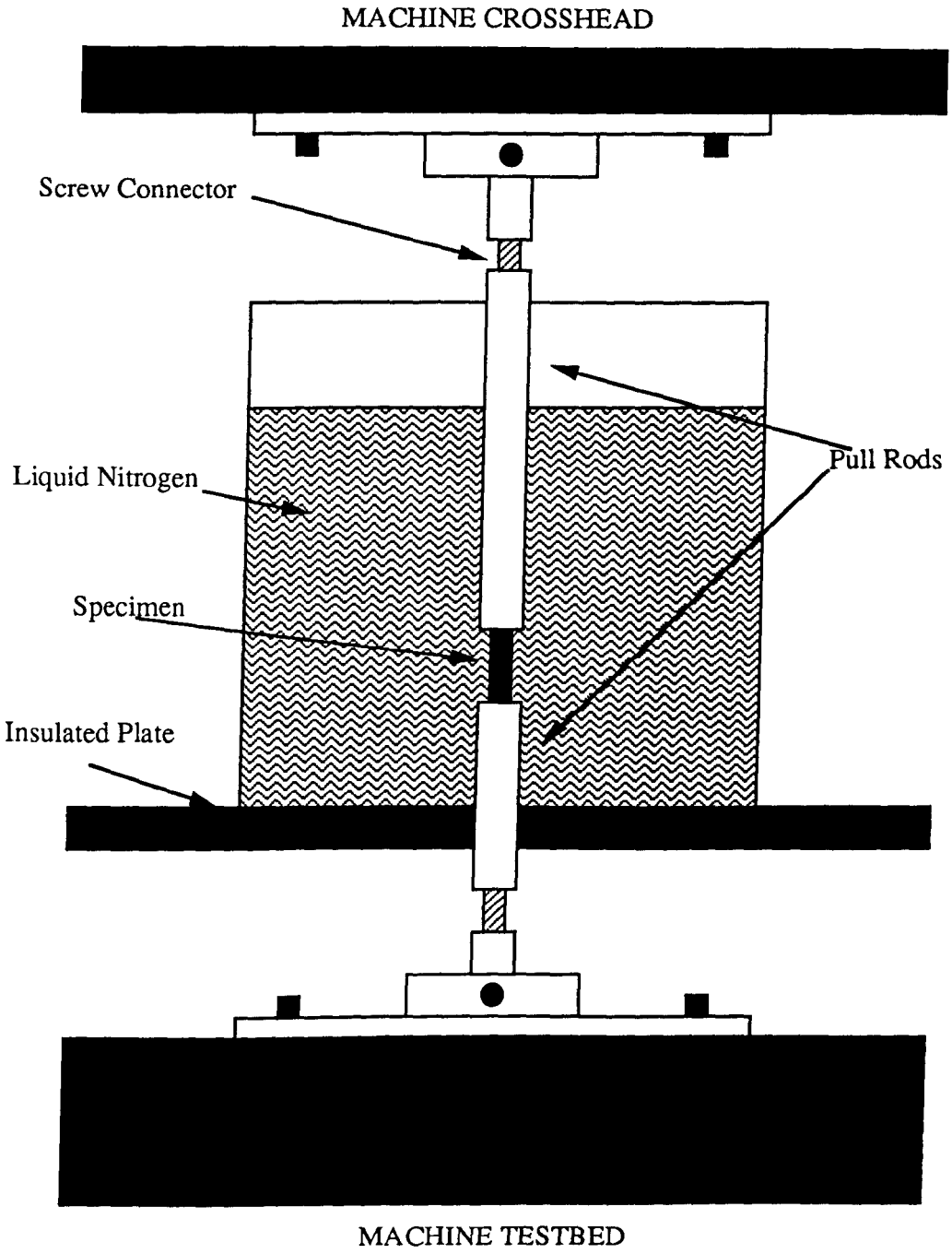

Figure 9.5: Liquid Nitrogen Test Setup for Notch Tensile Experiments.

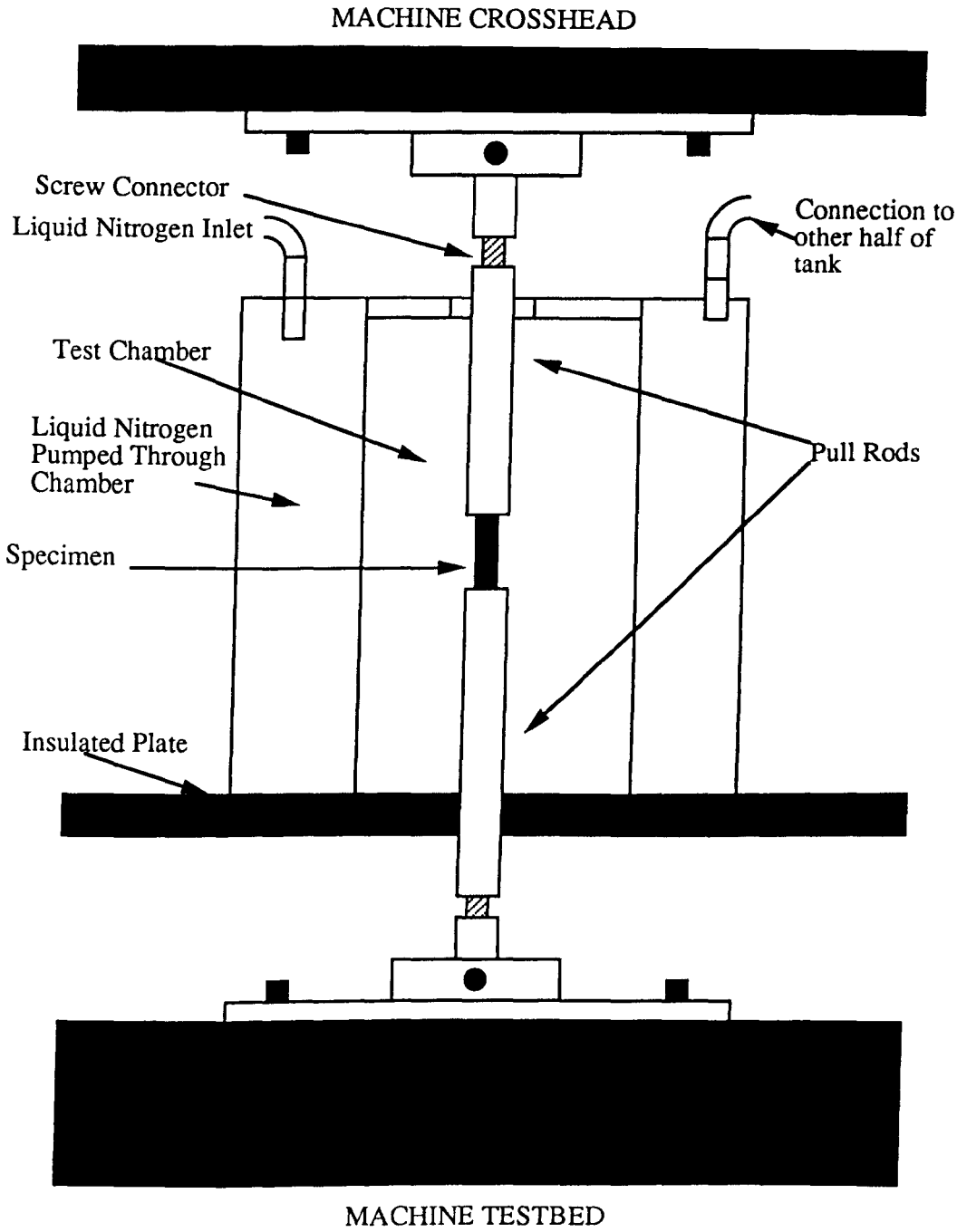

Figure 9.6: Low Temperature Test Setup for Notch Tensile Experiments.

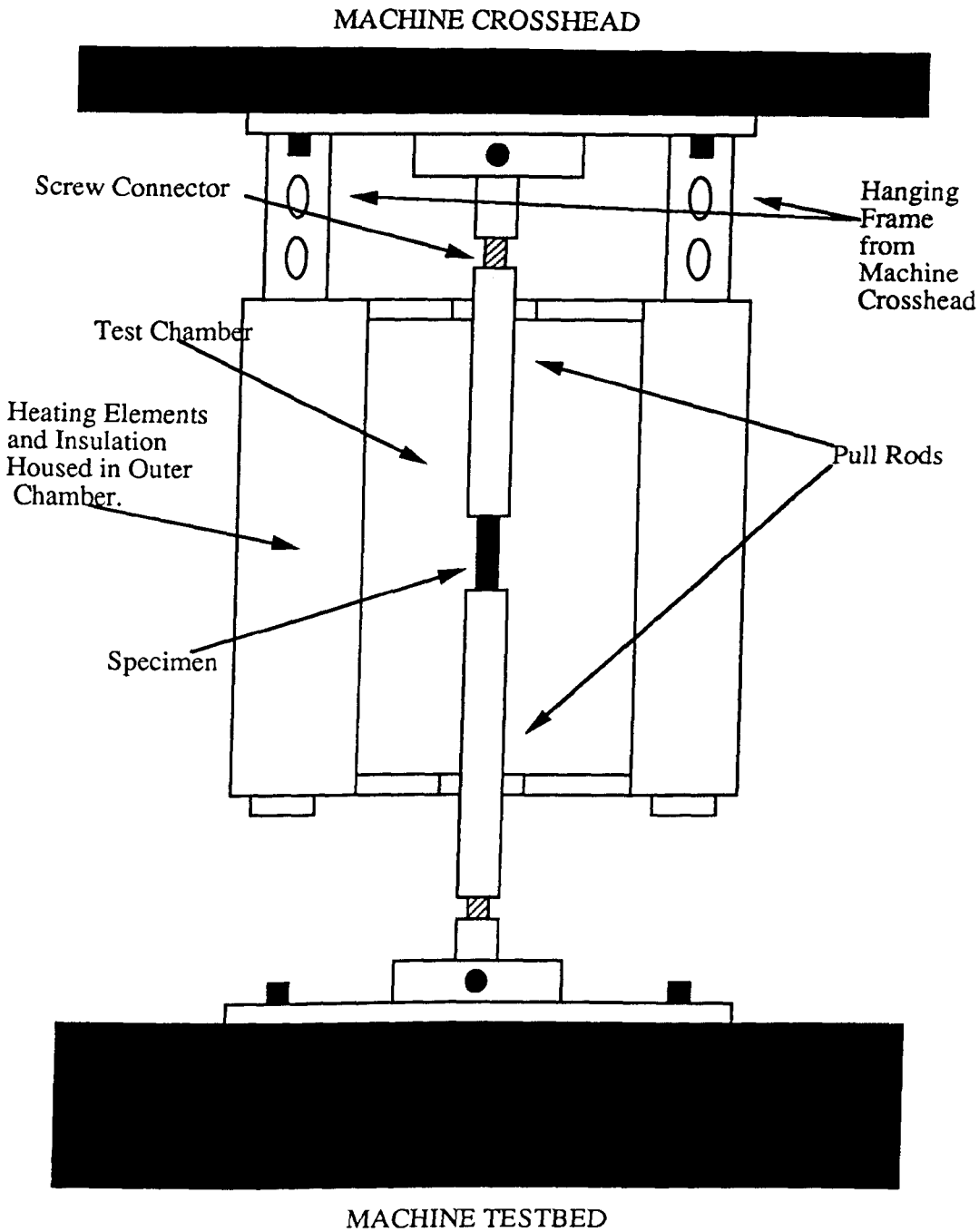

Figure 9.7: High Temperature Test Setup for Notch Tensile Experiments.

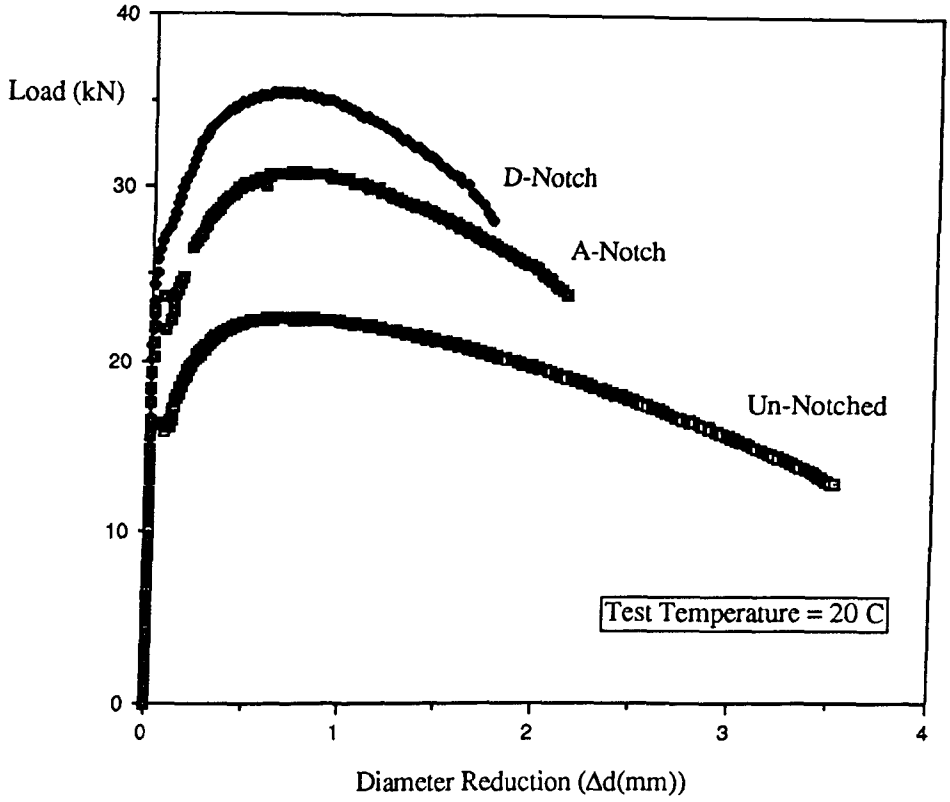

Figure 9.8: Applied Load versus Specimen Diameter Reduction.

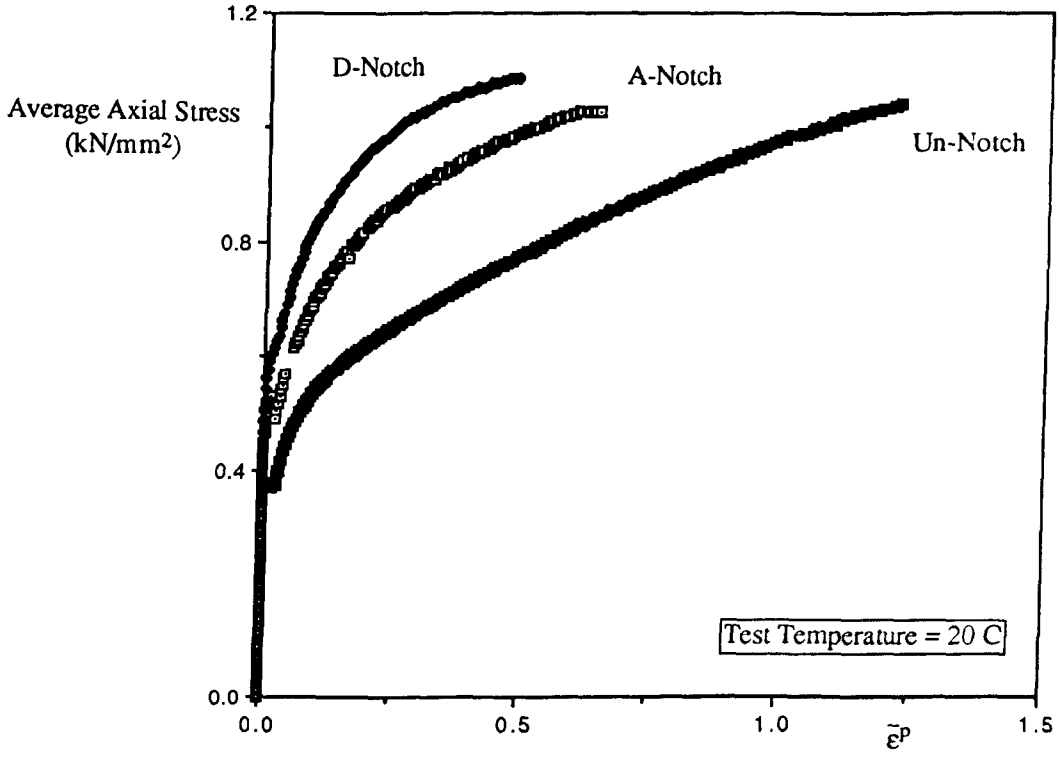

Figure 9.9: Average Axial Stress versus Plastic Strain.

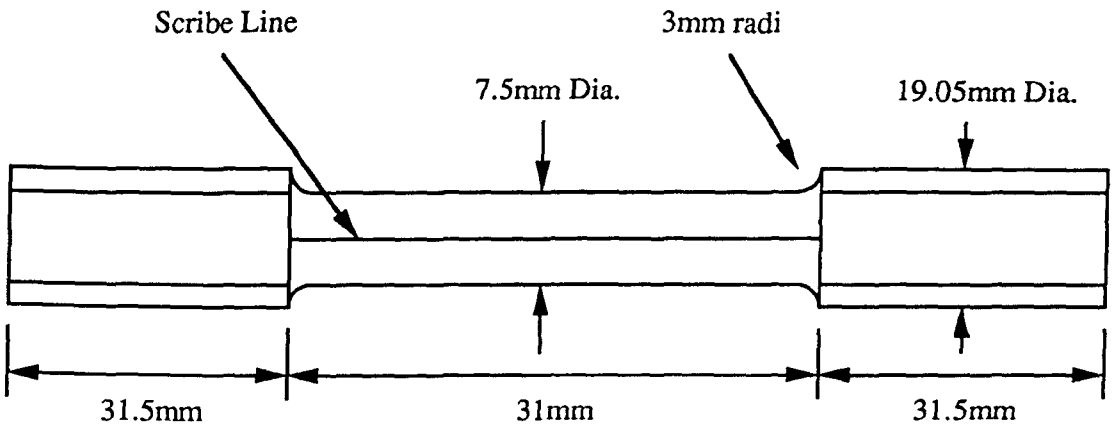

Figure 9.10: Torsion Experimental Specimen.

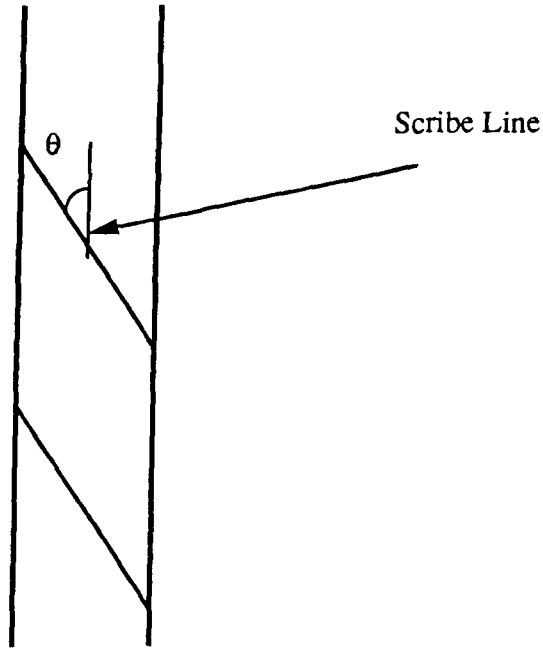

Figure 9.11: Angle of Twist of Torsion Specimen

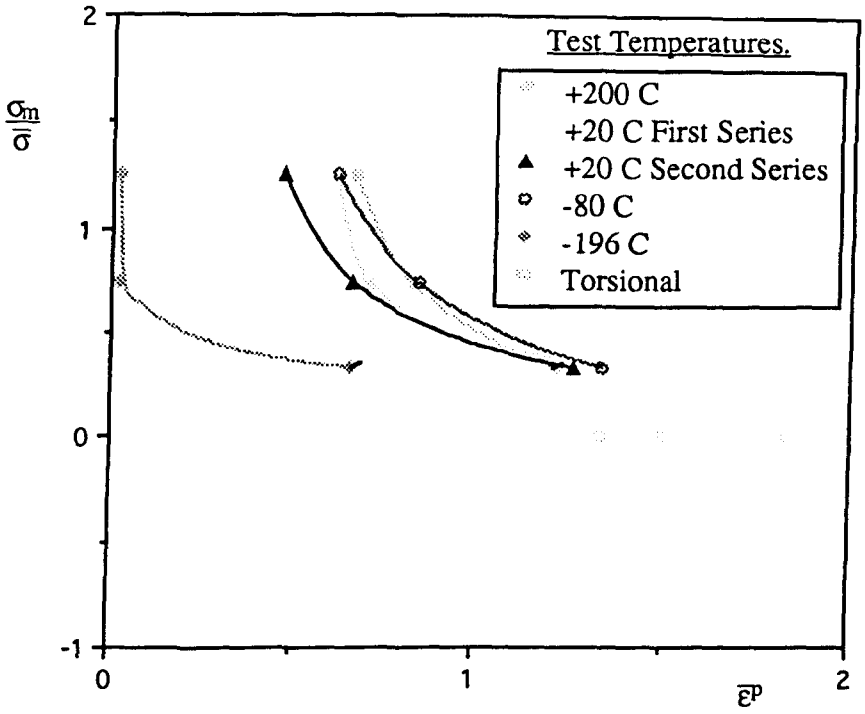

Figure 9.12: Stress Triaxiality for Temperature Tests.

Temperature (C)	Torsional Load (Nm)	Slope Angle (θ)	$\bar{\varepsilon}^p$
20	57.5	69	1.50
200	52.5	72.5	1.83
-80	67.5	66.5	1.33

Table 1: Torsional Experiment Results.

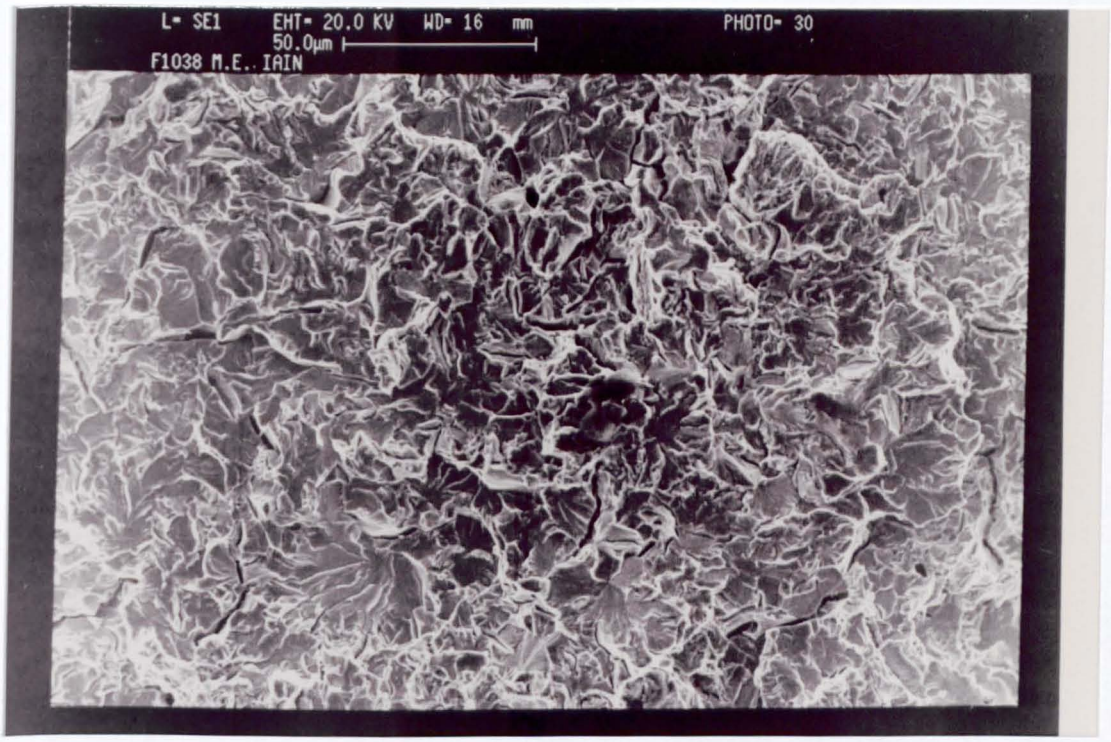

Figure 9.13: Cleavage Instability for Liquid Nitrogen Experiments.

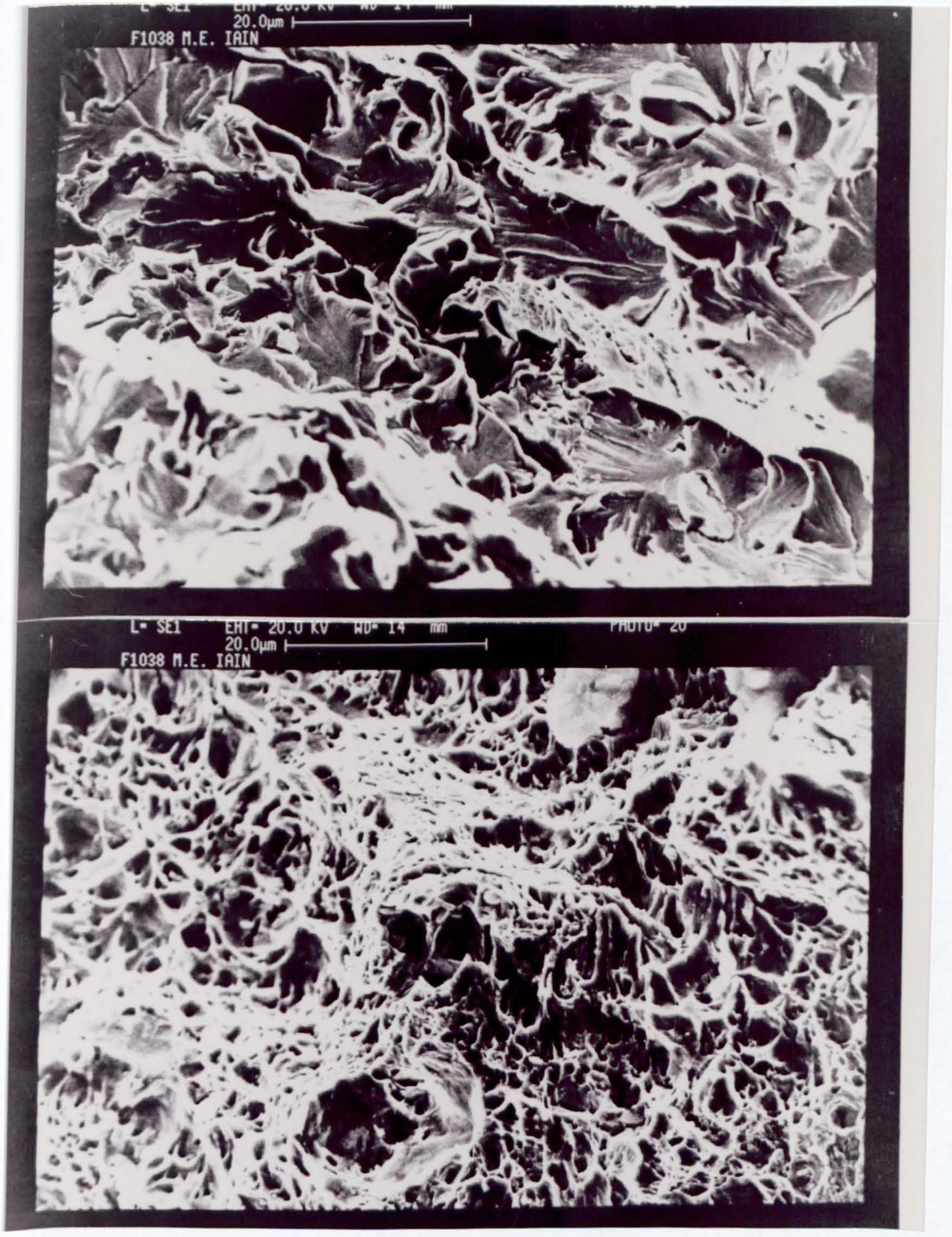

Figure 9.14a: Micromechanical Examination of Plane Tensile Specimen Experiment (-80 C).

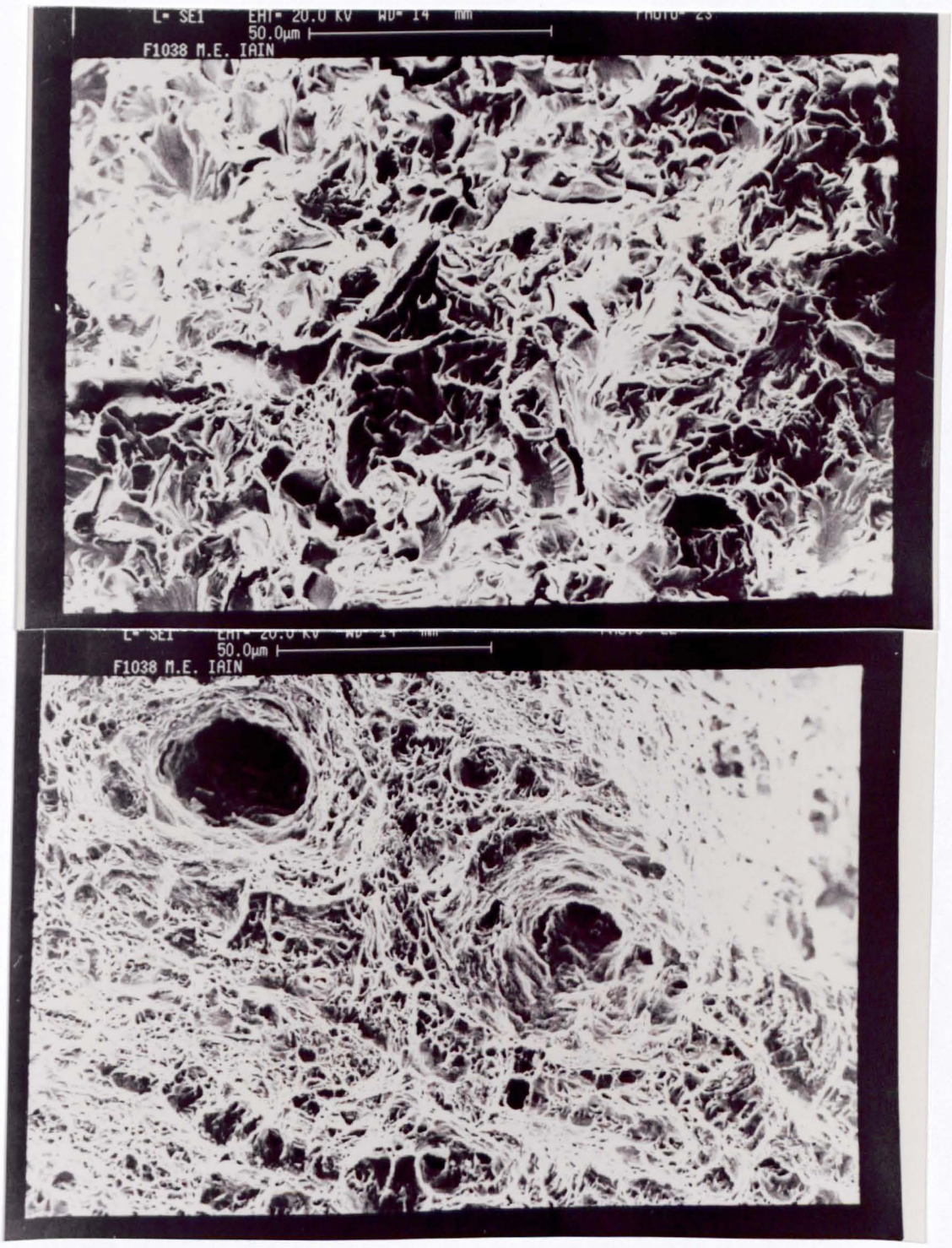

Figure 9.14b: Micromechanical Examination of A Notch Specimen Experiment (-80 C).

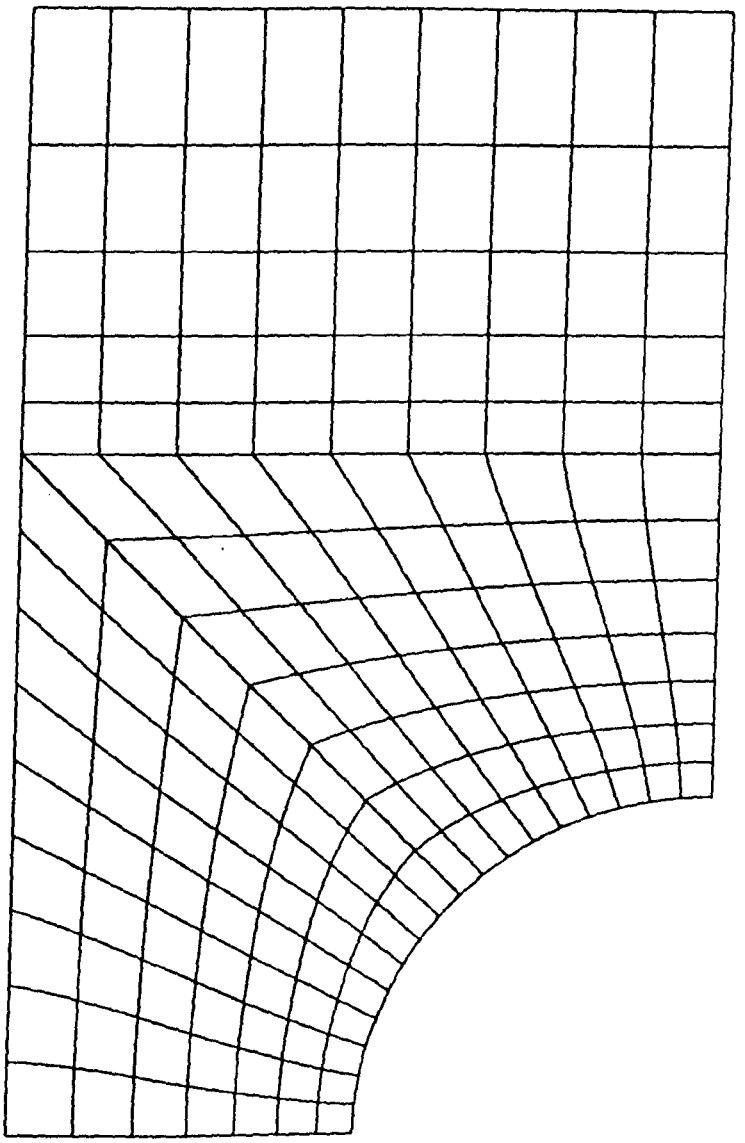

Figure 9.15: D Notch Finite Element Mesh.

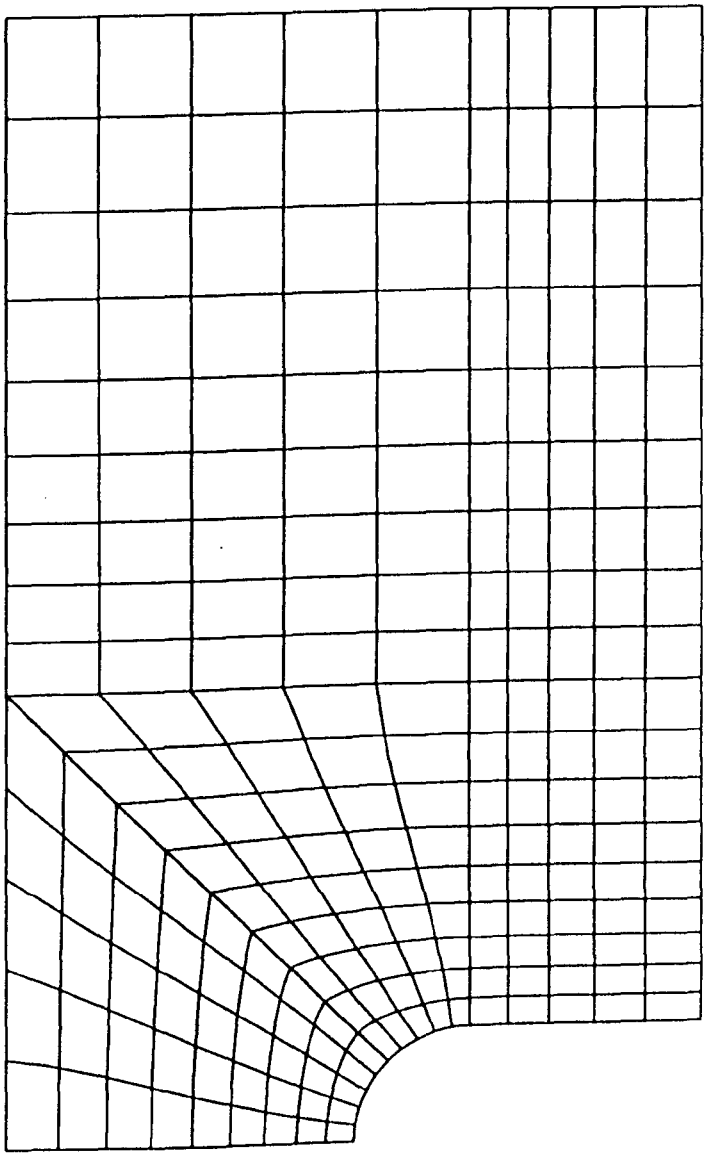

Figure 9.16: A Notch Finite Element Mesh.

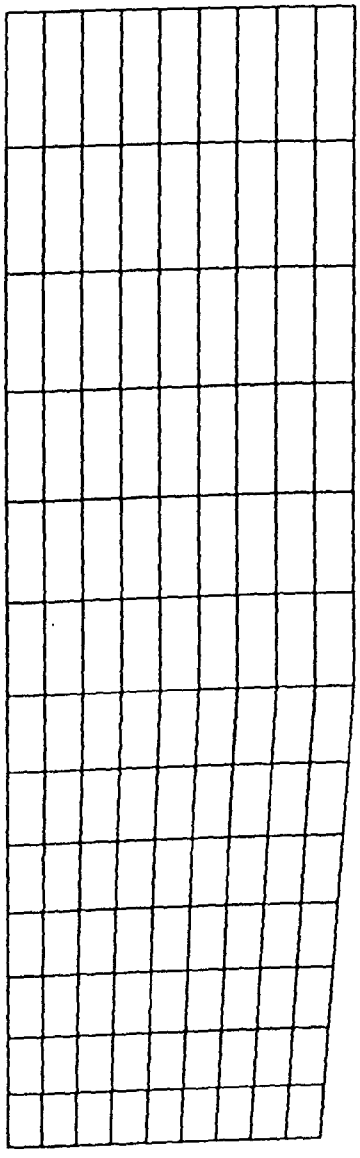

Figure 9.17: Plain Finite Element Mesh.

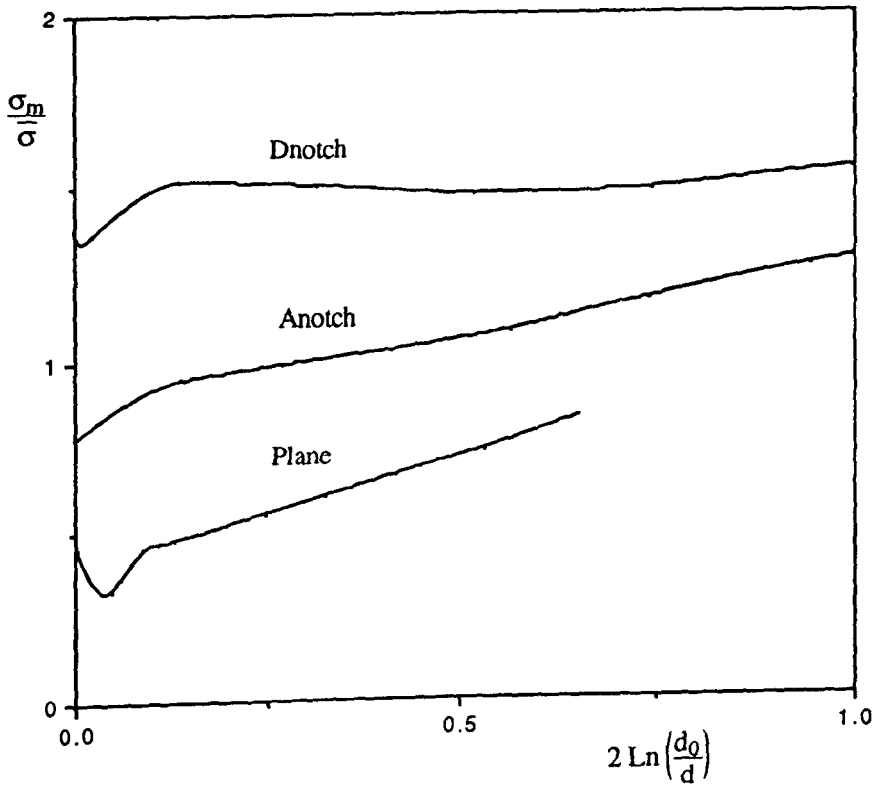

Figure 9.18: Triaxiality of Finite Element Analyses.

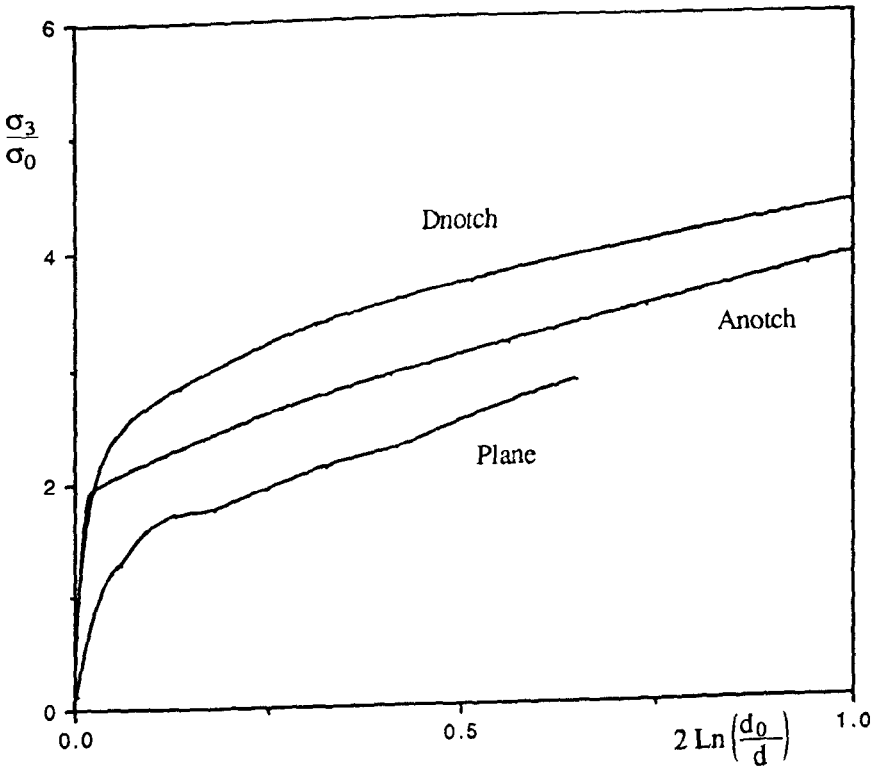

Figure 9.19: Maximum Principal Stress for Finite Element Analyses.

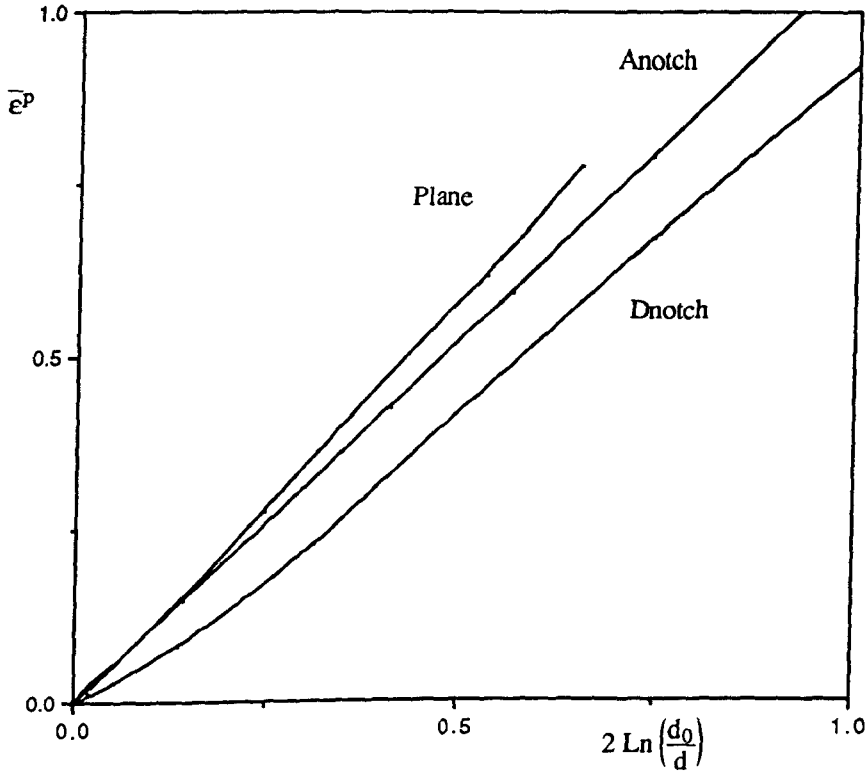

Figure 9.20: Eqivalent Plastic Strain for Finite Element Analyses.

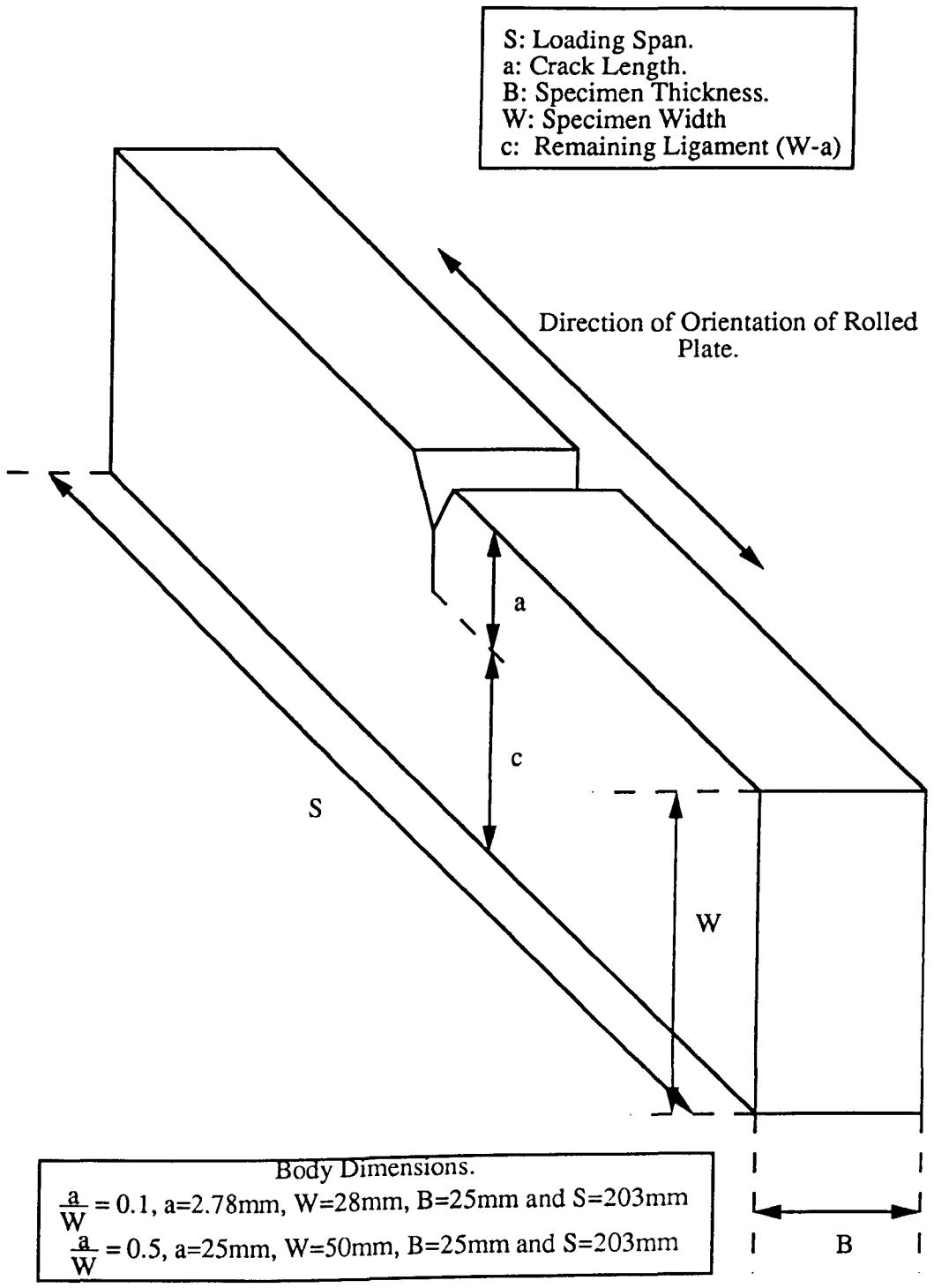

Figure 9.21: Diagram of Three Point Bend Specimen.

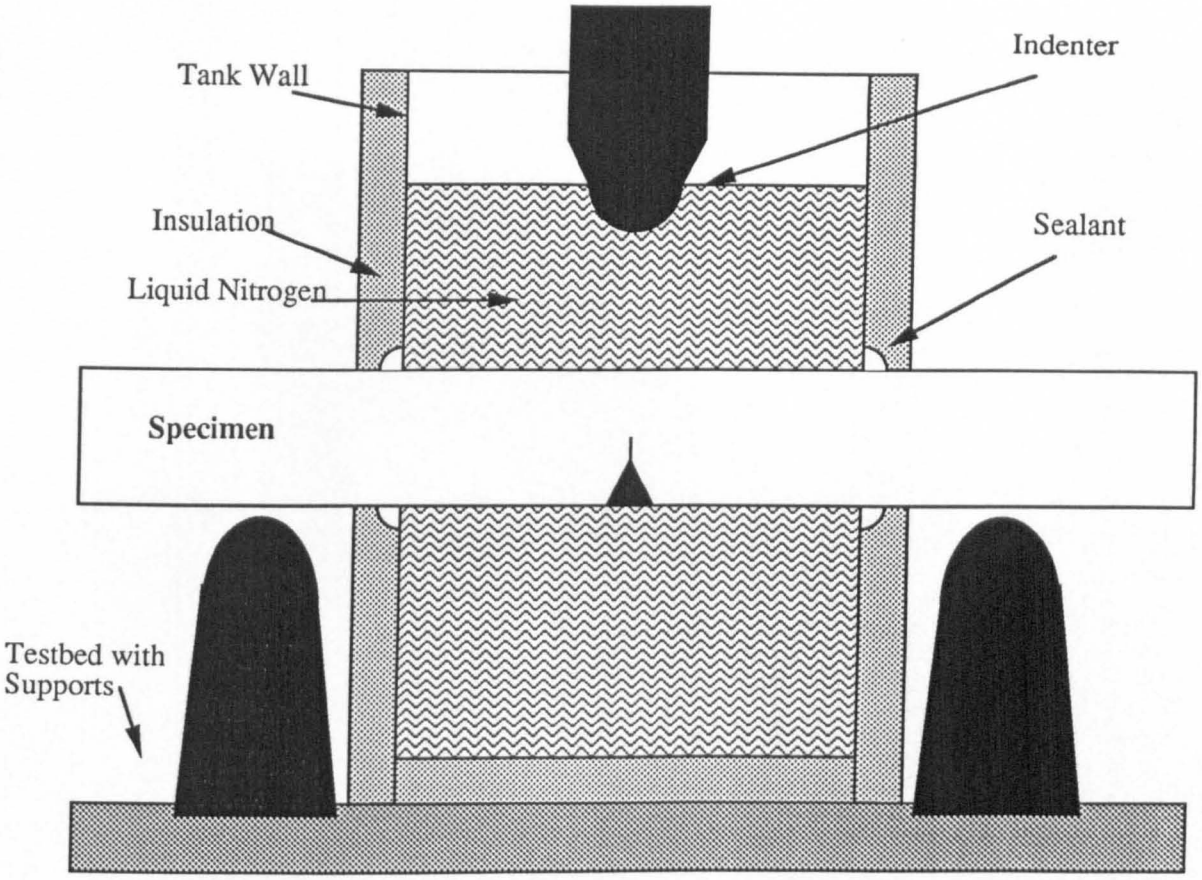

Figure 9.22: Liquid Nitrogen Temperature Experiment Set-Up.

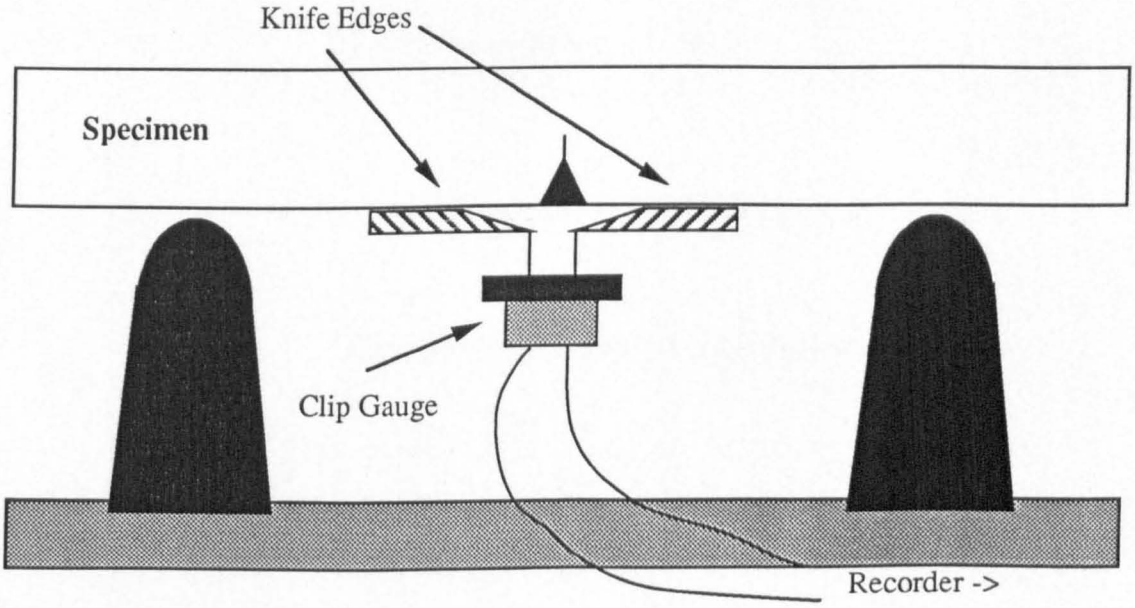

Figure 9.23: Three Point Bend Specimen with Clip Gauge Attached Knife Edges.

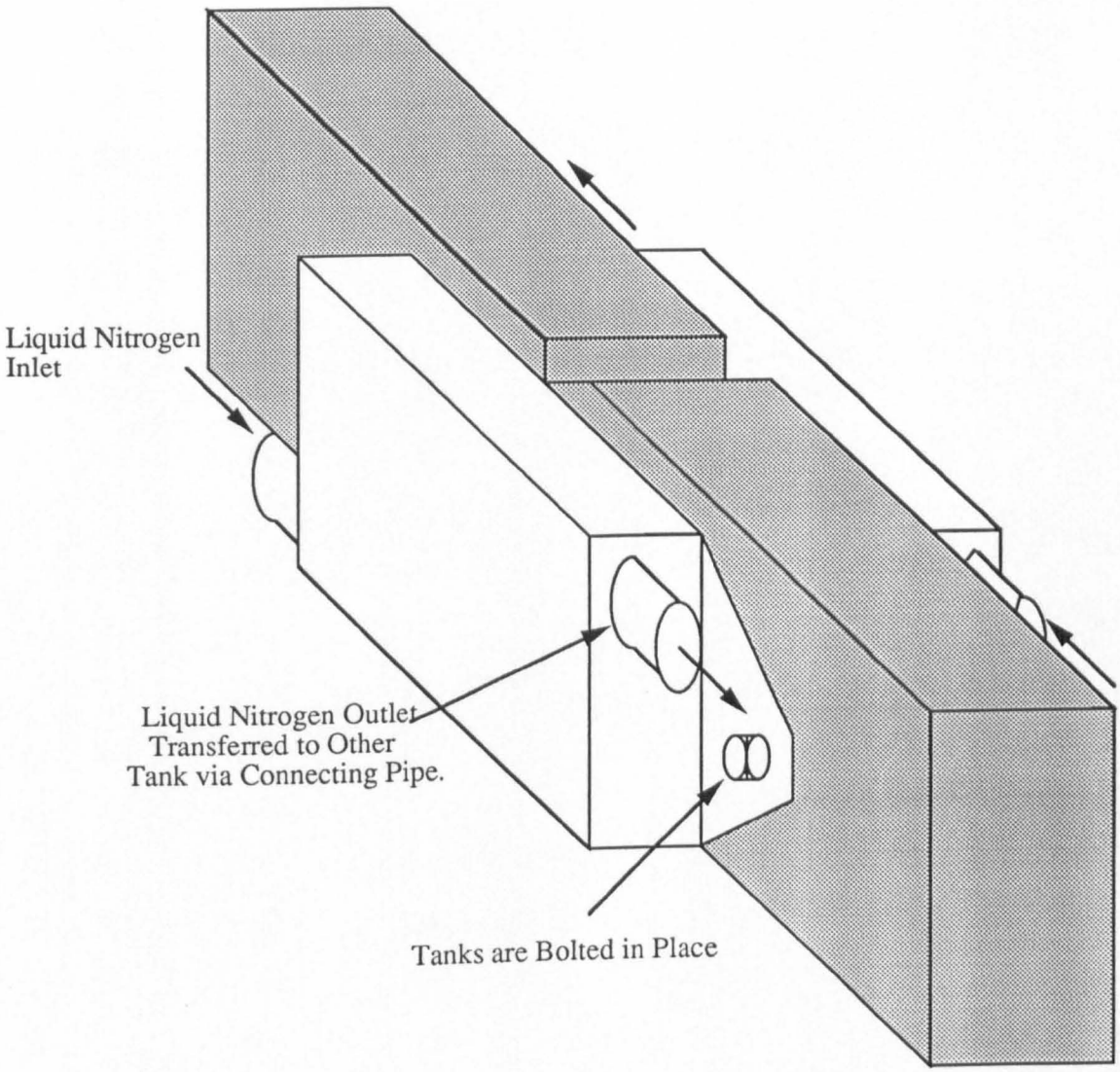

Figure 9.24: Tank and Specimen Arrangement.

Test No.	$\frac{a}{W}$	Temperature(°C)	Δa (mm)	δ_t (mm)	J_c (MN/m)	Experimental Mode
2	0.5	-196	-	-	0.0127	Cleavage
3	0.5	+20	0.393	0.79	0.766	Ductile
4	0.5	-196	-	-	0.0129	Cleavage
5	0.5	+20	0.5	1.178	1.140	Ductile
6	0.1	+20	0.429	1.821	2.748	Ductile
7	0.1	-196	-	-	0.0113	Cleavage
8	0.1	-196	-	-	0.0102	Cleavage
9	0.1	+20	0.789	2.964	4.113	Ductile
10	0.1	-50	0.5	1.643	2.150	Ductile
11	0.1	-50	1.786	3.036	4.130	Ductile
12	0.5	-50	0.393	1.172	0.9216	Ductile
13	0.5	-50	-	-	1.907	Ductile
14	0.5	-100	-	-	0.1631	Ductile/Cleavage
15	0.1	-100	-	-	2.185	Ductile/Cleavage
16	0.1	-100	-	-	1.260	Ductile/Cleavage
17	0.5	+20	0.589	1.75	1.142	Ductile
18	0.5	-142	-	-	0.0304	Cleavage
19	0.1	-138	-	-	0.294	Cleavage
20	0.5	+20	0.00	0.53	0.595	Ductile
21	0.5	+20	1.794	2.71	2.555	Ductile
39	0.5	-50	0.00	0.741	0.889	Ductile
40	0.5	-50	0.274	1.00	1.175	Ductile

Figure 9.25: Results of Three Point Bend Experiments.

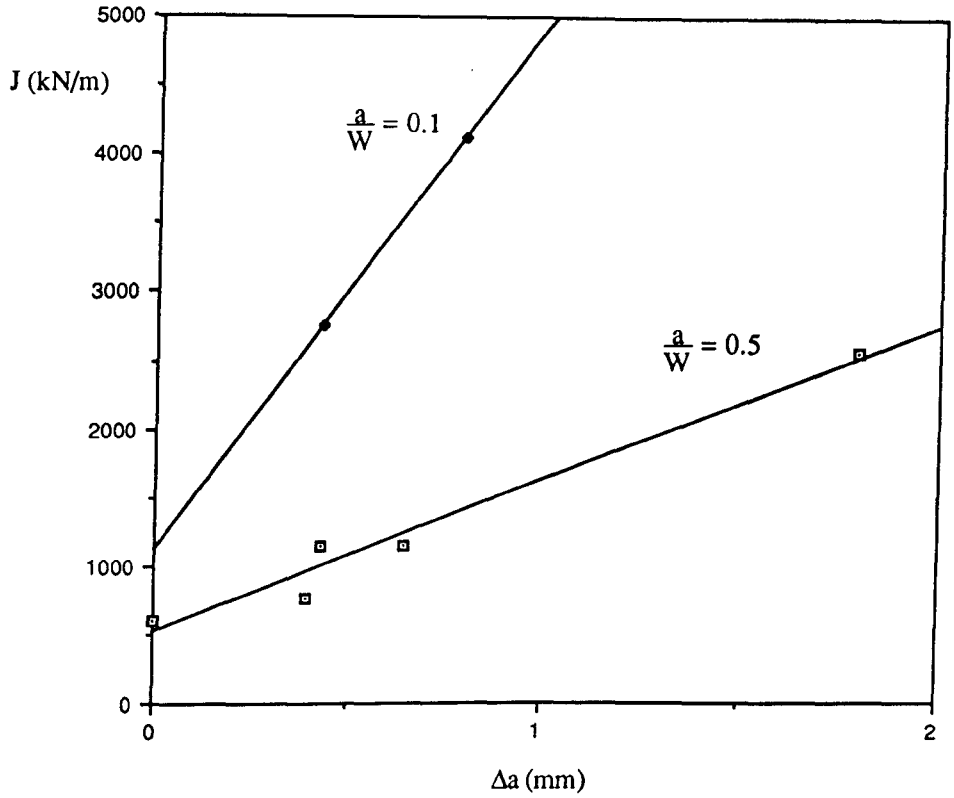

Figure 9.26: J versus Crack Extension at Room Temperature (SEC 3PB).

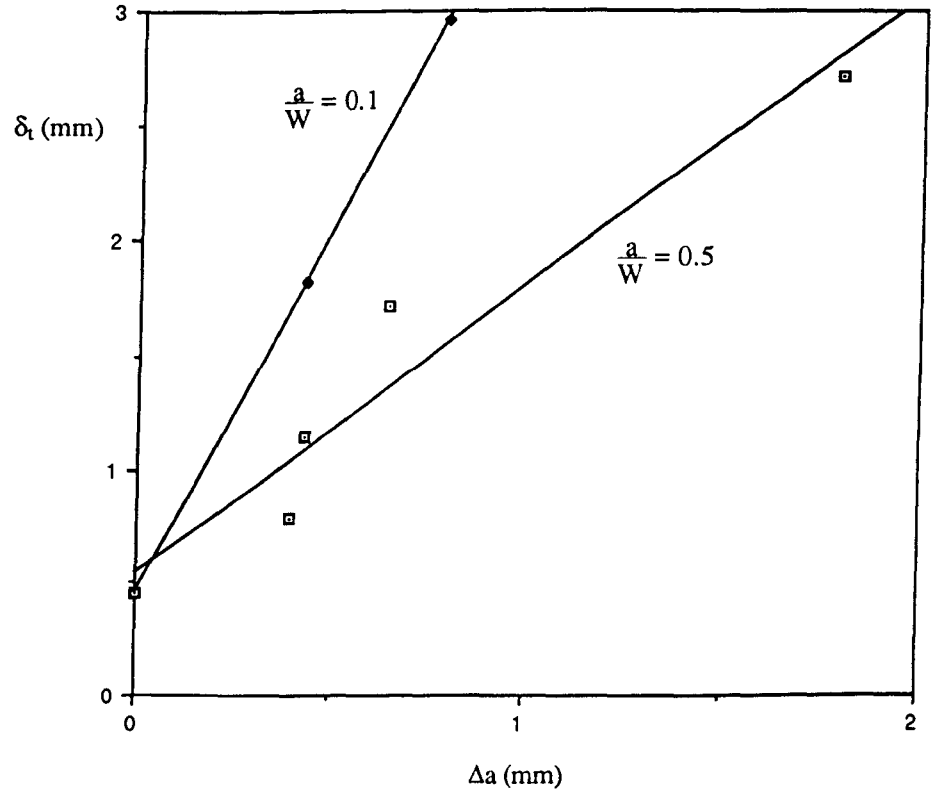

Figure 9.27: Crack Tip Opening versus Crack Extension at Room Temperature (SEC 3PB).

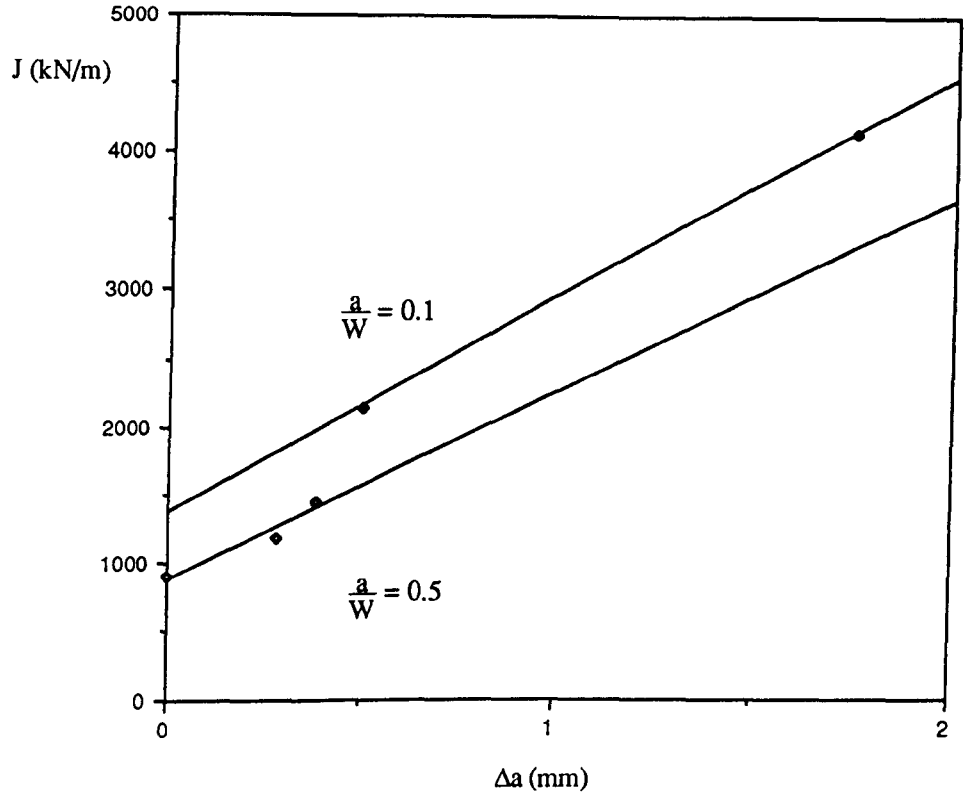

Figure 9.28: J versus Crack Extension at -50 C (SEC 3PB).

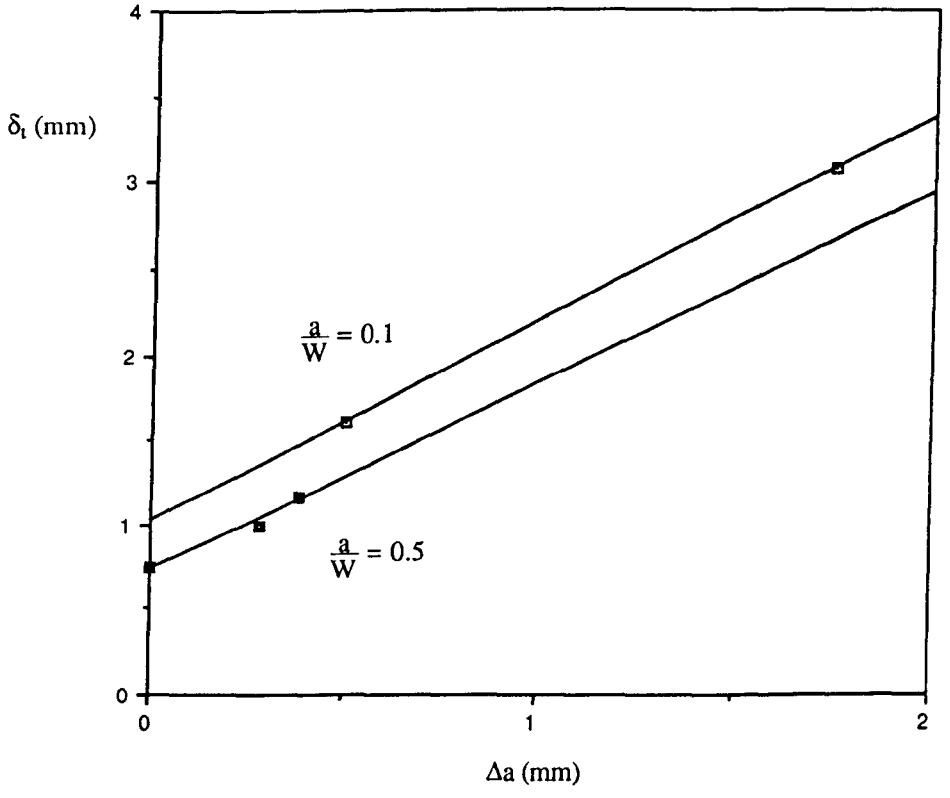

Figure 9.29: Crack Tip Opening versus Crack Extension at -50 C (SEC 3PB).

Figure 9.30: Detailed Crack Tip Photograph.

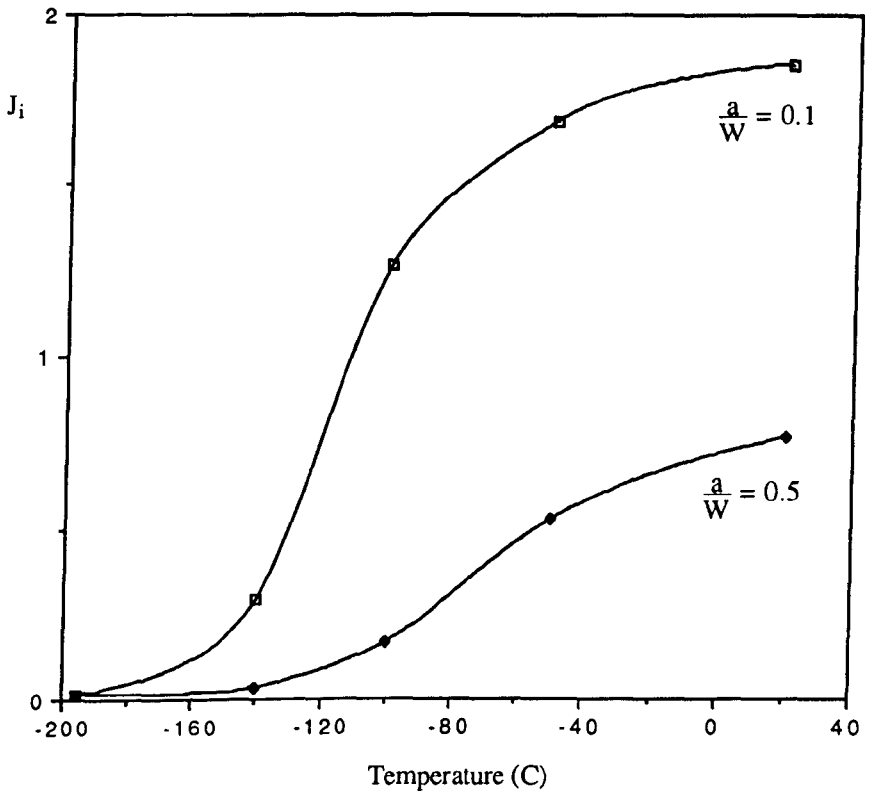

Figure 9.31: Transition Curve for BS4360 Grade 50D.

Final Conclusions.

The object of this work was to investigate and expand upon two parameter engineering fracture mechanics. There is no unique method for quantifying the degree of crack tip constraint, however the work within this thesis concentrated on the second term of the Williams expansion (T). The validity of this approach has been questioned at high levels of plasticity beyond limit load. However there is no doubt that the T-stress correctly identifies the plane strain geometries which lose constraint and does so beyond the confines of small scale yielding.

Unmodified boundary layer formulations (T=0) were used to investigate the validity of the HRR field as the generic small scale yielding reference solution. The results of which showed that the HRR field was only rigorously correct at the crack tip since at finite distances from the tip the associated higher order terms became significant. From these analyses the use of the HRR field was shown to be lacking, especially in relation to compressive T-stresses. Single parameter characterisation of these stress fields is therefore impossible and the small strain solution is proposed as an appropriate small scale yielding reference solution.

Effects of out of plane strain on elastic-plastic crack tip fields were also considered. Comparisons were made between full field solutions of geometries with tensile and compressive T stresses and compressive and tensile out of plane strains. In near plastic strain conditions elastic-plastic crack tip fields are found to be dominated by in-plane effects. The loss of J-dominance was attributable to the ingress of the remote compression field due to bending. In bodies which exhibit tensile T stresses crack tip deformation was shown to be limited by the ingress of the compression field induced by the applied bending moment. In bodies which exhibit compressive T stresses the influence of the compression field was reduced due to the size of the ligament in short crack problems.

A line-spring analysis allowing the determination of the first and second terms of the Williams (1957) expansion is presented for semi-elliptical cracks in tubular T-Joints expanding upon the work of Al-Ani (1988). These results provided good agreement with the full continuum analyses . This agreement therefore confirms the observations that the line-spring method is an accurate and computationally inexpensive method to infer the degree of crack tip constraint.

A J-T description of elastic-plastic crack tip fields has been combined with local failure criteria to indicate the effect of constraint on toughness. Such failure loci can be interpreted in terms of the effect of size and geometry on lower shelf toughness and the ductile-brittle transition temperature as measured by the maximum temperature at which cleavage initiation can occur. This transition temperature has been shown to decrease with crack tip constraint. This model also predicts the size dependence of the transition temperature for short and deeply cracked geometries.

Existing failure assessment methodologies are ultra conservative in the case of constraint dependent failures. Proposed is a practical engineering approach to account for crack tip constraint within integrity analyses through matching constraint dependent toughness. This allows a modified Failure Assessment Diagram to be generated relating a particular structure to a specific failure curve. The simplicity of this constraint based approach is underlined by the fact that no plasticity analyses have to be undertaken. This methodology therefore allows the major structural advantages of the enhanced toughness of low constraint structures to be utilised, solving the problem of geometry and constraint dependent toughness. This is achieved by using a modified Failure Assessment Diagram in which the toughness used to normalise the applied stress intensity factor is the constraint matched value, which recovers the original Failure Assessment Diagram with simply modified axes. This methodology has subsequently been adopted in the latest revision of R6.

References.

ABAQUS	1988a	Theory Manual, Hibbit, Karlsson and Sorenson. Inc., Providence, R. I.
	1988b	Users Manual, Hibbit, Karlsson and Sorenson. Inc., Providence, R. I.
ABAQUS	1993a	Theory Manual, Hibbit, Karlsson and Sorenson. Inc., Providence, R. I.
	1993b	Users Manual, Hibbit, Karlsson and Sorenson. Inc., Providence, R. I.
Aboutarabi, A. A.	1985	Ph.D. Thesis, Department of Mechanical Engineering, University of Glasgow.
Ainsworth, R. A.	1984	Engineering Fracture Mechanics, 19, 633.
Ainsworth, R. A.	1992	R6 Newsletter, 5, Nuclear Electric, Berkely.
Al-Ani, A.M.	1988	M.Sc. Thesis, Department of Mechanical Engineering, University of Glasgow.
Al-Ani, A.M.	1991	Ph.D. Thesis, Department of Mechanical Engineering, University of Glasgow.
Al-Ani, A. M. and Hancock, J. W.	1991	J. Mech. Phys. Slds., 39, 23.
Amazigo, J. C.	1978	SIAM-AMS Proceedings, Fracture Mechanics, 12,125
Anderson,T.L. and. Dodds R.H	1991	J. Testing and Evaluation, 19, 123.
Argon, A. S., Im, J. and Safoglu, R.	1975	Metal. Trans.A, 6A, 261.
A.S.T.M.	1988	Annual Book of A.S.T.M. Standards, A.S.T.M., Philadelphia, PA., USA.
Barenblatt, G. I.	1962	Adv. Appl. Mech., 7, 55.
Barsoum, N. O.,	1976	Int. J. Num. Method Eng., 10,25.
Bennet, P. E. and Sinclair, G. M.	1966	J. Basic. Eng., Trans., ASME Series D, 88,518.

Beremin, F. M.,	1983	Metal. Trans. A., 14A, 2277.
Berg, C. A.	1962	Proceedings '4th US National Congress of Applied Mechanics', ASME, NY.
Betegón, C	1990	Ph.D. Thesis , University of Oviedo, Spain.
Betegón, C. and and Hancock, J.W.	1991	'Fracture Behaviour and Design of Materials Structures', ECF8,999, Materials and Structures ,U.K.
Betegón, C. and Hancock, J.W.	1991	J. Appl. Mech., 58, 104.
Bilby, B. A., Cardew, G. E., Goldthorpe, R. and Howard, I.	1986	'Size effects in Fracture', I. MechE., London, 37.
Bridgman, P. W.	1952	'Large Plastic Flow and Fracture', McGraw and Hill, New York.
B. S. 7448 Part 1	1991	'Fracture Mechanics Toughness Tests', British Standards Institute, London.
Cherepanov, G. P.	1967	J. Appl. Math. Mech., 31, 305.
Crandall, S. H. and Dahl, N.C.	1959	An Introduction to the Mechanics of Solids, McGraw-Hill, NY.
Curry, D. A., and Knott, J. F.	1976	Metal Science, 10, 1.
Curry, D. A., and Knott, J. F.	1978	Metal Science, 12, 511.
Curry, D. A., and Knott, J. F.	1979	Metal Science, 13, 341.
Dodds, R. H., Anderson, T. L. and Kirk, M. T.	1991	Int. J. Frac., 48, 1
Dowling, A. R. and Townley, C.	1975	Int. J. Press. Ves., 3, 77.
Du, Z.-Z. and	1989	J. Press. Vess. Tech., 111, 247.

Hancock, J. W.		
Du, Z.-Z. and	1991	J. Mech. Phys. Slds., 22, 17.
Hancock, J. W.		
Dugdale, D. S.	1960	J. Mech. Phys. Slds., 8, 100
EPRI	1981	EPRI NP-1931, Project 1237-1, Electric Power Institute.
Eshelby, J. D.	1968	'Stress Analysis of Cracks.', ISI Publications, 13,121.
Ewing, D.	1968	J. Mech. Phys. Slds., 16, 205.
Green, A.P. and	1956	J. Mech. Phys. Slds., 4, 128.
Hundy, B.B.		
Griffiths, A. A.	1921	Phil. Trans. Roy. Soc., A221, 163.
Haigh, B. P.	1923	Rept.Brit. Assoc., 358.
Hancock, J. W. and	1976	J. Mech. Phys. Slds., 24, 147.
MacKenzie, A. C.		
Hancock, J. W. and	1983	J. Mech. Phys. Slds, 31, 1.
Brown, D. K.		
Hancock, J. W.,	1991	ASTM Symposium on Constraint Effects in
Reuter, W. A.,		Fracture, Indianapolis.
and Parks, D. M.		
Hill, R	1952	J. Mech. Phys. Slds., 1, 19.
Henshell, N. B.,	1975	Int. J. Num. Eng., 9, 249.
and Shaw, K. G.		
Holzmann, M and	1971	J. Iron Steel Inst., 209, 836.
Man, J.		
Huang, X. and	1986	J. Eng. Frac. Mech., 30, 25.
Hancock, J. W.		
Hutchinson, J. W.	1968	J. Mech. Phys. Slds., 16, 12.
Hutchinson, J. W.	1978	J. Mech. Phys. Slds., 26, 163.
Ilyushin, A. A.	1946	Prikadnaia Matematika i Mekhanika, 10,347.
Inglis, C. E.	1913	Trans. Inst. Nav. Arch., 55, 219.

Irwin, G. R. and Kies, J. A.	1958	Weld. Res. Supl., 17, 95.
Irwin, G. R.	1957	J. Appl. Mech., 24, 361.
Karstensen, A., Nekkal, D. and Hancock, J. W.	1994	to be published.
Kfouri, A. P.	1986	Int. J. Frac., 30, 301.
Kirkcaldy, D.	1860	Proc. Scot. Shipbuilders Assoc., Appendix,74.
Knott, J. F.	1966	J. Iron Steel Inst., 204, 104.
Knott, J. F.	1967	J. Mech. Phys. Slds., 15, 97.
Knott, J. F.	1973	'Fundamentals of Fracture',London.
Kumar, V.and. Shih, C.F	1981	ASTM STP 700, 406, ASTM, Philadelphia, Pa.
Kumar, V., German, M.D and Shih, C. F.	1981	EPRI Report NP-1931, Palo Alto, CA., USA
Larsson, S. G. and Carlsson, A. J.	1973	J. Mech. Phys. Slds., 21, 263.
Levers, P. S. and Radon, J. C.	1983	Int. J. Frac., 19, 311.
Levy, N., Marcal, P. V., Ostergren, W. J. and Rice, J. R.	1971	Int. J. Frac. Mech., 4, 143.
Li, Q.F.	1985	Engineering Fracture Mechanics, 22, 9.
Li, Q.F.,Zhou, L. and Li, S	1986	Engineering Fracture Mechanics, 23, 925.
Li, F. Z. and Wang, Z.	1986	Scientia Sinica (Series A), 19, 311.
Lin, T., Evans, A. G. and Ritchie, R.O	1986	J. Mech. Phys. Slds.,5, 477.
Ludwik, P. and	1923	Stahl und Eisen, 43, 999.

Scheu, R.		
McClintock, F. A. and Irwin, G. R.	1965	ASTM STP381, 84, ASTM, Philadelphia, Pa.
McClintock, F. A	1968	J. Appl. Mech., 35, 363.
MacKenzie, A. C., Hancock, J. W. and Brown, D. K.	1977	Engineering Fracture Mechanics, 9, 167.
McMeeking, R. M.	1977	J. Mech. Phys. Slds., 25, 357.
McMeeking, R. M. and Parks, D. M.	1979	ASTM STP668, 175, ASTM, Philadelphia, Pa.
Miller, A. G. Containing	1987	'Review of Limit Loads of Structures Defects', Nuclear Electric Publication TPRD/B/0093/N82.
Milne, I., Ainsworth, R. A., Dowling, A. R. and Stewart, A. T.	1988	Int. J. Press. Vessels and Piping., 32, 1.
Mudry, F.,	1989	'The Assessment of CrackedComponents by Fracture Mechanics', ed L .H.Larson, 133, EGF4, MEP, London.
Murakami, Y.	1987	'Stress Intensity Handbook', Vol. 1, Pergamon.
Oates, G.	1968	J. Iron Steel Inst., 206, 930.
Oates, G.	1969	J. Iron Steel Inst., 207, 353.
O'Dowd, N.P. and Shih, C.F.	1991	J. Mech Phys Slds, 39,989.
O'Dowd, N.P. and. Shih, C.F	1992	J. Mech Phys Slds, 40,1041
Orowan, E.,	1948	Rep. Prog. Phys., 12, 185.
Parks, D. M.	1974	Int. J. Frac., 30, 301.
Parks, D.M.	1991	'Some Topics in Deformation and Fracture' ed A.Argon Springer-Verlag.

Parks, D. M. and. Wang, Y. Y	1988	ASME Symposium on 3D effects in Fracture, ASME, New York.
Paris, P. C.	1972	ASTM STP 514, 21, ASTM, Philadelphia, Pa..
PATRAN	1988	Users Manual, PDA Engineering, Costa Mesa, California.
PATRAN	1990	Users Manual, PDA Engineering, Costa Mesa, California.
PD6493	1991	"Guidance on methods for assessing the acceptability of flaws in fusion welded
structures.",		B.S.I.
R6, Revision 3	1986	"Assessment of the Integrity of Structures containing Defects.", R/H/R6-Revision 3.
Rice, J. R.	1968	J. Appl. Mech., 35, 379.
Rice, J. R.	1969	Fracture (ed. Liebowitz), 2, 213.
Rice, J. R. and Rosengren, G. F.	1968	J. Mech. Phys. Slds., 16, 1.
Rice, J. R. and Johnson, M. A.	1970	'Inelastic Behaviour of Solids', McGraw-Hill, New York.
Rice, J. R. and Levy, N. J.	1972	J. Appl. Mech., 39, 185.
Rice, J. R. and Tracey, D.	1969	J. Mech. Phys. Slds., 17,201.
Rice, J. R. and Tracey, D.	1972	'Computational Fracture mechanics', Brown University, Providence, Rhode Island.
Rice, J. R.	1972	Int. J. of Solids and Structures, 8, 751.
Rice, J. R.,	1974	J. Mech. Phys. Slds., 22, 17.
Rice, J. R.,	1976	Theoretical and Applied Mechanics, 1, 207.
Rice, J. R., Paris, P. C. Merkle, J. G. and	1973	ASTM STP536, 231, ASTM, Philadelphia, Pa.
Ritchie, R. O., Knott, J. F.and Rice, J. R.	1973	J. Mech. Phys. Slds., 21,395.

Robinson, G. H. and Tetelman, A. S.	1974	ASTM STP559, 139, ASTM, Philadelphia, Pa.
Rooke, D. P.and Cartwright, D. J.	1976	"Compendium of Stress Intensity Factors", H.M.S.O., London.
Rosenfield, A. R., Dai, P. K. and Hahn, G, T.	1966	Proceedings '1st International Conference on Fracture',Sendai 1965, 1,223.
Sham, T.- L.	1991	Int. J. Fracture., 48, 81.
Sharma, S. M. and. Aravas, A	1991	J. Mech. Phys. Slds., 39, 1043.
Shih, C. F.	1981	J. Mech. Phys. Slds., 29, 305.
Shih, C. F.	1983	Brown University Report, MRL E-147, Brown University, USA.
Shih, C. F. and German, M. D.	1981	J. Appl. Mech., 53, 27.
Shih, C.F,. O'Dowd, N.P and Kirk, M.T	1991	ASTM Symposium on Constraint Effects in Fracture, Indianapolis
Shih, C. F., German, M. D. and Kumar, V.	1981	Int. J. Press. Ves., 9, 159.
Smith, E. Fracture,	1966	Proc. Conf. Physical Basis of Yield and 36, Inst. Phys. and Phys. Soc., Oxford.
Stump, D. M. and Zywicz, E.	1993	Eng. Frac. Mach., 45, 61.
Sumpter, J. D. G. and Turner, C. E.	1973	Second Int. Conf. on Press. Vessel Tech., 2, 1095, ASME.
Sumpter, J. D. G. and Turner, C. E	1976	ASTM STP 601, 3, ASTM,Philadelphia, Pa.
Sumpter, J. D. G.	1982	Int. J. Press Ves. and Piping., 10,169.
Sumpter, J. D. G.	1986	Design against Fracture In Weld Structures, ARE, Dumfermline , Scotland. 16.

Sumpter, J. D. G.	1987	Fatigue Fract. Eng. Mat. Struc., 10,479.
Sumpter, J. D. G. and, Hancock, J. W.	1991	Int. J. Press Ves. and Piping., 45,207.
Sumpter, J. D. G.	1991	ASTM Symposium on Constraint Effects in Fracture, Indianapolis.
Sumpter, J. D. G. and, Forbes, A. T.	1992	Proccedings '1st Int. Shallow Crack Conf.', TWI, Cambridge.
Sumpter, J. D. G.	1993	'Constraint Effects in Fracture', Philadelphia., Pa.
Tada, H., Paris, P. and Irwin, G.	1974	'The Stress Analysis of Cracks Handbook', Del Research Corporation.
Tetelman, A. S., Wilshaw, T. R. and Rau Jr., C. A.	1968	Int. J. Frac. Mech., 4, 147.
Thomson, R. D. and Hancock, J. W.	1984	Int. J. Frac. Mech., 24, 209.
Tracey, D.	1976	J. Eng. Mats and Tech., 98,146, ASME.
Wang, Y.Y.	1991	PhD Thesis Department of Mechanical Engineering M.I.T. Cambridge, Mass.
Weibull, W.	1939	Ing. Vetenskap. Akad. Handl., 12, 153.
Wells, A. A.	1961	The Crack Propagation Symposium, 210, Cranfield
Westergaard, H. M.	1939	J. Appl. Mech., 61, 49.
Williams, M. L.,	1957	J. Appl. Mech., 24, 111.
Wilshaw, T. R., Rau, C. A. and Tetelman, A. S.	1968	Engineering Fracture Mechanics, 1, 191.
Xia, L., Wang, T. C. Shih, C. F. and	1993	J. Mech. Phys. Slds., 41,665.
Yang, S., Chao, Y. J. and Sutton, M. A.	1993a	Engineering Fracture Mechanics, 45, 1.

Yang, S., Chao, Y. J. and Sutton, M. A.	1993b	Acta Mechanica, 98, 79.
Zienkiewicz, O. C.,	1971	'Finite Element Methods in Engineering Science.', McGraw and Hill.